University of California
Los Angeles

Dynamics and Multiplicity of Brown Dwarfs and Young, Low Mass Stars

A dissertation submitted in partial satisfaction
of the requirements for the degree
Doctor of Philosophy in Astronomy

by

Quinn Morgan Konopacky

2009

The dissertation of Quinn Morgan Konopacky is approved.

Edward Young

Ian McLean

Andrea Ghez, Committee Chair

University of California, Los Angeles

2009

Table of Contents

List of Figures

List of Tables

Acknowledgments

Thinking back on these 23 years of school, I find it almost difficult to comprehend that I am now standing near the very end of this scholastic journey and am about set off on fresh new endeavors. I cannot imagine having been able to make it this far without the support of so many individuals that it has been my honor to call family and friends.

First, I thank my parents, Mark and Candice. I realize continually how amazing these two individuals are and how lucky I am to call them Dad and Mom. Thanks Daddy, for buying me that telescope on a hot summer day in Portland circa 1997, and for inspiring me to be an allstar academically. I can only pretend to be as smart as you are. Sorry I didn't quite become a naturopath, Ma, but I've got a Dr. in front of my name anyway! You always nursed my ills and healed my troubled body and spirit. And you always made me feel good about myself even when I didn't want to. I am continually thankful for your love and unending support. Mom and Dad, this is for you.

I thank my sisters, Courtney and Hylary. Though they remind me that I belong in a box labeled "dorks and dweebs", they do so in the most heartfelt of ways. Thanks Court for giving me competition and a level of performance to work towards. And thanks Hyls for being my eternal playmate, a quality that I believe is underappreciated for stress relief and good times. I never laugh so hard as when I'm with you guys. Now I get to be Dr. Dork and Dweeb!

I thank my aunt and uncle, Marion and Tommy Powell, for always making me feel like the greatest kid/young adult on the planet. I don't think it is possible to describe the inner warmth that you two can give to someone. And thanks to my cousins, Paige and Blake, for all the fun growing up and the continued fun

we have now, and for the support in my scholastic endeavors.

Two family members who had an impact on my success have passed away during my time in graduate school. I thank my grandfather, Peter Konopacky, for his excitement about my academic achievements, which was conveyed by a continuous stream of newspaper clippings about astronomy. I also thank my great aunt, Allyne Brust, for being the first person to really get me thinking about pursuing astronomy as a career. I guess one never really knows how impactful a little glow-in-the-dark star poster will be.

I thank my graduate school advisor, Andrea Ghez, for allowing me to be a part of her research team. I feel incredibly fortunate to have had the opportunity to be mentored by a scientist of your caliber. The skills of carefulness, consistency, thoroughness, and persistence cannot have been taught better than they have by you, with words of encouragement always sprinkled in with the toughest lessons. No matter what my future work or research projects, I feel very confident that I have now have the right attitude and mindset to be a real scientist. Thank you for giving me that confidence. I also thank my dissertation committee, Michael Jura, Ian McLean, and Edward Young, for their support and encouragement.

I thank my former and future boss, Bruce Macintosh. Thank you for taking the time to train me to be an astronomer. I now know from experience that it is not always the easiest to teach a very green undergrad about research, but you are an amazing teacher and I am fortunate that I was trained by you. I am excited to be able to come back fully trained and ready to repay you for your efforts!

I also thank my several academic mentors who were not my direct supervisors but were instrumental in the completion of my thesis. Thank you Gaspard Duchêne, Caer McCabe, and Travis Barman for support, training, and stimulat-

ing discussions. Thank you for taking my ideas and questions seriously even if they were a bit naive at times. Thank you Russel White, for coming through when I was in a major pinch, with an assist from John Bailey, the most talented undergraduate I have ever seen.

I thank my longest running close friend, Lacey Townsend, for being a constant presence in my life. Even though we've lived in different cities for 10 years, I feel fortunate that you have made an effort to maintain our friendship. I thank the ever-fabulous Terry Beth Cherry for not only being my most surprising friend, but incredibly loyal, fun, and supportive. I would never have guessed when I was sitting with you in a tiny playhouse in Santa Monica watching a play where a woman with a green face spoke in nonsensical tongues that we'd be going on 6 years as roommates and 10 years as friends. I'm pretty lucky!

I thank Jessica Lu for allowing me the use of the unbelievable supercomputer in her head for some of my silly "learning to be a scientist" questions. I don't think I could have made it through graduate school without you. Thanks for letting me go along for your ride for those years. And thank you for being an amazing friend on top of everything else. I thank Sylvana Yelda for great friendship, good laughs, help with random Python questions, outlets for various departmental and scholastic frustrations, and shawarma dinners. I'll try not to steal all your comedy material, even though I want to most of the time. I thank my Bobsey Twin, Emily Rice, for company on various world travels and scientific endeavors. From the downpours of Toronto to the Millenium Wheel of London, the beaches of Kona to the wheelchairs of Waikoloa, you've been a terrific partner in crime. I also thank those grad school buddies who provided support, help, and fun on all different occasions: grads Seth Hornstein, Xi Chen, Tuan Do, Erin "Smithy" Smith, Karen Peterson, Matthew Barczys, Chao-Wei Tsai, Ryan Mallery, Alaina

Henry, Steve Berukoff, and postdocs Stan Metchev, Nate McCrady, Marshall Perrin, and Leo Meyer.

Thank you Shelley Wright, for all the reasons you already know, manifesting in the form of incredible risotto, loud pirate wenches, outstanding margaritas, Veuve champagne, eggplants, yummy pies, Obamapalooza, and untold hours of support. The future is very bright indeed.

I acknowledge that results presented in this thesis are based on published works with additional coauthors. In particular, Chapter Two is a version of Konopacky et al. (2007b) and Chapter Three is derived from Konopacky et al. (2007a). Support for my thesis work was provided by NASA Astrobiology Institute, and the Packard Foundation, and the NSF Science & Technology Center for AO, managed by UCSC (AST-9876783). Additional support was provided NASA Graduate Student Research Program (NNG05-GM05H) through JPL and the UCLA Dissertation Year Fellowship program. This thesis makes use of data products from the Two Micron All Sky Survey, which is a joint project of the University of Massachusetts and the Infrared Processing and Analysis Center/California Institute of Technology, funded by the National Aeronautics and Space Administration and the National Science Foundation. This thesis also presents data obtained at the W.M. Keck Observatory, which is operated as a scientific partnership among the California Institute of Technology, the University of California and the National Aeronautics and Space Administration. The Observatory was made possible by the generous financial support of the W.M. Keck Foundation. I also wish to recognize and acknowledge the very significant cultural role and reverence that the summit of Mauna Kea has always had within the indigenous Hawaiian community. I am most fortunate to have the opportunity to conduct observations from this mountain.

Vita

1980	Born, Santa Barbara, California, USA.
2003	B.S. (Astrophysics) University of California, Los Angeles
2003-2004	Teaching Assistant Division of Astronomy and Astrophysics University of California, Los Angeles.
2004-2005	Research Assistant Division of Astronomy and Astrophysics University of California, Los Angeles.
2005	M.S. (Astronomy) University of California, Los Angeles.
2005-2008	NASA Graduate Research Fellowship (GSRP) Sponsored through Jet Propulsion Laboratory Pasadena, CA.
2008-2009	Dissertation Year Fellowship University of California, Los Angeles Los Angeles, CA.

Publications

Smith, N., Foley, R. J., Bloom, J. S.; Li, W., Fillippenko, A. V., Gavazzi, R., Ghez, A., Konopacky, Q., Malkan, M.A., Marshall, P. J., Treu, T, Woo, J-H, "Late Time Observations of SN2006gy: Still Going Strong", 2008, The Astrophysical Journal, 686, 485

Tanner, A., Beichman, C., Akeson, R., Ghez, A., Grankin, K. N., Herbst, W., Hillenbrand, L, Huerta, M, Konopacky, Q., Metchev, S., Mohanty, S., Prato, L., Simon, M, "SIM PlanetQuest Key Project Precursor Observations to Detect Gas Giant Planets around Young Stars", 2007, The Astronomical Society of the Pacific, 119, 747

Konopacky, Q. M., Ghez, A. M., Rice, E. L., Duchêne , G., "New Very Low Mass Binaries in the Taurus Star-forming Region", 2007, The Astrophysical Journal, 663, 394

Konopacky, Q. M., Ghez, A. M., Duchêne , G., McCabe, C., Macintosh, B. A., "Measuring the Mass of a Pre-Main Sequence Binary Star throught the Orbit of TWA 5A", 2007, The Astronomical Journal, 133, 2008

Duchêne , G., Beust, H., Adjali, F., Konopacky, Q. M., Ghez, A. M., "Accurate Stellar Masses in the Multiple System T Tauri", 2006, Astronomy & Astrophysics, 457, 9

Blake, C. H., Bloom, J. S., Starr, D. L., Falco, E. E., Skrutskie, M., Fenimore, E. E, Duchêne , G., Szentgyorgyi, A., Hornstein, S., Prochaska, J. X., McCabe, C., Ghez, A., Konopacky, Q, Stapelfeldt, K., Hurley, K., Campbell, R., Kassis, M., Chaffee, F., Gehrels, N., Barthelmy, S., Cummings, J. R., Hullinger, D., Krimm, H. A., Markwardt, C. B., Palmer, D., Parsons, A., McLean, K., Tueller, J., "An Infrared Flash Contemporaneous with the γ-rays of GRB 041219a", 2005, Nature, 7039, 181

Kaisler, D., Zuckerman, B., Song, I., Macintosh, B. A., Weinberger, A. J., Becklin, E. E., Konopacky, Q. M., Patience, J., "HD 199143 and HD 358623: Two Recently Identified Members of the β Pictoris Moving Group", 2004, Astronomy & Astrophysics, 414, 175

Malkan, M., Webb, W., Konopacky, Q., "A Hubble Space Telescope Search for Lyman Continuum Emission from Galaxies at $1.1 < z < 1.4$", 2003, The Astrophysical Journal, 598, 878

Macintosh, B.A., Becklin, E. E., Kaisler, D., Konopacky, Q., Zuckerman, B, "Deep Keck Adaptive Optics Searches for Extrasolar Planets in the Dust of ϵ Eridani and Vega", 2003, The Astrophysical Journal, 594, 538

Abstract of the Dissertation

Dynamics and Multiplicity of Brown Dwarfs and Young, Low Mass Stars

by

Quinn Morgan Konopacky

Doctor of Philosophy in Astronomy

University of California, Los Angeles, 2009

Professor Andrea Ghez, Chair

This thesis addresses the formation and evolution of very low mass (VLM) stellar objects using their multiplicity and dynamics. First, we surveyed thirteen VLM ($M \lesssim 0.2\ M_{\odot}$) objects in the Taurus star-forming region using near-infrared speckle imaging techniques on the W.M. Keck 10 m telescope. Of these thirteen, five were found to be binary. These new systems have properties that differ significantly from older field VLM binaries in that the young systems have wider separations and lower mass ratios, supporting the idea that VLM binaries undergo significant dynamical evolution $\sim$5 - 10 Myr after their formation.

Second, we present a pilot study for our dynamics work in which we completed a five year monitoring campaign of the close binary TWA 5Aab in the TW Hydrae association, using speckle and adaptive optics on the Keck telescopes. Our observations allowed us to determine this system's astrometric orbit. We calculate a total mass of $0.71 \pm 0.14\ M_{\odot}\ (D/44\ pc)^3$ for this system.

Finally, we present the results of a 3 year monitoring program of a sample of 26 VLM field binaries using both astrometric and spectroscopic data obtained in conjunction with the laser guide star adaptive optics system on the Keck

telescope. By combining astrometry and spectroscopy, degeneracies in orbital parameters can be resolved and individual component masses can be obtained. We present relative orbits for 15 of these systems, which allow us to derive the total system mass. In addition, we find the absolute orbits for 6 systems in our sample, which allows us to derive individual masses. We compare our dynamical mass measurements to the predictions of theoretical evolutionary models and find that there are systematic discrepancies, where both models considered either underpredict or overpredict the correct mass. The discrepancies are a function of spectral type, with late M through mid L systems tending to have their masses underpredicted, while one T type system has its mass overpredicted. These discrepancies imply that either the temperatures predicted by evolutionary and atmosphere models are inconsistent for an object of a given mass, or the mass-radius relationship or cooling timescales predicted by the evolutionary models are incorrect.

CHAPTER 1

Introduction

Unraveling the mysteries surrounding the formation and evolution of stars and planets is one of the fundamental goals of modern astrophysics. Over the last several decades, continual advances in technology and telescope facilities have enabled the discovery of stellar objects with a range of masses and luminosities, existing in a variety of Galactic environments. The stellar mass function now extends from extremely massive stars ($\sim$100 $M_{\odot}$; e.g., Figer et al. 1998) down to incredibly small stellar objects ($\sim$0.01 $M_{\odot}$; e.g., Zapatero Osorio et al. 2008). In addition, star formation has been observed in both nearby Molecular Clouds and in the most extreme, turbulent regions of the Galaxy previously believed to be inhospitable to star formation (e.g., Ghez et al. 2003). These discoveries have necessitated a paradigm shift in the way star formation is understood and modeled as a continuous process, and have challenged some of the most basic tenets of the classic theory of stellar evolution.

Among the most significant discoveries that changed our conception of star formation was that of brown dwarfs. Originally postulated to exist by Kumar (1963), brown dwarfs are objects that are never massive enough to sustain hydrogen burning in their cores, making them a class of objects distinct from stars often referred to as "substellar". The first calculations by Kumar (1963) showed that these objects should be less massive than $\sim$0.1 $M_{\odot}$. More detailed calculations have now shown that this mass limit is in fact closer to $\sim$0.08 $M_{\odot}$ (e.g., Grossman

et al. 1974, D'Antona & Mazzitelli 1985, Burrows et al. 1993, Chabrier et al. 2000), and that brown dwarfs have masses extending all the way into the planetary mass regime ($\sim$0.01 $M_{\odot}$). With the first identification of bonafide brown dwarfs by Becklin & Zuckerman (1998) and Nakajima et al. (1995), the era of discovery and characterization of this unique class of objects began, and continues to the present day. Detailed characterization of newly discovered brown dwarfs led to the definition of two new spectral classes: the L dwarfs ($T_{Eff} \sim$ 1400 - 2300 K), and the T dwarfs ($T_{Eff} \sim$ 600 - 1400 K, Kirkpatrick 2005). With these discoveries, we now seek a comprehensive theory of star formation that accounts for these very low mass (VLM) objects. In addition, we seek an accurate description of the physics of ultracool objects, which in turn provides a detailed account of the evolution of their fundamental properties.

Observations of brown dwarfs in systems of multiple components probe both the formation and evolution of substellar objects. By determining the multiplicity properties of VLM objects, constraints on the processes by which they form can be achieved. The most fundamental parameter in determining the properties and evolution of a brown dwarf is its mass, and therefore empirical mass measurements are of critical importance. Brown dwarf masses can be measured by finding the orbital solutions for sources that are part of binary systems. These mass measurements, in turn, can be used to gain new insight into the evolutionary processes at work in substellar objects.

The goal of this thesis is to provide new constraints on both the formation and evolution of very low mass objects using their multiplicity and dynamics. Recent achievements in ground-based observations using high spatial resolution techniques have made it possible to achieve this goal. Section 1.1 describes current theories of brown dwarf formation and the details of modeling the evolution

of these objects after they form. Section 1.2 describes current observations of the multiplicity properties of VLM objects, and discusses previous dynamical mass measurements. Chapter 2 describes the results from this thesis work of a multiplicity survey of VLM objects in the Taurus star-forming region (adapted from Konopacky et al. 2007a). Chapter 3 then presents a pilot study for our dynamical mass work in which the orbital solution for a young, but slightly higher mass, binary, TWA 5a (adapted from Konopacky et al. 2007b), is found. Chapter 4, which forms the bulk of this thesis, presents the results of a 3 year astrometric and spectroscopic monitoring campaign of known VLM binaries. Orbital solutions are derived for these sources, providing mass measurements which are used to test evolutionary models. Finally, Chapter 5 summarizes the results of this thesis and discusses future directions that will allow for even more comprehensive tests and constraints of the formation and evolution of these objects.

1.1 Theories on the Formation and Evolution of Very Low Mass Objects

1.1.1 Formation Scenarios

One cause of changes in theories of star formation stems from the fact that in the traditional Jeans theory of star formation, the minimum mass of an object that can collapse is well-above the typical mass of a brown dwarf. Thus, formation theories adjusted to account for substellar objects have generally fallen into two camps - those that predict their formation in a mechanism similar to stars, modified to account for the lower required Jeans mass, and those that favor an independent formation mechanism.

Among the theories in favor of a star-like formation mechanism is that of

formation of very low-mass cores in turbulent clouds (i.e., Padoan and Nordlund, 2004). By invoking the process of turbulent fragmentation, which assumes molecular clouds possess super-sonic turbulence that allows for the creation of small, dense cores, the minimum Jeans mass can be driven down into the substellar regime. Observations of star forming molecular clouds have suggested that supersonic turbulence does exist within these clouds (Padoan et al. 2002). Additional work has shown that Jeans masses can be lowered in a star forming cloud by invoking a combination of turbulent velocities and the gravitational potential of the forming cluster itself (Bonnell et al. 2008). In this scenario, higher mass stars would tend to form first and their gravitational potential would generate very dense filaments of gas flowing into the cluster, out of which very low mass objects could form.

Moving into formation mechanisms dissimilar to that of stars, another well-studied method of brown dwarf formation is that of fragmentation of disks around higher mass stars. Such fragmentation has been demonstrated in models of both isolated (i.e., Rice et al. 2003, Goodwin & Whitworth 2007, Stamatellos & Whitworth 2009) and interacting disks (i.e., Watkins et al. 1998). In isolated disks, the disk fragmentation is caused by either the generation of spiral density waves or insufficient disk relaxation time, which creates lumpy structures. For interacting disks, a gravitational impulse on one disk from another generates an instability that can then fragment. For the majority of these scenarios the brown dwarfs eventually become unbound from their host star, forming the field population of free-floating substellar objects.

A more exotic theory of brown dwarf formation is that of ejection from natal cloud cores (i.e., Bate et al. 2002). In this theory, a number of pre-stellar embryos all accrete from the same reservoir of material. Dynamical interactions between

these embryos then cause some pre-stellar objects to be ejected from cloud, separating them from accretable material before they have attained a sufficient mass for hydrogen burning. Another investigated method of brown dwarf formation is that of photo-erosion of cores by nearby OB stars (i.e., Whitworth and Zinnecker, 2004). This allows for the generation of cores via more traditional mechanisms and does not require special initial conditions. Additionally, it accounts for the substantial impact high-mass stars have on their surrounding environment.

Many of these formation scenarios make testable predictions of the expected multiplicity of brown dwarfs. If stars and brown dwarfs form in a continuous process, the multiplicity properties of low mass objects should be roughly equivalent to that of higher mass counterparts. Thus, in various turbulent fragmentation scenarios, a relatively high binary fraction is predicted for both stellar and substellar objects (i.e., Padoan & Nordlund 2004), which is observed to be the case for stars in a variety of environments (e.g., Ghez et al. 1995, Duquennoy & Mayor 1991). Though the multiplicity of brown dwarfs is not extensively explored in most studies on disk fragmentation, a fair number of wide brown dwarf companions to high mass stars are expected in this scenario (Goodwin & Whitworth 2007). In the ejection scenario of brown dwarf formation, the violent dynamical interactions that give rise to brown dwarfs make it difficult for anything but the tightest binaries to survive, implying a multiplicity fraction of $<10\%$ (Bate et al. 2002). Therefore, if brown dwarfs are observed to have a relatively high rate of multiplicity, they are more likely to have formed in a manner similar to stars than by an independent mechanisms.

1.1.2 Evolutionary Models

The first detailed structural models of brown dwarfs were calculated by Grossman et al. (1974), balancing gravitational collapse with thermal and electron degeneracy pressure. Since that time, the understanding of both the interior and atmospheric properties of these objects has improved, resulting in more powerful models predicting how the fundamental properties of brown dwarfs evolve, including predictions of their observational properties in common passbands (i.e., Baraffe et al. 1995). However, the complicated nature of the physics incorporated into these models require numerous assumptions, where small changes in parameters will generate dramatically different results.

There are currently two sets of brown dwarf evolutionary models that are widely used: those of Burrows et al. (1997) and those of Chabrier et al. (2000). For their interior physics, Burrows et al. (1997) use the equations of state from Saumon et al. (1995), which treats the partial degeneracy of the interiors and allows for the physically sound derivation of interior/atmosphere boundary conditions. They also use the mixing length theory for the treatment of convection in these objects, where the mixing length is set to the pressure scale height. With these boundary conditions determined, Burrows et al. (1997) then employ techniques typically used in the modeling of planetary atmospheres, under the assumption brown dwarfs have similar atmospheric properties. They treat atmospheric opacities by accounting for the fact that several atomic and molecular species will condense at low temperatures. In these models, condensates are considered to be sequestered below the photosphere and thus are not included as an atmospheric opacity source.

The second set of popular substellar models are those of Chabrier et al. (2000). These models make use of the equation of state of Saumon et al. (1995), and

the mixing length theory of convection. They also incorporate the effects of conduction in the interiors of these objects, which becomes increasingly important as they age. In addition, they consider three types of atmospheres. The first, "NextGen", is based on atmospheres that are free of dust opacity and condensation. The second, called "DUSTY", includes the complete set of dust species described in the work of Allard et al. (2001), and take into account both the scattering and absorption properties of the dust. The final atmospheric model, called "COND" assumes that all dust-forming elements have condensed out of the atmosphere at sufficiently low temperatures, leading to their exclusion as opacity sources (which closely mirrors the Burrows et al. (1997) treatment). The principle behind these particular choices is that they likely represent the extrema of possible solutions, bracketing the true form of a brown dwarf atmosphere.

Complete calculation of these models, incorporating both the interior and atmospheric physics, allows for the generation of theoretician's H-R Diagrams, showing the predicted evolution for an object of a given mass. However, due to the different assumptions made in these models, their predicted masses are discrepant from each other by between 10 and 40% (see Figure 4.1). Therefore, depending on which model is used, different properties of substellar objects will be obtained, such as the classification of whether a source fall above or below the stellar substellar boundary or the relative number of stars to brown dwarfs in a star forming region. Both Burrows et al. (1997) and Chabrier et al. (2000) have placed a substantial emphasis on the atmospheric physics incorporated into their models, making clearly different assumptions. The atmospheric physics is thus an often-blamed culprit for discrepancies. Though work has been done to calibrate atmospheric models through spectral synthesis modeling (e.g., Cushing et al. 2008, Rice et al. 2009), little has been done in terms of comparing the predictions of evolutionary models to observed fundamental parameters to attempt to

shed light on the correct atmospheric model. Conversely, the assumptions about the interior physics of these objects appears to be much more similar. However, it is important to note that although the Burrows et al. (1997) models should agree quite well with the COND version of Chabrier et al. (2000) if the atmospheres are the only difference, there are clearly differences between them, implying that variable approaches to the interior physics are in part responsible for the discrepant mass predictions. Additionally, the combined interior and atmospheric physics of these objects drives important relationships such as the mass-radius relationship and cooling curves as a function of mass, neither of which have been throughly calibrated observationally. To combat these issues, calibration of these models is required via comparison of their predictions to empirical measurements.

1.2 The Properties of VLM Multiple Systems and Previous Dynamical Mass Measurements

Shortly after the initial discovery of brown dwarfs, it was recognized that constraining their multiplicity properties would have important implications not only for the constraint of formation scenarios, but also for future dynamical mass measurements. A number of surveys were conducted with the goal of discovering brown dwarf binaries. Initial surveys were primarily performed using high spatial resolution imaging afforded by the Hubble Space Telescope (HST). These surveys (Koerner et al. 1999, Reid et al. 2001, Bouy et al. 2003, Burgasser et al. 2003, Gizis et al. 2003) first targeted the field brown dwarfs discovered by the 2 Micron All Sky Survey (2MASS, Cutri et al. 2003), the Deep Near Infrared Survey of the Southern Sky (DENIS, The Denis Consortium, 2005) and the Sloan Digital Sky Survey (SDSS, Adelman-McCarthy et al. 2007). Additional surveys were performed using the Gemini Telescope's Hokupa'a curvature wavefront sensing

adaptive optics (AO) system (Close et al. 2002, 2003, Siegler et al. 2003, 2005). In addition, several spectroscopic surveys have probed field brown dwarfs for very close companions (Basri & Martín 1999, Joergens & Guenther 2001, Reid et al. 2002, Guenther & Wuchterl 2003, Kenyon et al. 2005, Joergens 2006, Basri & Reiners 2006). The net result of these surveys led to the discovery of comparatively low binary fraction amongst VLM objects in the field. Imaging surveys showed a binary fraction of between 7-15% for separations greater than $\sim$1 AU. By contrast, early M dwarfs have a $\sim$30% binary fraction (Delfosse et al. 2004). In addition, there appears to be a statistically significant truncation of binary separations above $\sim$20 AU, and systems tend to come in nearly equal mass pairs with mass ratios $\geq$0.8. Exploring these properties in more detail, Close et al. (2003) determined that field VLM binaries are more tightly bound than higher mass binaries, with a much higher minimum binding energy than what is predicted from normal dynamical evolution.

Later surveys of young VLM objects in star forming regions, performed primarily with HST, showed slightly different, though consistent, results (Martín et al. 2003, Kraus et al. 2005, 2006, Bouy et al. 2006). Binary fractions closer to 20% were observed in these studies, again with relatively tight separations and roughly equal masses. As younger sources more likely reveal the pristine outcome of the star formation process, the consistency between surveys of young and field VLM objects suggested that the low binary fraction and higher binding energies of these sources was due to their formation mechanism. The truncation of the separations of these objects coupled with the low multiplicity fraction suggested that perhaps a violent dynamical formation, like that of the ejection scenario, was possible. The census of young VLM object multiplicity is far from complete, with only a limited number of star forming regions probed and many VLM objects still to be imaged. More surveys are necessary to determine if these trends

continue to hold (see Chapter 2).

The discovery of large numbers of VLM binaries through these surveys lent itself naturally to the determination of dynamical masses. In the past, spectroscopic binaries have been primarily used to determine mass since they tend to be at closer separations, and hence have shorter orbital periods. Indeed, the first dynamical mass derived for a binary brown dwarf was for that of PPL 15 (Basri & Martín 1999), which has a semi-major axis of 0.03 AU. However, since many of these visual VLM binaries have separations <5 AU, dynamical masses can also be derived for these systems in a reasonable time frame for an observing program (with the advantage of providing a direct measure of the binary inclination). In order to find the orbital solution of visual binaries, high resolution imaging of these systems over extended periods of time are required to map a large fraction of the orbit. Systems that are capable of such monitoring include HST or large (8-10 m) ground based telescopes with adaptive optics systems (Wizinowich et al. 2000).

Prior to 2006, few visual binaries had mass determinations because of limitations in ground based high resolution technology. Adaptive optics (AO) on ground-based telescopes uses guide stars to monitor the turbulence of the Earth's atmosphere. AO systems can correct distortions in real time of the incoming guide star wavefront to create high angular resolution observations comparable to the diffraction limit of the telescope (Wizinowich et al. 2000). Natural guide star adaptive optics (NGS AO), which uses actual stars as guide stars, is limited to stars that are brighter than ∼13 in the R band. Because brown dwarfs are intrinsically cool objects, they are quite faint at optical wavelengths and rarely meet this criteria (Chiu et al. 2006). This limited monitoring of brown dwarf binaries with NGS AO to sources that were companions to brighter stars. Although in-

frared wavefront sensors like that on the Very Large Telescope (VLT) allow for more brown dwarfs to be monitored at high spatial resolution, the magnitude cut-off of ∼12 removes many faint, cool brown dwarfs as possible targets. Following the development of NGS AO technology, the first visual binary with a dynamical mass determination was the tight, nearby system GJ 569B ab (Lane et al. 2001). Monitoring of this system was performed from the with NGS AO, using the bright early M dwarf companion as the AO guide star. Next, 2MASS 0746+20 AB had its orbital solution determined by Bouy et al. (2004), using HST, speckle imaging at Keck, and adaptive optics monitoring on the VLT. Finally, the VLM binary HD 130948BC recently had its dynamical mass determined using NGS AO, as it is a companion binary to the G2V star, HD 130948 A (Dupuy et al. 2009a).

In 2006, the Laser Guide Star Adaptive Optics system came online at the W.M. Keck II telescope (Wizinowich et al. 2006), dramatically expanding the possible sample of VLM binaries that could be monitored from the ground. The system uses an 15 Watt sodium laser to excite sodium atoms high in the Earth's atmosphere, generating a ∼10.5 magnitude artificial guide star that can be used to monitor and measure atmospheric turbulence. This laser therefore allows for high resolution observations of optically faint sources.

To demonstrate the improvements afforded by the advent of LGS AO, Figure 1.1 plots the apparent R band magnitude of all known, visual, northern hemisphere VLM binaries as of 2007 (Burgasser et al. 2007) versus their R-K color. The figure shows the sources that were observable at high resolution with NGS AO (2 sources), and those that are now observable with Keck LGS AO. With this new technology, 70% of all visual VLM binaries can be monitored. Capitalizing on this, two binaries that can only be observed with LGS AO have recently had their dynamical masses measured (through surveys performed in parallel with

that presented in Chapter 4). One is 2MASS 1534-29AB, the first T dwarf with a dynamical mass measurement (Liu et al. 2008), and the other is LHS 2397a AB (Dupuy et al. 2009b). These orbital determinations are representative of the dramatic improvement in data quality and sample afforded by LGS AO, but still are only a handful of measurements. Full characterization and calibration of evolutionary model predictions requires a much larger sample of mass measurements across the entirety of the substellar regime, including objects of late M, L, and T spectral types. Additionally, all previous dynamical mass determinations for these visual binaries, except that of GJ 569B ab (Zapatero-Osorio et al. 2004, Simon et al. 2006), have been made using the *relative* orbit of the components. This means that only the total system masses have been measured. If individual component masses for these binaries could be determined, a feat currently only possible from the ground, they would offer an extremely powerful test of the evolutionary models (see Chapter 4).

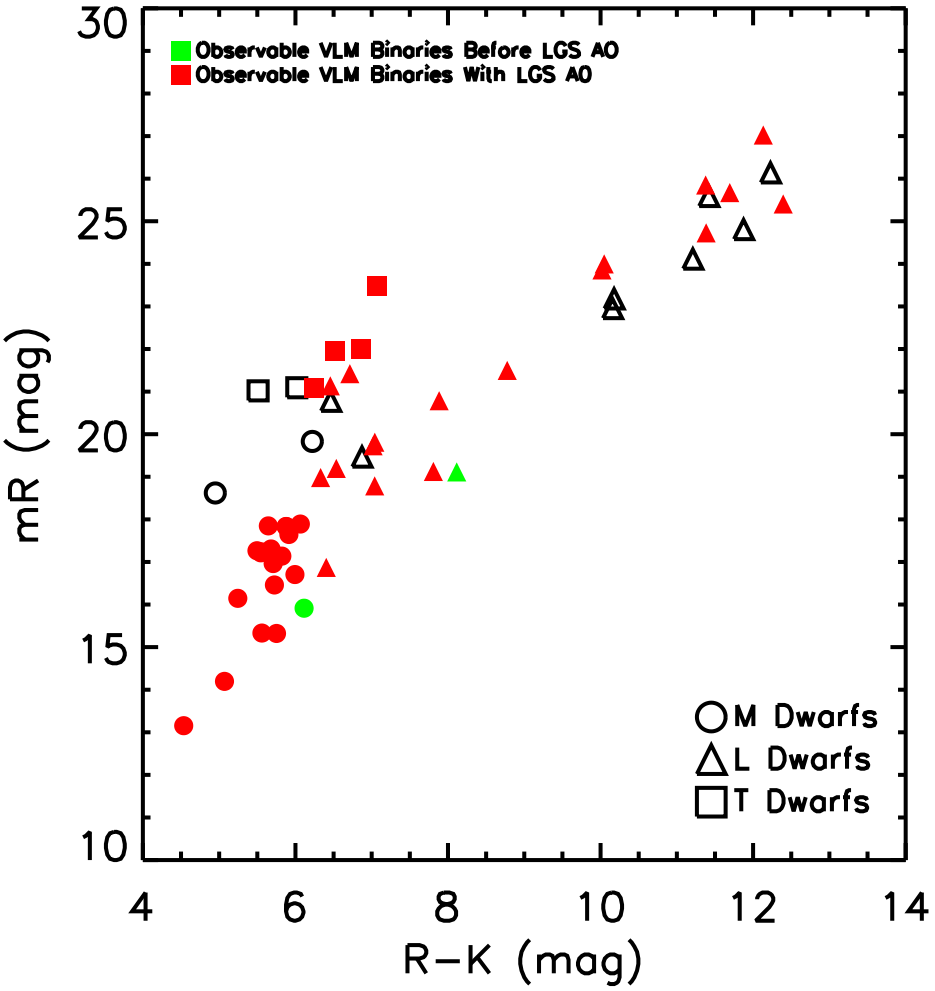

Figure 1.1 Apparent R-band magnitude versus R-K color for all VLM visual binaries known as of 2007 (Burgasser et al. 2007) that are observable with Keck observatory. The spectral type of each source is denoted by symbol. Apparent R band magnitude is plotted because the Keck AO system guides at optical wavelengths. Those sources that were observable using NGS AO are colored green. Only two sources are observable with NGS AO (GJ 569Bab and HD 130948BC), and both are companion systems to higher mass stars. With the Keck LGS AO system, 70% of all VLM visual binaries can be monitored at high spatial resolution.

CHAPTER 2

New Very Low Mass Binaries in the Taurus Star-Forming Region

Since the first observational detection of brown dwarfs - objects whose mass ($\lesssim$0.08 $M_\odot$) is too small for them to achieve hydrogen fusion but larger than the majority of known planets - the mechanism for their formation has been a hotly pursued and elusive puzzle. Current theories include formation of very low-mass cores in turbulent clouds (e.g. Padoan and Nordlund, 2004), additional fragmentation in higher-mass cores (e.g. Boss 2002), fragmentation out of high mass discs (e.g. Rice et al. 2003), premature ejection from a natal cloud core (e.g. Bate et al. 2002), and photo-erosion of cores by nearby OB stars (e.g. Whitworth and Zinnecker, 2004). Over the past few years, extensive surveys of star-forming regions have been undertaken to identify larger numbers of VLM members (e.g. Zapatero Osorio et al. 2000, Ardila et al. 2000, Luhman 2004a, Guieu et al. 2006). By studying the properties of brown dwarfs and VLM stars at very young ages, one may gain substantial insight into their origins.

One such property that is useful for gaining this insight is multiplicity fractions of VLM stars and brown dwarfs. Many formation scenarios make predictions as to the percentage of these objects that would be expected to be found in binaries. A number of field VLM star and brown dwarf multiplicity studies have been carried out and have found very low overall binary fractions ($\sim$5-10%), mass

ratio distributions that are strongly peaked toward equal masses, and a sharp decline in the binary fraction beyond separations of 20 AU (e.g. Burgasser et al., 2003, Close et al., 2003, Bouy et al., 2003, Gizis et al. 2003). When compared with higher mass studies of field stars (e.g. Duquennoy & Mayor 1991), these suggest that the maximum binary separation decreases with mass. However, these results may be affected by dynamical evolution given the substantial age of the targets. Indeed, multiplicity studies of stellar objects have shown evidence for dynamical evolution, as the binary fraction of these objects is generally found to be much higher in young star-forming regions than in the field (e.g. Ghez et al. 1993, Leinert et al. 1993, Simon et al. 1995). Thus, surveys of younger ($\sim$1 - 5 Myr) VLM systems are much more likely to reveal the pristine outcome of the brown dwarf formation process. Such work has just begun over the last few years and includes studies in Upper Scorpius (distance = 145 pc, age $\sim$ 5 Myr; Kraus et al. 2005, Bouy et al. 2006) and Taurus (distance = 140 pc, age $\sim$1-5 Myr; Kraus et al. 2006). To date, only a handful of young, VLM binaries have been detected.

In this paper, we report the discovery of five new VLM binaries in Taurus. In contrast to field VLM binaries, the majority of these new binaries have separations greater than 20 AU. These new binaries increase the number of known young systems by $\sim$50% and suggest a higher binary fraction among young, VLM objects. In §2, we describe our observations and analysis, in §3 we present our results, in §4 we compare our results to other work and discuss the implications for brown dwarf formation scenarios, and in §5 we summarize our findings.

2.1 Observations and Data Analysis

The observations were made using the Keck I 10 m telescope with the facility Near Infrared Camera (NIRC, Matthews & Soifer 1994, Matthews et al. 1996) in speckle imaging mode on 2004 December 19 and 2005 November 12-13. In its high angular resolution modes, NIRC has a pixel scale of 20.45 ± 0.03 mas/pixel. The total field of view of NIRC in this mode is $5\farcs2$. For each target, four to six stacks of 190 images, each 0.137 seconds integration time, were obtained through the K band-pass filter ($\lambda_o = 2.2$ μm, $\Delta\lambda = 0.4$ μm). Along with these target stacks, we obtained stacks of darks, sky, and point source calibrators, all of which are used in the reduction process. Using these stacks, we generate power spectra of each of the targets using Fourier transform techniques (Labeyrie 1970). The procedure of speckle data analysis, including the creation of power spectra, are described in some detail in Konopacky et al. (2007) and Ghez et al. (1995), and this study uses the same approach. Binary star power spectra exhibit a characteristic sinusoidal pattern, which is used to obtain the binary separation, position angle, and flux ratio. Shift-and-Add images (Christou 1991) were also generated from each data set to enhance our sensitivity to high flux ratio, wide binary systems. Table 1 lists all targets observed, as well as the point sources used for calibration.

All targets were selected from Luhman (2004a) and Guieu et al. (2006) based upon their K band magnitudes. Theses two studies found 22 and 17 new VLM objects in the Taurus star-forming region, respectively. Among the stars from these studies, fifteen are brighter than the speckle magnitude limit of K $\lesssim$11, which is required to achieve sufficient signal-to-noise in a single short exposure image. During three nights at Keck, we observed thirteen of these targets, six from Guieu et al. (2006) and seven from Luhman (2004a) (J04554757 and J04555288 from

Table 2.1. Speckle Observation Summary of VLM Taurus Objects

Target	Sp. Type	K (mag)[a]	Date of Observation	Calibrator	Ref[b]
CFHT-Tau 7	M6.5	10.4	2005 Nov 13	FZ Tau	2
CHFT-Tau 17	M5.75	10.8	2005 Nov 13	DO Tau	2
CFHT-Tau 18	M6.0	8.7	2005 Nov 13	FZ Tau	2
CFHT-Tau 19	M5.25	10.5	2005 Nov 13	SAO 76547	2
CFHT-Tau 20	M5.5	9.8	2005 Nov 12	FZ Tau	2
CFHT-Tau 21	M1.25	9.0	2005 Nov 13	SAO 76547	2
J04161210	M4.75	10.3	2004 Dec 19	CW Tau	1
J04213459	M5.5	10.4	2005 Nov 13	SAO 76547	1
J04284263	M5.25	10.5	2004 Dec 19	SAO 76628	1
J04380083	M7.25	10.1	2004 Dec 19	DO Tau	1
J04403979	M5.5	10.2	2005 Nov 13	DO Tau	1
J04442713	M7.25	10.8	2005 Nov 13	SAO 76727	1
J04554535	M4.75	10.5	2005 Nov 12	SU Aur	1

[a]From the 2MASS point source catalog

[b]Source identified as VLM object by Luhman (2004; Ref 1) or Guieu et al. (2006; Ref 2)

Luhman (2004a) were not observed). While there has been a range of definitions of VLM objects in the literature, in this study we define a VLM object as an object with a mass $\lesssim$0.2 $M_{\odot}$. One of the targets observed during this program, CFHT-Tau 21, has a spectral type of M1.25 and is not a VLM object by our definition. Thus, we report it here for completeness, but exclude it from further analysis. Table 1 lists the spectral type and total K band magnitude for each of the target stars. Our VLM sample has spectral types that range from M4.75 to M7.25 and corresponding masses that range from 0.2 $M_{\odot}$ to 0.05 $M_{\odot}$ at the average age of Taurus ($\sim$3 Myr).

2.2 Results

Of the thirteen targets observed, five were found to be binaries. The parameters of each binary system are summarized in Table 2. As listed in Table 3, sensitivity estimates show that, in general, companions with ΔK = 3 could have been

detected at the 3σ confidence level, all the way down to an angular separation of $0\farcs02$, the minimum detectable separation using the speckle technique (see Ghez et al. 1993, Konopacky et al. 2007). Using the models of Baraffe et al. (1998, $\alpha = 1.0$), these 3σ magnitude difference sensitivities can be converted to an estimate of detectable q (where $q \equiv M_{secondary} / M_{primary}$). For all of the targets in the sample, the ΔK to q conversion is quite similar and is well-described by the equation $q = 0.077\Delta K^2 - 0.526\Delta K + 0.966$. This survey therefore was generally sensitive to q $\sim$0.23 at $\sim$3 AU, a region of parameter space completely inaccessible to many past surveys. Figure 1 shows the 3σ sensitivity limits on q versus distance from the primary source.

Because only one epoch of data on these targets has thus far been obtained, the physical association of the five binaries via common proper motions cannot be confirmed. Instead, Table 2 lists the probability of association based upon the number of sources of comparable brightness to the secondaries in the region and the separation of the two stars. These probabilities were calculated following the method of Brandner et al. (2000), using their equation 1. The 2MASS All-Sky Point Source Catalog Statistics Service[1] was used to find the number of sources of comparable brightness to the secondary within one square degree centered on the primary. These source densities were then used to calculate the probability that these objects are chance background sources. These probabilities are given in Table 2. We find that all are likely to be physically associated with probabilities of the secondary being a background object of $\lesssim 10^{-4}$, and thus conclude that the detected binaries are physically associated with each other.

The observed properties can be used to estimate the component masses and mass ratios using pre-main sequence evolutionary models. Luhman (2004a) and

[1]http://irsa.ipac.caltech.edu/applications/Stats/

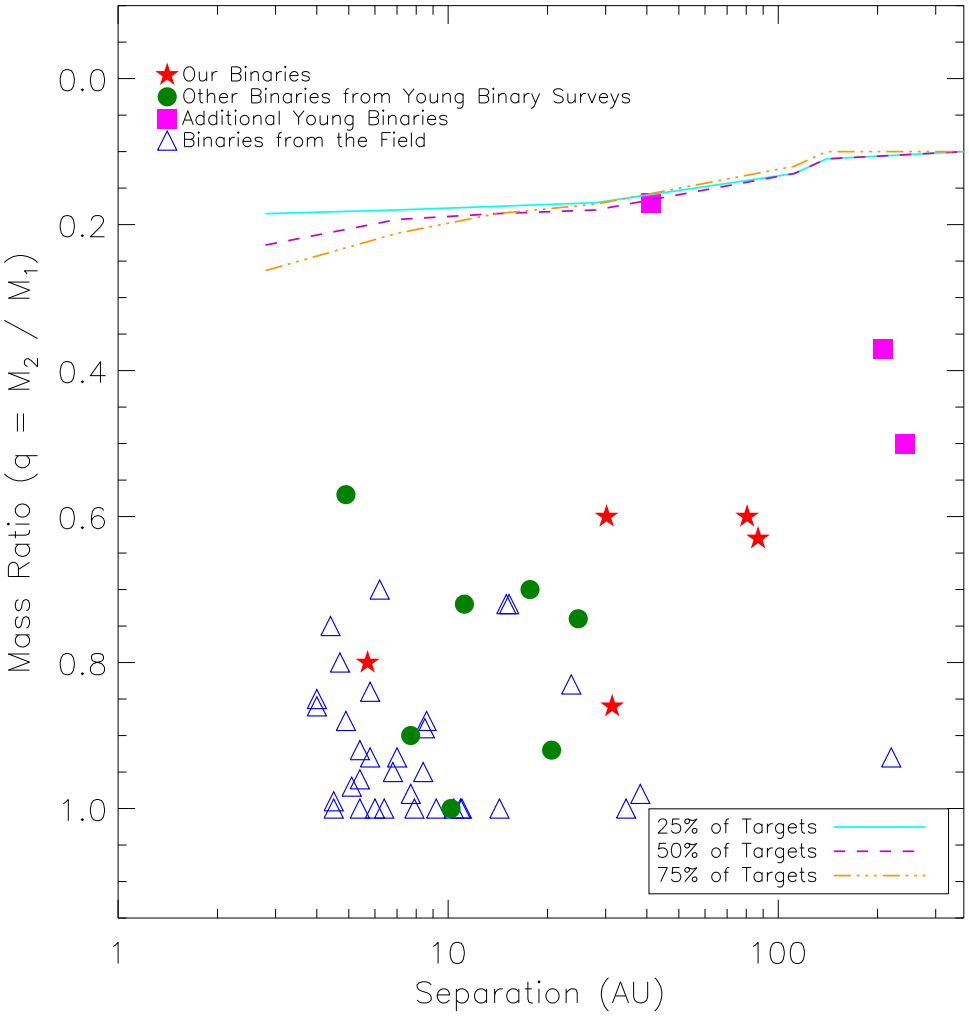

Figure 2.1 The mass ratio q versus the separation (in AU) of the VLM binaries found in our survey and those found in other studies of both young and old VLM binaries. This figure demonstrates the differences in the parameters of the old and the young samples. The truncation of field VLM binaries at separation > 20 AU and $q < 0.8$ is not seen amongst young VLM binaries. Also shown are the 3σ sensitivity limits of our survey. The lines represent the sensitivities of the best 25, 50, and 75% of our sample. Quoted sensitivities are from the 50% curve.

Table 2.2. Taurus VLM Binary System Properties

Target	Sep. (“)	P.A. (degrees)	Flux Ratio (K)	M_K Primary	M_K Secondary	Prob. of Background Object	∼Primary Mass ($M_\odot$)	∼Secondary Mass ($M_\odot$)
CFHT-Tau 7	0.224 ± 0.002	292.92 ± 0.17	1.40 ± 0.09	5.26 ± 0.18	5.61 ± 0.20	4.6×10^{-6}	0.07	0.06
CHFT-Tau 17	0.575 ± 0.002	235.37 ± 0.31	3.70 ± 0.55	4.62 ± 0.18	6.08 ± 0.27	1.1×10^{-4}	0.1	0.06
CFHT-Tau 18	0.216 ± 0.002	268.56 ± 0.34	2.28 ± 0.25	2.92 ± 0.18	3.77 ± 0.19	1.7×10^{-6}	0.1	0.06
J04284263	0.621 ± 0.007	349.97 ± 0.83	2.29 ± 0.39	5.07 ± 0.18	5.97 ± 0.26	6.3×10^{-5}	0.15	0.06
J04403979	0.041 ± 0.003	289.98 ± 4.59	2.08 ± 0.29	4.59 ± 0.29	5.68 ± 0.94	3.3×10^{-7}	0.15	0.08

Guieu et al. (2006) list for each target an estimated extinction value A_V (in the case of the binaries, we assume this value is the same for both components). The absolute K-band magnitudes for the targets were calculated using these values, m_K, and a distance of 140 $\pm$ 10 pc (Bertout et al. 1999) for Taurus. The unresolved spectral types were used to estimate the temperatures of the brighter component of each pair, via the temperature scale in Luhman et al. (2003). Thus, using M_K and these temperatures, a mass and age for each primary was found using the theoretical models of Baraffe et al (1998). Subsequently, the masses of the secondary components were found via interpolating along the isochrone derived for the primary to find the mass consistent with the M_K values for each secondary. The masses derived from this method are given in Table 2 and Table 3. As shown in Figure 2, all five secondaries are likely to be substellar, in addition to one out of five of the primaries.

For the majority of the targets, the calculated ages are consistent with the age of Taurus. However, a few targets have an M_K and temperature that predict an age younger than 1 Myr (see Figure 2), which is beyond the range covered by the Baraffe et al. (1998) models, but is occasionally seen among T Tauri stars (Kenyon & Hartmann 1995). Hence, in the case of these systems, we fix the age to 1 Myr and use this, with the temperature of the target, to estimate its mass. One of the binaries, CFHT-Tau 18, falls into this category. In this case, a new estimate of M_K for the primary component was derived by fixing its age, which was then used to derive the mass of the secondary (via the ΔK calculated from the flux ratio). Since the model masses are quite independent of age and luminosity at this stage of evolution, this age adjustment has negligible impact on the derived masses.

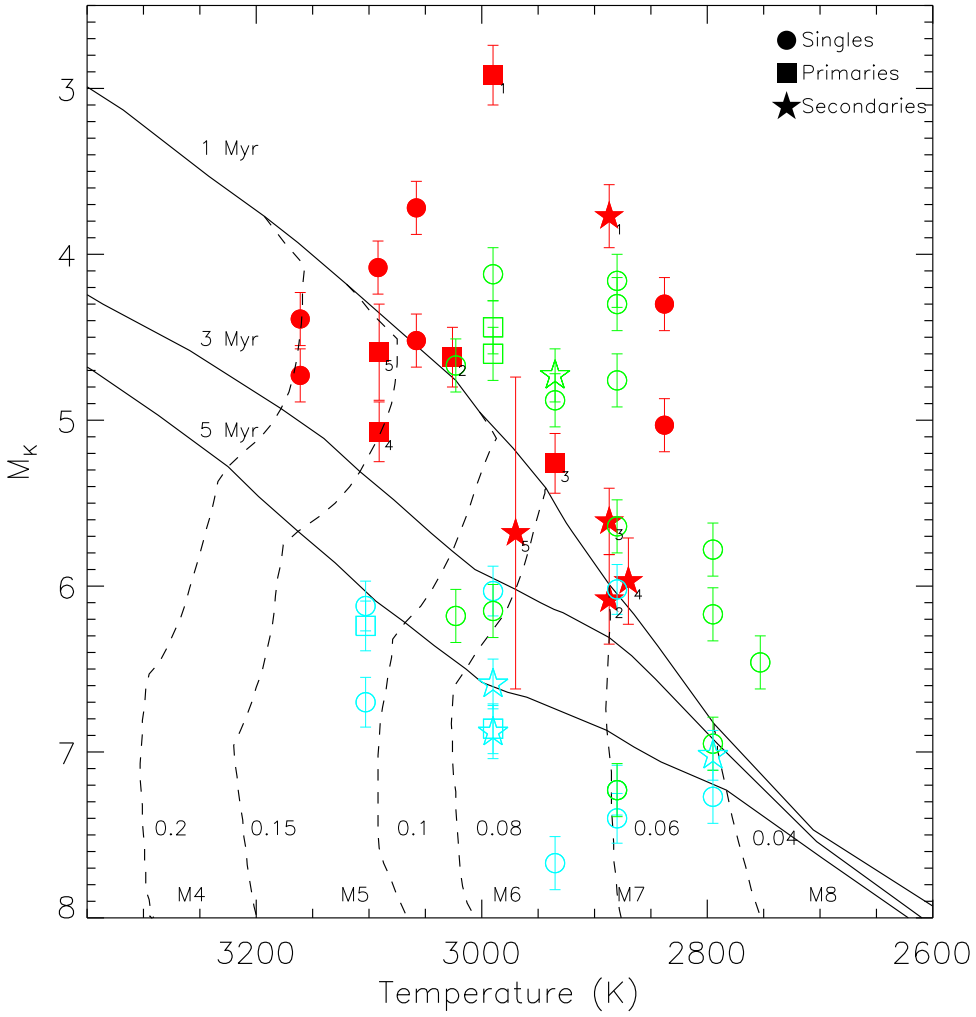

Figure 2.2 The temperatures and absolute K-band magnitudes of each of our targets and those of the companions found (filled red symbols). The primaries and secondaries that correspond to each other are numbered as such. The isochrones shown are those of the age of Taurus, ∼1-5 Myr, and several mass tracks are also shown, as well as the spectral types that correspond to various temperatures (Luhman et al. 2003). It is clear from this figure that several targets are substantially brighter than would be expected for members of Taurus, giving age estimates younger than 1 Myr (where the Baraffe et al. 1998 tracks end). This lead us to use only the temperatures to estimate the appropriate mass, after fixing the age to 1 Myr. Also shown are those targets from other surveys of young, VLM stars that we use to construct an our entire sample of VLM targets from star-forming regions (green and blue open symbols). The green open symbols are sources also in Taurus, while the blue symbols are sources in Upper Scorpius, which appropriately cluster around slightly older isochrones than the Taurus members.

Table 2.3. Limits on Mass Ratio for Undetected Companions to Single Taurus VLM Stars

Target	Est. Mass ($M_\odot$)	0.″02	0.″05	0.″1	0.″2	0.″8	1.″0
CFHT-Tau 19	0.15	0.28	0.15	0.13	0.12	0.10	0.10
CFHT-Tau 20	0.12	0.32	0.32	0.120	0.17	0.10	0.10
CFHT-Tau 21	0.70	0.79	0.35	0.24	0.19	0.10	0.10
J04161210	0.20	0.19	0.19	0.19	0.19	0.14	0.12
J04213459	0.12	0.35	0.18	0.17	0.14	0.10	0.10
J04380083	0.05	0.50	0.50	0.50	0.50	0.50	0.30
J04442713	0.05	0.18	0.17	0.16	0.15	0.12	0.10
J04554535	0.20	0.26	0.26	0.26	0.26	0.16	0.10

Note. — These values represent the 3σ limits on q, the mass ratio, as a function of distance from the primary for each of the targets found to be single in our sample.

2.3 Discussion

The discovery of five binaries in a sample of twelve VLM objects increases the number of known, young, VLM binaries by $\sim$50%. This enables a more statistically robust assessment of VLM binary properties. In order to derive an unbiased binary star fraction from our magnitude-limited survey ($m_k \lesssim 11$), we remove the one binary, CFHT-Tau 7, that has a primary with $m_k > 11$ when resolved into its constituent components. This leaves four binaries in a sample of eleven objects. Only two other similar surveys of young, VLM objects exist in the literature[2]. Kraus et al. (2005) surveyed 12 VLM objects in Upper Scorpius and found three binaries, and more recently, Kraus et al. (2006) targeted 22 VLM objects in Taurus and found two binaries. Figures 1 and 2 plot the properties of the binaries from these two surveys, along with those found in our study. Combining all three

[2]Recently, Bouy et al. (2006) presented a number of new binaries they found in Upper Scorpius. These binaries are quite interesting in that many are quite wide and a number are VLM. However, they do not include in their work the complete list or number of targets they observed. Thus, for the purposes of this paper, we cannot include these binaries in our binary fraction analysis.

surveys (eight binaries out of 45 targets) yields a binary fraction of 18 ± 4%, with *no* evidence of a difference between the two star-forming regions.

The VLM binary fraction in nearby star-forming regions appears to be higher than that found in the field. To make a direct comparison, we define a binary fraction over the same separation (4 to 100 AU) and mass (0.04 to 0.2 $M_{\odot}$) range covered by the combined young, VLM sample. Specifically, the field statistics are culled from the works of Close et al. (2003), Bouy et al. (2003), and Gizis et al. (2003), which survey objects of late M and early to mid-L spectral types, with the surveys of mid-M type stars of Siegler et al. (2005) and Reid and Gizis (1997, using only the stars of spectral type M5-M9 in their sample) and the T dwarf survey of Burgasser et al. (2003); all surveys included are reported to be complete to at least q $\sim$ 0.5. This produces a sample of 39 binaries among 219 objects, which results in a bias-corrected (see Burgasser et al. 2003 for method) field VLM binary fraction of 8 ± 2%. This value is a factor of two less and 2.2σ lower than the young, VLM binary fraction.

In addition to the binary fractions discussed above, the properties of VLM systems, namely the separation and the mass ratio, show differences as a function of age. Figure 1 plots the binary mass ratio for the young and field surveys discussed above, along with three other binaries discovered with high angular resolution imaging (Luhman 2004b, Chauvin et al. 2005, White et al. 1999, Bouy et al. 2006), as a function of separation. In contrast to the field population, young, VLM binaries frequently have separations larger than 20 AU, as well as smaller (more unequal) mass ratios. This suggests that the young VLM binaries are wider and have a flatter mass ratio distribution than field binaries, or equivalently that many of the young VLM binaries have smaller binding energies than their older counterparts.

The differences in these parameters are quantified with both one-dimensional and two-dimensional K-S tests, comparing the separations and mass ratio distributions of these field VLM binaries with the young VLM binaries. In one dimension, the separation distributions have a 1% probability of similarity and the mass ratio distributions have a 0.02% probability of similarity. Additionally, in two dimensions, the distribution of both parameters taken together has only a 0.07% probability of similarity. Thus, we can say with a fairly high degree of certainty that the properties of young VLM binaries differ substantially from those of old VLM binaries.

These differences support the idea that there may be substantial evolution in the properties of VLM binaries ∼5-10 Myr after their formation (Burgasser et al. 2006). The disruption of binaries with separations greater than 20 AU via interactions with their environment, i.e. their formative cluster, shortly after their initial formation would seem to be a plausible zeroth-order explanation for the disparity. As further evidence of this idea, if we assume that evolution will eventually lead to the disruption of the four binaries found here with separations greater than 20 AU, we can calculate a new binary fraction - the fraction that will survive to eventually become a field binaries. This leaves a total of four out of 45 binaries, which yields a binary fraction of $9 \pm 5\%$. This number is perfectly consistent with the field binary fraction we calculate above.

However, the situation becomes substantially more complicated when comparing VLM binaries to stellar binaries. As noted by both Close et al. (2003) and Burgasser et al. (2006), there appears to be a discrepancy between the minimum observed binding energy of stellar binaries and VLM binaries. This binding energy discrepancy is shown in Figure 2.3. Three of the binaries discovered here have a binding energy below the previously determined limit, with a minimum

around -10^{42} erg. This minimum is still quite discrepant from what is observed amongst field binaries, which appear to have a minimum binding energy of about -10^{41} erg. The stellar binding energy cutoff can be explained by the work of Weinberg et al. (1987), who show that normal interactions with the other stars and giant molecular clouds in the Galaxy typically provide a "velocity kick" of less than 1 km s^{-1}, sufficient to truncate a stellar mass binaries with separations beyond $\sim$0.1 pc. However, generating a binding energy cutoff like that observed amongst the VLM binaries necessitates a velocity kick roughly three times this value.

One method of generating the higher velocity kicks for VLM objects is from the ejection scenario for VLM star and brown dwarf formation (Bate et al. 2002), which predicts typical velocity kicks of $\sim$3 km s^{-1} very early in the formation process. However, numerous authors have noted the implausibility of the ejection scenario, as it predicts not only a very low frequency of binary brown dwarf systems (5% or less), but also generates binary brown dwarfs with separations of less than 10 AU. Although recent work by Umbreit et al. (2005) shows that it is possible to form more brown dwarf binaries via ejection than initially assumed, they find a semi-major axis distribution that is severely truncated at wider separations, with no brown dwarf binaries created at separations greater than 20 AU. While this new study initally seemed a promising solution to the binding energy problem, it does not explain the young, wide binaries plotted in Figure 2.1.

A reasonable explanation of the binding energy discrepancy must now include the survival of some VLM binaries of separations greater than 20 AU up through at least a few million years after formation while at the same time account for the truncation seen in the field. On a number of occassions, the low-mass, low-density nature of Taurus has been invoked to explain difference observed between the

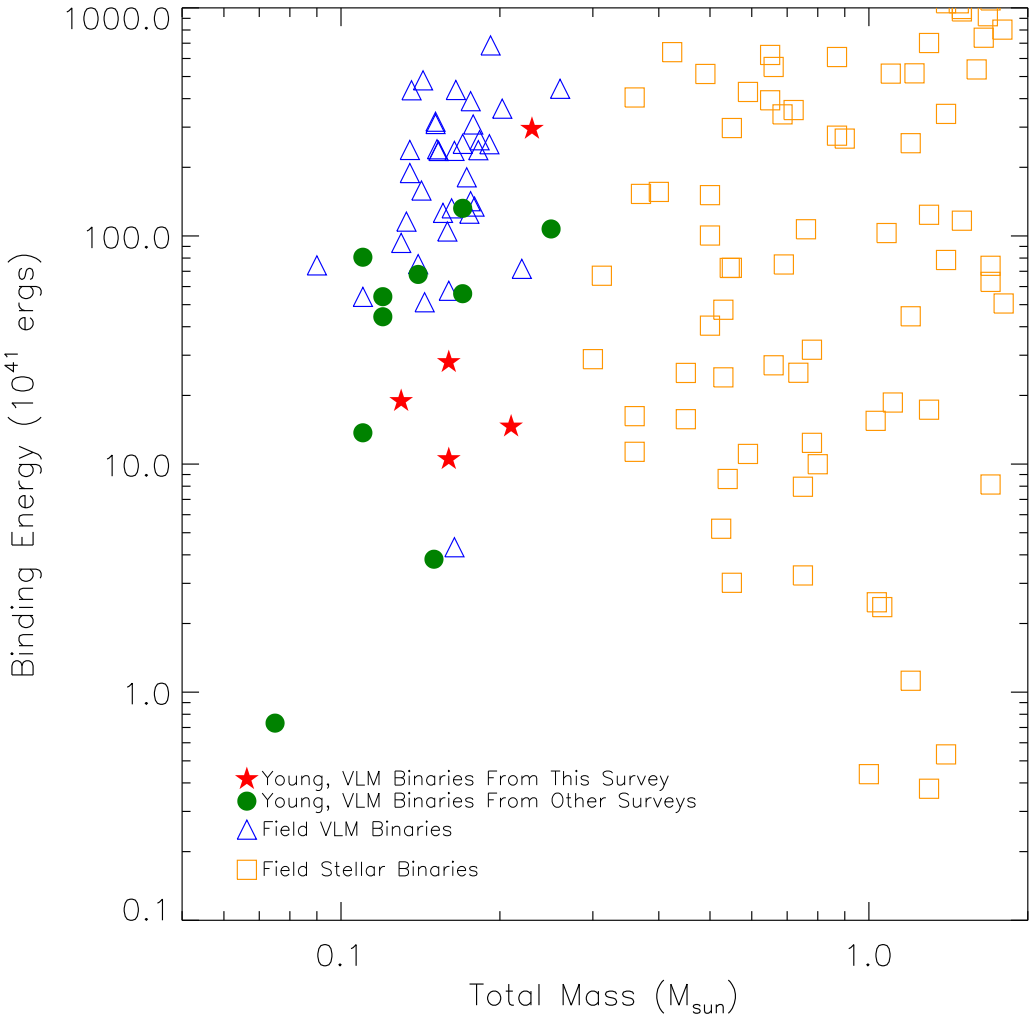

Figure 2.3 Binding energy as a function of total mass for the VLM binaries, both young and in the field, discussed above, in addition to a number of known, stellar binaries (Close et al. 1990, Duquennoy & Mayor 1991, Fischer & Marcy 1992, Reid & Gizis 1997, Reid et al. 2001). Though three of the new binaries in Taurus have binding energies below the limit from Close et al. (2003), they do not have binding energies as low as those of stellar binaries.

multiplicity properties of the region and regions like the high-density Orion. Thus, it could be argued that the multiplicity of VLM objects found in this study is not directly comparable to field VLM objects, which would most likely have formed in higher mass star forming regions. However, the similarity of the results presented here to those found in Upper Scorpius make this an unsatisfactory explanation - indeed, it has been argued that Orion is in fact also an unusual star-forming region and most stars form in intermediate mass regions like Upper Scorpius (e.g. Kroupa 1995). Thus, the existence of wide VLM binaries in numerous star-forming regions seems to be a significant trend.

The statistical significance of the trucation of wide, VLM field binaries both now in terms of their younger counterparts and stellar binaries therefore necessitates a plausible physical explanation for their disappearance over a longer timescale than has been previously suggested. As mentioned above, the work of Weinberg et al. (1987) suggests that disruption of such binaries once they survive to become field objects is unlikely. In addition, although their eventual disruption could potentially be due to interactions within star forming regions before they disperse, Kroupa et al. (2003) show from dynamical simulations that although many VLM binaries would be disrupted in very high density regions like the Orion Nebula cluster, the majority will not be disrupted in regions like Taurus. Disruption alone thus does not appear to be the cause of the discrepancy.

However, the dynamical events a VLM binary undergoes throughout its time in its formative cluster and its eventual evolution into a field object is clearly not so simple as it becoming either disrupted or not. Most interactions will have an effect on the properties of the binary, namely in terms of hardening or softening. Thus, it could be that the impact of such interactions will be greater on a VLM binary than on a stellar binary as a result of their small size relative to the average

perturbing object. For instance, Hills (1990) shows that the fractional change in binding energy is a fairly strong function of the ratio of the mass of the binary to the mass of the perturber, which would imply that hard VLM binaries on average get "harder" more quickly that stellar binaries. Such parameter evolution, first occuring in a star-forming region and then later in the field, could potentially account for some of the binding energy discrepancy. For instance, the simulations of Adams et al. (2006) show that interaction and disruption cross-sections in a star-forming region scale roughly as the square root of the mass of the primary star. More detailed calculations that take into account the effects of the relative mass of the binary with respect to the rest of the cluster and subsequently the field population should be performed to test these effects.

2.4 Summary

In a survey of thirteen newly-discovered VLM members of the Taurus star-forming region, we identified five new binary systems. Follow-up observations are still required to confirm that these binaries are associated. Proper motion measurements would provide the most definitive confirmation. Additional constraints could be applied in the interim by obtaining either colors or spectral types for the secondaries in these systems. Still, statistical arguments show that they are associated to a high degree of certainty. As a result of these discoveries, we were able to statistically compare the properties of young, VLM binaries to their older counterparts in the field. We found that our study and those of other young VLM objects suggest that the binary fraction of VLM objects is higher in star-forming regions like Taurus and Upper Scorpius than in the field. Additionally, four of our five binaries have separations beyond 20 AU, a configuration previously found to be rare for VLM binaries. These wide binaries, coupled with the statistically sig-

nificant truncation of field VLM binaries beyond 20 AU, suggest that dynamical evolution produces the observed field VLM binary properties. Along these lines, we find that it is difficult to produce these results using the ejection scenario of VLM object formation, as wide binaries are not expected to survive this process. Dynamical perturbations may play a roll in determining the final distribution of VLM binary systems, as their small mass relative to the average mass of a perturbing object cam cause them to be more readily hardened over time than stellar mass binaries. More simulations that take into the effects of the mass of a VLM binary with respect to the rest of either the cluster or the field population are needed to determine if such dynamics are sufficient to explain the binding energy discrepancy.

CHAPTER 3

Measuring the Mass of a Pre-Main Sequence Binary Star Through the Orbit of TWA 5A

Binary stars present a unique laboratory for the study of stellar evolution, as their orbital solutions give direct mass estimates. Though the mass of a star is the most fundamental parameter in determining its course of evolution, very few PMS stars have dynamically determined masses. In these few cases, astrometric and spectroscopic studies have lead to PMS mass determinations based on the orbital motion of a stellar companion or a circumstellar disk relative to the primary star (e.g. Ghez et al. 1995, Simon et al. 2000, Steffen et al. 2001, Woitas et al. 2001, Tamazian et al 2002, Duchene et al. 2003). Once measured, these masses can subsequently be used to constrain PMS evolutionary models. These models have been shown to be systematically discrepant in their predictions by up to factors of two in mass and ten in age - still, since there are so few well-determined PMS masses, little can currently be done to calibrate these tracks. This is particularly true in the lowest mass regime, where only three systems have total dynamical masses of less than $1M_{\odot}$ and only one single star has a dynamical mass measurement below $0.5M_{\odot}$ (Hillenbrand & White 2004). This study is part of an ongoing program to astrometrically determine the orbits of PMS stars and to help constrain these theoretical mass tracks. Young stars are particularly important to correctly calibrate, as this calibration will aid in the

subsequent calibration of young brown dwarf and planetary models.

The TW Hydrae association was originally discovered by Kastner et al. (1997), with only five members confirmed at that time. Since its discovery, 25 total members have been identified (e.g., Song et al. 2003, Makarov & Fabricius 2001). The association has been shown to be quite young (∼8-12 Myr) via lithium abundance tests, space motions, and placement of its members on the HR diagram (e.g., Zuckerman & Song 2004). Additionally, TW Hydrae is quite nearby, with an average distance of ∼50 pc (e.g., Makarov & Fabricius 2001, Mamajek 2005). This makes TW Hydrae one of the closest associations of young stars to the Earth and thus is an ideal region for studying spatially resolved PMS binaries, as they are likely to have orbital periods as short as a few years.

With these ideas in mind, we began to monitor TWA 5, the fifth of the five original members of the TW Hydrae association identified by Kastner et al. (1997). TWA 5 is composed of at least three components. The pair that we analyze here is TWA 5Aa-Ab, which had a separation of ∼0.″06 when it was discovered by Macintosh et al. (2001). TWA 5A also has a brown dwarf companion, TWA 5B, located ∼2″ away (Webb et al. 1999, Lowrance et al. 1999, Neuhauser et al. 2000, Mohanty et al. 2003). Finally, TWA 5Aab is suspected to contain at least one spectroscopic pair based upon large radial velocity variations (Torres et al. 2003, Torres 2005 private communication).

In this paper, we present the results of six years of speckle and adaptive optics (AO) observations of TWA 5Aab with the W.M. Keck 10 m telescopes. In §2, we describe our data reduction techniques, and in §3 we present our orbital solution for the system. In §4, we discuss comparisons of our derived orbital parameters with mass and age predictions from theoretical PMS tracks and make recommendations for future studies of this system.

3.1 Observations and Data Analysis

3.1.1 Speckle Data

TWA 5Aab was observed using the Keck I 10 m telescope with the facility Near Infrared Camera (NIRC, Matthews & Soifer 1994, Matthews et al. 1996) roughly once a year from 2001 to 2005 (see Table 1 for exact dates). In its high angular resolution mode, NIRC has a pixel scale of 20.44 ± 0.03 mas/pixel (see Appendix A for details of NIRC's pixel scale and orientation). Three to four stacks of 190 images, each 0.137 seconds long, were obtained through the K band-pass filter ($\lambda_o = 2.2$ μm, $\Delta\lambda = 0.4$ μm). They were taken in stationary mode, meaning the Keck pupil is fixed with respect to the detector during the observations, but the sky rotates. The rotation rate is sufficiently slow that it is negligible for individual exposures, but not over the entire stack. Stacks of four dark frames were also taken with each object stack. Additionally, identical stacks of a point source calibrator star (TWA 1 for 2001-2002 observations, TWA 7 for 2003-2005 observations) and an empty portion of sky were obtained immediately before or after the target stacks.

The stacks are processed using image reduction and speckle data anaylsis techniques. Specifically, each image is first dark and sky subtracted, flat fielded, and bad pixels repaired. The images are then individually corrected for a minor optical distortion in the NIRC camera (J. Lu et al. in prep). The object, calibrator, and sky stacks are then Fourier transformed and squared to obtain stacks of power spectra. Next, the calibrator stacks and sky stacks are each averaged together (without rotation). The extraction of the object's intrinsic power spectra utilizes the convolution theorem, which gives the relation:

$$O = \frac{I - < S >}{< C > - < S >}, \tag{3.1}$$

where O is the object power spectrum, I is the initial squared Fourier transform of the object, <S> is the averaged, squared power spectrum of the sky, and <C> is the averaged, squared power spectrum of the calibrator. Each power spectrum of the object is then rotated so that north is up; these rotated power spectra are combined to obtain an average power spectrum for the stack. Finally, those individual stacks were also averaged together to produce a final power spectrum. This sequence is necessary due to the lack of azimuthal symmetry of the Keck I pupil.

Since a binary star in the image domain is essentially two delta functions, the power spectra can be approximated as a sinusoid with the functional form:

$$P(\vec{f}) = \frac{R^2 + 1 + 2Rcos(2\pi \vec{f} \cdot \vec{s})}{R^2 + 1 + 2R}, \tag{3.2}$$

where R is the flux ratio of the binary star and $\vec{s}$ is the vector separation of the two stars. This function is fit to our two-dimensional power spectra over all spatial frequencies from 2.68 arcsec^{-1} to 17.6 arcsec^{-1} (this procedure is described in detail in Ghez et al. 1995). The lower cutoff is imposed to avoid spatial frequencies that are corrupted by small changes in the atmospheric conditions between the object and the calibrator, whereas the upper cutoff is imposed to reject excess noise at the highest spatial frequencies. This fitting procedure gives a very accurate estimate of the binary star's separation and flux ratio for components separated by more than $\lambda/2$D, leaving only a 180^o position angle ambiguity. This ambiguity is resolved by reanalyzing the original images using the method of shift and add. The brightest speckle in the speckle cloud in each image of the stack is shifted to a common position, and then all the images are added together to produce a diffration-limited core surrounded by a large, diffuse halo. These images allow us to determine the correct orientation of the position angles of TWA 5A. In one epoch (2002), the binary separation was less than $\lambda/2$D, and

hence the first minimum of the power spectrum was not measured; without this measurement, the separation and the flux ratio are degenerate. For this epoch, we fix the flux ratio to the weighted average of the K-band flux ratio measurements of all the other epochs and fit only the separation, as there is no evidence of photometric variability over the course of our observations. Uncertainties for all parameters are determined by fitting each of the individual, stack-averaged images that contribute to the final image by the same procedure, and then taking the RMS of those values with respect to the average value; for the 2002 epoch we also account for the uncertainty in the weighted-average flux ratio, which is taken to be the RMS of the individual K-band flux ratio measurements at all other epochs.

3.1.2 Adaptive Optics Data

TWA 5Aab was also observed using the Keck II 10 m telescope with the AO system and the facility near-infrared camera, NIRC 2 (K. Matthews et al., in prep), on 2005 February 16 and again on 2005 December 12. For these measurements, we used observations of the Galactic Center to establish that NIRC 2's narrow camera (which we used) has a plate scale of 9.961 $\pm$ 0.007 mas pixel^{-1} and columns that are at a PA of -0.015 $\pm$ 0.134^o relative to North (J. Lu et al., in prep). In February, five images, each of 0.2 second exposure time and 30 coadds, were taken through the FeII narrow band pass filter (λ_o = 1.65 μm, $\Delta\lambda$ = 0.03 μm). In December, six, six, and three images of 0.181 second exposure time and 50 coadds were taken through the J (λ_o = 1.248 μm, $\Delta\lambda$ = 0.163 μm), H (λ_o = 1.633 μm, $\Delta\lambda$ = 0.296 μm), and K-prime (λ_o = 2.124 μm, $\Delta\lambda$ = 0.351 μm) band pass filters, respectively. These images were processed using the same standard data reduction techniques listed above, and then shifted and combined

Table 3.1. TWA 5A Binary Star Parameters

Date of Observation	Filter	λ_o (μm)	Separation (arcseconds)	Position Angle (degrees)	Flux Ratio (Ab/Aa)	Speckle or AO?	Source[a]
2000 Feb 20	H	1.648	0.0548 ± 0.0005	205.9 ± 1.0	1.09 ± 0.02	AO	2
2000 Feb 22	K'	2.127	0.054 ± 0.003	204.2 ± 3.0	1.11 ± 0.07	AO	3
	H	1.648			1.09 ± 0.08	AO	3
	J	1.26			0.94 ± 0.05	AO	3
2001 May 06	K	2.2	0.0351 ± 0.0002	12.67 ± 1.06	1.26 ± 0.09	Sp	1
2002 May 23	K	2.2	0.013 ± 0.003	313.66 ± 2.99	1.24 ± 0.08[b]	Sp	1
2003 Dec 05	K	2.2	0.0306 ± 0.0004	227.41 ± 5.49	1.22 ± 0.04	Sp	1
2004 Dec 18	K	2.2	0.0515 ± 0.0009	32.10 ± 2.22	1.39 ± 0.09	Sp	1
2005 Feb 16	FeII	1.65	0.053 ± 0.001	32.59 ± 5.22	1.29 ± 0.18	AO	1
2005 May 27	K	2.2	0.0574 ± 0.0003	29.68 ± 0.35	1.23 ± 0.04	Sp	1
2005 Dec 12	Kp	2.124	0.0571 ± 0.001	29.99 ± 2.26	1.10 ± 0.05	AO	1
	H	1.633	0.0571 ± 0.002	28.89 ± 0.99	1.09 ± 0.03	AO	1
	J	1.248	0.0568 ± 0.005	28.41 ± 3.15	1.05 ± 0.13	AO	1

[a]1 = This work; 2 = Macintosh et al. 2001; 3 = Brandeker et al. 2003

[b]Flux ratio fixed in this epoch

to produce a final image.

Astrometry and flux ratios were then obtained using the IDL package StarFinder (Diolaiti et al. 2000). The wide brown dwarf companion to the system, TWA 5B, was visible in all AO images taken and thus was used as the empirical point-spread function required by the StarFinder fitting algorithm. Both components of the close binary were successfully fit by StarFinder in all cases. Errors were calculated by fitting the components in all individual images that contributed to the combined images and finding the RMS of the values derived therein.

3.2 Results

Figure 1 shows the calibrated power spectra and our resulting fits for all five speckle measurements of TWA 5Aab and Figure 2 displays our 2005 AO images. We supplement our observations with the following measurements that also spatially resolved TWA 5Aab: the original discovery measurement by Macintosh et

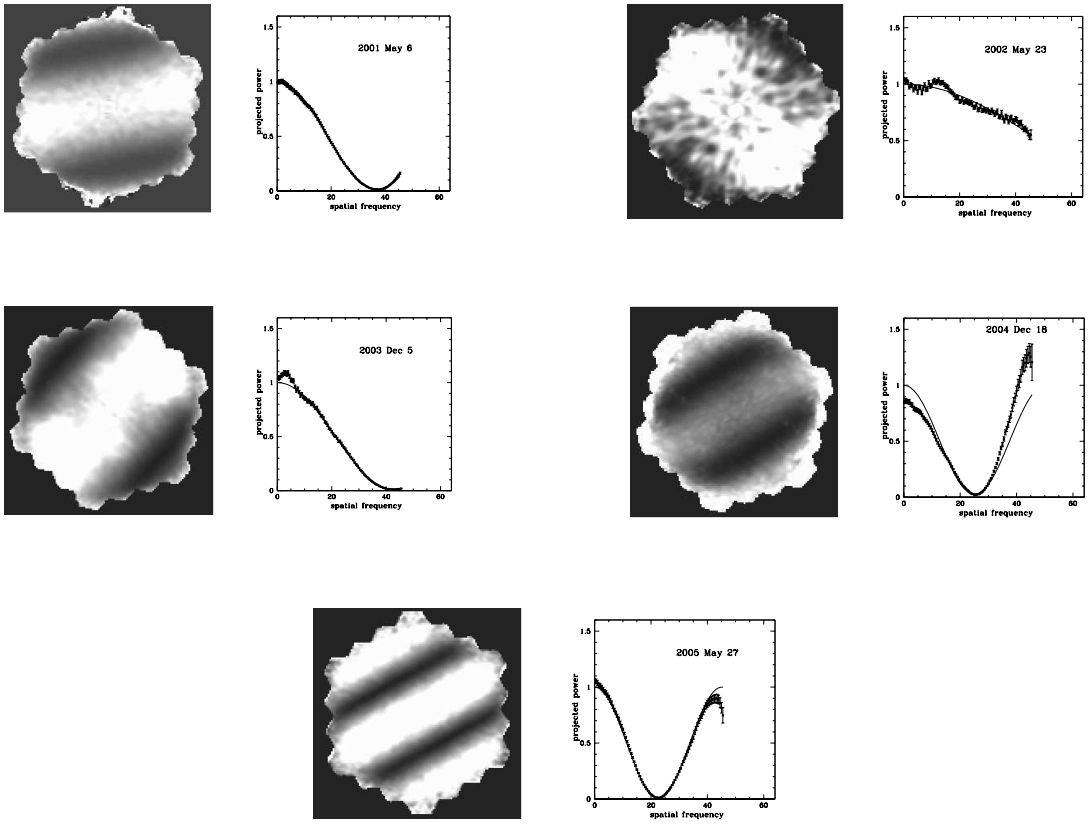

Figure 3.1 The two-dimensional visibilities for all the speckle data are shown in combination with plots of one-dimensional cuts through the visibilities. The points represent actual data, while the solid lines show the best fit of Equation 1 to this data. The data from 2002 clearly illustrates that the separation of the binary during this epoch was below the diffraction limit. The degeneracy of the separation and flux ratio in this fit (where the first minimum was not reached) necessitated the fixing of the flux ratio in this epoch to obtain the correct separation. The results of this analysis can be seen in Figure 3. The slight discrepancy in the 2004 fit comes from discrepancy between the calibrator and the object, stemming from large scale changes in seeing on short timescales. However, the large error bars on this data point account for this variation and thus they do not weigh heavily in our orbital fit.

al. (2001), and another taken two days later by Brandeker et al. (2003). Table 1 lists all separation, position angle, and flux ratio measurements that are used in this study.

Over the six years that the components of TWA 5A have been spatially resolved, the binary has undergone a full orbit (see Figure 3), allowing an accurate estimate of its orbital parameters. We calculate an orbital solution for TWA 5A using the Thiele-Innes method (e.g., Hilditch 2001), minimizing the χ^2 between the model and the measurements, which are converted from angular separation and position angle to right ascension and declination. Our model incorporates the following 7 standard orbital elements: P (period), A (semi-major axis), e (eccentricity), i (inclination), T_o (time of periapse passage), Ω (longitude of the ascending node), and ω (argument of pericenter). With nine two-dimensional astrometric measurements, there are eleven degrees of freedom in our fit. The best fitting model produced a χ^2 of 8.91 with 11 degrees of freedom. Furthermore, of the nine data points used in the fit, seven are within 1σ and two are within 2σ of the model, suggesting that our fit is good. The 1σ uncertainties in the model parameters are estimated by changing the values of χ^2 by one (Bevington & Robinson 1992). Table 2 lists the best-fit orbital parameters and their uncertainties and Figure 3 shows our solution for the projected orbit of TWA 5A. This astrometric solution yields a mass normalized by the distance cubed of 0.71 $\pm$ 0.14 $M_\odot$ /(D/44 pc)^3.

3.3 Discussion and Conclusions

With a well-determined astrometric orbit for TWA 5A, it is possible to begin to compare dynamical estimates of M/ (D/44 pc)^3 with those inferred from theoretical PMS tracks. By comparing the quantity M/ (D/44 pc)^3, we preserve the

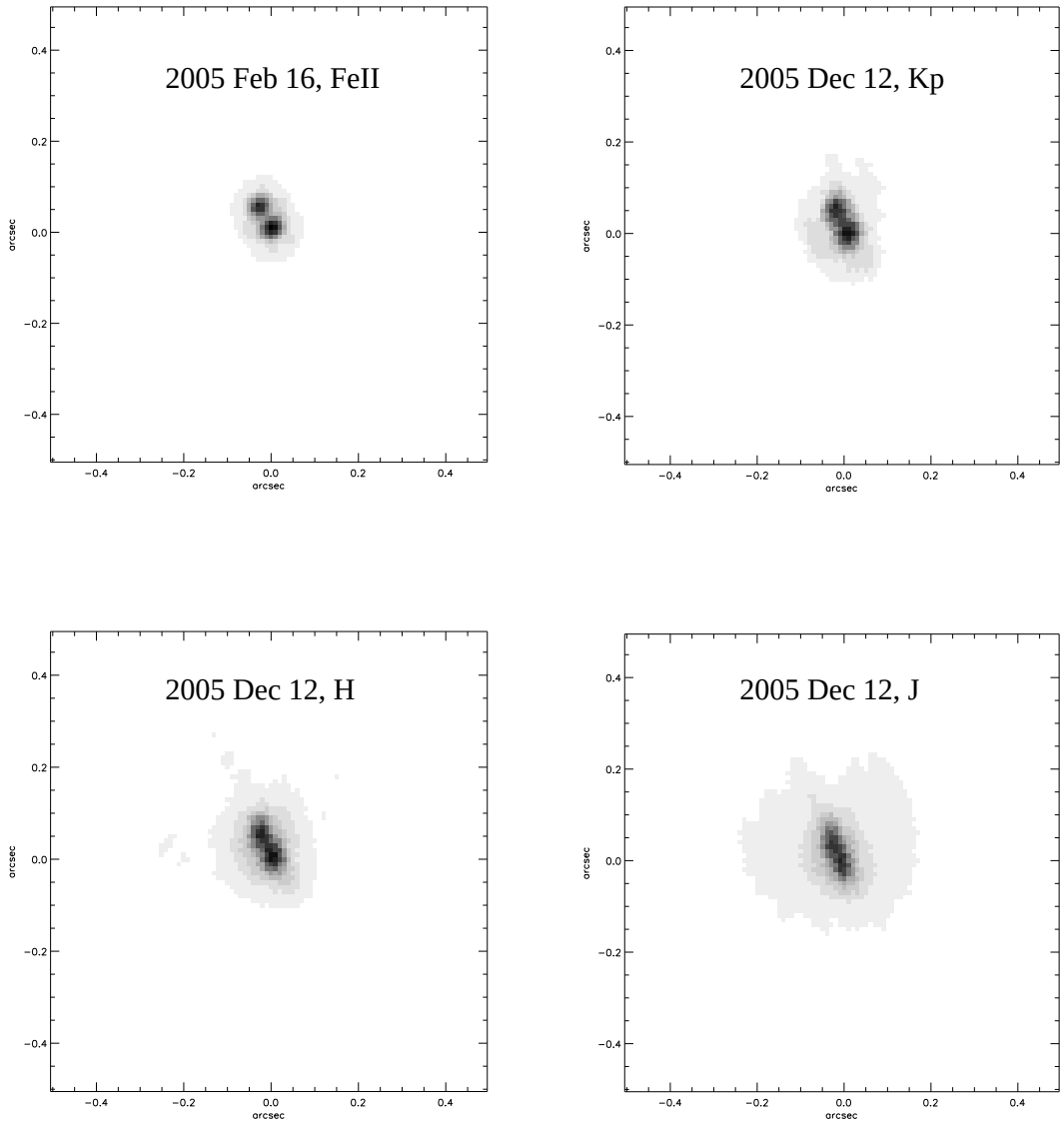

Figure 3.2 NIRC 2 AO images of TWA 5A taken on 2005 February 16 and 2005 December 12. In all images, north is up and east is to the left. Component TWA 5Aa is to the southwest and component TWA 5Ab is to the northeast.

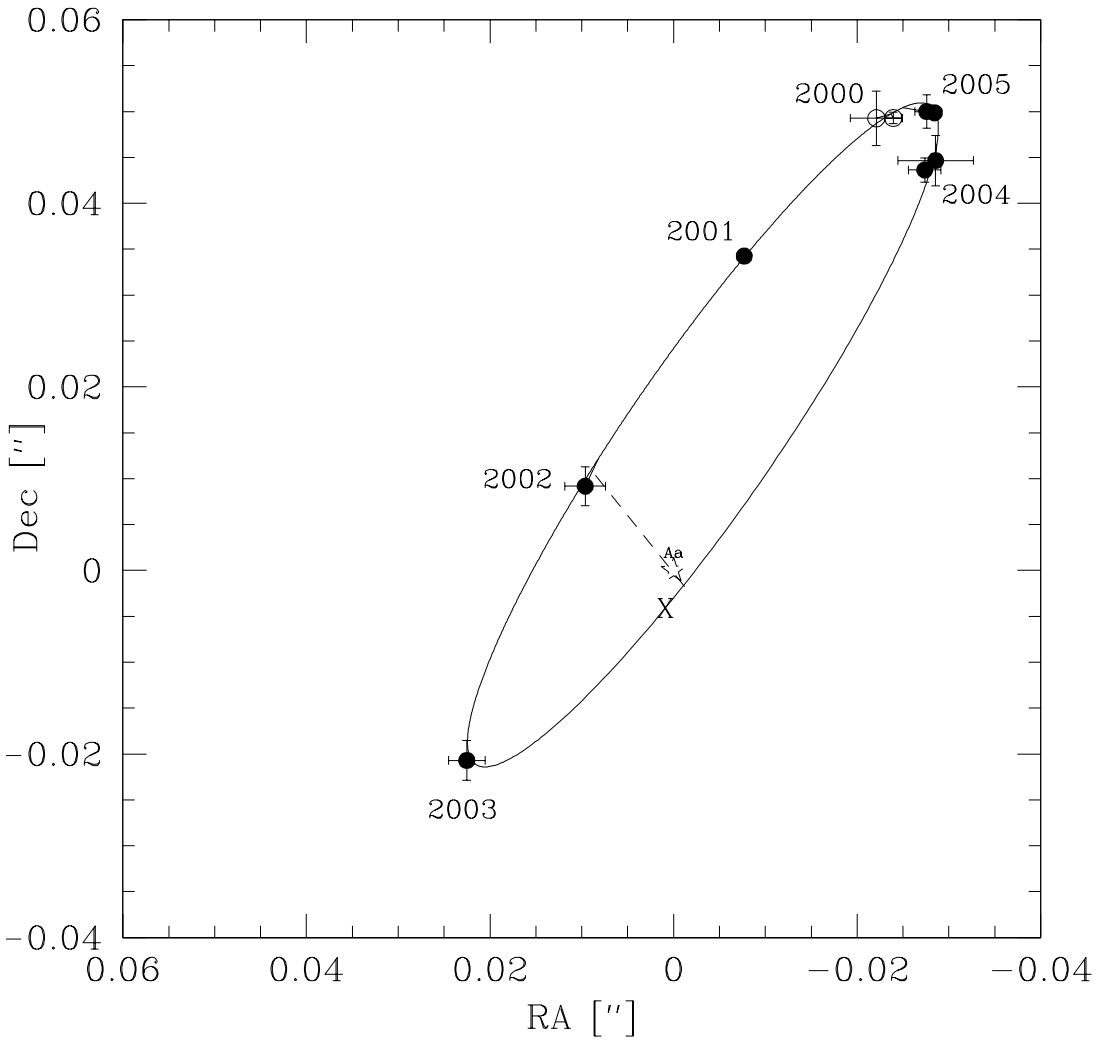

Figure 3.3 Orbital solution for TWA 5Aa and TWA 5Ab. Filled circles represent the data taken in this study, while the open circles represent data taken from the literature (both in 2000). The star at [0,0] marks the position of TWA 5Aa; the lines from the data points to the ellipse indicate where the fit believes the point should lie on the orbit. The dashed line through the center represents the line of nodes and the 'X' marks the location of closest approach. The parameters for this orbit are given in Table 2.

Table 3.2. Orbital Parameters of TWA 5A

P (years)	5.94 ± 0.09
A ($''$)	$0\farcs066$ ± 0.005
T_o (years)	2004.34 ± 0.09
e	0.78 ± 0.05
i (degrees)	97.4 ± 1.1
Ω (degrees)	37.4 ± 0.9
ω (degrees)	255 ± 3

high precision of the astrometric data in the analysis. Here we investigate the predictions of M/ (D/44 pc)^3 and age from the models by Baraffe et al. 1998 (α = 1.0), D'Antona & Mazzitelli 1997, Palla & Stahler 1999, Siess et al. 2000, and Swenson et al. 1994.

Model estimates of mass and age require both effective temperature and bolometric luminosity as inputs. Effective temperatures are estimated from the unresolved spectral type for TWA 5A and component flux ratios. The photometric analysis performed here and elsewhere (see Table 1) shows that the two components of TWA 5A have nearly equal brightness out to 1.6 μm. We therefore assume that the components have the same spectral type and assign it to be M1.5 ± 0.5, the spectral type found from a spatially unresolved spectrum (Webb et al. 1999). This is consistent with the J-H colors for each component, which are calculated by combining the 2MASS unresolved magnitudes with the flux ratios measured here (J-H[M1.5] = 0.67; Leggett et al. 1992). We estimate the temperature of these components using a conversion of spectral type to effective temperature given in Luhman et al. (2003). These temperatures are intermediate between dwarf and giant stars, thus making them appropriate for PMS stars like TWA 5A. Bolometric luminosities are estimated using our H band magnitudes and the corresponding H band bolometric corrections for PMS stars (Luhman

2005, private communication), along with the kinematic distance for TWA 5A of 44 ± 4 pc (Mamajek 2005). These input values are given in Table 3.

The uncertainties in M/ (D/44 pc)^3 and age from each model are estimated through Monte Carlo simulations. This is necessary to account for the correlation between input values. The bolometric correction used for determining the luminosity stems from the effective temperature. Additionally, the luminosities of the primary and the secondary are correlated, as they are calculated from the same parameters, namely the total flux and the flux ratios. The Monte Carlo simulation for each model is run with 10^5 points sampled from independent, gaussian distributions of total H-band flux densities, H-band flux density ratios, distances, and effective temperatures. These runs produce distributions of predicted M/ (D/44 pc)^3 and ages.

Figure 4 shows the dynamical mass normalized by the distance-cubed and with it the estimated age of the TW Hydrae association (10 ± 2 Myr, based on comparison with the β Pictoris moving group, Zuckerman & Song 2004), compared with the model predictions as determined by the Monte Carlo simulations. While the input values are generally treated as independent variables, the Monte Carlo simulations demonstrate that it is important to consider the existing correlations between input values, as the resulting uncertainties are otherwise significantly underestimated (by up to a factor of five depending upon the model). With this proper treatment, the dynamical mass and age estimates are within 2σ of all five tracks. For this age, TWA 5A provides the second dynamical test of PMS tracks and the first below a solar mass.

While it is reassuring that current models agree with these measurements, we are unable to distinguish between the model tracks. Future improvements in the precision of both the distance and the temperature would allow for a more

Table 3.3. TWA 5 System Photometry

Component	Sp. Ty.	m_K	m_H	m_J	J-H	H-K	Log[Temp] (K)	Log[Lum] ($L_\odot$)
TWA 5Aa	M1.5 ± 0.5	7.39 ± 0.04	7.69 ± 0.04	8.40 ± 0.07	0.71 ± 0.08	0.30 ± 0.06	3.56 ± 0.01	-0.80 ± 0.08
TWA 5Ab	[M1.5 ± 0.5]	7.62 ± 0.08	7.79 ± 0.05	8.45 ± 0.15	0.66 ± 0.16	0.17 ± 0.09	3.56 ± 0.01	-0.84 ± 0.08

Note. — The apparent K, H, and J band magnitudes for TWA5Aa and Ab are computed using 2MASS measurements of the combined magnitudes and the flux ratio measurements given in Table 1. The spectral type for TWA 5Ab is assumed to be roughly the same as TWA 5Aa, given that the two components have nearly equal brightness. Temperatures are estimated from the scalings given in Luhman et al. 2003, while bolometric luminosities are calculated using the kinematic distance and H band bolometric corrections (Luhman 2005, private communication).

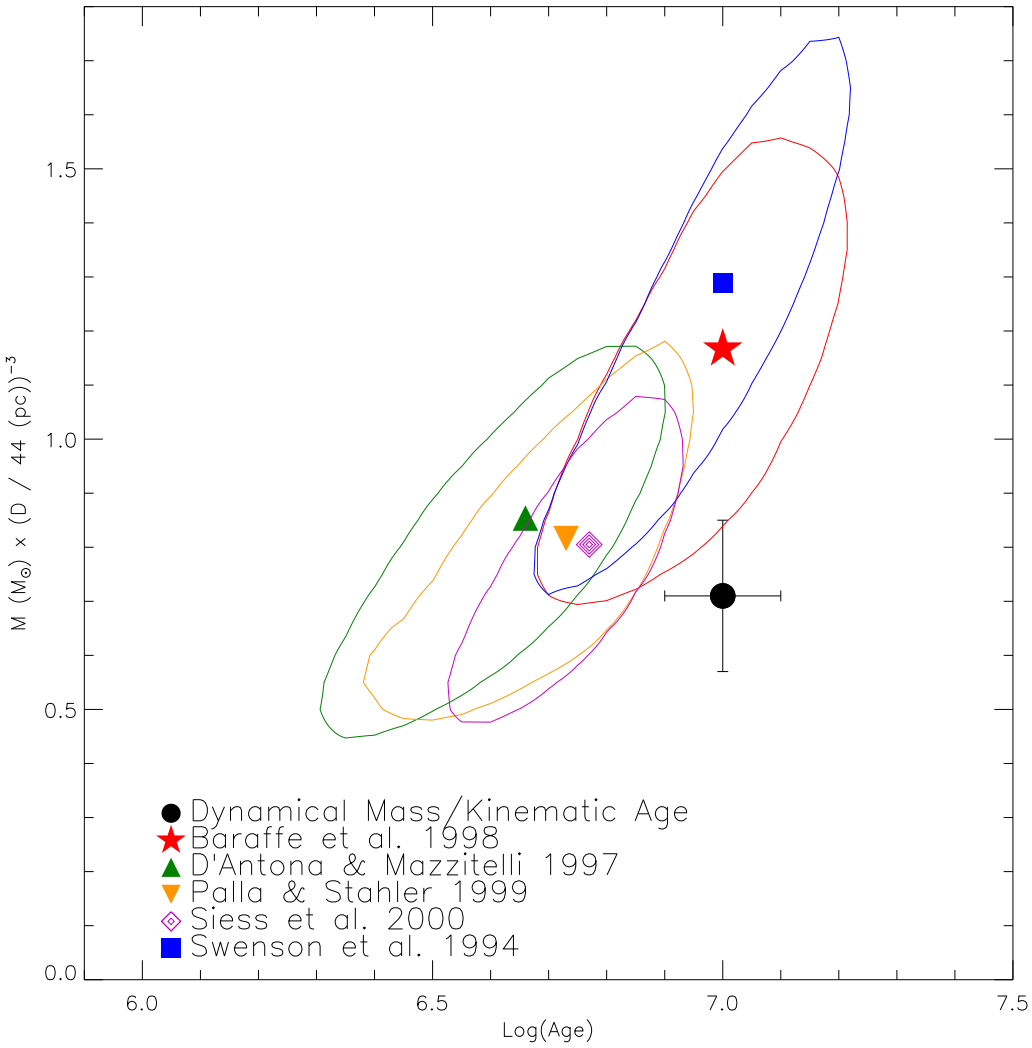

Figure 3.4 Mass and age for TWA5Aa+b calculated from the dynamical solution and predicted from each of the five theoretical models considered. The age shown here is the age predicted for the primary, but the age predictions for both components are consistent with each other. The masses are divided by the distance cubed, as the distance is a source of systematic uncertainty and is not necessary to include in this comparison.

illuminating comparison between the theoretical models. The temperature uncertainties on the components of TWA 5A could be substantially reduced with spatially resolved spectral types, which should drive the uncertainty in the temperature down to ± one quarter of a spectral subclass. Uncertainties in the distance could also be substantially reduced. Typical uncertainties in new parallax measurements are on the order of a few milliarcseconds, with improvements on these results promised in the near future (Vrba et al. 2004). A separate method to determine the distance is the addition of spatially resolved radial velocities, which would allow an independent distance estimate from the orbital parameters. In principle, a factor of two improvement in the distance uncertainty could be achieved. These radial velocity measurements would also improve the total mass estimate, as would additional astrometric measurements, and would also eventually allow for the determination of *individual* masses of each of the components. However a potential complication is the possible existence of an additional component in the system (Torres et al. 2003). Another possible method of determining the individual masses of the components of TWA 5A is to use absolute astrometry with respect to TWA 5B, as was done recently for T Tau S (Duchêne et al. 2006). If we just take the improvements expected from future parallax measurements, spatially resolved spectra, and additional astrometry, we expect to be able to distinguish between the tracks at the 2-3σ level.

Future spatially resolved spectral types would also address the marginal inconsistency between the J-H and H-K colors for the primary. Currently, we have assumed that this arises from a small K-band excess (2σ). Torres et al. (2003) suggest that an additional component may be present in the system. If this component were particularly low mass, it could give rise to the apparent K band excess of the primary. Alternatively, the infrared excess could arise from circumstellar material. Mohanty et al. (2003) report the detection of strong Hα

emission in an unresolved, high resolution spectrum of TWA 5A, implying at least one of the components is accreting. However, no mid-infrared excess has been detected in unresolved measurements. Given the tightness of the TWA 5A binary, any disk material is likely to be localized to a very radially thin reservoir of material near the dust sublimation radius. In either case, disk or low mass companion, the cause of the infrared excess should not have a large impact on the track comparison.

In summary, our solution to the orbit of this system and the subsequent determination of its mass shows that these young, nearby associations of stars are excellent laboratories for the study of low-mass star formation. There are likely other systems in TW Hydrae with similar close companions that will yield more mass estimates within a short time, much like we have seen here. Thus monitoring of these systems will greatly aid in the constraint of PMS mass tracks in the near future.

3.4 Appendix: NIRC Plate Scale and Orientation

NIRC's pixel scale and orientation are calibrated relative to NIRC 2 using observations of the Galactic center (see Table 4). While NIRC's pixel scale has been stable, known engineering adjustments have introducted slight rotations in the camera over time. Four out of five of TWA5A speckle measurements were taken at a time with NIRC's orientation is well-characterized by the Galactic center experiment. The 2003 measurement, however, was taken during a period of multiple engineering adjustments and no Galactic center data. We therefore bound its orientation by the measurements taken of the Galactic Center just before and after it, which leads to an absolute offset of 0.032 ± 0.719^o. For all of our observations, we use a constant plate scale of 20.45 ± 0.03 mas/pixel.

Table 3.4. Absolute NIRC Position Angle Offsets and Uncertainties

Epoch(s)	No. of Measurements	Absolute PA (deg)
1998 April - 1998 August	4	-0.40 ± 0.135
1998 October - 2002 July	11	-0.884 ± 0.143
2003 April - 2003 September	3	0.761 ± 0.135
2004 April - 2005 May	4	-0.728 ± 0.196

CHAPTER 4

Dynamical Masses of Very Low Mass Binaries

Characterizing the fundamental properties of brown dwarfs is an important step in unlocking the physics of substellar objects, including gas giant planets. These very cool objects have internal and atmospheric properties unique from those of stars, including partially degenerate interiors, dominant molecular opacities, and atmospheric dust formation (Chabrier & Baraffe 2000). Brown dwarfs also represent a substantial fraction of the galactic stellar content, and are bright and numerous enough to be studied in great detail with current technology (Kirkpatrick 2005). Thus, these substellar objects present an ideal laboratory in which to study the physical processes at work in very low mass objects that both approach and overlap the planetary mass regime.

Mass is the most fundamental parameter in determining the properties and evolution of a brown dwarf; unfortunately it is also one of the most difficult to measure. Masses of brown dwarfs are typically inferred from the comparison of measured luminosities and temperatures with predictions from theoretical models. However, masses obtained in this way from different models can be discrepant, especially amongst the lowest mass objects (Hillenbrand & White 2004; Tamazian et al. 2002; Liu et al. 2008). These discrepancies stem from physical assumptions about the interior and atmospheric properties of these highly complex objects (Burrows et al. 1997; Chabrier et al. 2000). An essential step toward properly calibrating these models and constraining their physics is to

obtain dynamical mass measurements of brown dwarfs.

By determining the orbital solutions of brown dwarfs that are part of binary systems, masses can be measured. Orbital measurements are normally made by monitoring either spectroscopic binaries using high resolution spectroscopy or visual binaries using high resolution imaging. Amongst very low mass (VLM) objects, two spectroscopic binaries have had their orbital solutions calculated (Basri & Martin 1999, Stassun et al. 2006). Spectroscopic orbital solutions provide the mass ratio of the components of the binary (unless the system is eclipsing, in which case component masses can be derived, Stassun et al. 2006). Five VLM visual binaries have also had their orbital solutions derived via astrometric monitoring (Lane et al. 2001, Bouy et al. 2004, Liu et al. 2008, Dupuy et al. 2009a, Dupuy et al. 2009b). Of these five systems, four have been monitored using adaptive optics (AO) on the W.M. Keck II telescope. In particular, the advent of laser guide star adaptive optics (LGS AO) at Keck has drastically increased the number of VLM objects that can be observed at high spatial resolution (Wizinowich et al. 2006). In a survey done in parallel to the work presented here, both the orbit of 2MASS 1534-29 AB (Liu et al. 2008) and LHS 2397a AB (Dupuy et al. 2009b) were derived using data obtained in conjunction with LGS AO system. Total system masses are derived when only astrometric measurements are obtained for visual binaries, as is the case for four out of five of these measurements.

The most powerful tests of theoretical evolutionary models can be performed if the individual component masses of a binary are known (as was demonstrated by Stassun et al. 2006). Individual component masses allow for the comparison of objects to the predictions of models free of assumptions about their relationship to their companion, and also provide definitive determination of whether an

object is substellar if it is near the stellar/substellar boundary. Other than eclipsing binaries, one of the best ways to derive component masses is to monitor a visual binary using high resolution spectroscopy in combination with astrometry. Derivations of both the total system mass with astrometry and the mass ratio with spectroscopy can be combined to give individual masses for the components.

The relative radial velocity expected between the components of visual binaries is typically less than 10 km/s. Thus, in most cases, visual binaries monitored with unresolved high resolution spectroscopy will not have a measurable velocity shift much beyond the systemic velocity of the system - more likely, the absorption lines of the combined system will appear broadened. In order to measure the radial velocities of each component, it is desirable to have spatially resolved, high resolution spectroscopic observations. The high spectral resolution (R$\sim$25000), near-infrared spectrograph NIRSPEC, offered on Keck II in conjunction with the LGS AO system, enables these necessary observations. By yielding high resolution spectra of each component, NIRSPEC provides the ability to determine individual component radial velocities and to derive the mass ratio of a visual binary. This method has been shown to be possible in the case of GJ 569Bab, where a combination of astrometric and spatially-resolved spectroscopic monitoring provided component masses (Zapatero Osorio et al. 2004, Simon et al. 2006). Measurements such as these are currently not possible from space, as there is no instrument that achieves the necessary spectral resolution. We now seek a larger sample of mass measurements across a range of spectral types in order to systematically test evolutionary models.

We present the first results from our ongoing monitoring campaign of VLM visual binaries using the LGS AO system on the Keck II telescope. Over the course of three years, we have monitored a total of 26 VLM binaries. We present

the relative orbital solutions for 15 systems, tripling the current number of mass measurements for VLM objects, and the absolute orbits for 6 systems. In section 4.1, we describe our sample selection and in section 4.2 we discuss our astrometric and spectroscopic observations. In section 4.3, we outline our data analysis procedures and in section 4.4, we describe our derivation of orbital solutions. In section 4.5, we derive bolometric luminosities and effective temperatures for the components of the binaries, and in section 4.6, we discuss the distribution of eccentricities as determined by our sample. In section 4.7 we present the comparison of our findings to evolutionary models. We then discuss the implications of our model comparison in section 4.8. We summarizes our findings in section 4.9.

4.1 Sample Selection

4.1.1 Initial Sample

The initial sample for this project was culled from Burgasser et al. (2007), which listed the 68 visual, VLM binaries known as of 2006. Three cuts were applied to this initial list. First, the binaries had to be observable with the Keck telescope LGS AO system, so we imposed a declination $>$ -35 degrees requirement, which reduced the possible number of targets to 61. Second, the operation of the LGS AO system requires a tip-tilt reference source of apparent R magnitude < 18 within an arcminute of the source, and therefore VLM binaries without a suitable tip-tilt reference were also cut. This lowered the total number of observable targets to 49, 80% of the northern hemisphere sample.

Third, we required that useful dynamical mass estimates would likely be obtained by 2009 (i.e., within a PhD timescale). To assess the required precision

for our dynamical mass estimates, we calculated the predicted masses for the two most commonly used sets of evolutionary models, those of Burrows et al. (1997) and Chabrier et al. (2000), across the entire range of temperatures and luminosities spanned by both models. We calculated the percent difference between the predictions of each model with respect to the prediction of Burrows et al. (1997). The results of this assessment are shown in Figure 4.1, which displays in color the offset between the models across the H-R diagram (with the discrepancies averaged in 50 K temperature increments and 0.1 $\log(L/L_{\odot}$ increments). As the figure demonstrates, we found that the difference in the mass predictions of the two models varied from anywhere from a few percent to greater than 100%. We therefore chose a precision goal of 10% because at this level the majority of the models predictions could be distinguished and because this level of precision was reasonable to expect given our observing strategy.

To implement our third cut, a series of Monte Carlo simulations were performed. In these simulations, the total system mass for each target was assumed based on the estimated spectral types of the binary components and held constant for all runs. Additionally, the semi-major axis of the orbit was chosen by sampling from the range of possible values between 1/2 and two times the original separation measurement. From these assumptions, a period was calculated, and T_o (time of periapse passage) was randomly selected from the range allowed by this period. All other orbital parameters for an astrometric orbit, which include e (eccentricity), i (inclination), Ω (longitude of the ascending node), and ω (argument of pericenter), where randomly selected from among the complete range of possible values of each parameter. Although it has been shown amongst higher mass field stars that the eccentricity distribution is not flat ($f(e) \sim 2e$, Duquennoy & Mayor 1991), it is unclear whether this distribution holds for VLM binaries, so we opted to sample from a flat eccentricity distribution.

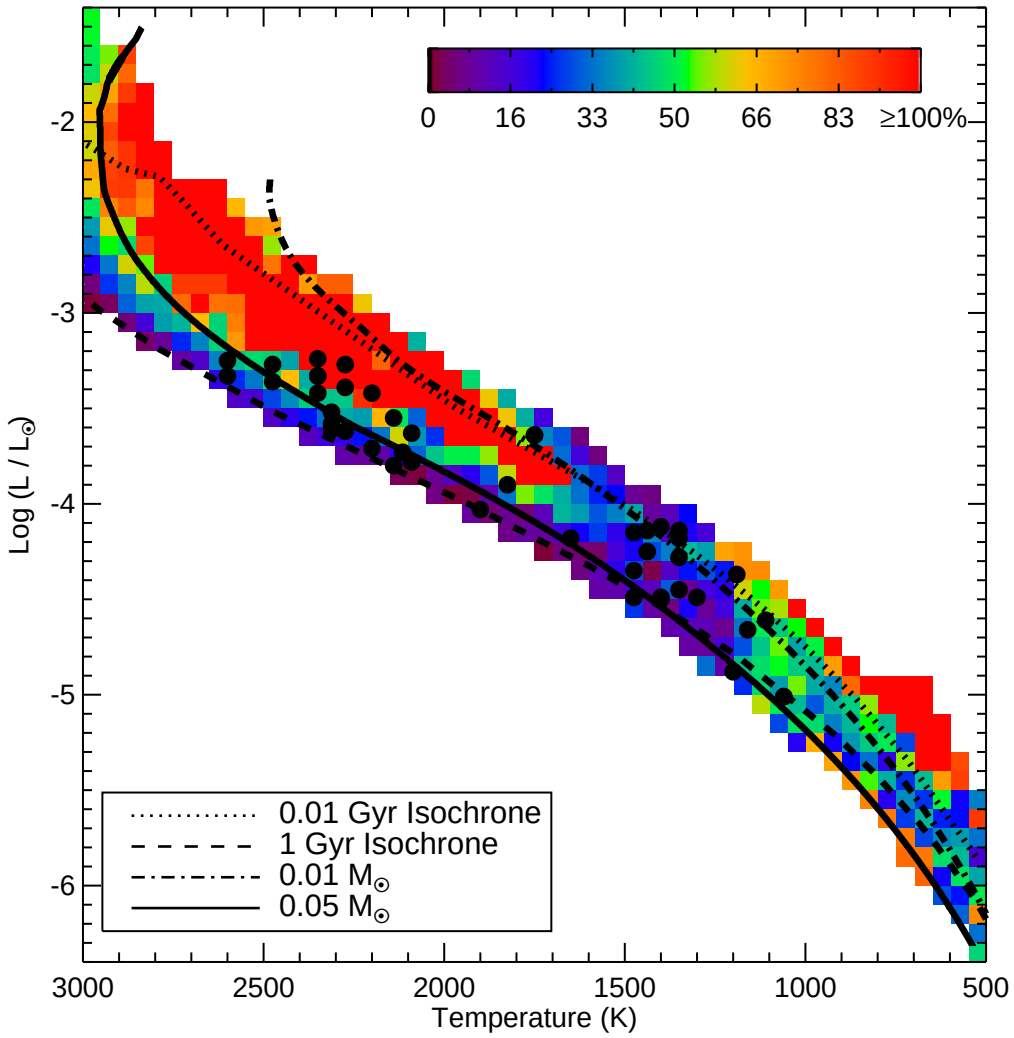

Figure 4.1 Percent discrepancy in mass predictions between the Burrows et al. (1997) evolutionary and the Chabrier et al. (2000) evolutionary models, over the range on the H-R diagram with complimentary coverage. The colors represent the level of the discrepancy in units of percent of the mass predicted by the Burrows et al. (1997) models, as shown by the scale bar. For the majority of the H-R Diagram, the discrepancy between the model predictions is $\gtrsim$10%, with a number of regions having discrepancies greater than 100%. Overplotted are two isochrones and lines of constant mass from the Burrows et al. (1997) models for points of reference. In addition, the overplotted filled points show the rough location of the sources in our full sample. The largest discrepancies are at the youngest ages, but the discrepancies are still substantial for older objects.

Using these simulated orbits, it was possible to generate simulated sets of "astrometric datapoints" corresponding to the likely times of measurement. We planned on two observing campaigns per year, one in June and one in December. These dates were chosen to coincide with the two times per year that NIRSPEC is offered behind the LGS AO system at Keck (see section 4.2). The sky coordinates of each binary then determined whether we simulated one or two astrometric data points per year. We also generated simulated sets of relative radial velocity measurements, which could be predicted from orbital parameters chosen for each run. These simulated measurements were chosen to correspond to appropriate observing dates. All synthetic data points were combined with already existing measurements, the number of which varied from source to source. While the majority of sources initially had only one previous astrometric measurement, others had up to six. Synthetic astrometric datapoints were also assigned uncertainties based on the average uncertainty normally obtained for measurements of binary stars using the Keck AO system with NIRC2 ($\sigma \sim 1$ mas). Although the average uncertainty in relative radial velocity measurements with NIRSPAO was not known at the time, other observations with NIRSPEC suggested using a conservative uncertainty of about 1 km/s. All datapoints where then used to run the orbital solution fitter, which uses the Thiele-Innes method (e.g., Hilditch 2001), minimizing the χ^2 between the model and the measurements (see Ghez et al. 2008). A chi-squared cut of 10 was imposed to account for the fact that in some simulated orbital solutions could not generate astrometric measurements corresponding to real data points in those systems with multiple measurements. In this way, we were able to utilize more information than simply separation and estimated mass to calculate likelihood of accurate mass measurement in a system. A total of 1000 simulated orbital solutions were created for each system.

From each of these simulations, the predicted uncertainty in dynamical mass

could be determined. All those systems for which 66% of the simulations yielded precisions of 10% or better in mass were put in the final sample. This generated a sample of 21 targets that we began monitoring in the spring of 2006. These sources are listed in Table 4.1. Figure 4.2 shows the results of our simulations, plotting the percent of solutions with precise mass estimates versus the initial binary separation. The spectral type of the primary component is denoted by symbol, and sources included in our initial sample are colored red. The variation in percent of solutions with separation stems from the variation in the estimated masses of the components and the number of previous measurements at the start of our monitoring program.

Table 4.1. Initial VLM Binary Sample

Source Name	RA (J2000)	Dec (J2000)	Estimated Sp Types	Discovery Reference	2MASS K Band Mag.
LP 349-25AB	00 27 55.93	+22 19 32.8	M8+M9	13	9.569 ± 0.017
LP 415-20AB	04 21 49.0	+19 29 10	M7+M9.5	8	11.668 ± 0.020
2MASS J04234857-0414035AB[a]	04 23 48.57	-04 14 03.5	L7+T2	1	12.929 ± 0.034
2MASS J05185995-2828372AB[a]	05 18 59.95	-28 28 37.2	L6+T4	2	14.162 ± 0.072
2MASS J06523073+4710348AB[a]	06 52 30.7	+47 10 34	L3.5+L6.5	3	11.694 ± 0.020
2MASS J07464256+2000321AB	07 46 42.5	+20 00 32	L0+L1.5	4	10.468 ± 0.022
2MASS J09201223+3517429AB	09 20 12.2	+35 17 42	L6.5+T2	4	13.979 ± 0.061
2MASS J10170754+1308398AB[b]	10 17 07.5	+13 08 39.1	L2+L2	5	12.710 ± 0.023
2MASS J10471265+4026437AB	10 47 12.65	+40 26 43.7	M8+L0	6	10.399 ± 0.018
GJ 417BC[a]	11 12 25.67	+35 48 13.2	L4.5+L6	5	12.721 ± 0.028
GJ 569b AB	14 54 29.0	+16 06 05	M8.5+M9	14	∼9.8
LHS 2397a AB	11 21 49.25	-13 13 08.4	M8+L7.5	12	10.735 ± 0.023
2MASS J121711-031113AB	12 17 11.0	-03 11 13	T7.5+Y?	7	∼15.887[c]
2MASS J14263161+1557012AB	14 26 31.62	+15 57 01.3	M8.5+L1	6	11.731 ± 0.018
HD 130948 BC	14 50 15.81	+23 54 42.6	L4+L4	10	*sim*11.0
2MASS J15344984-2952274AB	15 34 49.8	-29 52 27	T5.5+T5.5	7	14.843 ± 0.114
2MASS J1600054+170832AB[a]	16 00 05.4	+17 08 32	L1+L3	5	14.678 ± 0.114
2MASS J17281150+3948593AB	17 28 11.50	+39 48 59.3	L7+L8	5	13.909 ± 0.048
2MASS J17501291+4424043AB	17 50 12.91	+44 24 04.3	M7.5+l0	8	11.768 ± 0.017
2MASS J18470342+5522433AB	18 47 03.42	+55 22 43.3	M7+M7.5	9	10.901 ± 0.020
2MASS J21402931+1625183AB	21 40 29.32	+16 25 18.3	M8.5+L2	6	11.826 ± 0.031
2MASS J22062280-2047058AB	22 06 22.80	-20 47 05.9	M8+M8	6	11.315 ± 0.027

[a]In all observations of these sources, the binary was never resolved. We report upper limits to the separations of these binaries, but no orbital solutions can be derived

[b]Source cut from sample due to additional astrometry showing that it was not likely to yield a mass to a precision of better than 10% in the required timeframe

[c]Flagged as having poor photometric quality in 2MASS catalog

Note. — References - (1) Burgasser et al. 2005 (2) Cruz et al. 2004 (3) Reid et al. (4) Reid et al. 2001 (5) Bouy et al. 2003 (6) Close et al. 2003 (7) Burgasser et al. 2003 (8) Siegler et al. 2003 (9) Siegler et al. 2005 (10) Potter et al. (2002) (11) Koerner et al. 1999 (12) Freed et al. 2003 (13) Forveille et al. 2005 (14) Martin et al. 2000

4.1.2 Sample Refinement

Upon commencement of the monitoring campaign, it became clear that sample refinement and adjustment of observing priorities was required. Three sources had tip/tilt stars that did not allow for successful observation (2MASS 0423-04, GJ 417B, and 2MASS 1217-03). It is possible that some of these tip/tilt stars were actually resolved galaxies. In addition, 2MASS 1217-03 was later reobserved with HST and determined to not be resolved, making it unlikely to be a binary (Burgasser et al. 2006). Three sources were successfully observed, but were unresolved in all NIRC2 observations (2MASS 0518-28, 2MASS 0652+47, and 2MASS 1600+17). It is possible that these sources have orbits that take them below the Keck diffraction limit. The source 2MASS 1047+40 was possibly marginally resolved in our first epoch of data in 2006 June, but all other measurements were unresolved. We report all unresolved measurements as upper limits. Finally, one source, 2MASS1017+13 was observed and resolved in 2006 November, but subsequent iterations of our Monte Carlo techniques showed that with this new epoch of data, the source was no longer "likely" to yield a mass with the necessary precision. We therefore also ceased additional observations of this target.

Additionally, a few targets were added to the monitoring program as it progressed. First, it was recognized that some sources did not make the cut because of the thesis timescale constraint, but with a slightly longer period of monitoring could have their masses derived to a high level of accuracy. In particular, the timescale cut introduced an obvious bias to sources with higher predicted masses, or earlier spectral types. Therefore, we added three objects included in Burgasser et al. (2007) to the NIRC2 monitoring program to provide initial epochs of data for future mass determination. These three objects are shown on Figure 4.2 in blue. All three were of spectral type L or T (we did not add additional M dwarfs

to our sample because of the large number of M dwarfs included in our initial sample). All three had a >50% probability of a precise dynamical mass estimate in our initial Monte Carlos. These added sources are given in Table 4.2. Two additional sources were added to the sample that were discovered by Reid et al. (2006) after the initial publication of Burgasser et al. (2007). For these sources, we have calculated the likelihood that they will yield precise mass estimates by 2012. We do not include these sources on Figure 4.2 because the simulations we performed were different from our initial simulations, but we found that both sources had a >50% chance of yielding a precise mass estimate by 2012. We therefore added these two sources to our astrometric program as well. They are also listed in Table 4.2

4.2 Observations

4.2.1 Astrometric Data

Targets in our sample were observed astrometrically beginning in May of 2006. Observing was conducted twice a year between 2006 May and 2009 June UT using the Keck II 10 m telescope with the facility LGS AO system (Wizinowich et al. 2006; van Dam et al. 2006) and the near-infrared camera, NIRC2 (K. Matthews 2009, in preparation). The AO system, which is also used for obtaining radial velocities (see next section), uses the sodium laser spot (V$\sim$10.5) as the primary correction source for all but two systems. Tip/tilt references are listed in Table 4.3. NIRC2 has a plate scale of 9.963 $\pm$ 0.005 mas pixel^{-1} and columns that are at a PA of 0.13 $\pm$ 0.02^o relative to North (Ghez et al. 2008). The observing sequence for each object depended upon the brightness of the target, whether observations in multiple filters had been previously made, and whether

Table 4.2. Additional VLM Binary Sources

Source Name	RA (J2000)	Dec (J2000)	Estimated Sp Types	Discovery Reference	2MASS K Band Mag.
2MASS J07003664+3157266	07 00 36.64	+31 57 26.60	L3.5+L6	1	11.317 ± 0.023
2MASS J08503593+1057156	08 50 35.9	+10 57 16	L6+L8	3	14.473 ± 0.066
2MASS J10210969-0304197	10 21 09.69	-03 04 20.10	T1+T5	2	15.126 ± 0.173
2MASS J21011544+1756586	21 01 15.4	+17 56 58	L7+L8	4	14.892 ± 0.116
2MASS J21522609+0937575	21 52 26	+09 37 57	L6+L6	1	13.343 ± 0.034

Note. — References - (1) Reid et al. 2006 (2) Burgasser et al. 2006 (3) Reid et al. 2001 (4) Bouy et al. 2003

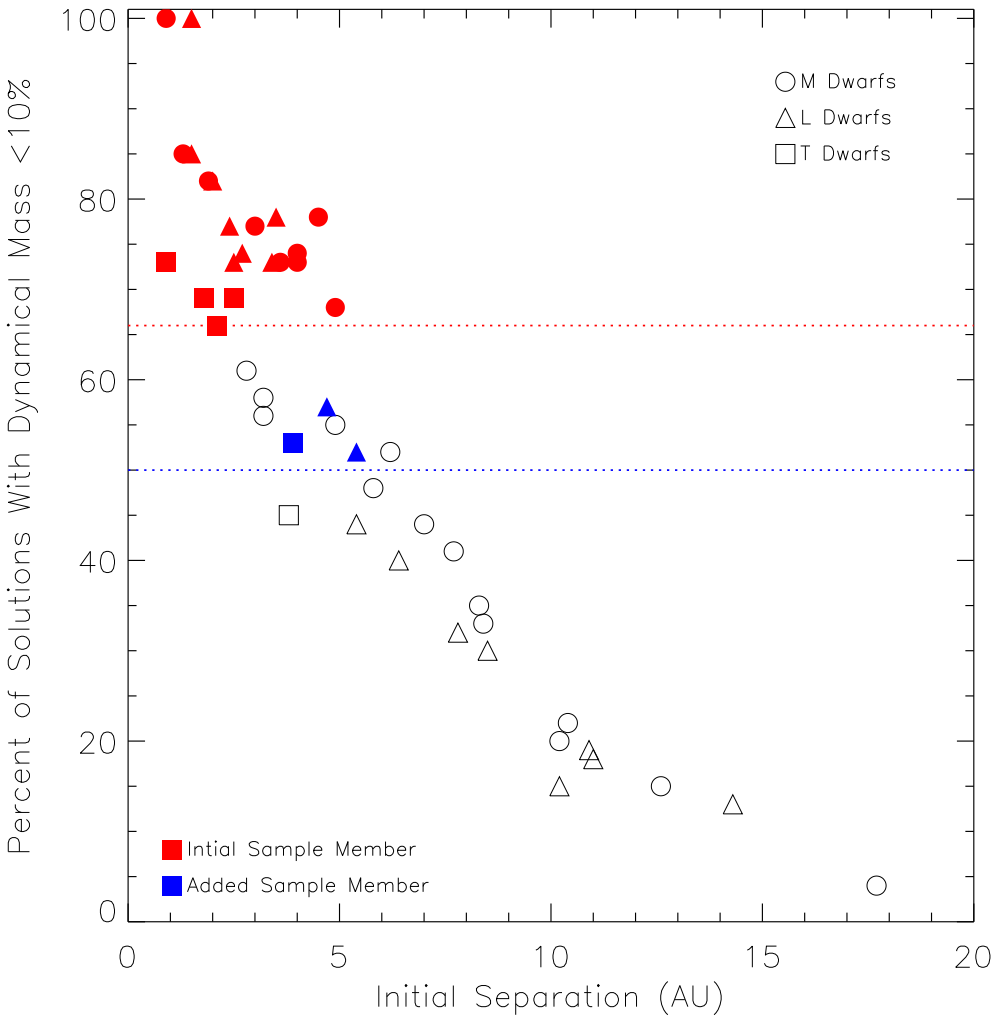

Figure 4.2 The percent of solutions in our Monte Carlo simulations that yielded a mass with $\lesssim$10% precision versus the initial separation of the binary. Sources included in our sample are denoted in red, with the red dotted line showing our cutoff of 66%. Additional sample members are denoted in blue, and were chosen because they had either L or T spectral types and because they had a probability of >50% of yielding a precise mass in our initial simulations (with an increased probability for high precision masses by 2012). The symbol type denotes the spectral type of the primary component.

the target was actually resolved into two components at that epoch. If the binary was not resolved, we could only obtain upper limits on the separation, which do not require a full observing sequence to estimate. We generally tried to take at least nine individual exposures on each target, though sometimes due to time constraints less exposures were taken. Table 4.3 gives the log of all imaging and photometric observations, listing when each target was observed, the filters through which it was observed and the exposure time and number of images taken in each filter, and the tip/tilt reference source used for each target. In many cases, the brown dwarf targets were bright enough to serve as their own tip/tilt reference, even though they are not bright enough for natural guide star observations.

Table 4.3. Log of NIRC2 LGS AO Observations

Target Name	Date of Observation (UT)	Tip/Tilt Reference	Filter	Exposure Time (sec x coadds)	No. of Frames
2MASS 0518-28AB	2006 Nov 27	USNO-B1.0 0615-0055823	K-prime	30x4	18
	2007 Dec 02		K-prime	30x4	9
	2008 Dec 18		K-prime	20x4	5
2MASS 0652+47AB	2006 Nov 27	USNO-B1.0 1371-0206444	K-prime	8x12	6
	2007 Dec 02		K-prime	5x12	9
2MASS 0746+20AB	2006 Nov 27	source	K-prime	2x30	9
	2007 Dec 01		K-prime	2x30	8
	2007 Dec 01		J	4x15	9
	2008 Dec 18		K-prime	2x30	8
	2008 Dec 18		H	2x30	6
2MASS 0850+10AB	2007 Dec 02	USNO-B1.0 1009-0165240	K-prime	30x4	9
	2008 Dec 18		K-prime	10x1	5
2MASS 0920+35AB	2006 Nov 27	USNO-B1.0 1252-0171182	K-prime	30x4	7
	2007 Dec 02		K-prime	30x4	4
	2007 Dec 02		J	30x4	2
	2008 May 30		K-prime	30x4	6
	2008 Oct 21		H	30x4	6
	2008 Dec 18		H	10x10	7
	2009 Jun 10		H	10x5	6
2MASS 1017+13AB	2006 Nov 27	USNO-B1.0 1031-0208442	K-prime	13x12	3
2MASS 1047+40AB	2006 Jun 21	source	K-prime	1x60	9
	2006 Nov 27		K-prime	2x30	12
	2007 Dec 02		K-prime	2x30	6
	2008 Dec 18		K-prime	1x30	9
2MASS 1426+15AB	2006 Jun 20	USNO B1.0-1059-0232527	K-prime	10x12	3
	2008 May 30		K-prime	10x12	8
	2008 May 30		J	15x5	5
	2009 May 02		K-prime	5x12	9
	2009 May 02		H	5x12	6
2MASS 1534-29AB	2006 Jun 20	USNO-B1.0 0601-0344997	J	30x4	9
	2008 May 30		K-prime	40x2	7
	2008 May 30		H	40x2	6
	2008 May 30		J	40x1	3
	2009 May 04		H	30x4	6
2MASS 1600+17AB	2007 May 20	USNO-B1.0 1071-0293881	K-prime	30x4	9
	2008 May 30		K-prime	10x1	2
2MASS 1728+39AB	2007 May 20	USNO-A2.0 1275-09377115	K-prime	30x4	5
	2008 May 30		K-prime	30x2	4
	2008 May 30		J	60x2	5
	2009 May 03		K-prime	30x2	7
	2009 Jun 11		H	30x4	9
2MASS 1750+44AB	2006 Jun 20	source	K-prime	20x4	8
	2007 May 17		K-prime	10x12	7
	2008 May 13		K-prime	10x12	6
	2008 May 30		H	5x12	6
	2008 May 30		J	10x1	4
	2009 May 01		K-prime	5x12	9
2MASS 1847+55AB	2006 May 21	source	K-prime	5x6	6
	2007 May 14		K-prime	1.452x1	9
	2008 May 20		K-prime	5x12	9
	2008 May 20		H	5x5	6
	2008 May 20		J	10x1	19

With only a few exceptions, all data used for astrometry were taken through the K-prime ($\lambda_o = 2.124$ μm, $\Delta\lambda = 0.351$ μm) band pass filter. Data in both the J Band ($\lambda_o = 1.248$ μm, $\Delta\lambda = 0.163$ μm) and H band ($\lambda_o = 1.633$ μm, $\Delta\lambda = 0.296$ μm) were also taken at some point for most targets to provide a complete set of spatially resolved, near-infrared photometry. The images were generally taken in a three position, 2.″5 x 2.″5 dither box, with three exposures per position (avoiding the lower left quadrant of NIRC2, which has significantly higher noise than the other three), which allowed sky frames to be generated from the images themselves. In addition, the wide dither box insures the incorporation of known residual distortion (Ghez et al. 2008, Yelda et al. 2009) in the camera into our final astrometric uncertainties.

4.2.2 Radial Velocity Data

Twelve objects in our astrometric sample were also observed using the NIR spectrograph NIRSPEC on Keck II (McLean et al. 2000) in conjunction with the LGS AO system (NIRSPAO). We used the instrument its in high spectral resolution mode, selecting a slit 0.″041 in width and 2.″26 in length in AO mode. We elected to observe in the K band, with a particular interest in the densely populated CO band head region ($\sim$2.3 μm), necessitating an echelle angle of 63 degrees and a cross-disperer angle of 35.65 degrees. The resolution in this setup is R$\sim$23000, and the total wavelength coverage spans 2.044 to 2.382 μm (orders 37-32), with breaks at 2.075-2.100 μm, 2.133-2.160 μm, 2.193-2.224 μm, 2.256-2.291 μm, and 2.325-2.362 μm, where portions of the K band orders were beyond the edges of the detector.

The components of each binary were rotated so that both fell simultaneously on the high resolution slit, which is rotated at an angle of 105.9^o with respect

Table 4.3—Continued

Target Name	Date of Observation (UT)	Tip/Tilt Reference	Filter	Exposure Time (sec x coadds)	No. of Frames
	2009 May 04		K-prime	5x12	9
2MASS 2140+16AB	2006 May 21	USNO-B1.0 1064-0594380	K-prime	5x1	12
	2006 Nov 27		K-prime	10x12	9
	2007 May 14		K-prime	7x5	9
	2007 Dec 02		K-prime	10x12	9
	2008 May 15		K-prime	10x12	9
	2008 May 30		H	5x12	4
	2008 May 30		J	10x1	4
	2008 Dec 19		K-prime	5x12	9
	2009 Jun 11		K-prime	5x12	8
2MASS 2206-20AB	2006 May 21	source	K-prime	5x6	9
	2006 Nov 27		K-prime	10x12	9
	2007 May 17		K-prime	10x3	8
	2007 Dec 02		K-prime	10x12	2
	2008 May 30		K-prime	5x12	9
	2008 May 30		H	5x6	3
	2008 May 30		J	10x1	6
	2009 Jun 11		K-prime	2.5x12	9
GJ 417BC	2007 Dec 02	USNO-B1.0 1258-0189170	K-prime	30x2	5
GJ 569BC	2009 Jun 11	GJ569A	K-prime	0.5x30	10
HD 130948BC	2007 May 11	HD 130948A	K-prime	2x30	12
	2007 May 11		H	2x60	12
	2007 May 11		J	4x15	12
	2007 May 11		L-prime	0.181x60	17
	2007 May 11		M-short	0.181x60	24
	2008 Apr 28		K-prime	0.1452x1	12
	2009 May 09		H	1x15	7
LHS 2397aAB	2006 Nov 27	source	K-prime	15x10	3
	2007 Dec 02		K-prime	8x15	3
	2007 Dec 02		J	10x15	6
	2008 May 30		K-prime	3x30	8
	2008 Dec 18		K-prime	2x30	8
	2008 Dec 18		H	1.5x30	6
	2008 Dec 18		J	2x30	6
	2009 Jun 10		K-prime	2x30	9
LP 349-25AB	2006 Nov 27	source	K-prime	1x30	5
	2006 Nov 27		H	1x30	5
	2006 Nov 27		J	1.5x30	3
	2007 Dec 02		K-prime	5x6	9
	2008 May 30		K-prime	1.452x20	7
	2008 Dec 19		K-prime	2x20	6
	2008 Dec 19		J	1.5x20	5
	2009 Jun 11		K-prime	0.5x20	12
LP 415-20AB	2006 Nov 27	source	K-prime	8x12	6
	2007 Dec 02		K-prime	6x12	9
	2008 Dec 18		K-prime	6x12	9
	2008 Dec 18		H	5x12	9

Table 4.4. Log of NIRSPAO-LGS K-band Observations

Target Name	Date of Observation (UT)	A0V Star Standard	Exposure Time (sec x coadds)	No. of Frames
2MASS J07464256+2000321AB	2006 Dec 16	HIP 41798	1200x1	4
	2007 Dec 04	HIP 41798	1200x1	6
	2008 Dec 19	HIP 41798	1200x1	6
2MASS J14263161+1557012AB	2007 Jun 08	HIP 73087	1200x1	4
	2008 Jun 01	HIP 73087	1200x1	4
	2009 Jun 12	HIP 73087	1200x1	4
2MASS J17501291+4424043AB	2008 May 31	HIP 87045	1200x1	4
	2009 Jun 12	HIP 87045	1200x1	6
2MASS J18470342+5522433AB	2007 Jun 08	HIP 93713	1200x1	4
	2008 Jun 01	HIP 93713	1200x1	5
	2009 Jun 13	HIP 93713	1200x1	3
2MASS J21402931+1625183AB	2007 Jun 09	HIP 108060	1200x1	4
	2008 May 31	HIP 108060	1800x1	3
	2009 Jun 13	HIP 108060	1800x1	2
2MASS J22062280-2047058AB	2007 Jun 09	HIP 116750	1200x1	3
	2008 Jun 01	HIP 109689	1200x1	4
	2009 Jun 12	HIP 109689	1200x1	4
GJ 569b AB	2007 Jun 09	HIP 73087	900x1	2
	2009 Jun 13	HIP 73087	900x1	4
HD 130948BC	2007 Jun 09	HIP 73087	1200x1	4
LHS 2397aAB	2007 Dec 04	HIP 58188	1800x1	2
	2008 May 31	HIP 61318	1800x1	3
	2008 Dec 19	HIP 58188	1800x1	3
	2009 Jun 12	HIP 61318	1800x1	2
LP 349-25AB	2006 Dec 16	HIP 5132	600x1	4
	2007 Dec 04	HIP 5132	900x1	1
	2008 Dec 19	HIP 5132	1200x1	4
	2009 Jun 12	HIP 5132	1200x1	4
LP 415-20AB	2008 Dec 19	HIP 24555	1200x1	4

to north. Typical observations consisted of four spectra of both components, each with 1200 second integration times, taken in an ABBA dither pattern along the length of the slit. In a few cases, more than four spectra were taken or a slightly different integration time was used, depending on the brightness of the object. Table 4.4 gives the log of our spectroscopic observations, listing the targets observed, the date of observation, the number of spectra, and the integration time for each spectrum. Each target observation was accompanied by the observation of a nearby A0V star to measure the telluric absorption in the target spectra.

4.3 Data Analysis

4.3.1 Astrometric Data Analysis

The NIRC2 data was initially processed using standard data reduction techniques for near-infrared images. Frames at differing dither positions were subtracted from each other to remove sky background, followed by the removal of bad pixels, division by a flat field, and correction for optical distortion with a model provided in the pre-ship review document[1] using standard techniques in IRAF and IDL. The binaries were then shifted to a common location in all frames and the images were median combined. Astrometry and flux ratios were obtained using the IDL package StarFinder (Diolaiti et al. 2000). An empirical point-spread function (PSF) is required by the StarFinder fitting algorithm. In the case of two sources, a suitable PSF star falls within the field of view of the NIRC2 observation of the source. However, in the majority of cases, no such PSF source is in the field of view. For these observations, we use either an image of a single star taken near in time to the images of the binary, or if no suitable single star was imaged, we use an idealized Keck PSF degraded to the calculated strehl ratio of the observation for PSF fitting. For this last case, the PSF is generated by first convolving an the idealized PSF with a Gaussian, such that the core is broadened to the appropriate FWHM. Next, a simulated "halo" is generated by adding a Gaussian with FWHM of $0\farcs5$ (average seeing halo at Keck), normalized such that the resulting strehl ratio matches the observations. Internal statistical measurement errors were calculated by fitting the components of the binaries in all individual images that contributed to the combined images and finding the RMS of the values derived therein.

[1] http://www2.keck.hawaii.edu/inst/nirc2/preship_testing.pdf

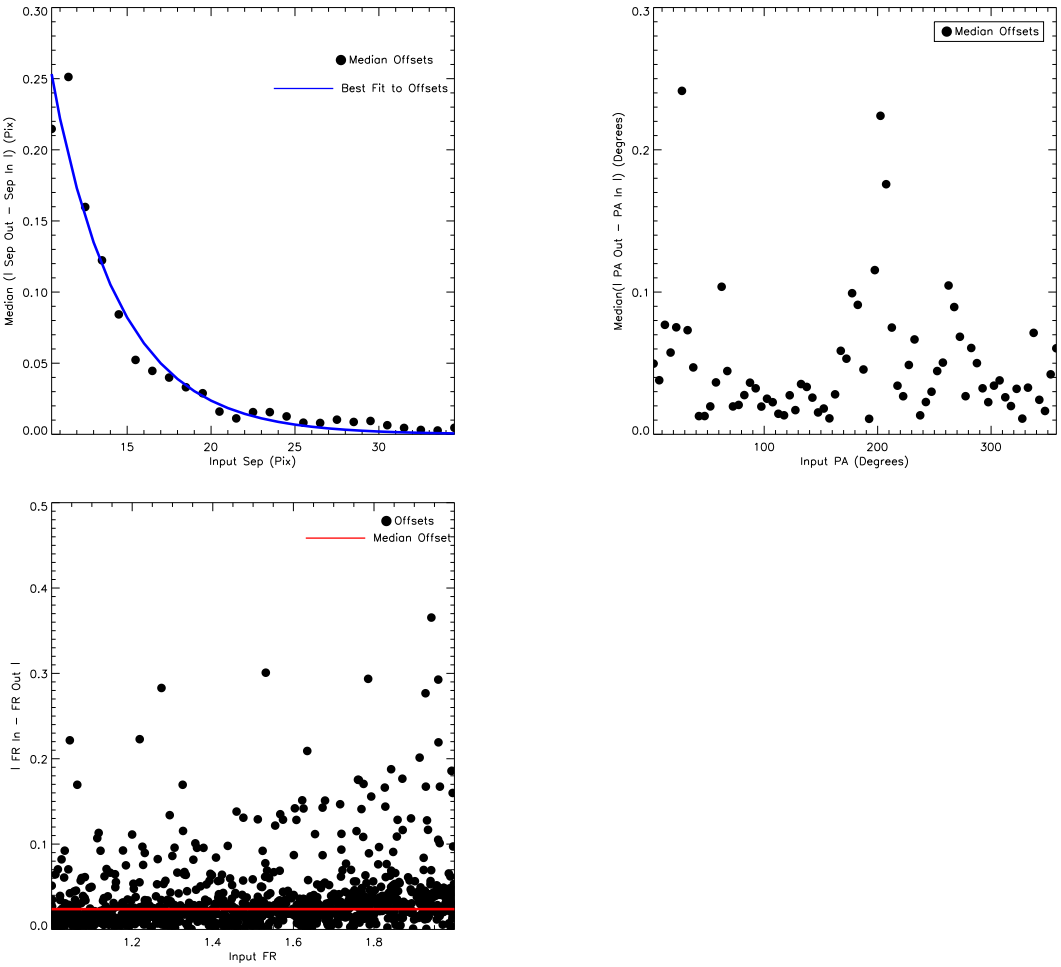

Figure 4.3 Results of PSF systematics simulation from 2006 May 21, using two observed PSFs. **Top Left**: Median offset in fit separation from input separation, binned in one pixel increments. The absolute value of these offsets is an exponentially decreasing function of separation. The blue line shows the fit of an exponential function to these offsets. We use this function to determine the additional uncertainty necessary for a source given its fit separation. **Top Right**: Median offset in fit position angle (PA) from input PA, binned in 5 degree increments. Because of variable PSF structure, the offsets have no obvious functional form. We therefore use these binned data to apply an additional uncertainty in PA given the PA of the binary. **Bottom Left** Measured absolute offsets in fit flux ratio from input flux ratio. The offsets appear to have no dependence on separation or position angle and seem roughly constant. We therefore use the median of all these values, represented by the red line, as the additional uncertainty in flux ratio for this epoch.

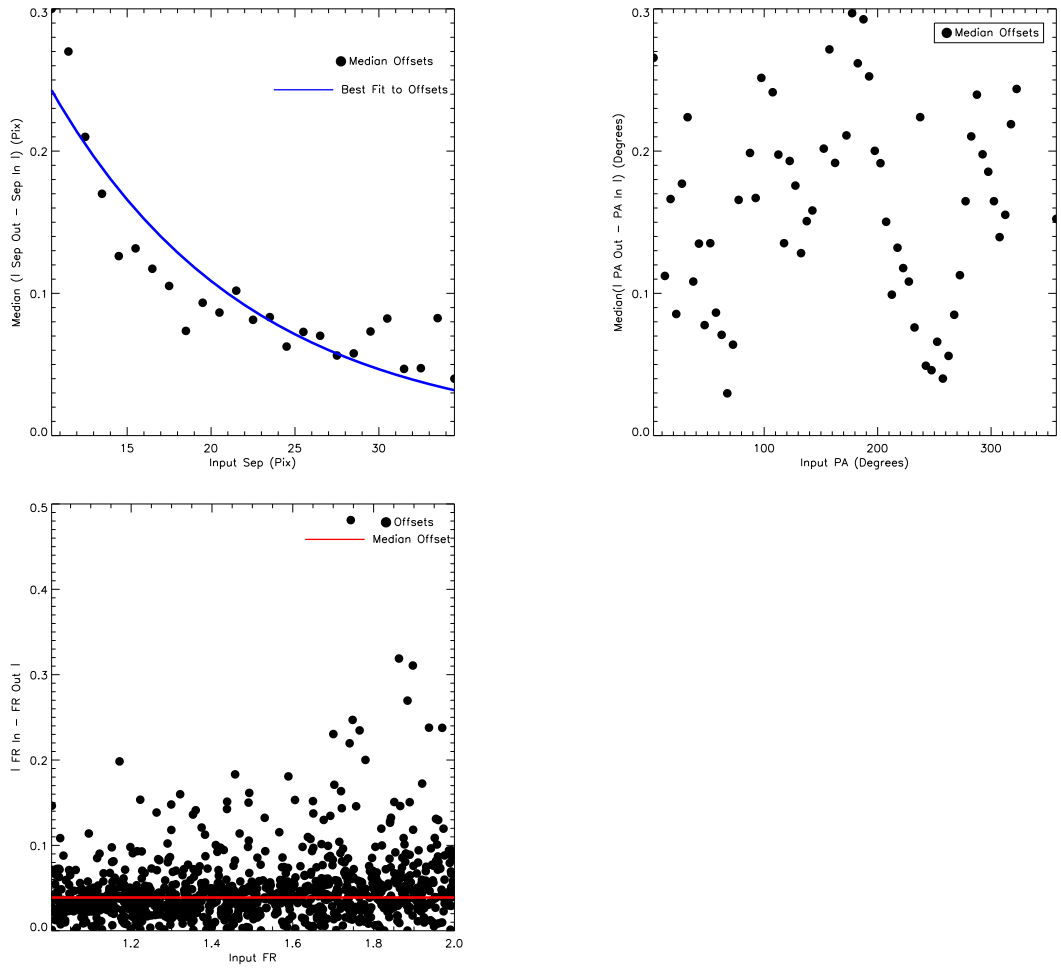

Figure 4.4 Results of PSF systematics simulation from 2006 May 21, using an observed PSF fit by a simulated PSF **Top Left**: Median offset in fit separation from input separation, binned in one pixel increments. The absolute value of these offsets is an exponentially decreasing function of separation. The blue line shows the fit of an exponential function to these offsets. We use this function to determine the additional uncertainty necessary for a source given its fit separation. **Top Right**: Median offset in fit position angle (PA) from input PA, binned in 5 degree increments. Because of variable PSF structure, the offsets have no obvious functional form. We therefore use these binned data to apply an additional uncertainty in PA given the PA of the binary. The largest differences between using a simulated PSF and an observed PSF are seen in the PA due to the variable PSF structure that is unmatched in the simulated PSF. **Bottom Left** Measured absolute offsets in fit flux ratio from input flux ratio. The offsets appear to have no dependence on separation or position angle and seem roughly constant. We therefore use the median of all these values, represented by the red line, as the additional uncertainty in flux ratio for this epoch.

Additional systematic uncertainties need to be accounted for when determining the final astrometric and photometric measurements for each of binary. First, absolute uncertainties in the plate scale and position of north given above are accounted for in all astrometry. A further, more complicated, source of uncertainty stems from using a PSF that is not imaged simultaneously with each binary, introducing systematic uncertainties in both astrometry and photometry. In particular, the variability of the AO performance over a given night generates time variable PSF structure that can contribute to slight offsets in astrometry and photometry. To estimate the additional uncertainty due to imperfect PSF matching, we performed simulations in which 1000 artificial binaries were generated using images of an image single sources with separations and flux ratios spanning the range observed for our sources. These artificial binaries were then fit with Starfinder using either a separate single source from the same night or simulated source as the PSF. This exercise was performed for every night in which observations were taken for both PSF types. Examples of the results of these simulations is shown in Figure 4.3 for the case of an observed PSF, and in Figure 4.4 for the case of a simulated PSF (from the night of 2006 May 21). We find in all simulations that median offsets between input and fitted separations are an exponentially decreasing function of the separation, meaning that fits to tighter binaries were more discrepant from the correct values than those to wide binaries. We also find that due to variable structure in AO PSF halos (even after accounting for pupil rotation), the offset in fitted position angle is a function of the position angle of the binary. Finally, the median offset in fitted flux ratio with respect to the input flux ratio was essentially constant for all separations and position angles. Therefore, for every measurement of each target, we compute the necessary uncertainties from imperfect PSFs based on the relationships detailed above, taking the median values of the measured offsets as the magnitude

of the additional uncertainty. The PSF uncertainties have the greatest impact on the tightest systems or on nights when the performance was poor (strehl ratios $\lesssim$20%). In about 25% of our measurements, this PSF uncertainty is larger than our statistical uncertainty. The astrometry and relative photometry for all sources at all epochs is given in Table 4.5. Those sources that were unresolved in our observations have upper limits on binary separation only. Uncertainties in Table 4.5 are listed separately for the purpose of illustrating the relative magnitude of each source of uncertainty, but for all further analysis, we add them together in quadrature to give a final uncertainty.

Table 4.5. NIRC2 LGS AO Results

Target Name	Date of Observation (UT)	Filter	Separation (pixels)[a]	Separation (arcseconds)[b]	Position Angle (degrees)[c]	Flux Ratio (Ab/Aa)[d]
2MASS 0518-28	2006 Nov 27	K-prime	< 6.40	< 0.064	—	—
	2007 Dec 02	K-prime	< 5.55	< 0.055	—	—
	2008 Dec 18	K-prime	< 6.55	< 0.065	—	—
2MASS 0652+47	2006 Nov 27	K-prime	< 3.05	< 0.030	—	—
	2007 Dec 02	K-prime	< 3.73	< 0.037	—	—
2MASS 0746+20	2006 Nov 27	K-prime	$29.924 \pm (0.058 \pm 0.013)$	0.2981 ± 0.0006	$233.93 \pm (0.08 \pm 0.03)$ [0.08]	$1.39 \pm (0.02 \pm 0.04)$
	2007 Nov 30	K-prime	$33.533 \pm (0.028 \pm 0.057)$	0.3341 ± 0.0007	$223.54 \pm (0.04 \pm 0.22)$ [0.23]	$1.39 \pm (0.01 \pm 0.03)$
	2007 Nov 30	J	$33.501 \pm (0.165 \pm 0.072)$	0.334 ± 0.002	$223.49 \pm (0.36 \pm 0.26)$ [0.45]	$1.60 \pm (0.14 \pm 0.04)$
	2008 Dec 18	K-prime	$35.240 \pm (0.032 \pm 0.002)$	0.3511 ± 0.0004	$214.31 \pm (0.06 \pm 0.02)$ [0.07]	$1.39 \pm (0.01 \pm 0.03)$
	2008 Dec 18	H	$35.268 \pm (0.036 \pm 0.039)$	0.3514 ± 0.0006	$214.38 \pm (0.10 \pm 0.07)$ [0.13]	$1.50 \pm (0.01 \pm 0.04)$
2MASS 0850+10	2007 Dec 01	K-prime	$8.927 \pm (0.197 \pm 0.215)$	0.089 ± 0.003	$158.71 \pm (0.93 \pm 0.13)$ [0.93]	$1.81 \pm (0.19 \pm 0.04)$
	2008 Dec 18	K-prime	$7.611 \pm (0.086 \pm 0.073)$	0.076 ± 0.001	$165.87 \pm (0.36 \pm 0.12)$ [0.37]	$2.12 \pm (0.10 \pm 0.03)$
2MASS 0920+35	2006 Nov 27	K-prime	$6.583 \pm (0.194 \pm 0.406)$	0.066 ± 0.004	$247.14 \pm (2.04 \pm 0.06)$ [2.04]	$1.36 \pm (0.08 \pm 0.04)$
	2007 Dec 01	K-prime	$7.561 \pm (0.292 \pm 0.232)$	0.075 ± 0.004	$244.91 \pm (3.23 \pm 0.27)$ [3.24]	$1.19 \pm (0.07 \pm 0.04)$
	2007 Dec 01	J	$6.623 \pm (1.50 \pm 0.66)$	0.066 ± 0.016	$247.7 \pm (1.6 \pm 0.2)$ [1.6]	$1.04 \pm (0.27 \pm 0.05)$
	2008 May 30	K-prime	$6.622 \pm (0.079 \pm 0.057)$	0.066 ± 0.001	$249.94 \pm (0.53 \pm 0.09)$ [0.54]	$1.75 \pm (0.09 \pm 0.03)$
	2008 Oct 20	H	4.714 ± 0.145	0.047 ± 0.001	252.3 ± 3.0	1.20 ± 0.07
	2008 Dec 18	H	3.753 ± 0.335	0.037 ± 0.003	247.6 ± 1.8	1.07 ± 0.05
	2009 Jun 10	H	< 2.63	< 0.0262	—	—
2MASS 1017+13	2006 Nov 27	K-prime	$8.777 \pm (2.403 \pm 0.295)$	0.087 ± 0.024	$83.11 \pm (4.98 \pm 0.06)$ [4.98]	$1.27 \pm (0.63 \pm 0.04)$
2MASS 1047+40	2006 Jun 21	K-prime	$3.178 \pm (0.169 \pm 0.153)$	0.032 ± 0.002	$126.77 \pm (4.44 \pm 0.05)$ [4.44]	$1.52 \pm (0.26 \pm 0.02)$
	2006 Nov 27	K-prime	< 4.68	< 0.047	—	—
	2007 Dec 02	K-prime	< 4.68	< 0.047	—	—
2MASS 1426+15	2006 Jun 19	K-prime	$26.565 \pm (0.054 \pm 0.018)$	0.265 ± 0.001	$343.07 \pm (0.47 \pm 0.04)$ [0.47]	$1.81 \pm (0.10 \pm 0.02)$
	2008 May 30	K-prime	$30.562 \pm (0.043 \pm 0.015)$	0.3045 ± 0.0005	$343.55 \pm (0.06 \pm 0.03)$ [0.07]	$1.82 \pm (0.02 \pm 0.03)$
	2008 May 30	H	$30.479 \pm (0.107 \pm 0.071)$	0.304 ± 0.001	$343.53 \pm (0.28 \pm 0.22)$ [0.36]	$2.02 \pm (0.05 \pm 0.02)$
	2009 May 02	K-prime	$32.389 \pm (0.046 \pm 0.015)$	0.3227 ± 0.0005	$343.69 \pm (0.06 \pm 0.05)$ [0.08]	$1.84 \pm (0.02 \pm 0.04)$
	2009 May 02	H	$32.375 \pm (0.038 \pm 0.017)$	0.3226 ± 0.0006	$343.84 \pm (0.06 \pm 0.05)$ [0.08]	$1.91 \pm (0.02 \pm 0.04)$
2MASS 1534-29	2006 Jun 19	J	18.649 ± 0.125	0.186 ± 0.001	15.57 ± 0.29	1.20 ± 0.04
	2008 May 30	K-prime	9.571 ± 0.121	0.095 ± 0.001	21.53 ± 0.84	1.23 ± 0.13
	2008 May 30	H	9.549 ± 0.131	0.095 ± 0.001	21.69 ± 0.82	1.38 ± 0.09
	2009 May 04	H	3.919 ± 0.118	0.039 ± 0.001	38.52 ± 3.25	1.28 ± 0.11
2MASS 1600+17	2007 May 20	K-prime	< 4.02	< 0.040	—	—
	2008 May 30	K-prime	< 3.90	< 0.039	—	—
2MASS 1728+39	2007 May 20	K-prime	$20.496 \pm (0.138 \pm 0.030)$	0.204 ± 0.001	$85.08 \pm (0.21 \pm 0.14)$ [0.25]	$1.83 \pm (0.03 \pm 0.02)$

Table 4.5—Continued

Target Name	Date of Observation (UT)	Filter	Separation (pixels)[a]	Separation (arcseconds)[b]	Position Angle (degrees)[c]	Flux Ratio (Ab/Aa)[d]
	2008 May 30	K-prime	20.790 ± (0.589 ± 0.026)	0.207 ± 0.006	101.33 ± (0.13 ± 0.03) [0.14]	1.97 ± (0.14 ± 0.03)
	2008 May 30	J	21.467 ± (0.045 ± 0.165)	0.214 ± 0.002	101.85 ± (0.12 ± 0.25) [0.28]	1.34 ± (0.02 ± 0.02)
	2009 May 03	K-prime	21.854 ± (0.019 ± 0.110)	0.218 ± 0.001	105.85 ± (0.48 ± 0.15) [0.50]	1.74 ± (0.02 ± 0.02)
	2009 Jun 11	H	21.868 ± 0.034	0.218 ± 0.0004	106.41 ± 0.08	1.52 ± 0.01
2MASS 1750+44	2006 Jun 19	K-prime	15.392 ± (0.443 ± 0.050)	0.153 ± 0.004	33.68 ± (2.47 ± 0.07) [2.47]	1.94 ± (0.13 ± 0.02)
	2007 May 17	K-prime	17.330 ± (0.161 ± 0.022)	0.173 ± 0.002	42.37 ± (0.28 ± 0.02) [0.28]	1.93 ± (0.02 ± 0.04)
	2008 May 13	K-prime	18.556 ± (0.020 ± 0.057)	0.1849 ± 0.0006	52.29 ± (0.05 ± 0.06) [0.08]	1.84 ± (0.02 ± 0.03)
	2008 May 30	J	19.321 ± (0.173 ± 0.201)	0.192 ± 0.003	53.78 ± (0.32 ± 0.16) [0.35]	2.41 ± (0.03 ± 0.02)
	2008 May 30	H	18.575 ± (0.115 ± 0.394)	0.185 ± 0.004	52.64 ± (0.91 ± 1.77) [1.99]	2.04 ± (0.11 ± 0.19)
	2009 May 01	K-prime	20.2779 ± (0.035 ± 0.011)	0.2020 ± 0.0004	60.31 ± (0.06 ±0.02) [0.07]	1.83 ± (0.01 ± 0.02)
2MASS 1847+55	2006 May 21	K-prime	15.289 ± (0.032 ± 0.076)	0.1523 ± 0.0008	110.90 ± (0.03 ± 0.01) [0.04]	1.30 ± (0.003 ± 0.02)
	2007 May 14	K-prime	17.335 ± (0.039 ± 0.059)	0.173 ± 0.007	114.01 ± (0.08 ± 0.04) [0.09]	1.28 ± (0.01 ± 0.02)
	2008 May 20	K-prime	19.202 ± (0.147 ± 0.052)	0.191 ± 0.002	116.71 ± (0.44 ± 0.04) [0.44]	1.28 ± (0.04 ± 0.02)
	2008 May 20	J	18.892 ± (0.133 ± 0.209)	0.188 ± 0.003	116.61 ± (0.28 ± 0.15) [0.32]	1.25 ± (0.01 ± 0.10)
	2008 May 20	H	19.245 ± (0.054 ± 0.389)	0.192 ± 0.004	116.64 ± (0.15 ± 2.71) [2.72]	1.30 ± (0.03 ± 0.19)
	2009 May 04	K-prime	20.726 ± (0.057 ± 0.008)	0.2065 ± 0.0006	118.74 ± (0.13 ± 0.01) [0.14]	1.28 ± (0.02 ± 0.03)
2MASS 2140+16	2006 May 21	K-prime	10.922 ± 0.061	0.1088 ± 0.0006	202.91 ± 0.54 ± 0	1.97 ± 0.04
	2006 Nov 27	K-prime	10.803 ± 0.126	0.108 ± 0.001	215.02 ± 1.16	1.94 ± 0.12
	2007 May 14	K-prime	10.816 ± 0.044	0.1078 ± 0.0004	223.50 ± 0.25	1.96 ± 0.05
	2007 Dec 01	K-prime	10.879 ± 0.209	0.108 ± 0.002	234.02 ± 0.66	1.95 ± 0.12
	2008 May 15	K-prime	11.067 ± 0.096	0.111 ± 0.001	243.28 ± 0.56	1.96 ± 0.07
	2008 May 30	J	12.021 ± 0.173	0.120 ± 0.002	241.41 ± 0.45	2.39 ± 0.34
	2008 May 30	H	11.491 ± 0.075	0.115 ± 0.001	242.9 ± 1.6	2.35 ± 0.38
	2008 Dec 19	K-prime	11.311 ± 0.390	0.113 ± 0.004	254.68 ± 0.32	1.94 ± 0.19
	2009 Jun 11	K-prime	11.478 ± 0.113	0.114 ± 0.001	263.34 ± 0.23	1.93 ± 0.09
2MASS 2206-20	2006 May 21	K-prime	13.068 ± (0.147 ± 0.133)	0.130 ± 0.002	128.99 ± (0.27 ± 0.13) [0.27]	1.04 ± (0.05 ± 0.02)
	2006 Nov 27	K-prime	12.747 ± (0.223 ± 0.165)	0.127 ± 0.003	138.65 ± (0.29 ± 0.04) [0.30]	1.06 ± (0.09 ± 0.04)
	2007 May 17	K-prime	12.313 ± (0.013 ± 0.035)	0.1227 ± 0.0004	147.68 ± (0.12 ± 0.02) [0.12]	1.03 ± (0.01 ± 0.04)
	2007 Dec 01	K-prime	12.199 ± (0.07 ± 0.18)	0.122 ± 0.002	160.40 ± (0.09 ± 0.27) [0.29]	0.97 ± (0.09 ± 0.04)
	2008 May 30	K-prime	12.394 ± (0.084 ± 0.042)	0.1235 ± 0.0009	169.58 ± (0.34 ± 0.04) [0.34]	1.11 ± (0.11 ± 0.03)
	2008 May 30	J	11.834 ± (0.104 ± 0.404)	0.118 ± 0.004	170.49 ± (0.35 ± 0.47) [0.59]	1.15 ± (0.03 ± 0.02)
	2008 May 30	H	11.543 ± (0.838 ± 0.453)	0.115 ± 0.009	169.82 ± (0.92 ± 0.35) [0.99]	1.04 ± (0.18 ± 0.19)
	2009 Jun 11	K-prime	12.588 ± (0.033 ± 0.123)	0.124 ± 0.001	190.52 ± (0.07 ± 0.03) [0.09]	1.05 ± 0.02
HD 130948 BC	2006 Jun 18[e]	Hn3	5.401 ± 0.279	0.109 ± 0.006	136.33 ± 3.68	—
	2007 May 11	K-prime	10.620 ± (0.058 ± 0.101)	0.1058 ± 0.001	131.63 ± (0.11 ± 0.03) [0.12]	1.21 ± (0.12 ± 0.03)

4.3.2 Spectroscopic Data Analysis

The basic reduction of the NIRSPAO spectra was performed with REDSPEC, a software package designed for NIRSPEC[2]. Object frames are reduced by subtracting opposing nods to remove sky and dark backgrounds, dividing by a flat field, and correcting for bad pixels. Spectral orders are spatially rectified by fitting the trace of each nod of telluric calibrators with third order polynomials, and then applying the results of those fits across the image. A first-order guess at the wavelength solution for the spectra is obtained using the etalon lamps that are part of the lamp suite of NIRSPAO (this is used as a starting point for our derivation of the true wavelength solution). Order 33 has very few OH sky lines or arc lamp lines to use for this purpose. To obtain the correct values of the wavelengths for the etalon lines, we followed the method described by Figer et al. (2003). The wavelength regime that Order 33 encompasses was found to be between $\sim$2.291 and $\sim$2.325 μm. The output we used from REDSPEC was therefore a reduced, spatially rectified and preliminarily spectrally rectified fits image of order 33.

As these systems are fairly tight binaries, cross-contamination can be an issue when extracting the spectra. This made the simple square-box extraction provided in REDSPEC unsuitable for these observations. We therefore extracted the spectra by first fitting a Gaussian to the trace of one component of the binary and subtracting the result of this fit from the frame to leave only the other component. The width of the Gaussian is allowed to vary with wavelength, although over the narrow wavelength range in covered by order 33, the variation is small. Typically the binaries are separated by more than a FWHM of this Gaussian, making the fit of the bright stars' trace unbiased by the other. In the few cases

[2]http://www2.keck.hawaii.edu/inst/nirspec/redspec/index.html

Table 4.5—Continued

Target Name	Date of Observation (UT)	Filter	Separation (pixels)[a]	Separation (arcseconds)[b]	Position Angle (degrees)[c]	Flux Ratio (Ab/Aa)[d]
	2008 Apr 28	K-prime	5.068 ± (0.069 ± 0.122)	0.0505 ± 0.001	122.82 ± (4.93 ± 0.05) [4.93]	1.15 ± (0.31 ± 0.04)
	2009 May 09	H	3.775 ± (0.318 ± 0.528)	0.038 ± 0.006	327.1 ± (5.0 ± 1.1) [5.1]	1.20 ± (0.13 ± 0.15)
LHS 2397a	2006 Nov 27	K-prime	9.672 ± (4.976 ± 0.259)	0.096 ± 0.050	300.01 ± (9.38 ± 0.38) [9.39]	1.77 ± (0.82 ± 0.04)
	2007 Dec 01	K-prime	14.629 ± (0.554 ± 0.155)	0.146 ± 0.006	19.95 ± (2.16 ± 0.13) [2.17]	10.16 ± (0.86 ± 0.04)
	2008 May 30	K-prime	15.983 ± (0.758 ± 0.034)	0.159 ± 0.008	37.77 ± (1.68 ± 0.26) [1.70]	12.21 ± (1.49 ± 0.03)
	2008 Dec 18	K-prime	19.813 ± (0.101 ± 0.013)	0.197 ± 0.001	50.27 ± (0.11 ± 0.04) [0.12]	13.2 ± (1.0 ± 0.03)
	2008 Dec 18	H	19.908 ± (0.276 ± 0.055)	0.196 ± 0.003	50.94 ± (0.37 ± 0.11) [0.39]	17.4 ± (1.2 ± 0.04)
	2009 Jun 10	K-prime	22.026 ± (0.035 ± 0.021)	0.2195 ± 0.0004	59.44 ± (0.08 ± 0.58) [0.59]	12.89 ± (0.39 ± 0.02)
LP 349-25	2006 Nov 27	K-prime	12.603 ± (0.049 ± 0.169)	0.126 ± 0.002	234.88 ± (0.17 ± 0.70) [0.72]	1.38 ± (0.02 ± 0.04)
	2006 Nov 27	J	12.439 ± (0.213 ± 0.129)	0.124 ± 0.002	236.67 ± (2.53 ± 0.06) [1.53]	1.64 ± (0.04 ± 0.04)
	2006 Nov 27	H	12.349 ± (0.093 ± 0.150)	0.123 ± 0.002	235.48 ± (0.46 ± 0.06) [0.47]	1.48 ± (0.08 ± 0.04)
	2007 Dec 01	K-prime	13.126 ± (0.400 ± 0.169)	0.131 ± 0.004	211.47 ± (1.61 ± 0.23) [1.62]	1.20 ± (0.10 ± 0.04)
	2008 May 30	K-prime	12.518 ± (0.120 ± 0.041)	0.125 ± 0.001	197.94 ± (0.40 ± 0.02) [0.40]	1.44 ± (0.04 ± 0.03)
	2008 Dec 19	K-prime	8.555 ± (0.080 ± 0.064)	0.085 ± 0.001	172.41 ± (0.81 ± 0.08) [0.82]	1.31 ± (0.08 ± 0.03)
	2008 Dec 19	J	8.944 ± (0.364 ± 0.095)	0.089 ± 0.004	173.17 ± (0.59 ± 0.12) [0.61]	1.63 ± (0.16 ± 0.05)
	2009 Jun 11	K-prime	6.653 ± (0.056 ± 0.354)	0.066 ± 0.004	129.62 ± (0.22 ± 0.04) [0.22]	1.34 ± (0.05 ± 0.02)
LP 415-20	2006 Nov 27	K-prime	4.616 ± (0.083 ± 0.541)	0.046 ± 0.005	35.11 ± (2.40 ± 0.85) [2.55]	1.77 ± (0.09 ± 0.04)
	2007 Dec 01	K-prime	9.617 ± (0.152 ± 0.206)	0.096 ± 0.003	52.45 ± (1.06 ± 0.12) [1.06]	2.53 ± (0.21 ± 0.04)
	2008 Dec 18	K-prime	11.215 ± (0.444 ± 0.044)	0.112 ± 0.004	62.56 ± (0.97 ± 0.10) [0.97]	1.42 ± (0.12 ± 0.03)
	2008 Dec 18	H	11.145 ± (0.179 ± 0.066)	0.111 ± 0.002	62.18 ± (1.26 ± 0.04) [1.36]	1.60 ± (0.19 ± 0.04)

[a]The first listed uncertainty is that due to the measurement itself, while the second is the systematic uncertainty due to imperfect PSF matching. If only one uncertainty is given, the source had a suitable PSF in the field of view.

[b]The uncertainties given are the empirically estimated statistical uncertainty, the PSF mismatch uncertainty, and the absolute plate scale uncertainty added in quadrature

[c]The first listed uncertainty is that due to the measurement itself, while the second is the systematic uncertainty due to imperfect PSF matching. In the paratheses is the combination of these two uncertainties along with the absolute uncertainty of the columns with respect to north. If only one uncertainty is given, the source had a suitable PSF in the field of view.

[d]The first listed uncertainty is systematic uncertainty due to the measurement itself, while the second is that due to imperfect PSF matching. If only one uncertainty is given, the source had a suitable PSF in the field of view.

[e]Data from the OSIRIS imager, which has a plate scale of 0.″02/pixel. This camera has not been fully characterized for distortion. However, the uncertainties on these measurements are such that they should account for distortion on this camera

where the traces were separated by less than about 7 pixels, the fitted FWHM would be artificially widened due to the presence of the companion. In these cases, we fixed the FWHM of the Gaussian to that measured for other, more widely separated sources observed on the same night. After the trace of one component was fitted and subtracted from the frame, the trace of the remaining component was then also fit with a Gaussian for extraction. We normalized this Gaussian such that the peak was given a value of one and corresponded to the peak of the trace in the spatial direction. We then weighted the flux of each pixel by the value of the normalized Gaussian at that pixel location, and then added these weighted fluxes together to get our final extracted spectrum. We do not remove telluric absorption from our order 33 spectra because telluric lines are used for radial velocity determination.

To measure radial velocities from our extracted spectra, we use the method detailed extensively by Blake et al. (2007) and White et al. (2009). Namely, using a combination of a spectral template appropriate for each target and a model of the telluric absorption of the atmosphere, it as possible to determine radial velocities for NIRSPEC spectra accurate to better than 1 km/s. Each extracted spectrum is therefore fit with a model in which the free parameters are the rotational velocity ($V\ sin\ i$[3]), the PSF of the spectrograph (assumed to be a Gaussian where the width is the free parameter), the flux normalization, and the wavelength solution. The model thus consists of a spectral template that has been convolved with a rotational broadening kernel, shifted by some radial velocity, multiplied by a telluric model, and then convolved with a Gaussian PSF. The details of this fitting procedure are described in Blake et al. (2007). The synthetic spectral templates we used for our fitting are derived from the

[3]While this method has been shown to produce reliable radial velocities, the $V\ sin\ i$'s have known systematics that are perhaps due to an additional degeneracy with PSF

PHOENIX atmosphere models (Hauschildt et al. 1999). We use order 33 templates of the appropriate temperature for each source. This fitting procedure also has known degeneracies between derived $V\ sin\ i$ and temperature, as lowering the temperature or increasing the $V\ sin\ i$ have similar effects on the lines in the CO bandhead. We therefore use multiple templates spanning 300 K in temperature to determine the systematic uncertainty in radial velocity due to our synthetic template. We find that this systematic amounts to approximately $\sim$0.2-0.3 km/s for most targets. The measured radial velocities from this method are reported in Table 4.6. In Figures 4.5 through 4.15, we show example fits for each of the sources with spectroscopic observations.

4.4 Orbital Analysis

4.4.1 Orbital Parameters from Relative Motion

To derive total mass estimates from relative orbital solutions for our sources, we combine our astrometric measurements from Section 4.3.1, previous astrometry reported in the literature, and the relative radial velocity between the components as determined in section 4.3.2. As described in Ghez et al. (2008), our model for an astrometric orbit always contains six free parameters: period (P), semi-major axis (a), eccentricity (e), time of periapse passage (T_o), inclination (i), position angle of the ascending node (Ω), and longitude of periapse passage (ω). We can remove the degeneracy in the values of Ω and ω which exists without information in this third dimension for the 11 of our 15 sources that have radial velocity information. The radial velocity data also allows distance to be a free parameter in the fit for those sources without a previously-measured parallax (5 systems). For those systems with a parallax measurement (9 systems), we do not

Table 4.6. Radial Velocity Measurements

Target Name	Date of Observation (UT)	Average SNR Primary (A)	Average SNR Secondary (B)	Rad. Velocity Primary (km/s)	Rad. Velocity Secondary (km/s)	ΔRV (km/s)
2MASS 0746+20AB	2006 Dec 16	52	44	55.60 ± 0.68	52.94 ± 0.68	-2.66 ± 0.96
	2007 Dec 04	72	59	55.18 ± 0.60	52.37 ± 1.12	-2.81 ± 1.27
	2008 Dec 19	66	56	56.06 ± 0.85	54.05 ± 2.30	-2.01 ± 2.45
2MASS 1426+15AB	2007 Jun 08	44	33	12.54 ± 0.43	14.41 ± 1.27	1.87 ± 1.34
	2008 Jun 01	50	36	12.67 ± 0.36	15.39 ± 1.40	2.72 ± 1.45
	2009 Jun 12	41	29	12.78 ± 0.49	15.00 ± 0.68	2.22 ± 0.84
2MASS 1750+44AB	2008 May 31	48	36	-17.52 ± 0.39	-15.89 ± 0.54	1.63 ± 0.67
	2009 Jun 12	41	31	-17.09 ± 0.53	-15.25 ± 1.31	1.84 ± 1.41
2MASS 1847+55AB	2007 Jun 08	69	60	-23.88 ± 0.32	-20.46 ± 0.29	3.42 ± 0.43
	2008 Jun 01	69	60	-24.15 ± 0.21	-20.09 ± 0.46	4.06 ± 0.51
	2009 Jun 13	39	36	-24.68 ± 0.60	-19.63 ± 1.00	5.05 ± 1.17
2MASS 2140+16AB	2007 Jun 09	43	28	13.90 ± 0.30	11.07 ± 1.21	-2.83 ± 1.25
	2008 May 31	58	40	13.62 ± 0.27	12.26 ± 1.62	-1.36 ± 1.68
	2009 Jun 13	38	26	13.47 ± 0.28	10.97 ± 2.00	2.50 ± 2.01
2MASS 2206-20AB	2007 Jun 09	47	39	13.66 ± 0.36	13.28 ± 0.48	-0.38 ± 0.66
	2008 Jun 01	54	48	13.14 ± 0.39	13.46 ± 0.51	0.32 ± 0.64
	2009 Jun 12	47	44	13.37 ± 0.24	12.75 ± 0.37	-0.62 ± 0.44
GJ 569b AB	2007 Jun 09	89	82	-10.49 ± 0.20	-4.90 ± 0.50	5.59 ± 0.54
	2009 Jun 13	86	67	-8.97 ± 0.36	-6.83 ± 0.27	2.14 ± 0.45
HD 130948Bc	2007 Jun 09	44	33	4.57 ± 2.61	-0.72 ± 1.05	-5.29 ± 2.81
LHS 2397aAB	2007 Dec 04	68	27	34.43 ± 0.86	34.84 ± 2.24	0.41 ± 2.40
	2008 May 31	114	44	33.85 ± 0.27	36.30 ± 0.86	2.45 ± 0.90
	2008 Dec 19	85	31	33.79 ± 0.37	35.30 ± 2.49	1.51 ± 2.52
	2009 Jun 12	103	33	33.51 ± 0.66	34.27 ± 2.02	0.76 ± 1.22
LP 349-25AB	2006 Dec 16	58	45	-11.91 ± 1.33	-6.57 ± 2.50	5.34 ± 2.83
	2007 Dec 04	63	58	-11.11 ± 3.00	-5.50 ± 3.02	5.67 ± 2.12
	2008 Dec 19	105	84	-9.89 ± 1.51	-6.78 ± 1.84	3.11 ± 0.98
	2009 Jun 12	114	98	-8.16 ± 0.49	-7.27 ± 1.35	0.89 ± 1.44
LP 415-20A	2008 Dec 19	42	32	41.13 ± 0.91	40.41 ± 1.06	-0.72 ± 1.40

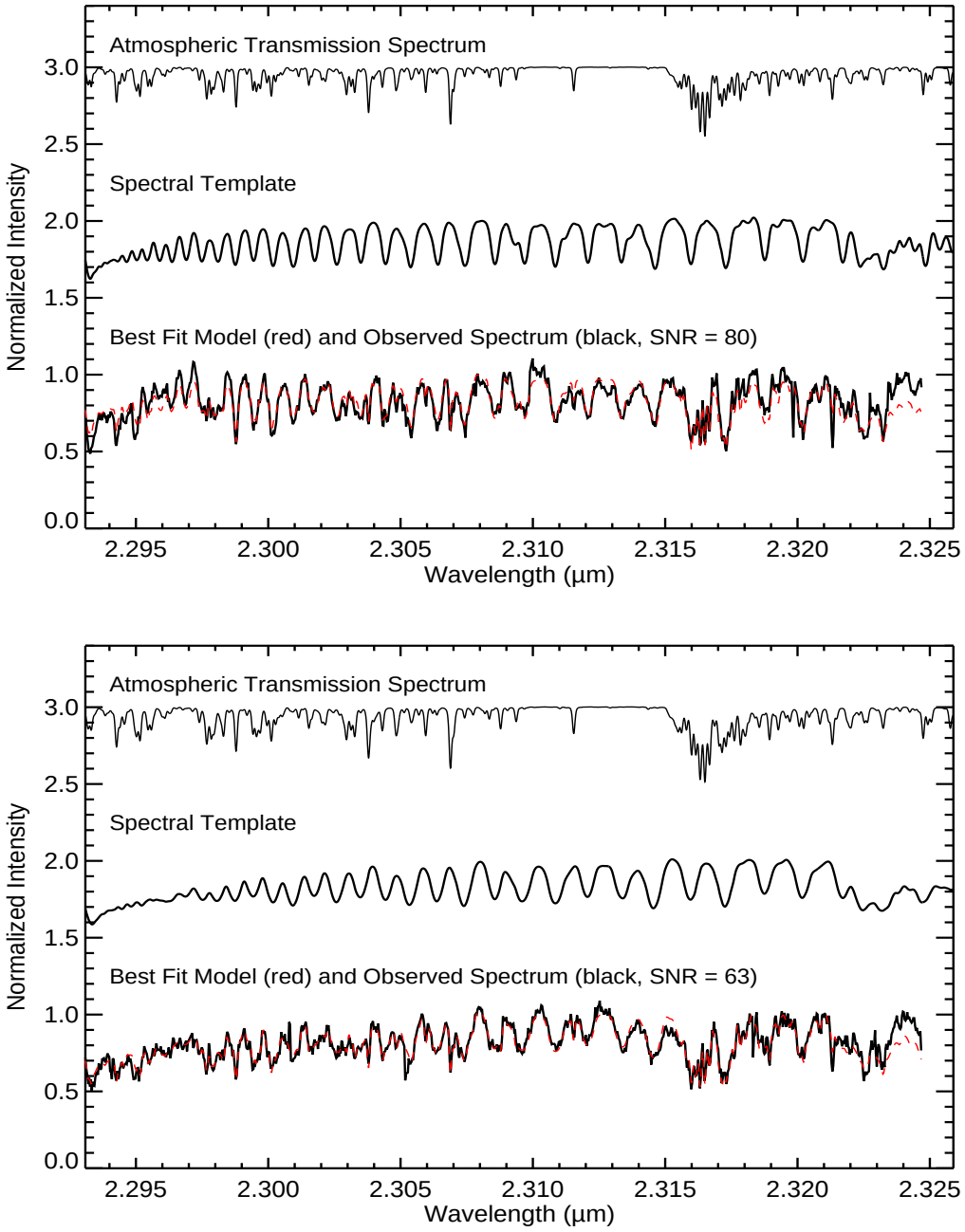

Figure 4.5 Example of a fit for radial velocity for the components of 2MASS 0746+20 A (**top**) and B (**bottom**) from the night of 2007 Dec 04. The atmospheric transmission spectrum used for wavelength calibration is shown, as well as the theoretical spectral template. On the bottom of each panel, we plot our actual spectrum in black (note that the telluric features have not been removed, as is necessary for the fitting) and overplot in red the best fitting model that combines the synthetic atmospheric and spectral templates.

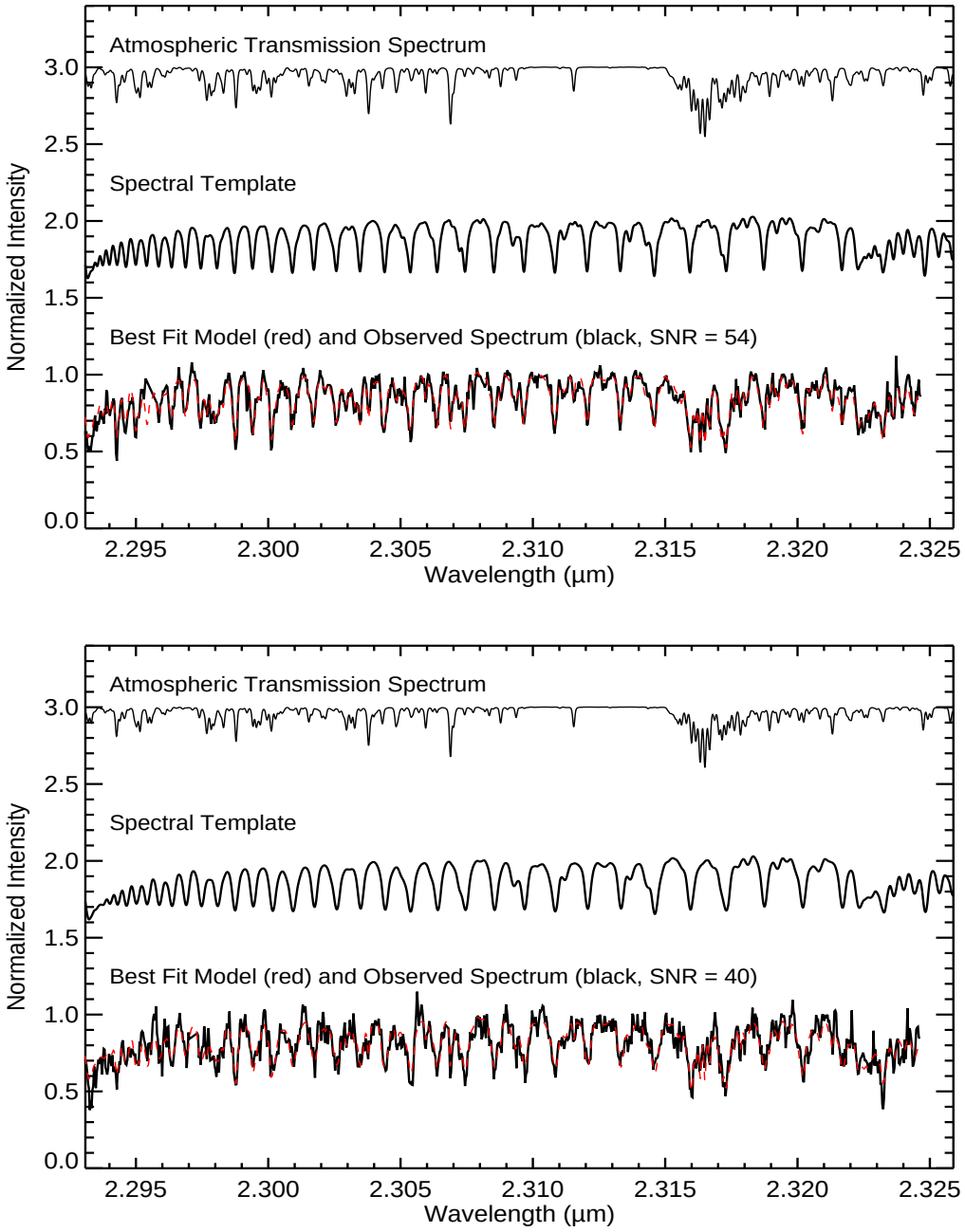

Figure 4.6 Example of a fit for radial velocity for the components of 2MASS 1426+15 A (**top**) and B (**bottom**) from the night of 2008 Jun 01. The atmospheric transmission spectrum used for wavelength calibration is shown, as well as the theoretical spectral template. On the bottom of each panel, we plot our actual spectrum in black (note that the telluric features have not been removed, as is necessary for the fitting) and overplot in red the best fitting model that combines the synthetic atmospheric and spectral templates.

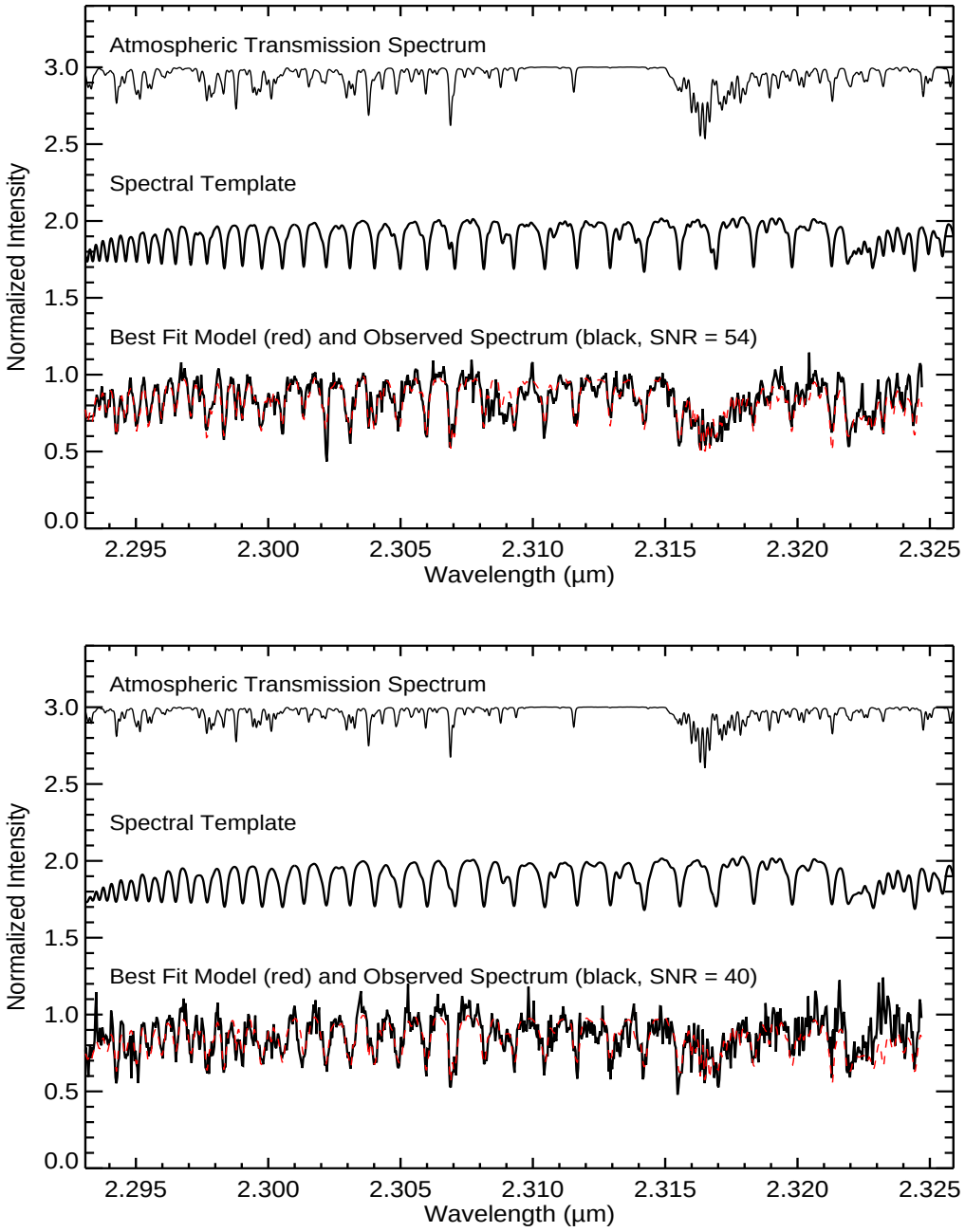

Figure 4.7 Example of a fit for radial velocity for the components of 2MASS 1750+40 A (**top**) and B (**bottom**) from the night of 2008 May 31. The atmospheric transmission spectrum used for wavelength calibration is shown, as well as the theoretical spectral template. On the bottom of each panel, we plot our actual spectrum in black (note that the telluric features have not been removed, as is necessary for the fitting) and overplot in red the best fitting model that combines the synthetic atmospheric and spectral templates.

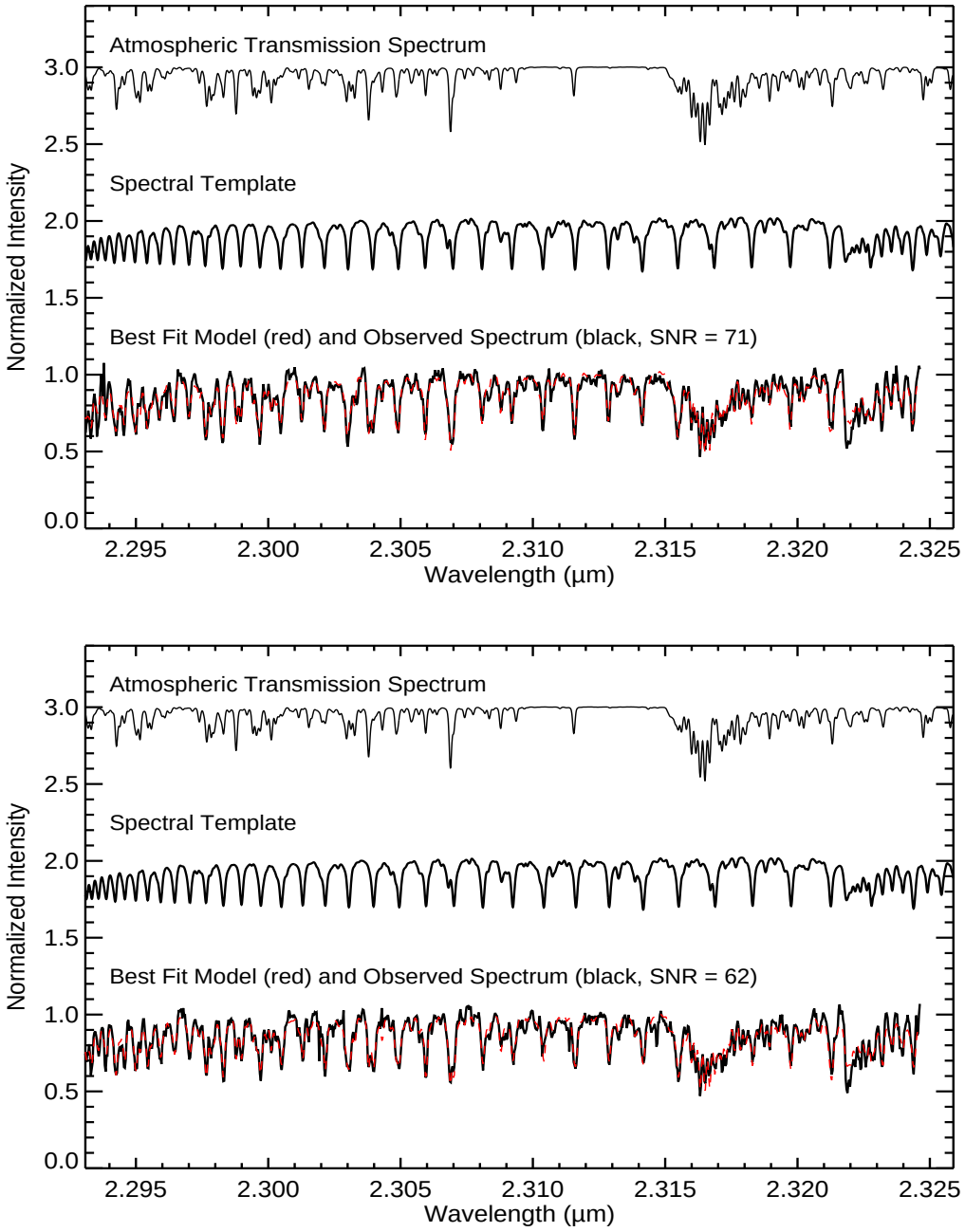

Figure 4.8 Example of a fit for radial velocity for the components of 2MASS 1847+55 A (**top**) and B (**bottom**) from the night of 2008 Jun 01. The atmospheric transmission spectrum used for wavelength calibration is shown, as well as the theoretical spectral template. On the bottom of each panel, we plot our actual spectrum in black (note that the telluric features have not been removed, as is necessary for the fitting) and overplot in red the best fitting model that combines the synthetic atmospheric and spectral templates.

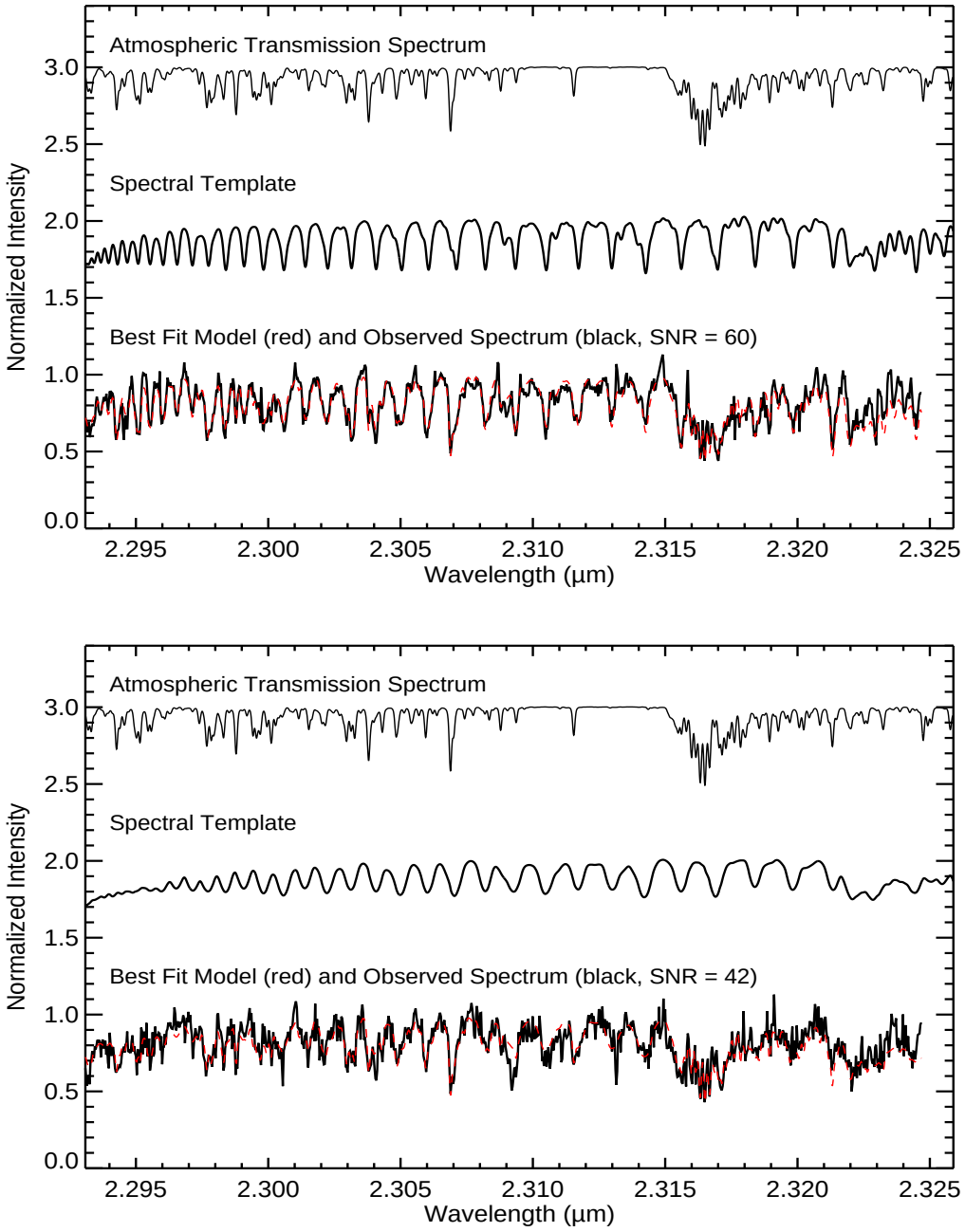

Figure 4.9 Example of a fit for radial velocity for the components of 2MASS 2140+16 A (**top**) and B (**bottom**) from the night of 2008 May 31. The atmospheric transmission spectrum used for wavelength calibration is shown, as well as the theoretical spectral template. On the bottom of each panel, we plot our actual spectrum in black (note that the telluric features have not been removed, as is necessary for the fitting) and overplot in red the best fitting model that combines the synthetic atmospheric and spectral templates.

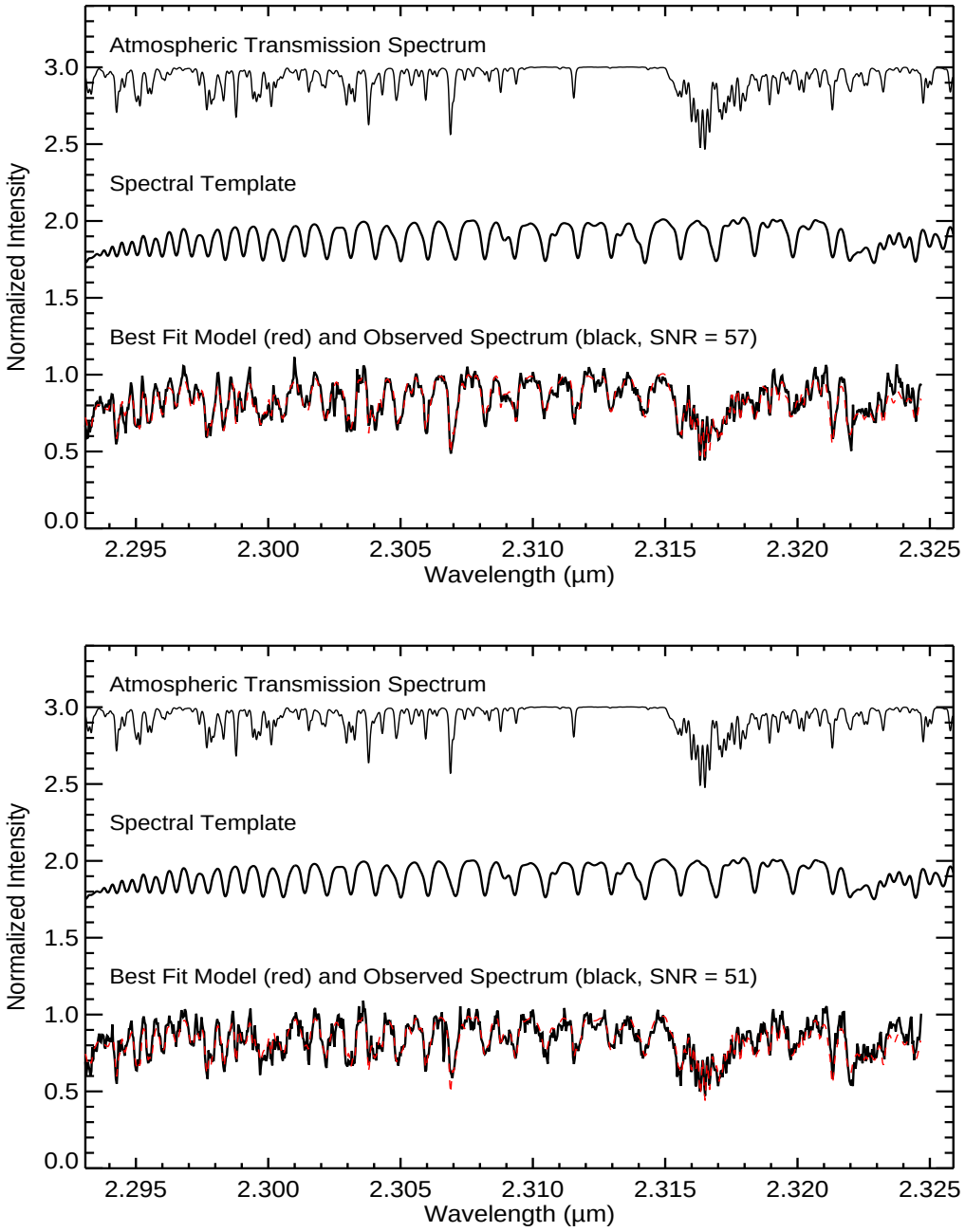

Figure 4.10 Example of a fit for radial velocity for the components of 2MASS 2206-20 A (**top**) and B (**bottom**) from the night of 2008 Jun 01. The atmospheric transmission spectrum used for wavelength calibration is shown, as well as the theoretical spectral template. On the bottom of each panel, we plot our actual spectrum in black (note that the telluric features have not been removed, as is necessary for the fitting) and overplot in red the best fitting model that combines the synthetic atmospheric and spectral templates.

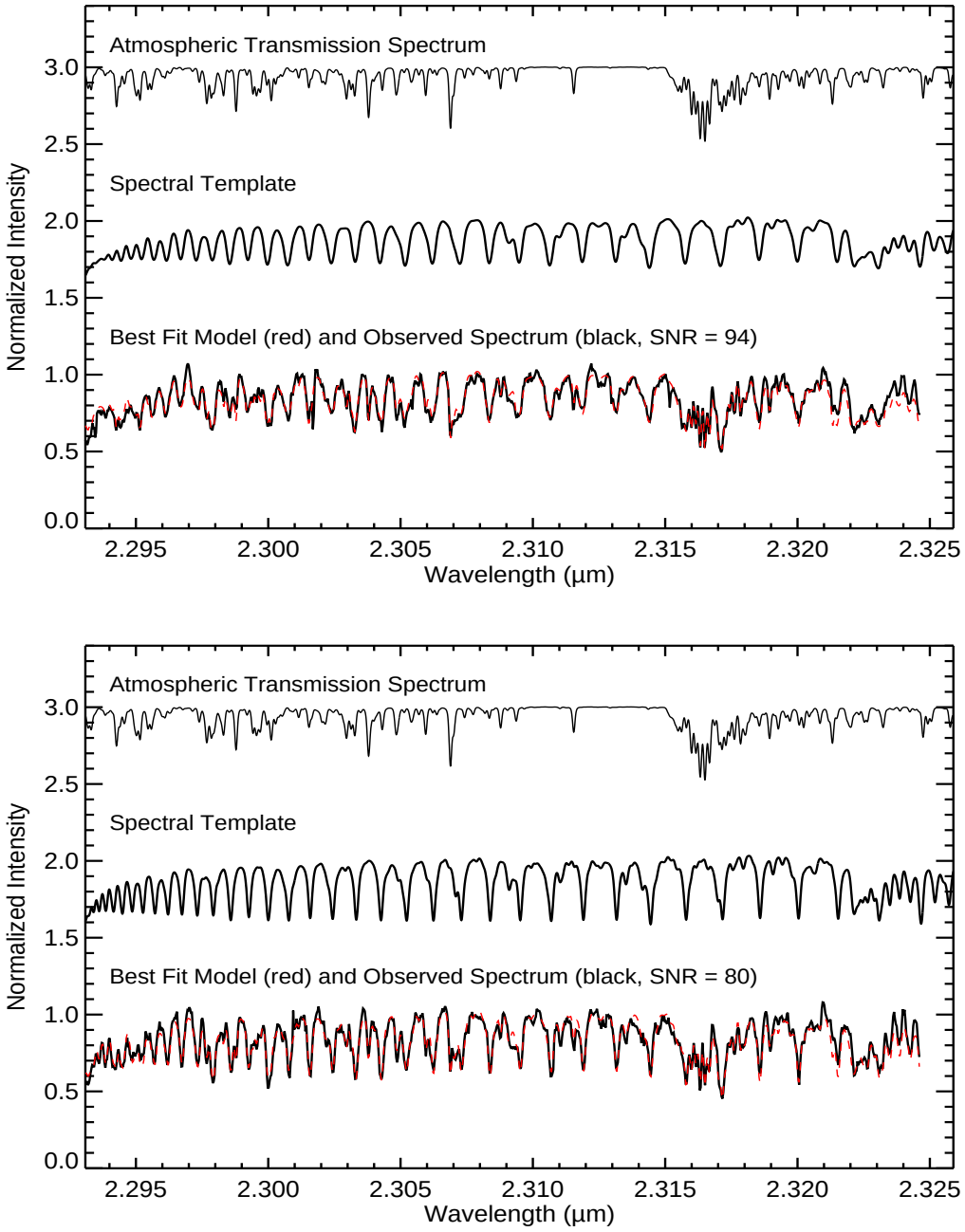

Figure 4.11 Example of a fit for radial velocity for the components of GJ 569B a (**top**) and b (**bottom**) from the night of 2007 Jun 09. The atmospheric transmission spectrum used for wavelength calibration is shown, as well as the theoretical spectral template. On the bottom of each panel, we plot our actual spectrum in black (note that the telluric features have not been removed, as is necessary for the fitting) and overplot in red the best fitting model that combines the synthetic atmospheric and spectral templates.

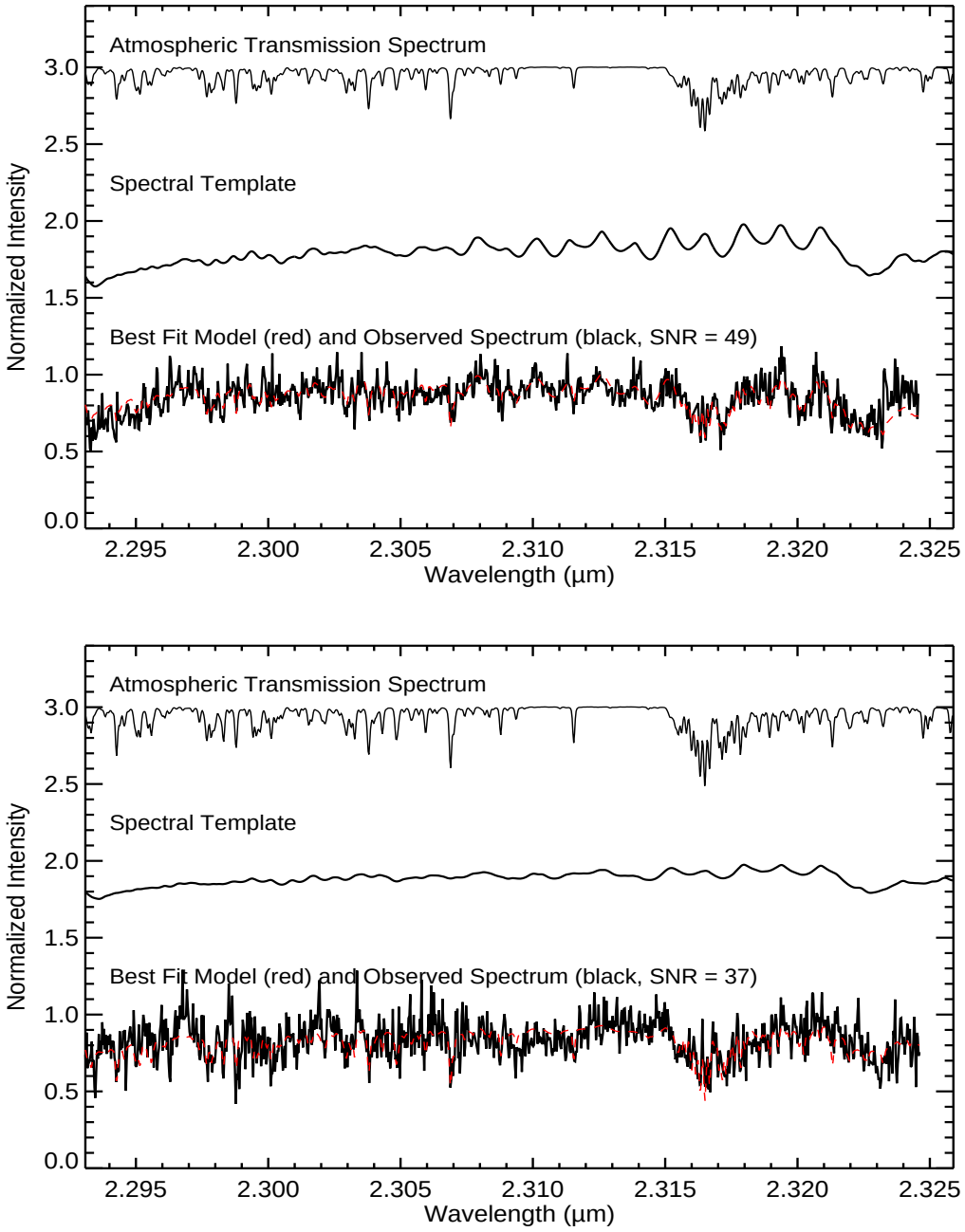

Figure 4.12 Example of a fit for radial velocity for the components of HD 130948 B (**top**) and C (**bottom**) from the night of 2007 Jun 09. The atmospheric transmission spectrum used for wavelength calibration is shown, as well as the theoretical spectral template. On the bottom of each panel, we plot our actual spectrum in black (note that the telluric features have not been removed, as is necessary for the fitting) and overplot in red the best fitting model that combines the synthetic atmospheric and spectral templates.

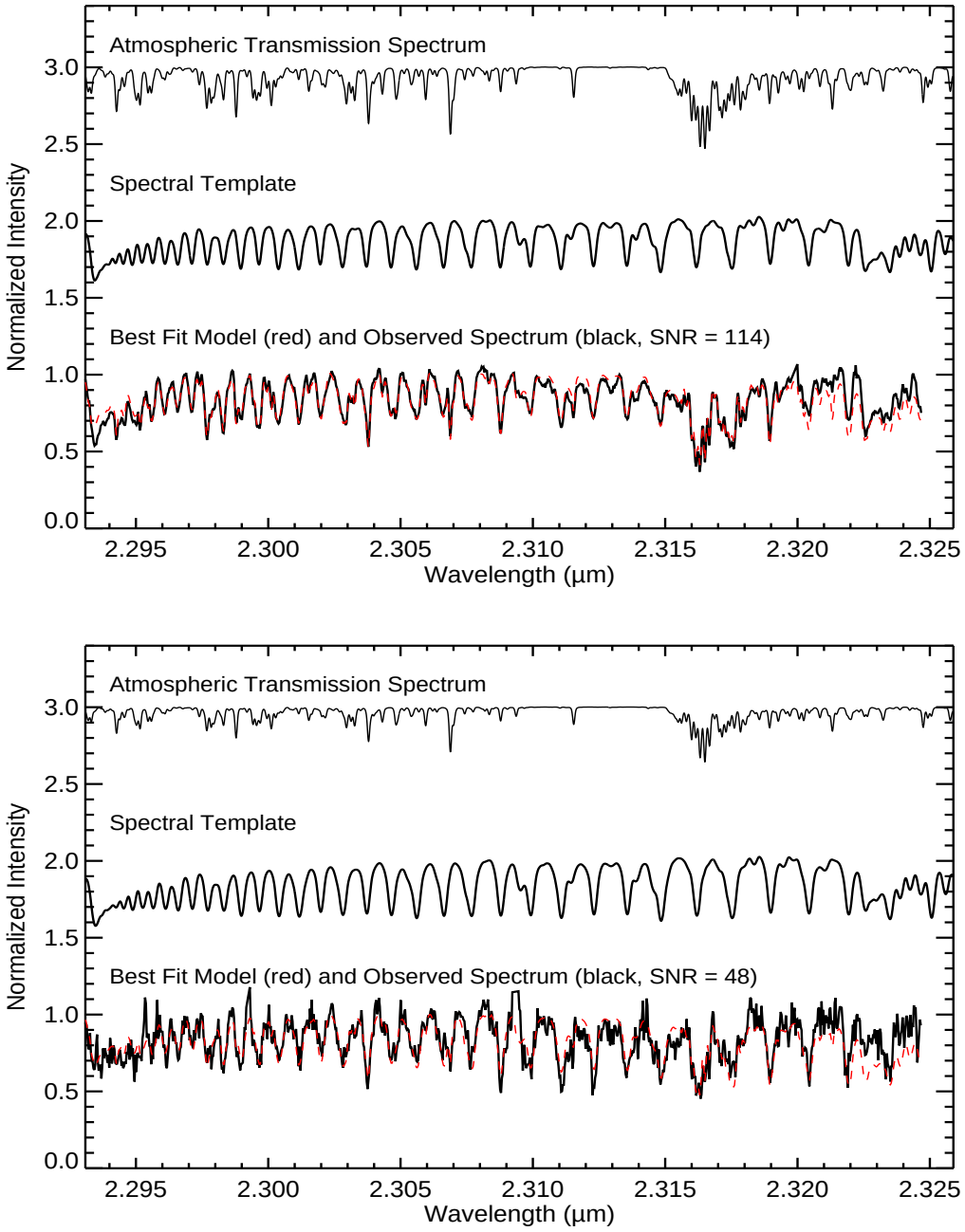

Figure 4.13 Example of a fit for radial velocity for the components of LHS 2397a A (**top**) and B (**bottom**) from the night of 2008 May 31. The atmospheric transmission spectrum used for wavelength calibration is shown, as well as the theoretical spectral template. On the bottom of each panel, we plot our actual spectrum in black (note that the telluric features have not been removed, as is necessary for the fitting) and overplot in red the best fitting model that combines the synthetic atmospheric and spectral templates.

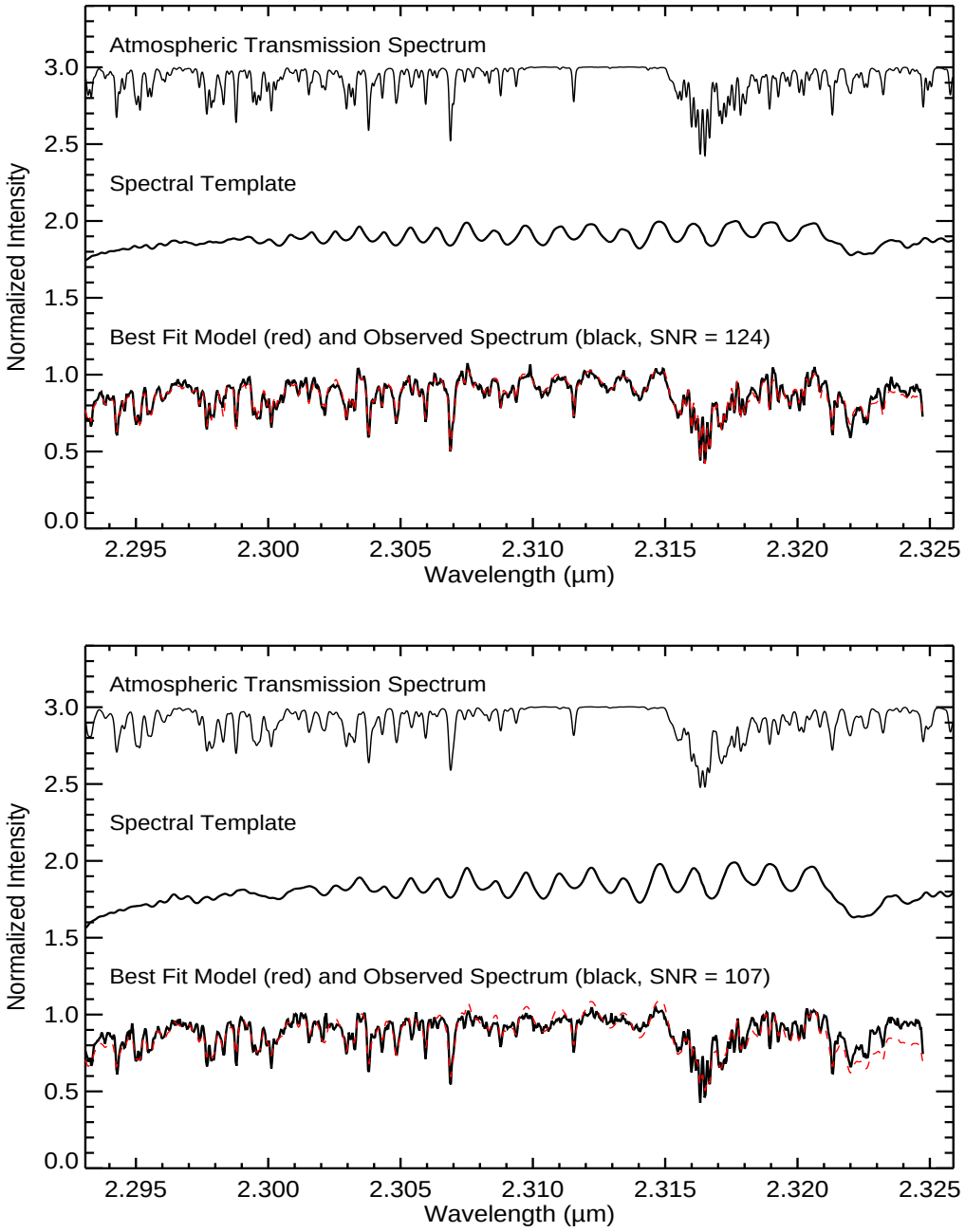

Figure 4.14 Example of a fit for radial velocity for the components of LP 349-25 A (**top**) and B (**bottom**) from the night of 2009 Jun 12. The atmospheric transmission spectrum used for wavelength calibration is shown, as well as the theoretical spectral template. On the bottom of each panel, we plot our actual spectrum in black (note that the telluric features have not been removed, as is necessary for the fitting) and overplot in red the best fitting model that combines the synthetic atmospheric and spectral templates.

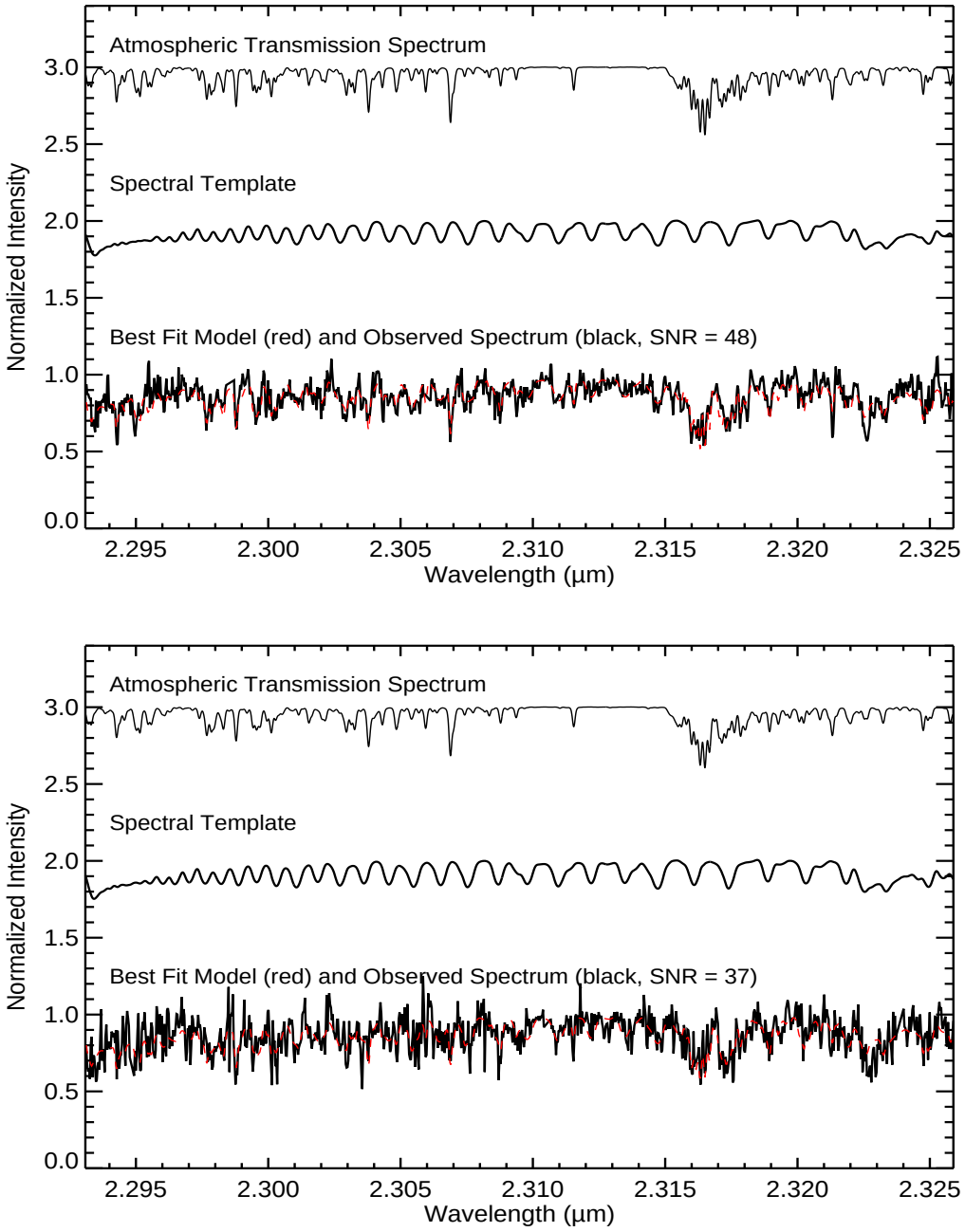

Figure 4.15 Example of a fit for radial velocity for the components of LP 415-20 A (**top**) and B (**bottom**) from the night of 2008 Dec 19. The atmospheric transmission spectrum used for wavelength calibration is shown, as well as the theoretical spectral template. On the bottom of each panel, we plot our actual spectrum in black (note that the telluric features have not been removed, as is necessary for the fitting) and overplot in red the best fitting model that combines the synthetic atmospheric and spectral templates.

allow distance to be a free parameter, but rather we constrain it to be consistent with the parallax distance and its uncertainties. The uncertainties on parallax measurements are smaller than those from fitting for distance as a free parameter, and the values are consistent in all cases. The distances, either used or derived in our fits, are given in Table 4.7. In the case of one system, 2MASS 0920+35, we had neither radial velocities nor a parallax measurement, so we use instead the photometric distance as determined from the relationship in Cruz et al. (2003), which is based on J band photometry and spectral type (here assumed to have an uncertainty of ±2 spectral subclasses). The best fit orbital parameter values are found by minimizing the total χ^2, which is found by summing the χ^2 of each data type ($\chi^2_{tot} = \chi^2_{ast} + \chi^2_{rv}$; see Ghez et al. (2008) for more details on this fitting procedure).

After the best fit is determined, the uncertainties in the orbital parameters are found via a Monte Carlo simulation. First, 10,000 artificial data sets are generated to match the observed data set in number of points, where the value of each point (including the distance when it was not being fit for) is assigned by randomly drawing from a Gaussian distribution centered on the true value with a width corresponding to the uncertainty on that value. Each of these artificial data sets is then fit with an orbit model as described above, and the best fit model is saved. The resulting distribution of orbital parameters represents the joint probability distribution function of those parameters. We obtain the uncertainties on each parameter as in Ghez et al. (2008), where the distribution of each parameter is marginalized against all others and confidence limits are determined by integrating the resulting one-dimensional distribution from the best fit out to a probability of 68%. On occasion, when one or more parameters are not well-constrained, the best fit value does not correspond to the peak of the probability distribution. However, in almost all cases the best fit value for

a parameter is within 1σ of the peak. The few fit parameters in which this is not the case are normally represented by bifurcated or poorly constrained flat distributions (see for example the distributions of e and ω for 2MASS 1847+55 AB, Figure 4.38).

The resulting best-fit orbital parameters and their uncertainties are given in Table 4.7. The astrometric orbital solutions are drawn in conjunction with both the astrometric and relative radial velocity data in Figures 4.16-4.30. The dotted blue lines represent the 1σ range of separations and relative radial velocities allowed at a given time based on the orbital solutions from the Monte Carlo. The distributions of orbital parameters for all sources are shown in Figures 4.31-4.45. The shaded regions on the histograms show the 1σ ranges of each parameter. If the distances were sampled from previous parallax measurements, they are denoted with a red histogram. These figures are alphabetically ordered based on the sources' names.

If Figure 4.46, we plot our current uncertainty in total system mass for each of the 15 systems with orbital solutions versus the initial binary separation. Of these 15 systems, 7 have reached this precision goal. We attribute the fact that the other 8 systems did not reach this goal to a few of the assumptions in our Monte Carlo. First, we assumed a constant mass value that was based on the spectral type of each system, but we have derived a variety of masses in our orbital solutions. Secondly, sampled uniformly from a semimajor axis distribution that was between 0.5 and 2 times the initial separation, which may have not been a wide enough range. Third, we assumed a distance to each system without previous parallax measurements and assigned an uncertainty of ± 5 pc, whereas we have fit for distances in a number of cases that have higher uncertainties than this value.

Table 4.7. Astrometric Orbital Parameters

Target Name	Fixed Dist. (pc)	Fit Dist. (pc)	Total System Mass ($M_\odot$)	Period (years)	Semi-Major Axis (mas)	Eccentricity	T_o (years)	Inc. (degrees)	Ω (degrees)	ω (degrees)	Best Fit Reduced χ^2
2MASS 0746+20AB	12.21 ± 0.05[b]	—	0.151 ± 0.003	12.71 ± 0.07	$237.3^{+1.5}_{-0.4}$	0.487 ± 0.003	2002.83 ± 0.01	138.2 ± 0.5	28.4 ± 0.5	354.4 ± 0.9	0.88
2MASS 0850+10AB	38.1 ± 7.3[c]	—	0.2 ± 0.2	24^{+69}_{-6}	126^{100}_{-32}	0.64 ± 0.26	2016^{+9}_{-24}	65 ± 12	96 ± 27	236^{+117}_{-171}	2.85
2MASS 0920+35AB	24.3 ± 5.0[a]	—	0.11 ± 0.11	$6.7^{+3.3}_{3.4}$	69 ± 24	$0.21^{+0.65}_{-0.21}$	2003.43 ± 1.15	88.6 ± 2.4	69.0 a± 1.5	317^{+43}_{-300}	0.92
2MASS 1426+15AB	—	34 ± 13	$0.11^{+0.08}_{-0.11}$	1985^{+2141}_{-1945}	2273 ± 1560	$0.85^{+0.10}_{-0.41}$	1998 ± 24	88.3 ± 0.8	344.8 ± 0.4	282^{+78}_{-210}	1.89
2MASS 1534-29AB	13.59 ± 0.22[d]	—	0.060 ± 0.004	23.1 ± 4.0	234 ± 30	0.10 ± 0.09	2006.4 ± 3.0	85.6 ± 0.4	13.4 ± 0.3	25^{+154}_{-25}	1.57
2MASS 1728+39AB	24.1 ± 2.1[c]	—	$0.15^{+0.25}_{-0.04}$	31.3 ± 12.7	220 ± 26	$0.28^{+0.35}_{-0.28}$	$2017\ ^{+4}_{-22}$	62 ± 7	118^{+11}_{-9}	94 ± 15	2.60
2MASS 1750+44AB	—	37.6 ± 12.3	0.20 ± 0.12	317 ± 240	728 ± 375	0.71 ± 0.18	2004.3 ± 1.8	44 ± 10	99 ± 6	267 ± 26	1.63
2MASS 1847+55AB	—	29.8 ± 7.1	$0.18^{+0.35}_{-0.13}$	44.2 ± 18.7	237 ± 36	$0.1^{+0.5}_{-0.1}$	2020^{+6}_{-28}	79^{+4}_{-2}	125 ± 3	68 ± 30	0.63
2MASS 2140+16AB	—	25 ± 10	0.10 ± 0.08	$20.1^{+5.3}_{-1.6}$	141^{9}_{-6}	0.26 ± 0.06	$2012.0^{+0.5}_{-2.0}$	$46.2^{2.5}_{-8.7}$	104 ± 7	223^{+10}_{-47}	0.50
2MASS 2206-20AB	26.67 ± 2.63[e]	—	0.16 ± 0.05	23.78 ± 0.19	168.0 ± 1.5	$0.000^{+0.002}_{-0.000}$	$2000.0^{+1.9}_{-3.2}$	44.3 ± 0.7	74.8 ± 1.0	326^{+28}_{-52}	2.32
GJ569B ab	9.81 ± 0.16[f]	—	0.126 ± 0.007	2.370 ± 0.002	90.8 ± 0.8	0.310 ± 0.006	2003.150 ± 0.005	33.6 ± 1.3	144.8 ± 1.9	77.4 ± 1.7	1.43
HD 130948BC	18.18 ± 0.08[f]	—	0.109 ± 0.002	9.83 ± 0.16	120.4 ± 1.4	0.16 ± 0.01	2008.6 ± 0.2	95.7 ± 0.2	313.3 ± 0.2	253.3 ± 3.9	2.12
LHS 2397a AB	14.3 ± 0.4[g]	—	0.144 ± 0.013	14.26 ± 0.10	215.8 ± 1.5	0.348 ± 0.006	2006.29 ± 0.04	40.9 ± 1.2	78.0 ± 1.5	217.7 ± 2.6	1.47
LP 349-25AB	13.19 ± 0.28[h]	—	0.121 ± 0.009	7.31 ± 0.37	141 ± 7	0.08 ± 0.02	2002.5 ± 0.8	118.7 ± 1.5	213.8 ± 1.1	109^{+37}_{-22}	2.15
LP 415-20AB	—	21 ± 5	0.09 ± 0.06	11.5 ± 1.2	108 ± 24	0.9 ± 0.1	2006.5 ± 0.2	55 ± 12	200 ± 40	73 ± 50	1.47

[a]No parallax measurement or radial velocity data exists - spectrophotometric distance used here

[b]Distance from parallax measurement by Dahn et al. (2002)

[c]Distance from parallax measurement by Vrba et al. (2004)

[d]Distance from parallax measurement by Tinney et al. (2003)

[e]Distance from parallax measurement by Costa et al. (2006)

[f]Distance from Hipparcos parallax for high mass tertiary companion

[g]Distance from parallax measurement by Monet et al. (1992)

[h]Distance from parallax measurement by Gatewood et al. (2009)

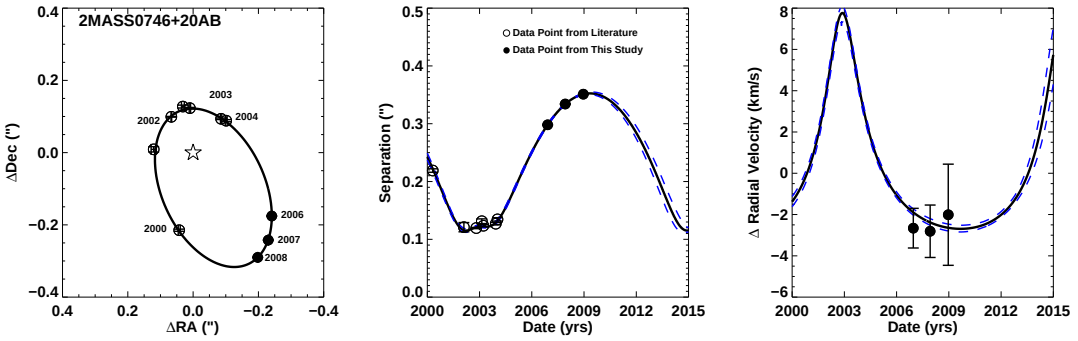

Figure 4.16 Best fit relative orbit for 2MASS0746+20AB. The left panel shows the relative astrometry data points overplotted with the best fit orbit. The middle panel shows separation of the components as a function of time overplotted with the best fit orbit. Finally, the right hand panel shows the relative radial velocity measurements as a function of time overplotted with the best fit orbit. Astrometric data from the literature is from Bouy et al. (2004). The blue dotted lines represent the 1σ allowed range of separations and relative radial velocities at a given time.

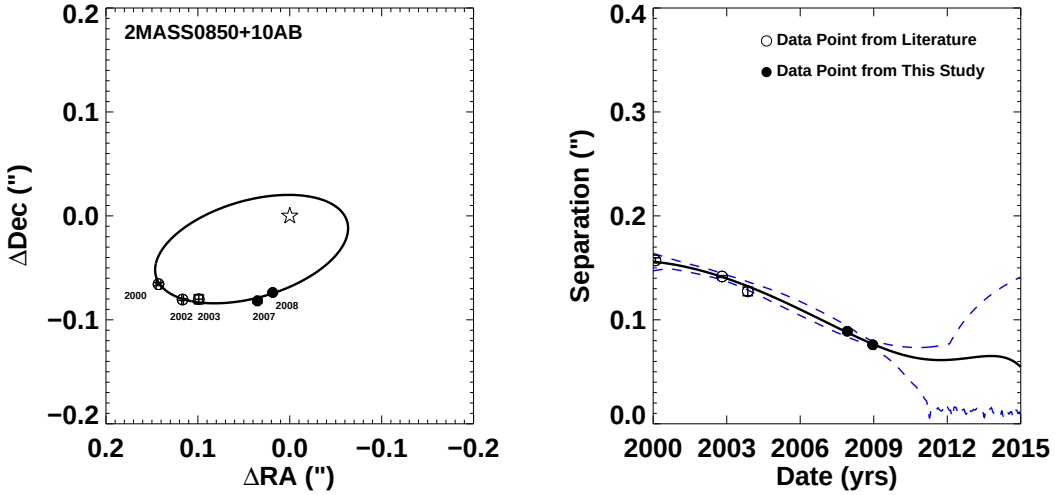

Figure 4.17 Best fit relative orbit for 2MASS0850+10AB. The left panel shows the relative astrometry data points overplotted with the best fit orbit. The right panel shows separation of the components as a function of time overplotted with the best fit orbit. For this fit, we have used the distance of Vrba et al. (2004). Astrometric data from the literature is from Reid et al. (2001) and Bouy et al. (2008). The blue dotted lines represent the 1σ allowed range of separations and relative radial velocities at a given time.

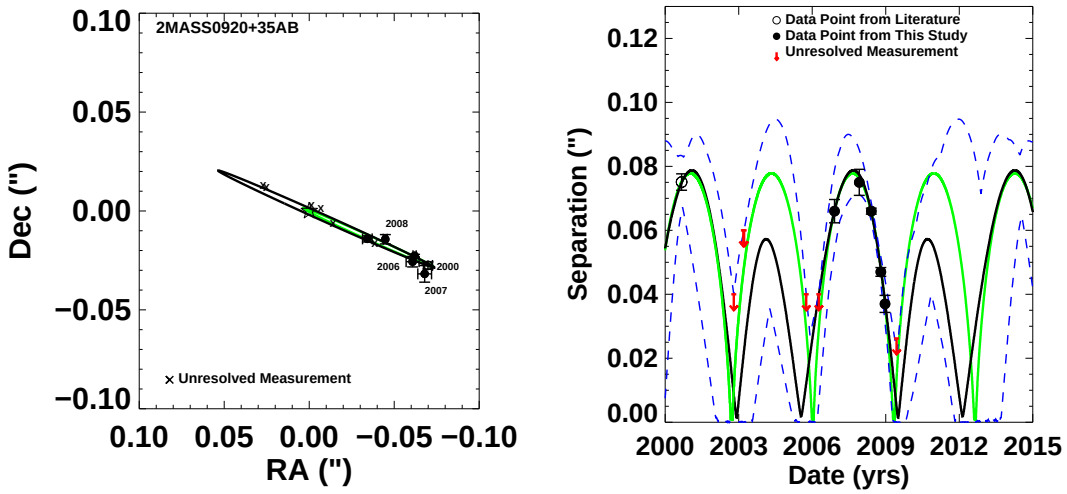

Figure 4.18 Best fit relative orbit for 2MASS0920+35AB. The left panel shows the relative astrometry data points overplotted with the best fit orbit. For this system, Bouy et al. (2008) obtained five unresolved measurements, for which they provide upper limits to the separation. We also obtained one unresolved measurement in 2009. We therefore only allow orbits for which the separation would be below those upper limits on those dates. The black line shows the best fit orbital solution (period ∼6.7 years), while the green line shows the other allowed solution which has a very short period (∼3.3 years) and a high eccentricity. The Xs denote the presumed position of the secondary on those dates for the best fit solution. The right panel shows the separation of the components as a function of time overplotted with the best fit orbit. The black line represents the best fit solution and the green line represents the other allowed, short period solution set. Also plotted are the upper limits on separation, showing that the best fit orbit clearly has separation values on those dates below these limits. This figure demonstrates more clearly that the upper limits allow for both solution sets. An astrometric measurement before mid-2010 should effectively rule out one or the other solution set. The blue dotted lines represent the 1σ allowed range of separations and relative radial velocities at a given time.

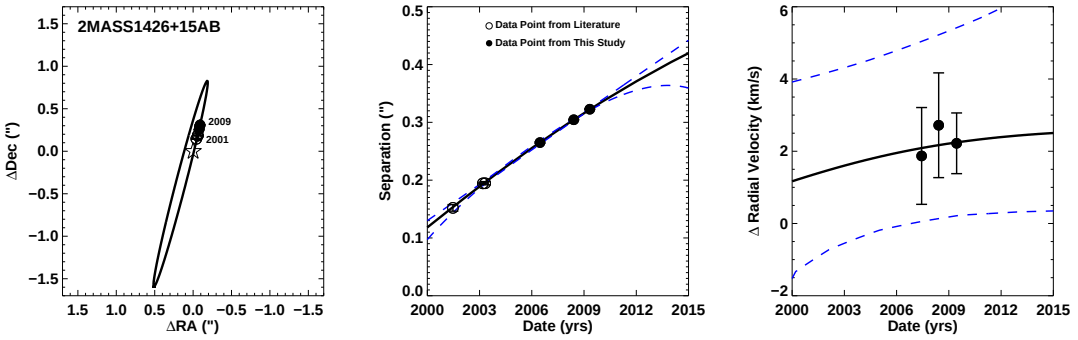

Figure 4.19 Best fit relative orbit for 2MASS1426+15AB. The left panel shows the relative astrometry data points overplotted with the best fit orbit. The middle panel shows separation of the components as a function of time overplotted with the best fit orbit. Finally, the right hand panel shows the relative radial velocity measurements as a function of time overplotted with the best fit orbit. Astrometric data from the literature is from Close et al. (2002), Bouy et al. (2003) and Bouy et al. (2008). The blue dotted lines represent the 1σ allowed range of separations and relative radial velocities at a given time.

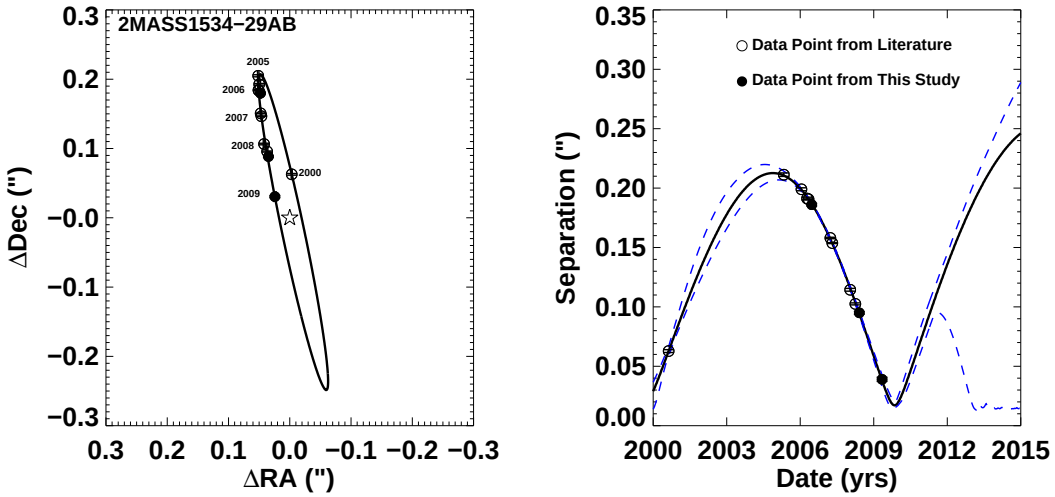

Figure 4.20 Best fit relative orbit for 2MASS1534-29AB. The left panel shows the relative astrometry data points overplotted with the best fit orbit. The right panel shows separation of the components as a function of time overplotted with the best fit orbit. Astrometric data from the literature is from Burgasser et al. (2003) and Liu et al. (2008). The blue dotted lines represent the 1σ allowed range of separations and relative radial velocities at a given time.

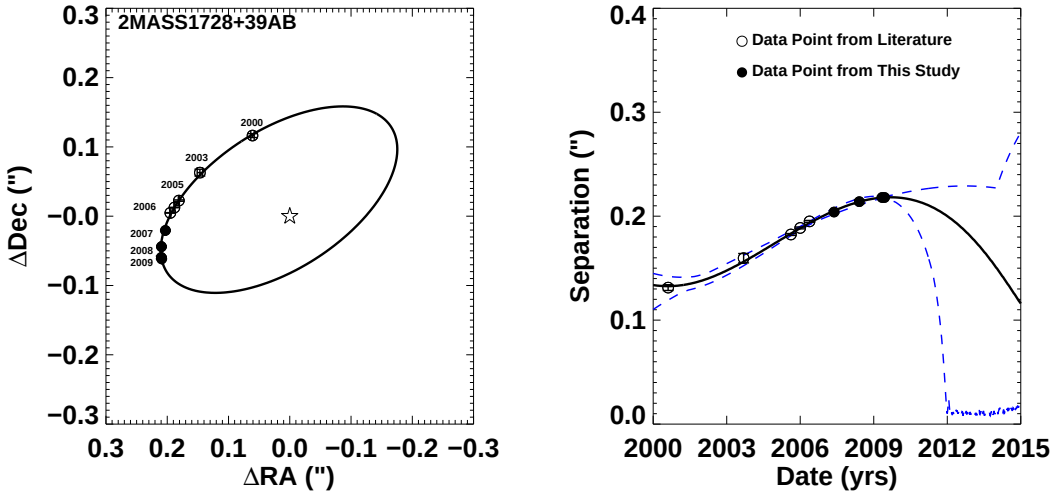

Figure 4.21 Best fit relative orbit for 2MASS1728+39AB. The left panel shows the relative astrometry data points overplotted with the best fit orbit. The right panel shows separation of the components as a function of time overplotted with the best fit orbit. Astrometric data from the literature is from Bouy et al. (2003) and Bouy et al. (2008). The blue dotted lines represent the 1σ allowed range of separations and relative radial velocities at a given time.

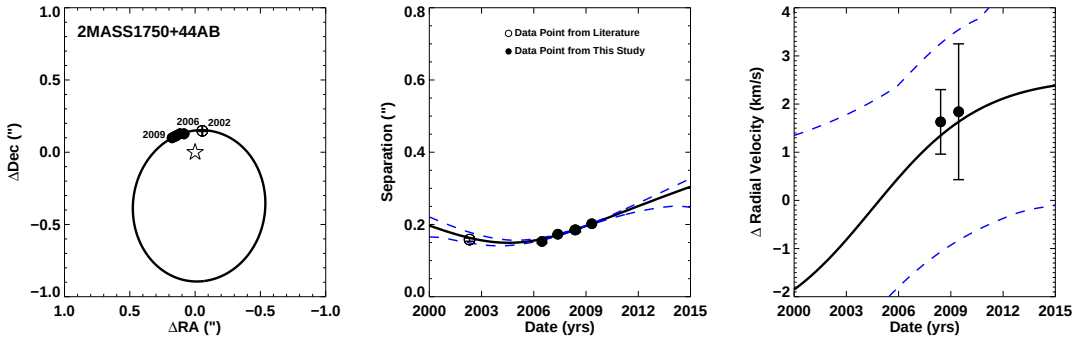

Figure 4.22 Best fit relative orbit for 2MASS1750+44AB. The left panel shows the relative astrometry data points overplotted with the best fit orbit. The middle panel shows separation of the components as a function of time overplotted with the best fit orbit. Finally, the right hand panel shows the relative radial velocity measurements as a function of time overplotted with the best fit orbit. Astrometric data from the literature is from Siegler et al. (2003). The blue dotted lines represent the 1σ allowed range of separations and relative radial velocities at a given time.

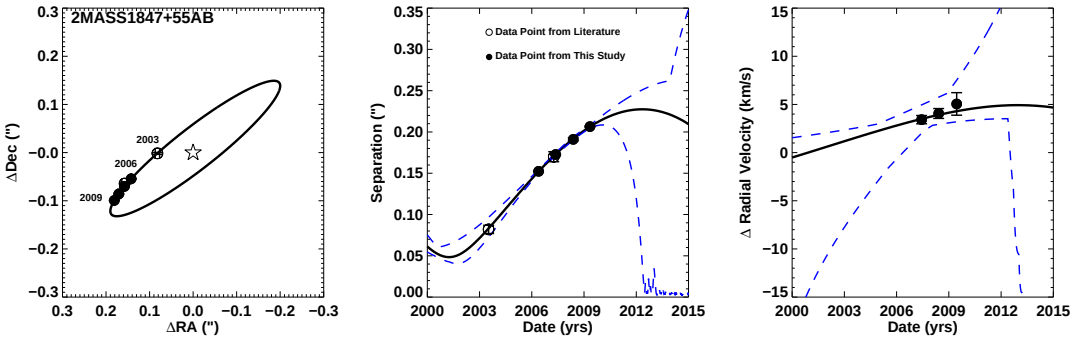

Figure 4.23 Best fit relative orbit for 2MASS1847+55AB. The left panel shows the relative astrometry data points overplotted with the best fit orbit. The middle panel shows separation of the components as a function of time overplotted with the best fit orbit. Finally, the right hand panel shows the relative radial velocity measurements as a function of time overplotted with the best fit orbit. Astrometric data from the literature is from Siegler et al. (2005) and Bouy et al. (2008). The blue dotted lines represent the 1σ allowed range of separations and relative radial velocities at a given time.

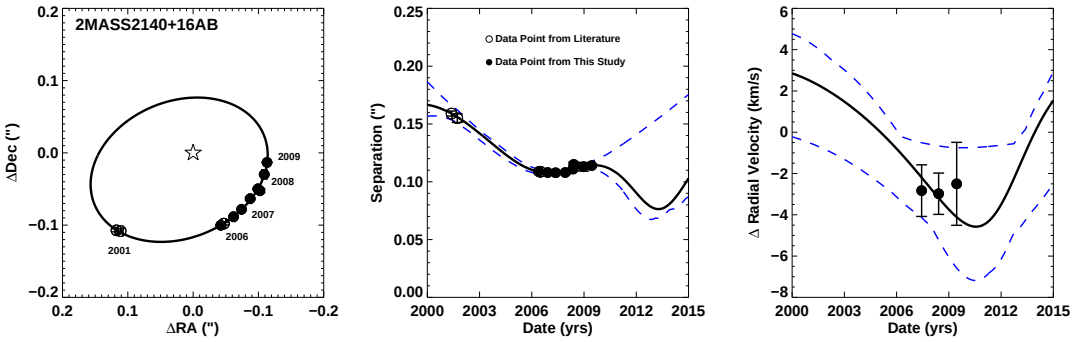

Figure 4.24 Best fit relative orbit for 2MASS2140+16AB. The left panel shows the relative astrometry data points overplotted with the best fit orbit. The middle panel shows separation of the components as a function of time overplotted with the best fit orbit. Finally, the right hand panel shows the relative radial velocity measurements as a function of time overplotted with the best fit orbit. Astrometric data from the literature is from Close et al. (2003), Bouy et al. (2003) and Bouy et al. (2008). The blue dotted lines represent the 1σ allowed range of separations and relative radial velocities at a given time.

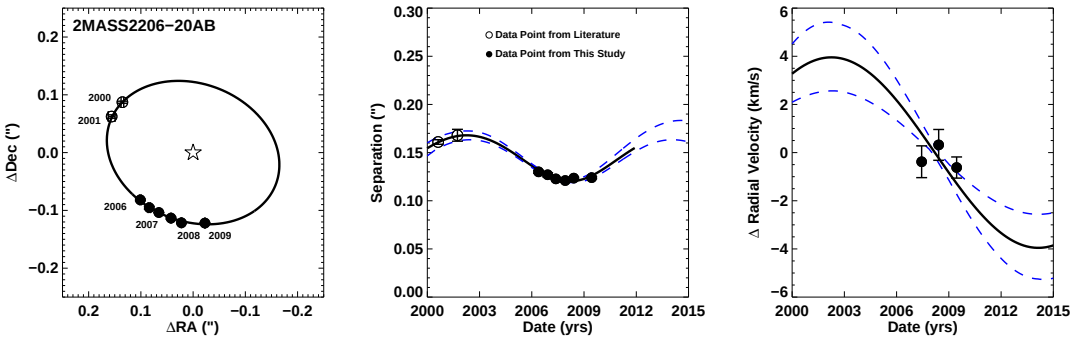

Figure 4.25 Best fit relative orbit for 2MASS2206-20AB. The left panel shows the relative astrometry data points overplotted with the best fit orbit. The middle panel shows separation of the components as a function of time overplotted with the best fit orbit. Finally, the right hand panel shows the relative radial velocity measurements as a function of time overplotted with the best fit orbit. Astrometric data from the literature is from Close et al. (2002) and Bouy et al. (2003). The blue dotted lines represent the 1σ allowed range of separations and relative radial velocities at a given time.

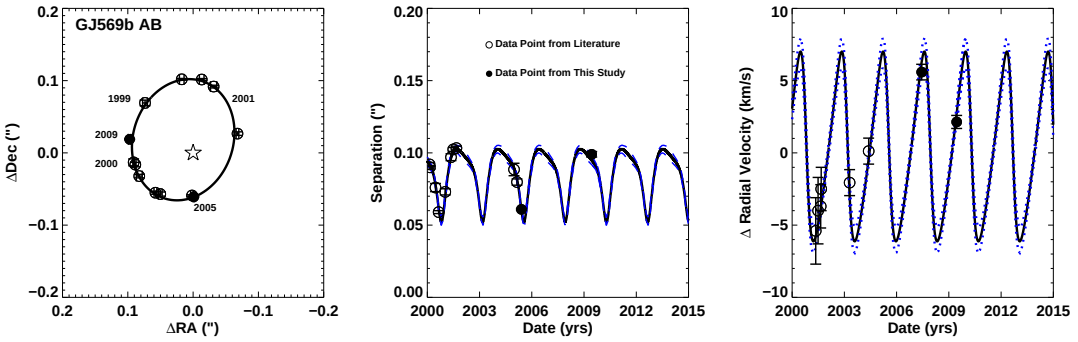

Figure 4.26 Best fit relative orbit for GJ 569Bab. The left panel shows the relative astrometry data points overplotted with the best fit orbit. The middle panel shows separation of the components as a function of time overplotted with the best fit orbit. Finally, the right hand panel shows the relative radial velocity measurements as a function of time overplotted with the best fit orbit. Astrometric and radial velocity data from the literature is from Zapatero Osorio et al. (2004) and Simon et al. (2005). The blue dotted lines represent the 1σ allowed range of separations and relative radial velocities at a given time.

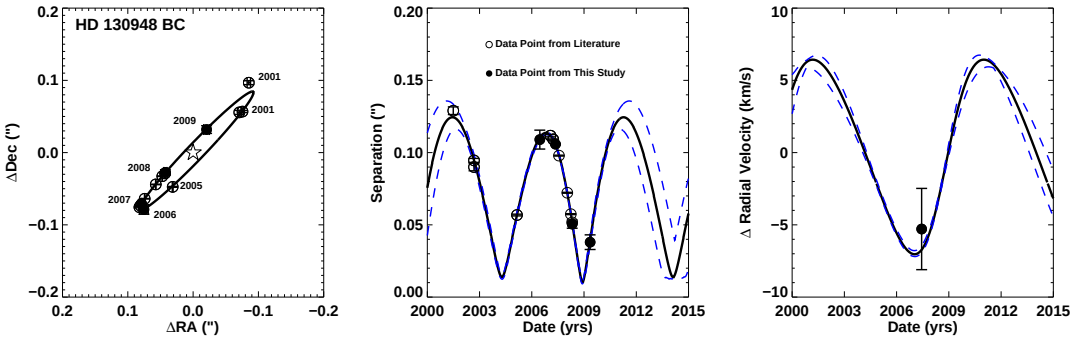

Figure 4.27 Best fit relative orbit for HD 130948BC. The left panel shows the relative astrometry data points overplotted with the best fit orbit. The middle panel shows separation of the components as a function of time overplotted with the best fit orbit. Finally, the right hand panel shows the relative radial velocity measurements as a function of time overplotted with the best fit orbit. Astrometric data from the literature taken from Potter et al. (2002) and Dupuy et al. (2009a). The blue dotted lines represent the 1σ allowed range of separations and relative radial velocities at a given time.

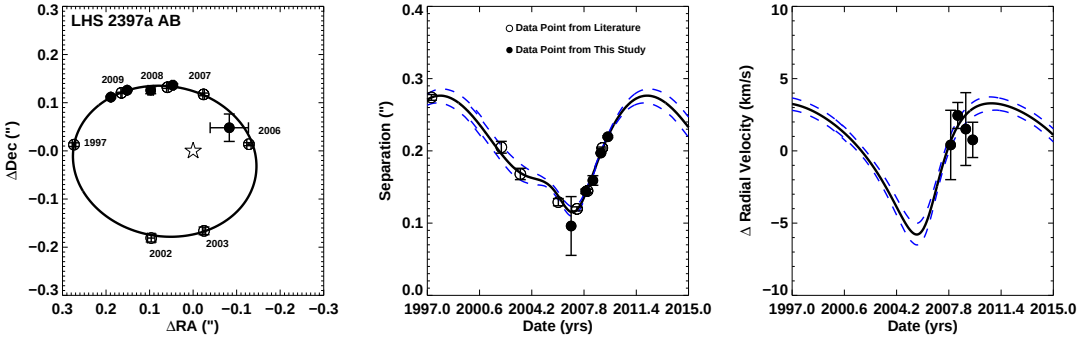

Figure 4.28 Best fit relative orbit for LHS 2397a AB. The left panel shows the relative astrometry data points overplotted with the best fit orbit. The middle panel shows separation of the components as a function of time overplotted with the best fit orbit. Finally, the right hand panel shows the relative radial velocity measurements as a function of time overplotted with the best fit orbit. Astrometric data from the literature taken from Freed et al. (2003) and Dupuy et al. (2009b). The blue dotted lines represent the 1σ allowed range of separations and relative radial velocities at a given time.

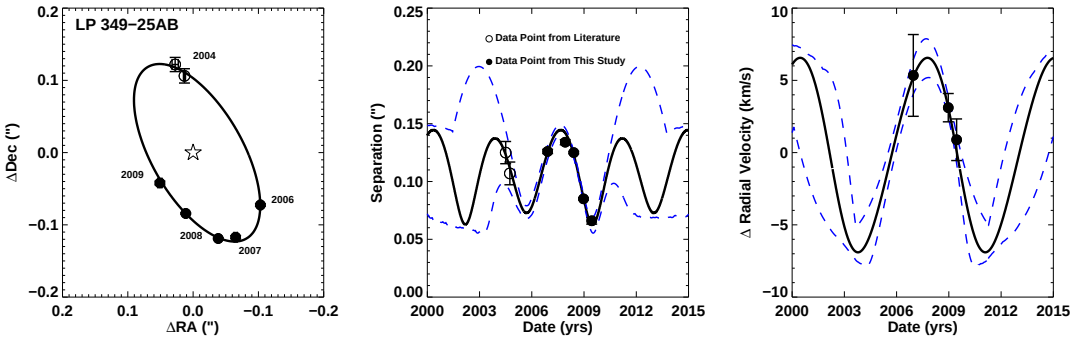

Figure 4.29 Best fit relative orbit for LP 349-25AB. The left panel shows the relative astrometry data points overplotted with the best fit orbit. The middle panel shows separation of the components as a function of time overplotted with the best fit orbit. Finally, the right hand panel shows the relative radial velocity measurements as a function of time overplotted with the best fit orbit. Astrometric data from the literature is from Forveille et al. (2005). The blue dotted lines represent the 1σ allowed range of separations and relative radial velocities at a given time.

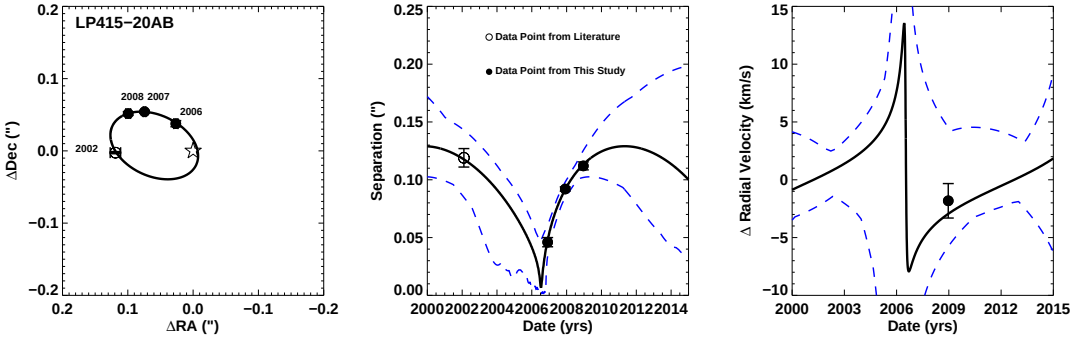

Figure 4.30 Best fit relative orbit for LP 415-20AB. The left panel shows the relative astrometry data points overplotted with the best fit orbit. The middle panel shows separation of the components as a function of time overplotted with the best fit orbit. Finally, the right hand panel shows the relative radial velocity measurements as a function of time overplotted with the best fit orbit. Astrometric data from the literature is from Siegler et al. (2005). The blue dotted lines represent the 1σ allowed range of separations and relative radial velocities at a given time.

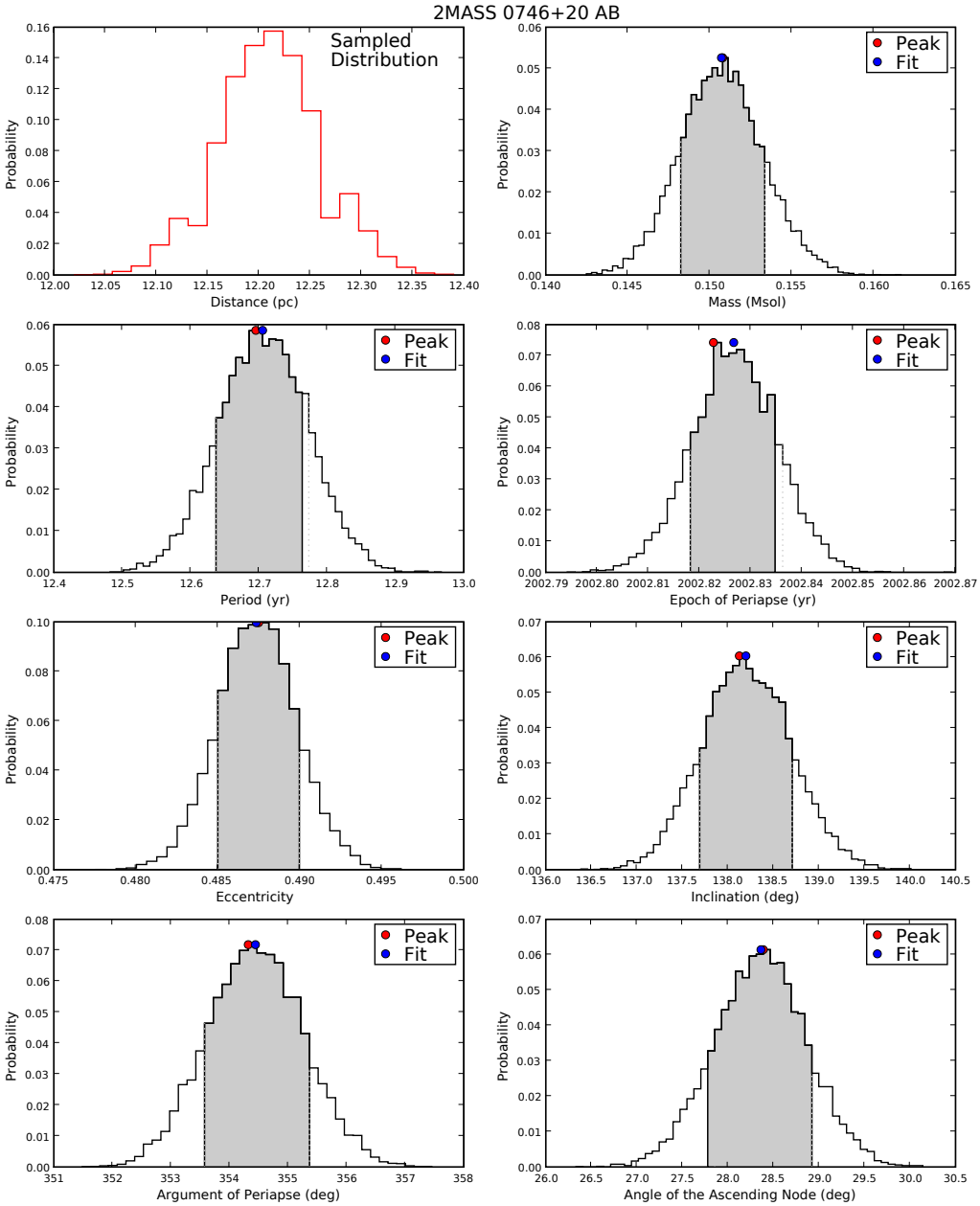

Figure 4.31 One-dimensional PDFs for the relative orbit (total system mass) of 2MASS 0746+20AB

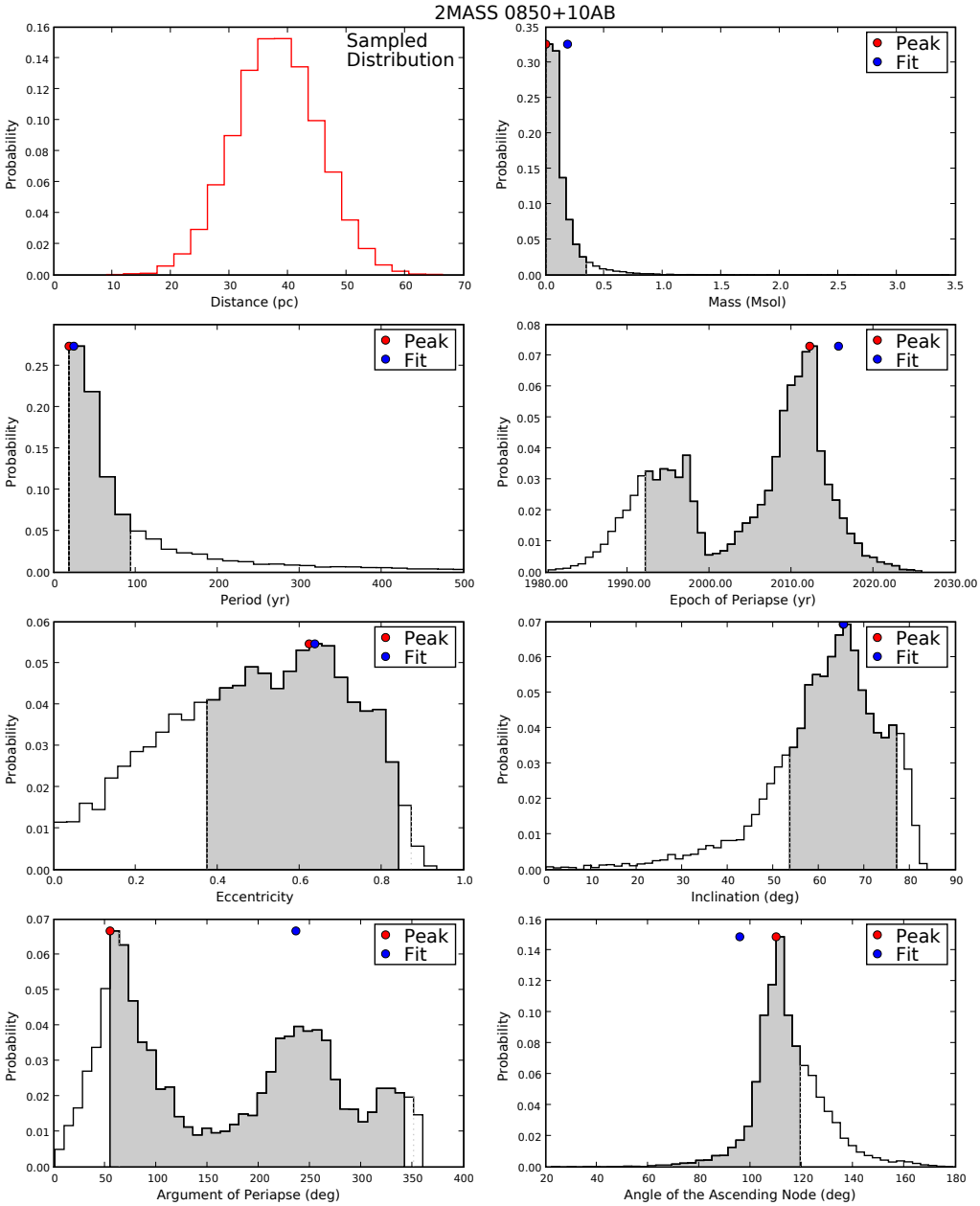

Figure 4.32 One-dimensional PDFs for the relative orbit (total system mass) of 2MASS 0850+10AB

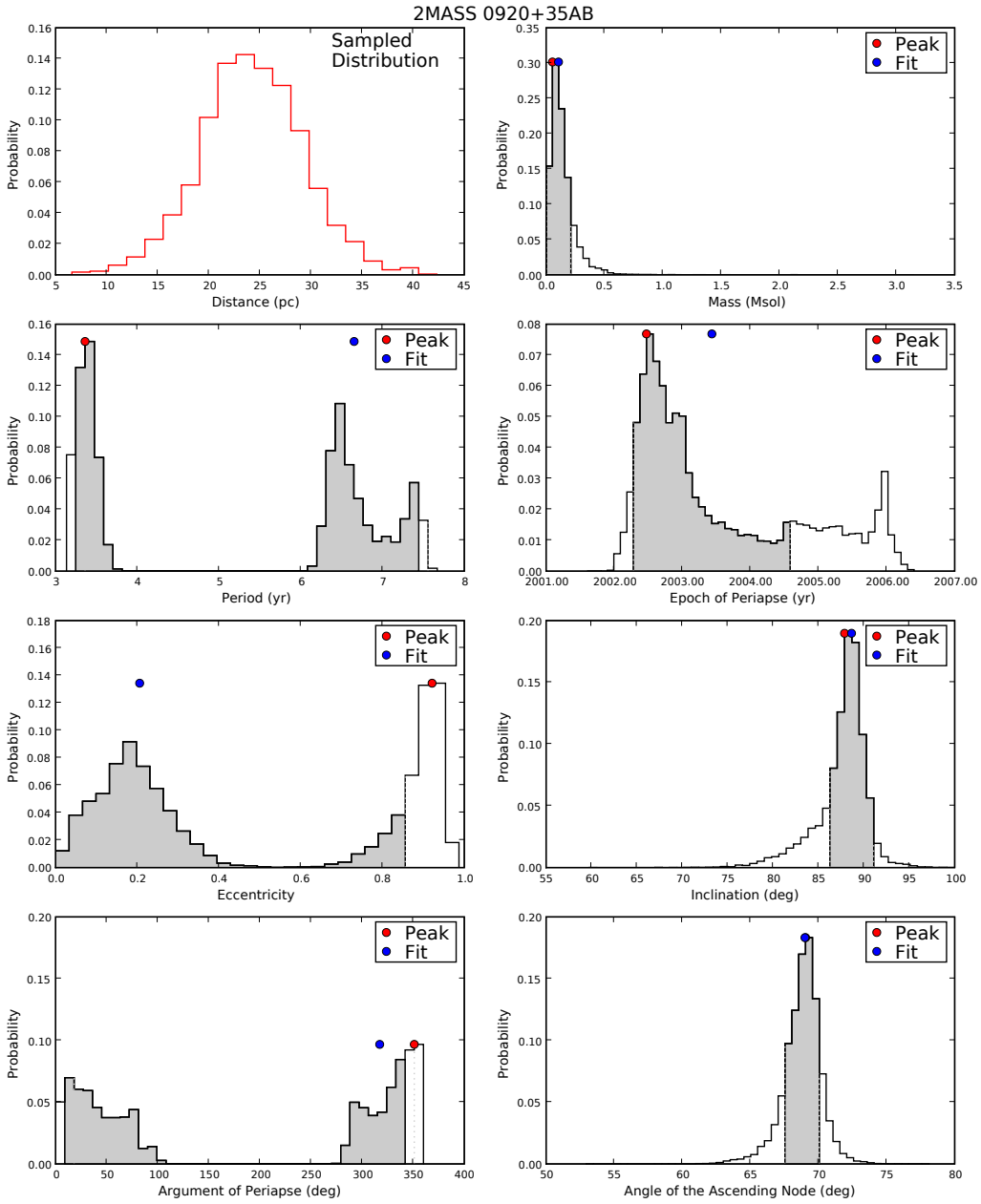

Figure 4.33 Full one-dimensional PDFs for the relative orbit (total system mass) of 2MASS 0920+35AB. A set of solutions exists with a period of ∼3.5 years and very high eccentricities, making the distributions of period, e and ω strongly bifurcated.

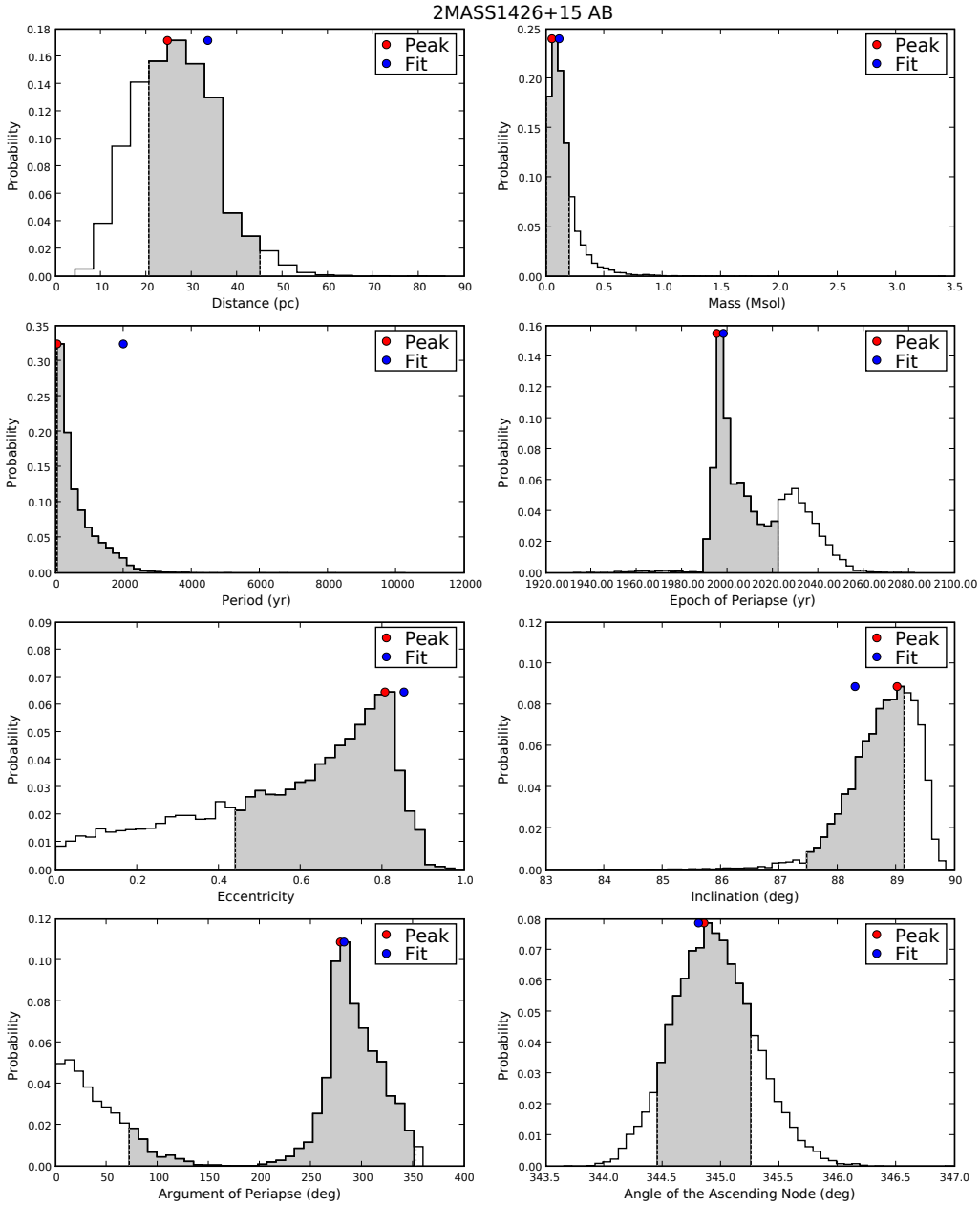

Figure 4.34 One-dimensional PDFs for the relative orbit (total system mass) of 2MASS 1426+15AB

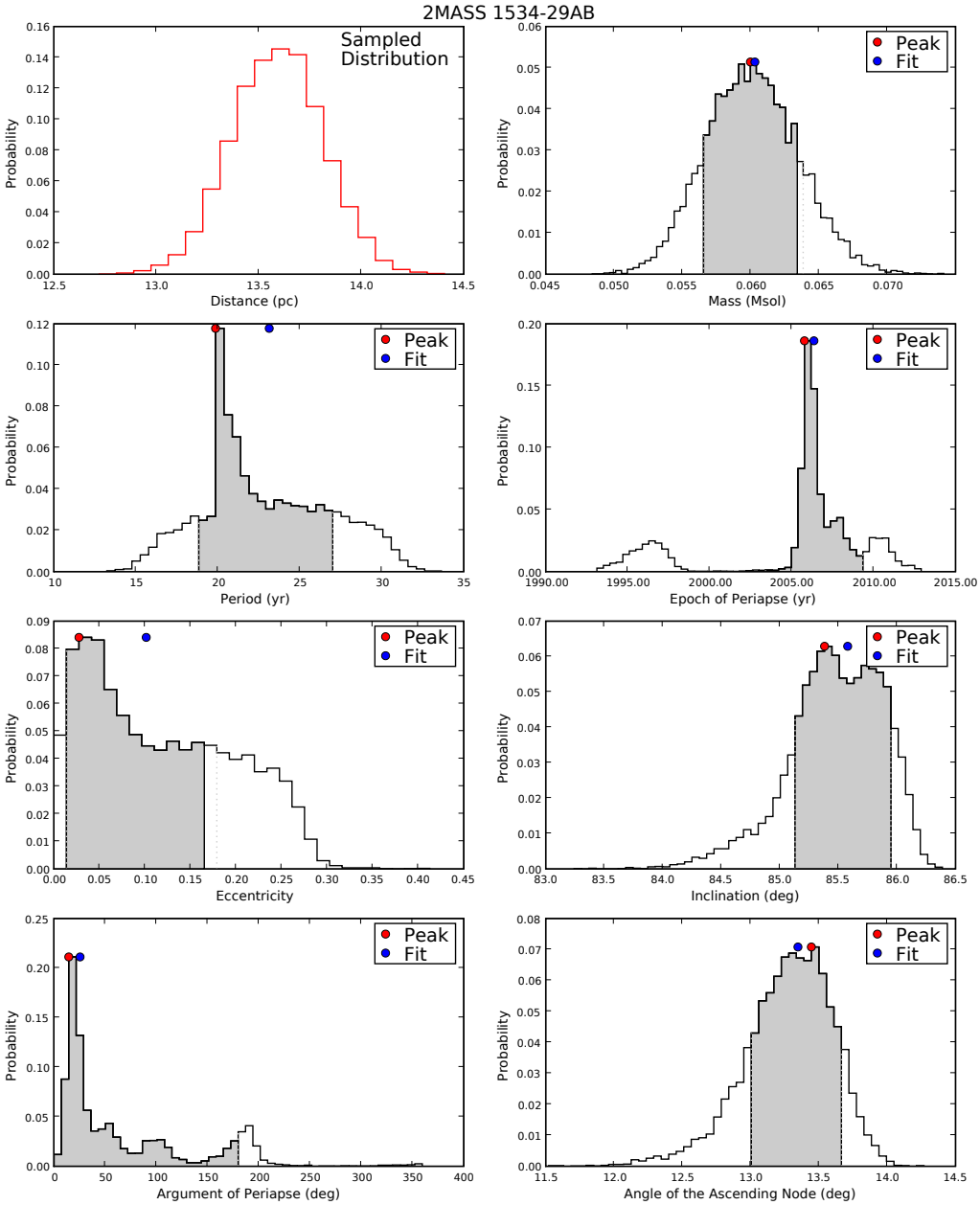

Figure 4.35 One-dimensional PDFs for the relative orbit (total system mass) of 2MASS 1534-29AB

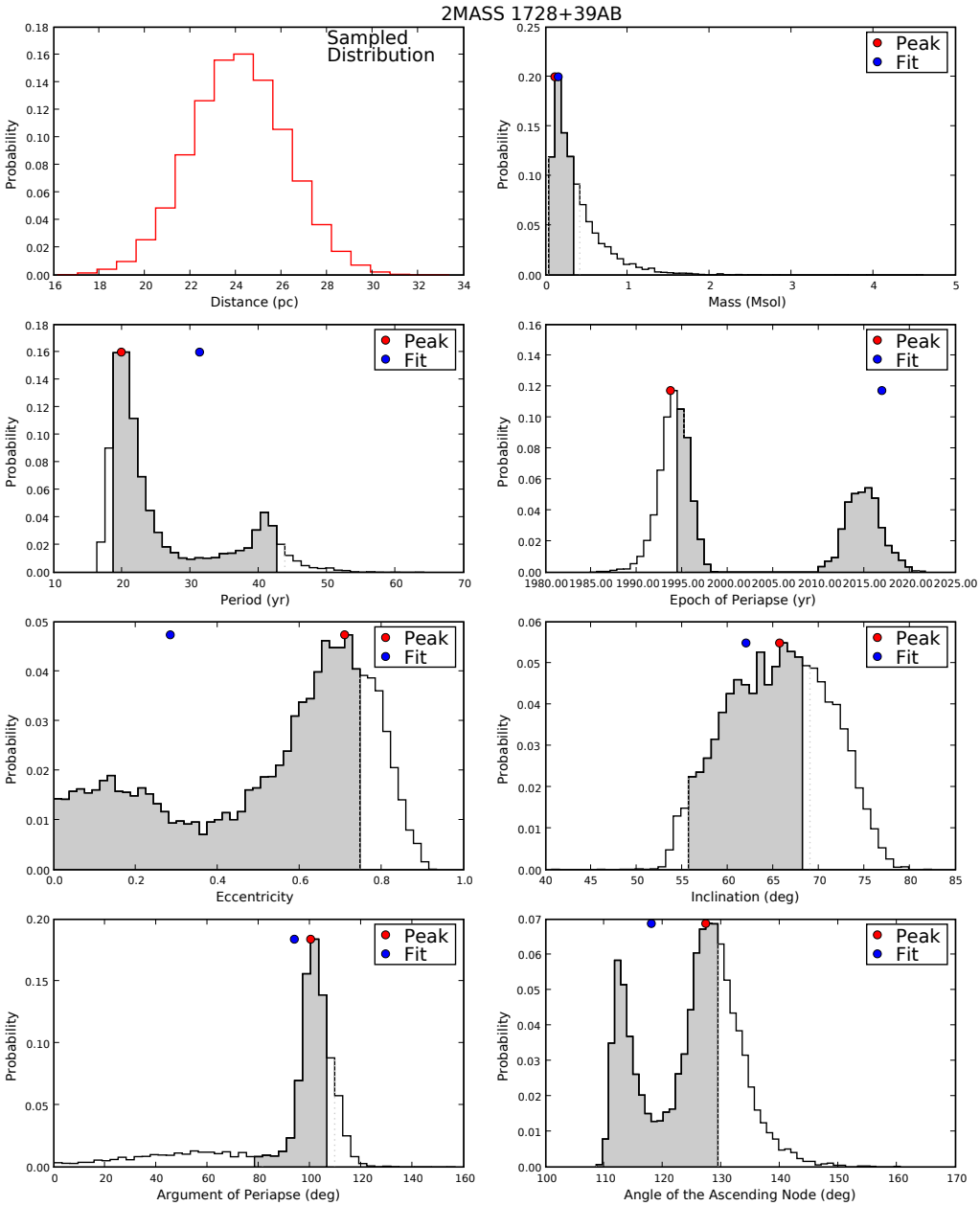

Figure 4.36 One-dimensional PDFs for the relative orbit (total system mass) of 2MASS 1728+35AB

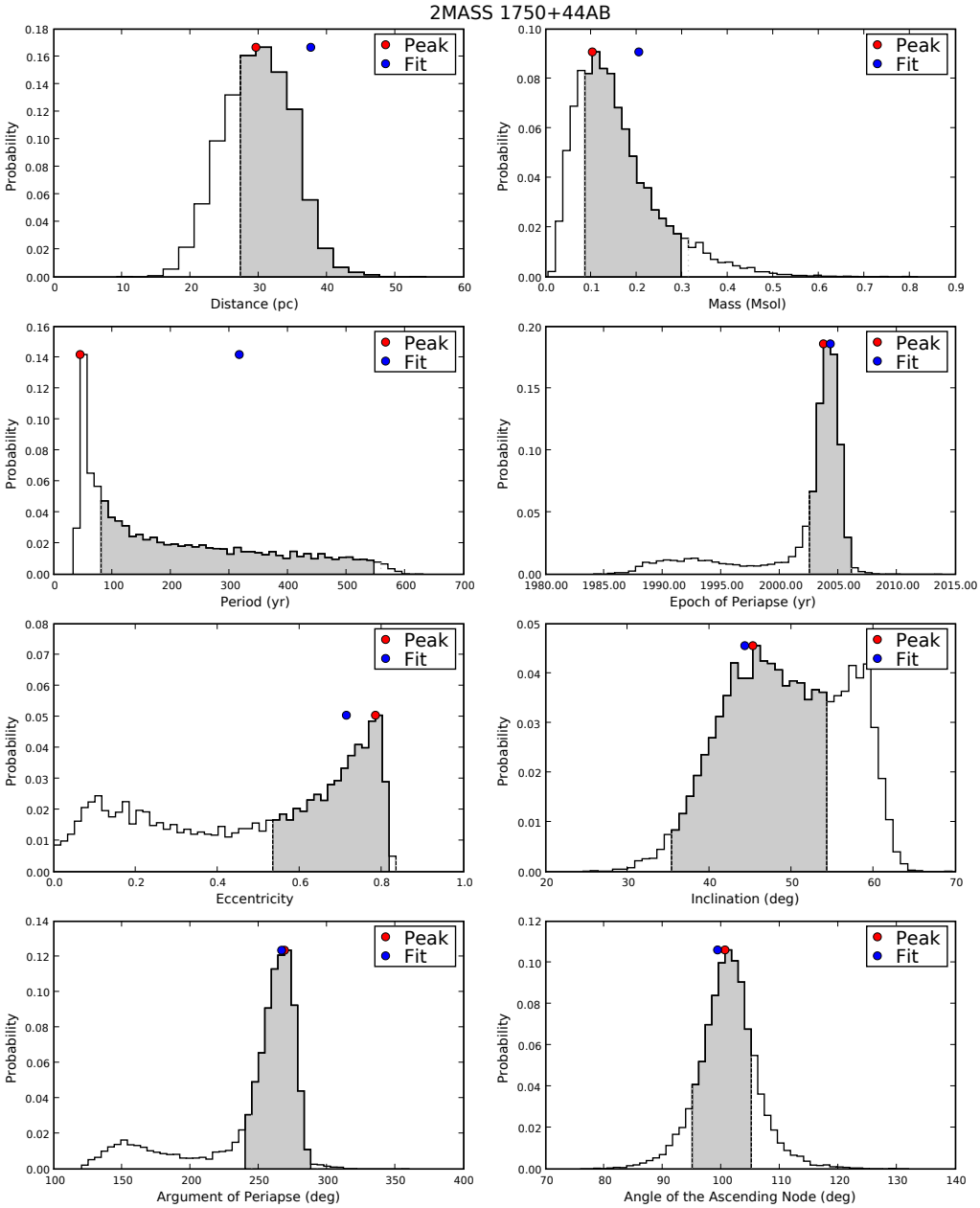

Figure 4.37 One-dimensional PDFs for the relative orbit (total system mass) of 2MASS 1750+44AB

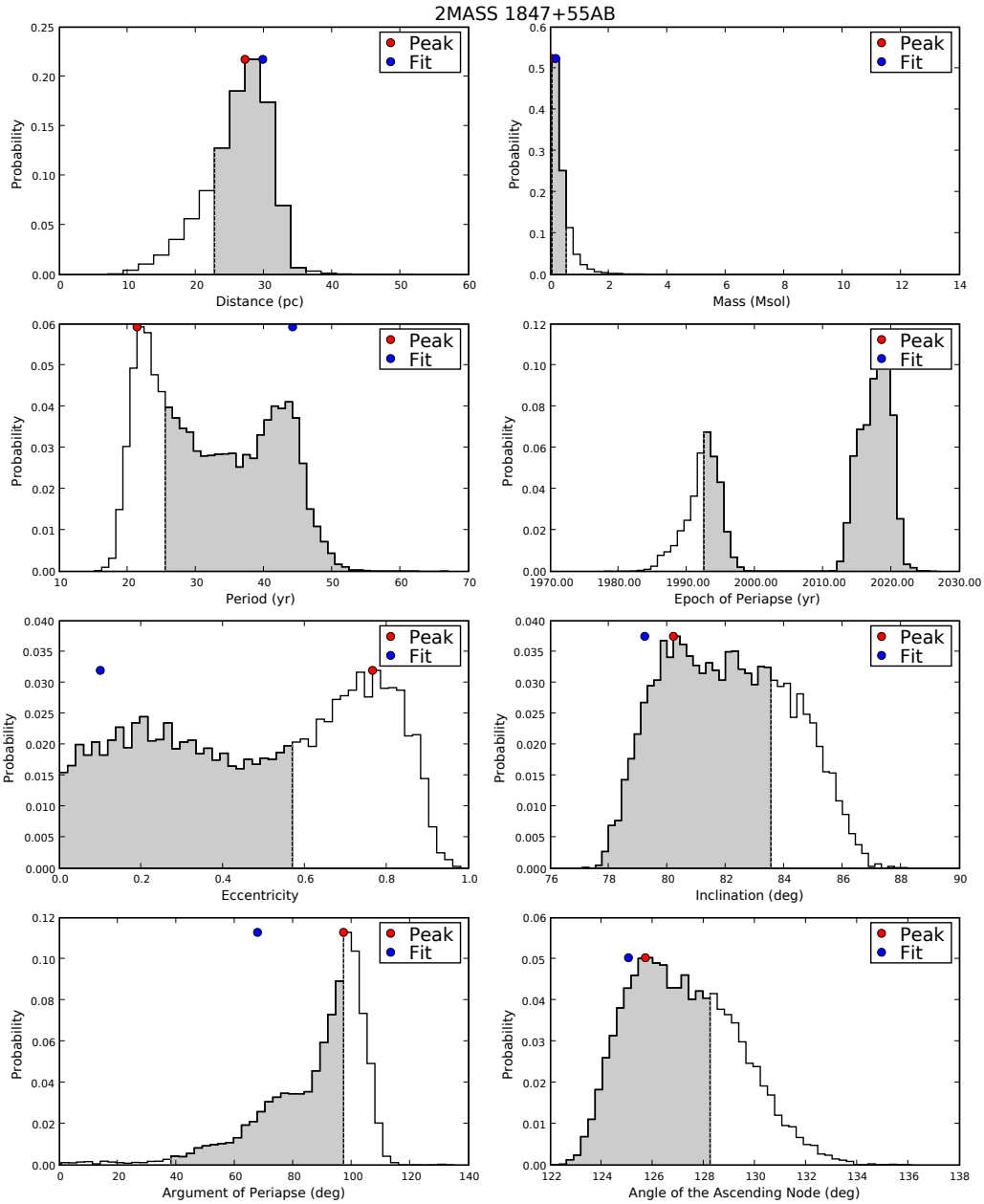

Figure 4.38 One-dimensional PDFs for the relative orbit (total system mass) of 2MASS 1847+55AB

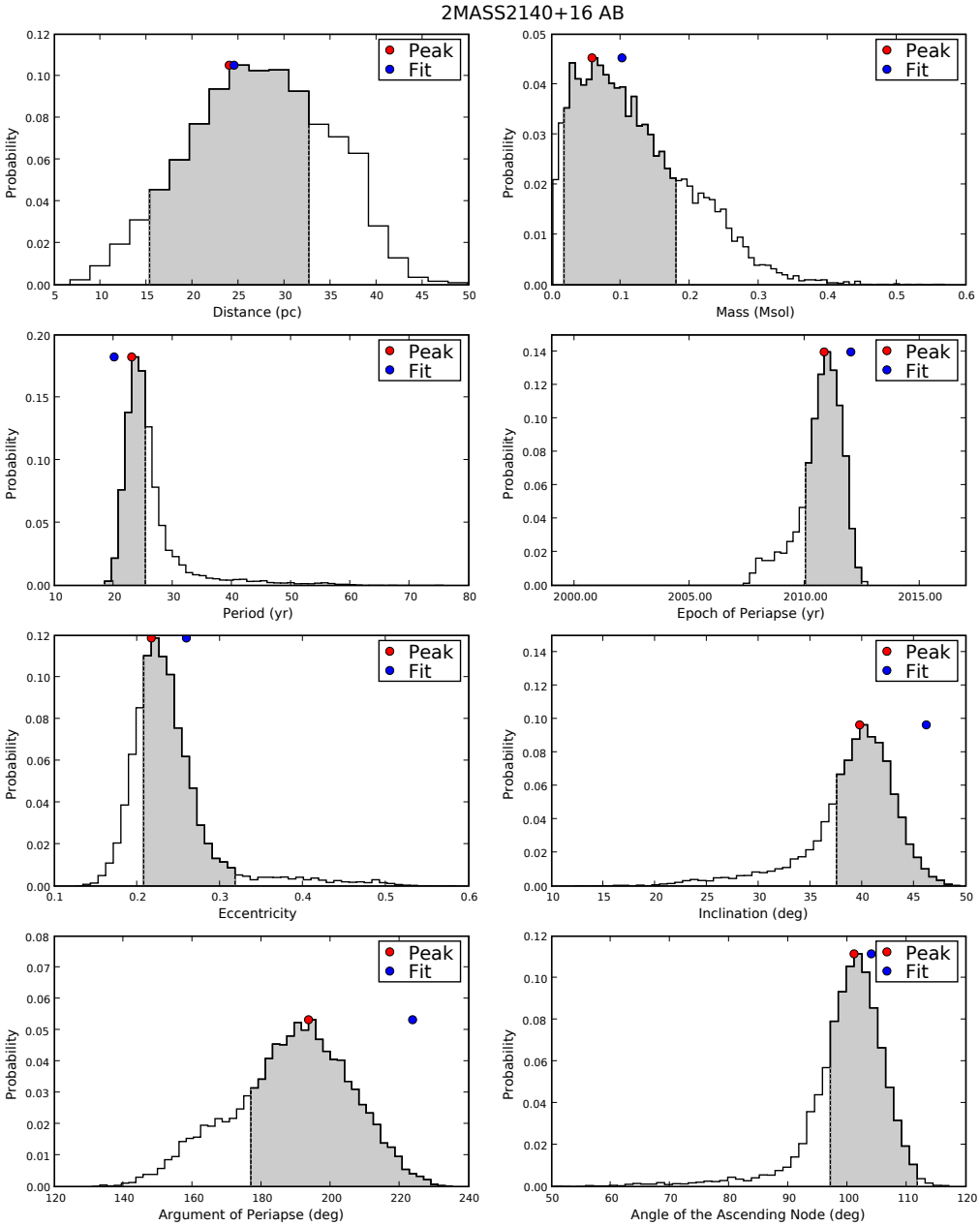

Figure 4.39 One-dimensional PDFs for the relative orbit (total system mass) of 2MASS 2140+16AB

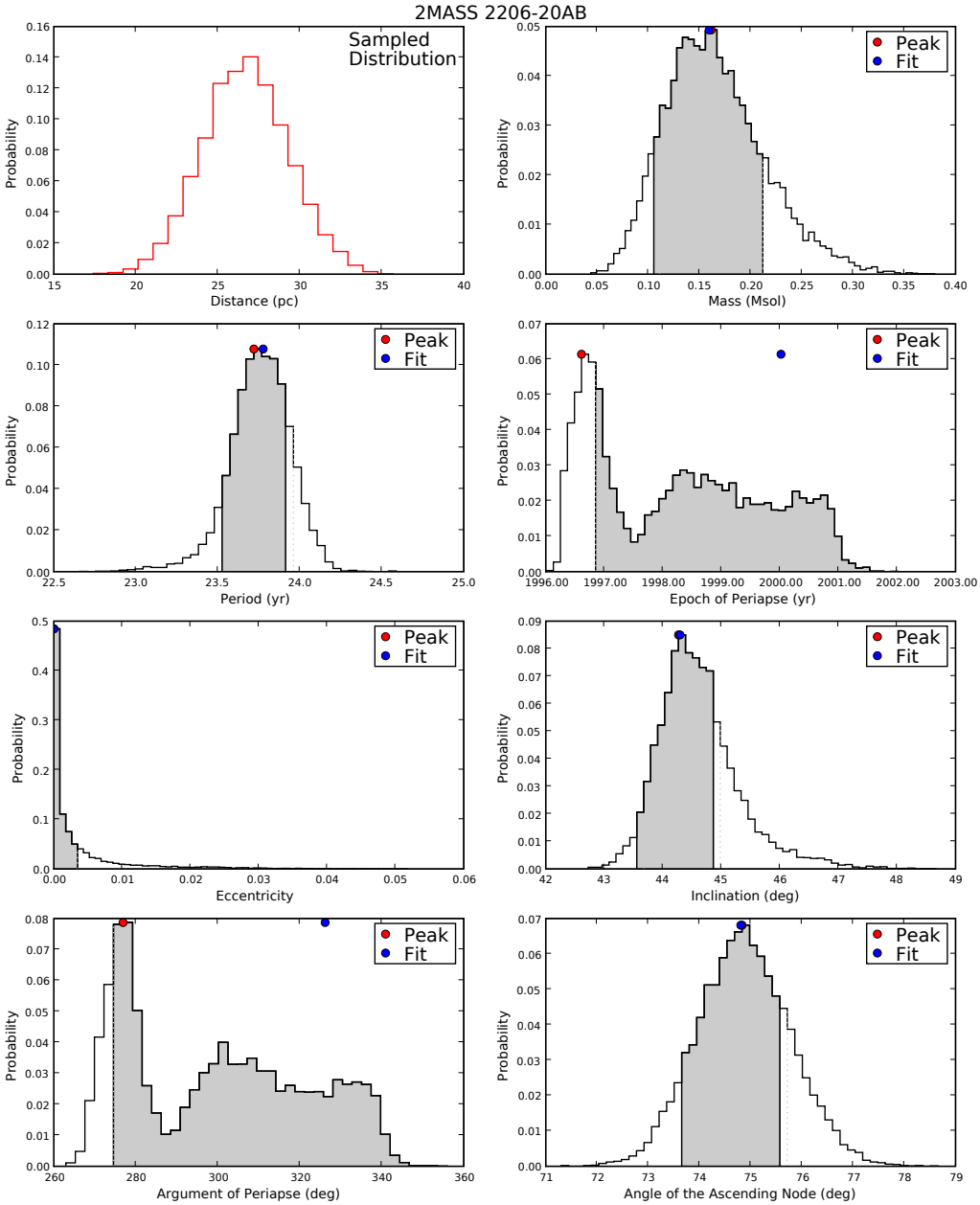

Figure 4.40 One-dimensional PDFs for the relative orbit (total system mass) of 2MASS 2206-20AB

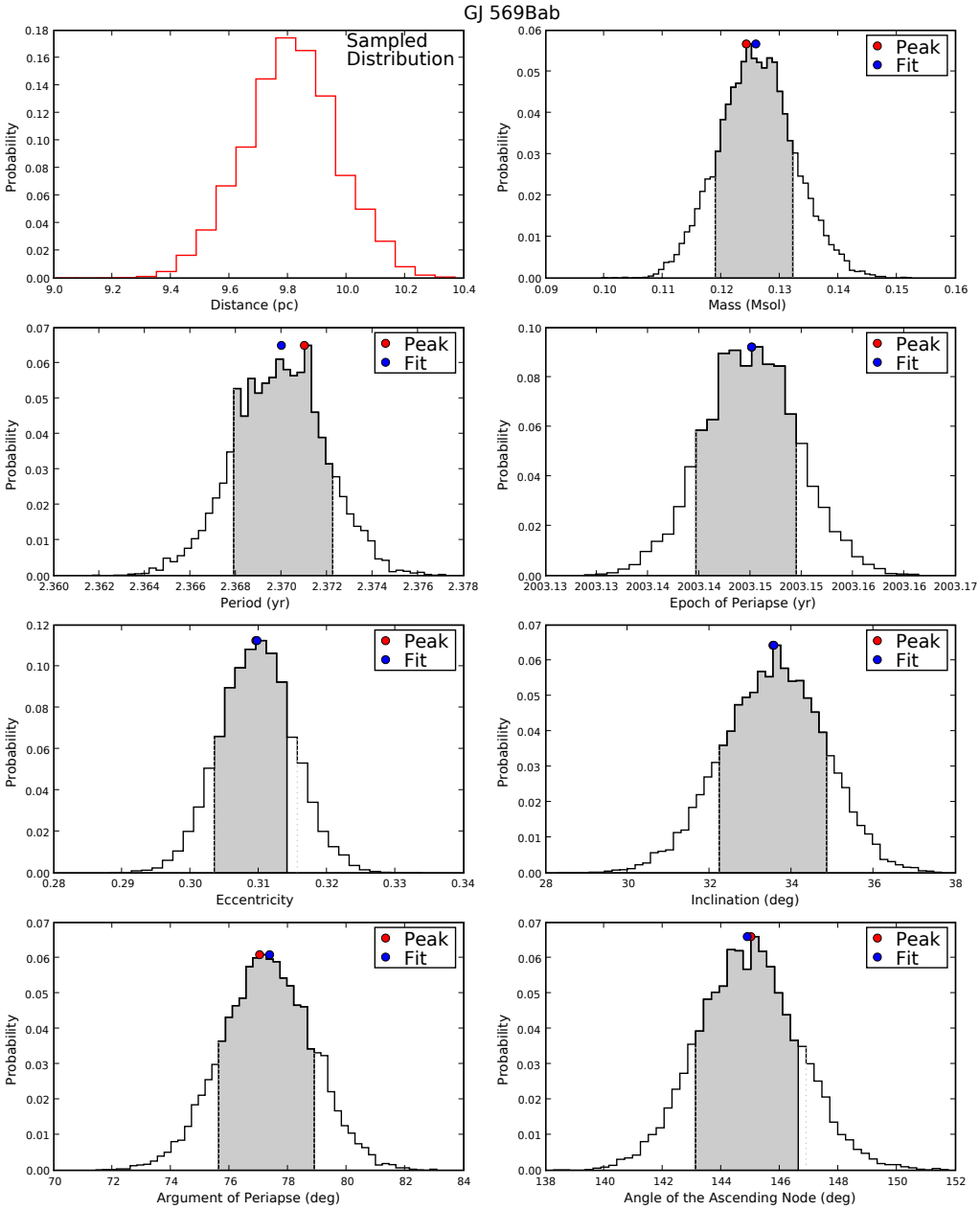

Figure 4.41 One-dimensional PDFs for the relative orbit (total system mass) of GJ569Bab

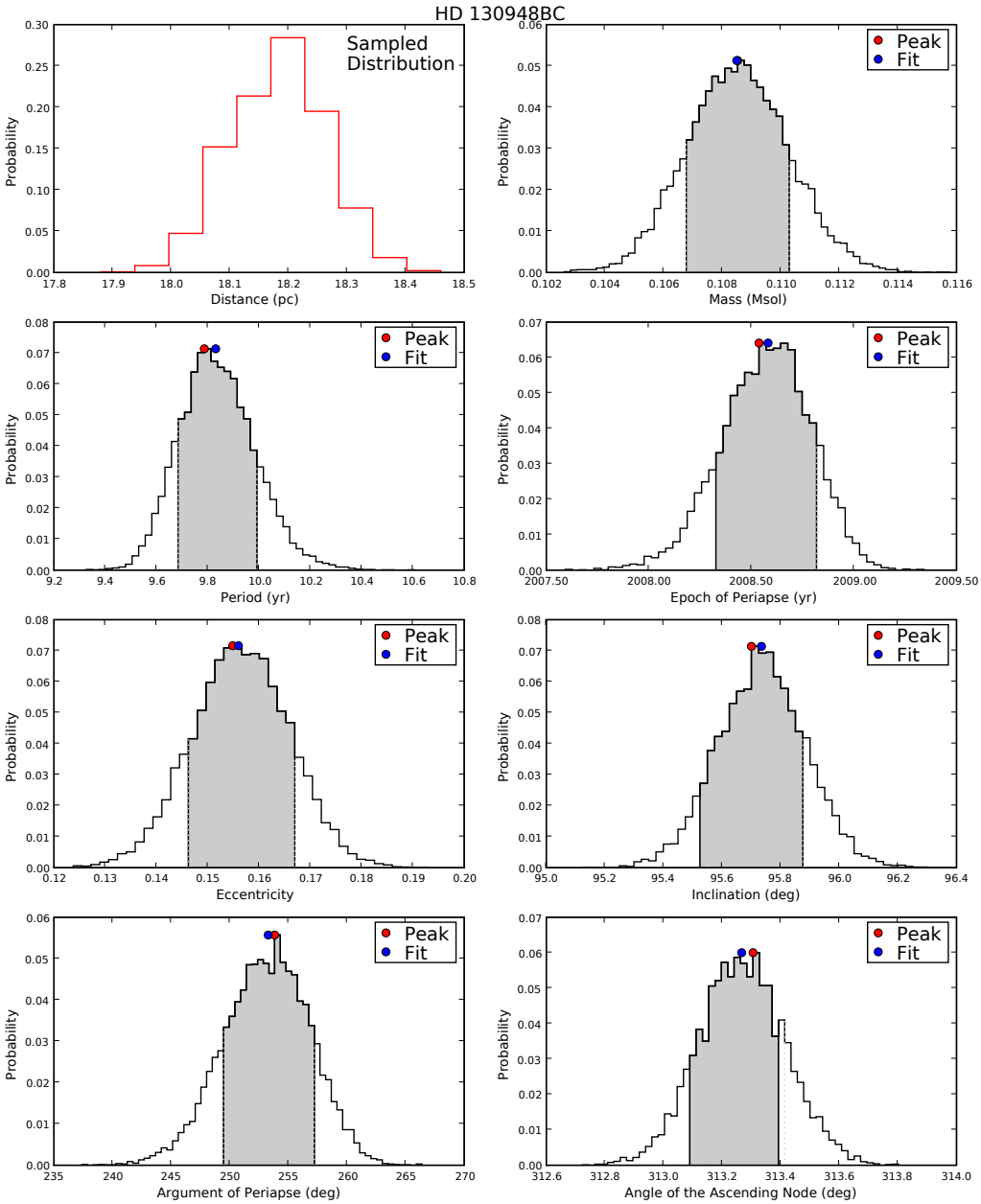

Figure 4.42 One-dimensional PDFs for the relative orbit (total system mass) of HD 130948 BC

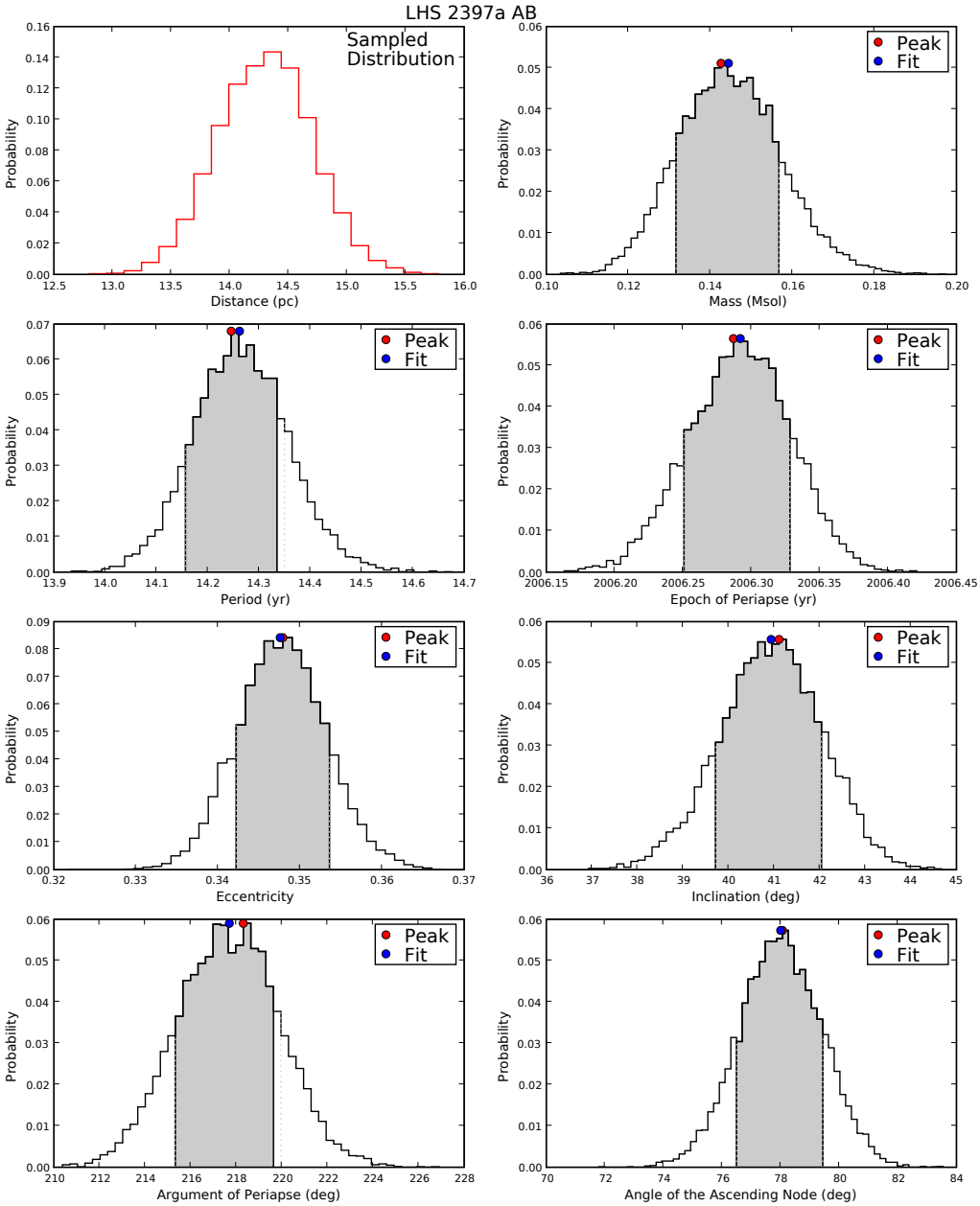

Figure 4.43 One-dimensional PDFs for the relative orbit (total system mass) of LHS 2397a BC

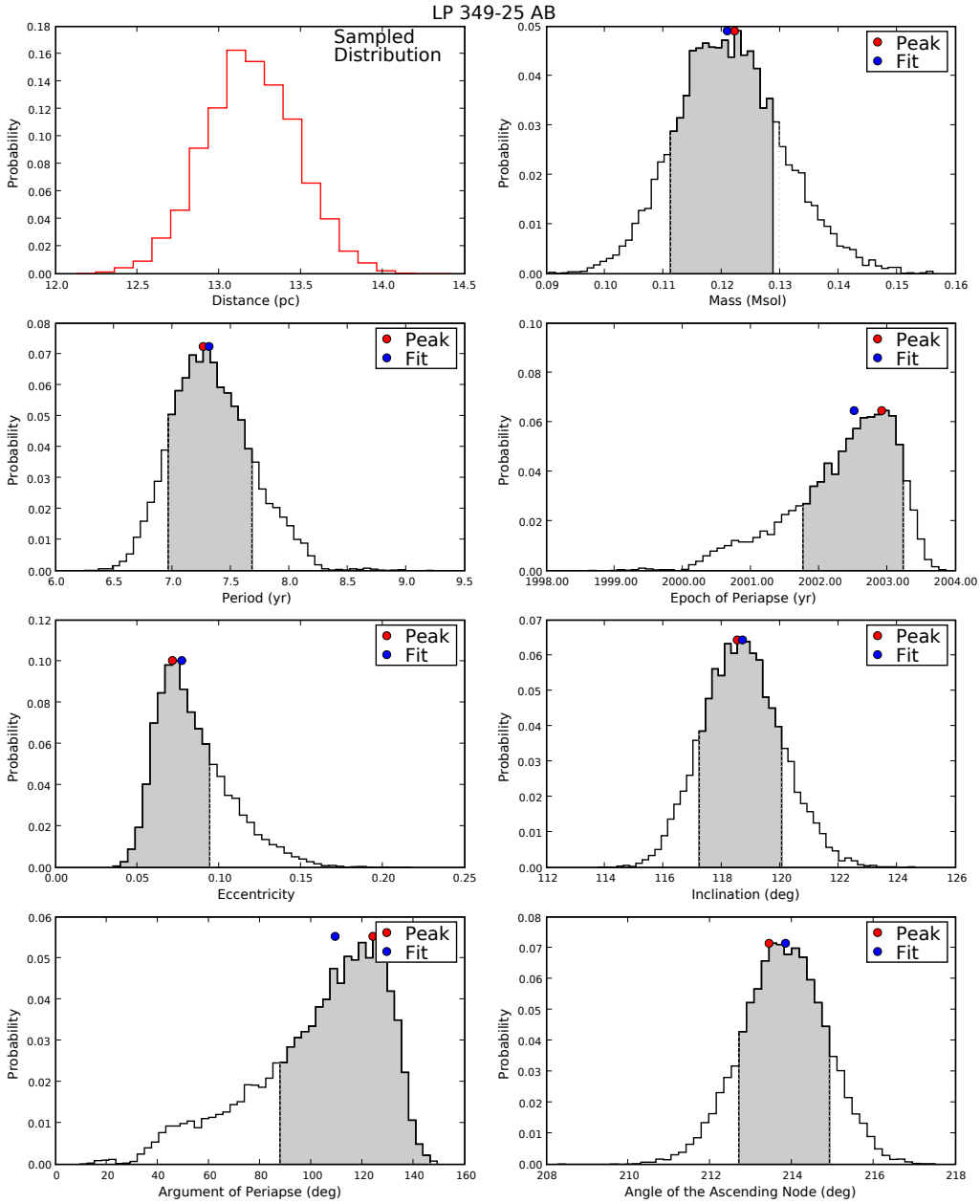

Figure 4.44 One-dimensional PDFs for the relative orbit (total system mass) of LP 349-25AB

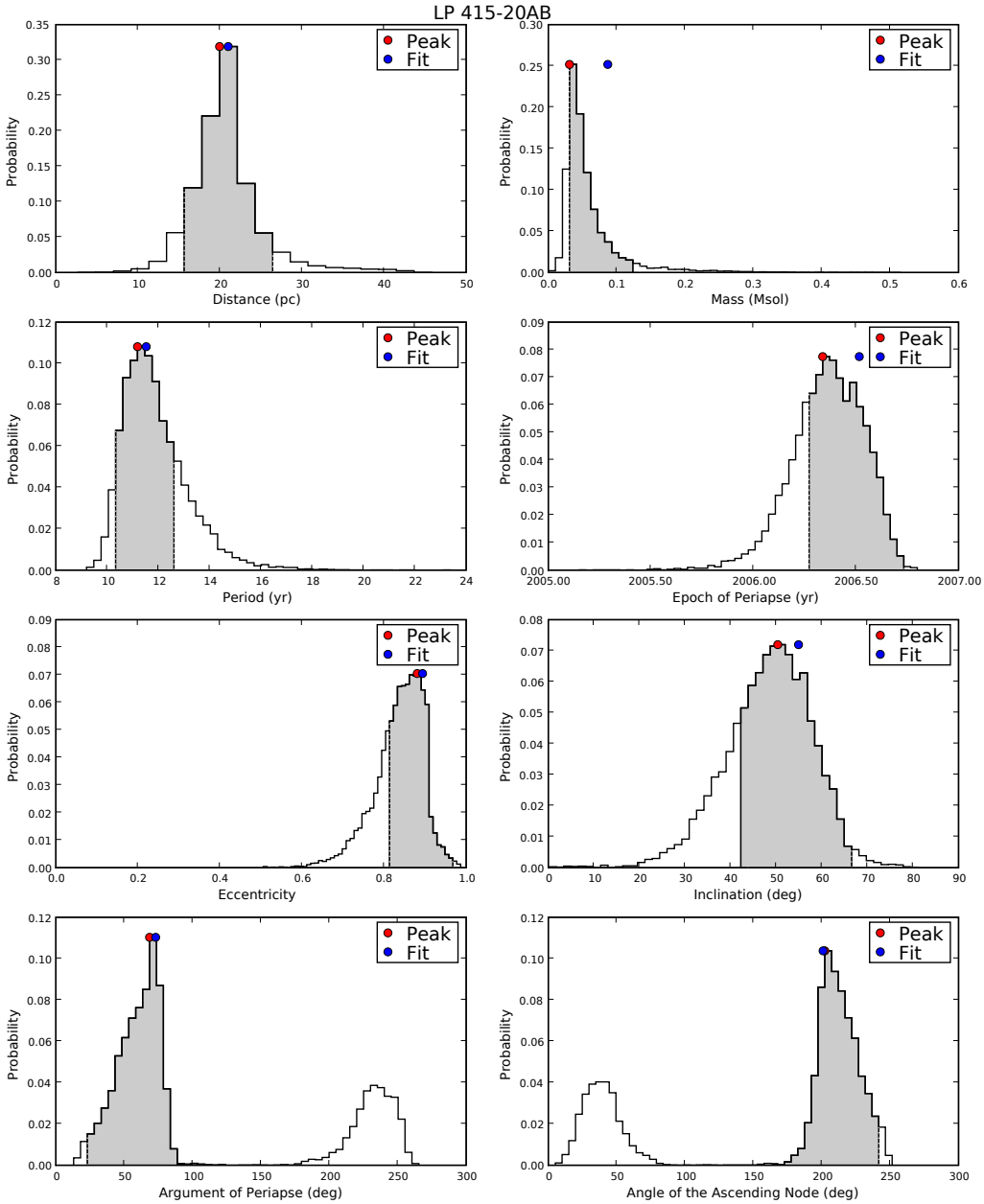

Figure 4.45 One-dimensional PDFs for the relative orbit (total system mass) of LP 415-20AB

4.4.2 Orbital Parameters from Absolute Motion

For 6 systems in our sample, sufficient absolute radial velocity measurements (at least 3) have been made and their relative orbits have been constrained enough to derive the first estimates of their absolute orbits, and hence the individual masses of the binary components. Common parameters between absolute and relative orbits, namely the P, T_o, e, and ω make it possible to only have to fit three free parameters: the semiamplitudes of the velocity curve for each component ($K_{Primary}$ and $K_{Secondary}$) and the systemic velocity (γ). We also have the additional constraint that $K_{Primary} + K_{Secondary} = 2\pi$ a sin$i$ / P $(1 - e^2)^{1/2}$. Since both inclination and semi-major axis are also constrained by the relative orbital solutions, this provides an additional constraint on the possible values of K, and hence the mass ratio, making it possible to eliminate $K_{Secondary}$ as a free parameter.

To first obtain the best fit solution for these parameters, we use our radial velocities from Table 4.6 and fix the values of P, a, T_o, e, i, and ω to perform a least-squares minimization between the equations for the spectroscopic orbit of each component and our data. We fully map χ^2 space (where in this case $\chi^2_{tot} = \chi^2_{Primary} + \chi^2_{Secondary}$) by first sampling randomly 100,000 times from a uniform distributions of $K_{Primary}$ and γ that are wide enough to allow mass ratios between 1 and 5 (where $M_{primary}$ / $M_{Secondary} = K_{Secondary}$ / $K_{Primary}$) for all sources except LHS 2397a AB, for which we allow for mass ratios between 1 and 10. This imposed range is validated based on the approximate spectral types of the components, none of which imply very large mass ratios for our binaries. Due to the larger difference in the spectral type of the components of LHS 2397a AB, we chose to be conservative and allow for the larger mass ratio range. Upon obtaining these initial χ^2 maps, we narrow our sampling range around the region

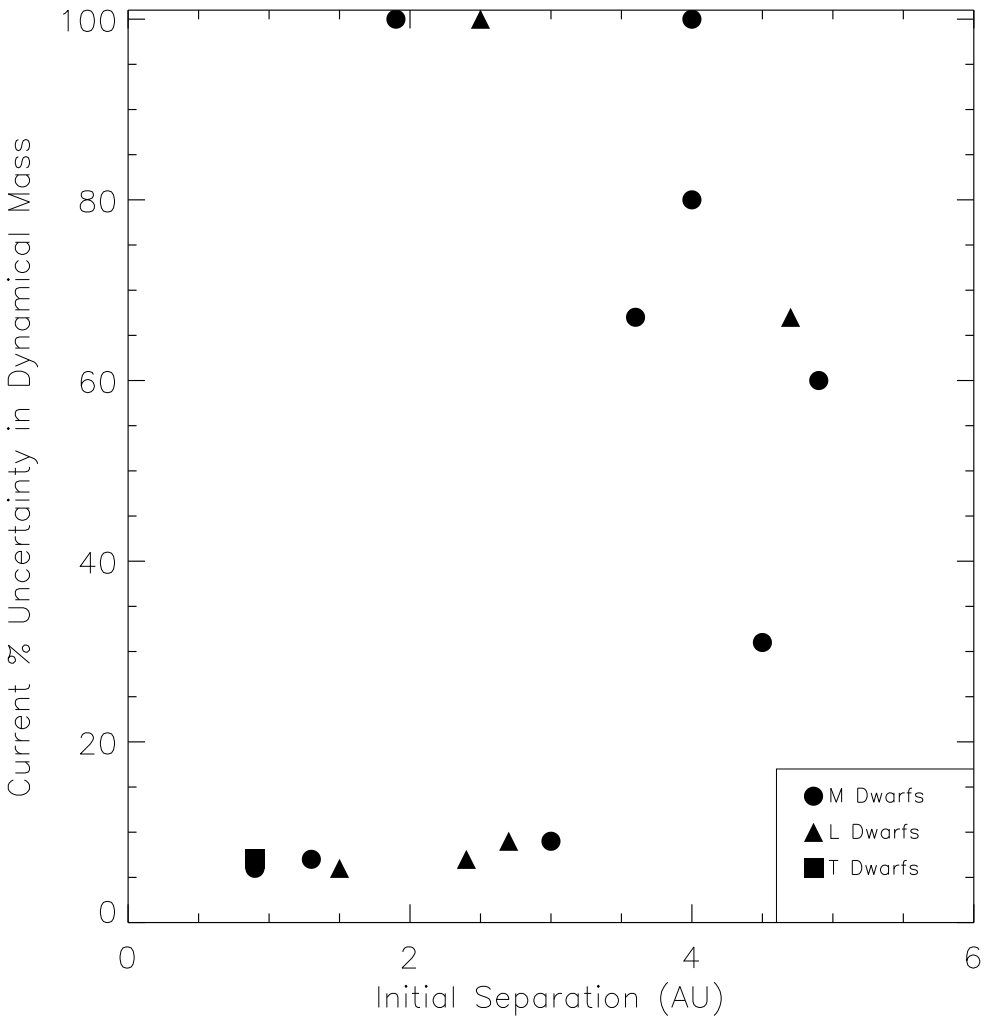

Figure 4.46 The total system mass precision plotted against the initial binary separation. About half of the systems for which we have derived masses did not reach this precision goal. This is likely due to either our assumption of a constant mass in the Monte Carlo, not allowing for a wide enough range of semimajor axes, or assuming too low an uncertainty in distance to the system.

of minimum χ^2, allowing for parameters within 3σ, based on $\Delta\chi^2$, of the original best fit. We again sample 100,000 times within this new range. This process is continued until we are satisfied that we have found the best fit parameters by fully mapping χ^2 space to enough precision that our best fit values do not change to within more than 1σ as determined by the range of parameters from fits with $\chi^2 \leq \chi^2_{BestFit} + 1$.

To determine the uncertainties on our fit parameters, we again perform a Monte Carlo simulation. We use the distributions of P, a, T_o, e, i, and ω derived from our astrometric orbit Monte Carlo as inputs into the fits to account for the uncertainty in these parameters. We also then resample our radial velocity measurements to generate 10000 artificial data sets such that the value of each point is assigned by randomly drawing from a Gaussian distribution centered on the true value with a width corresponding to the uncertainty on that value (as was done with the astrometric data). We then find the best fit solution for each of these data sets (coupled with the sampled parameters from the astrometric fits). As with the astrometric orbit, we find the uncertainties by marginalizing the resulting distribution of each parameter against all others and integrating the resulting one-dimensional distribution from the best fit out to a probability of 68%.

The resulting best-fit orbital parameters for the absolute motion and their uncertainties are given in Table 4.8. The absolute orbital solutions are drawn with the absolute radial velocity data in Figures 4.47-4.49 and the distributions of orbital parameters for all 6 sources are shown in Figures 4.50-4.55. By combining our mass ratio distribution derived with this data with the total system mass derived in Section 4.4.1, we have computed the first assumption-free estimates of the individual masses of the components for 5 of these 6 systems. These

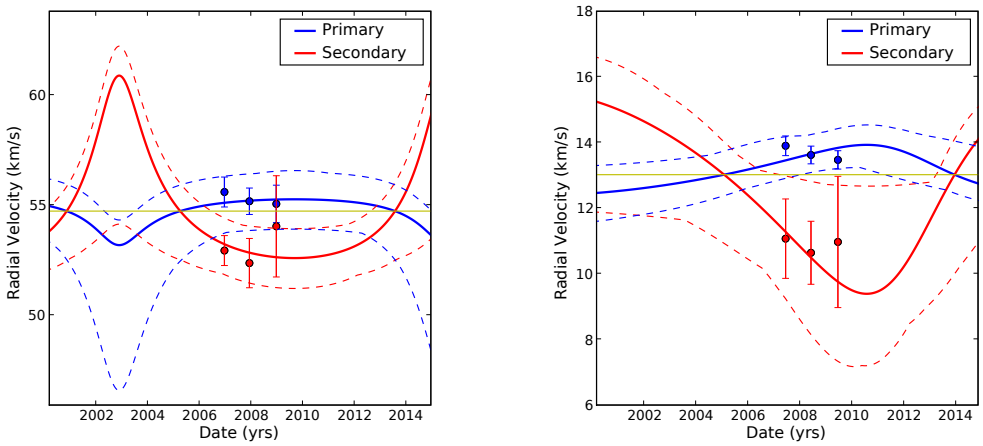

Figure 4.47 **Left:** Best fit absolute orbit for 2MASS 0746+20AB **Right:** Best fit absolute orbit for 2MASS 2140+16AB. Absolute radial velocity data points overplotted with the best fit orbits for both components. The green line represents the best fit systemic velocity. The dotted lines represent the 1σ allowed ranges of radial velocity at a given time.

individual masses are given in Table 4.8.

Table 4.8. Absolute Orbital Parameters

	Fit Parameters			Derived Properties			
Target Name	$K_{Primary}$ (km/s)	Center of Mass Velocity (km/s)	Best Fit Reduced χ^2	$K_{Secondary}$ (km/s)	Mass Ratio ($M_{Primary}$ / $M_{Secondary}$)	$M_{Primary}$ ($M_\odot$)	$M_{Secondary}$ ($M_\odot$)
2MASS 0746+20AB	$1.0^{+3.0}_{-0.1}$	54.7 ± 0.8	0.44	$4.1^{+0.1}_{-3.1}$	4.0 ± 0.1	$0.12^{+0.01}_{-0.09}$	$0.03^{+0.09}_{-0.01}$
2MASS 2140+16AB	0.8 ± 0.3	13.0 ± 0.2	0.9	3.1 ± 1.1	$4.0^{+0}_{-0.1}$	0.08 ± 0.06	$0.02^{+0.08}_{-0.02}$[a]
2MASS 2206-20AB	0.8 ± 0.2	13.3 ±0.2	2.2	3.1 ± 0.4	$4.0^{+0.0}_{-0.2}$	0.13 ± 0.05	$0.03^{+0.07}_{-0.02}$[a]
GJ 569b AB	2.7 ± 0.3	-8.0 ± 0.2[b]	0.56	3.8 ± 0.4	1.4 ± 0.3	0.073 ± 0.008	0.053 ± 0.006
LHS 2397a AB	1.7 ± 1.2	34.6 ± 1.4	0.41	2.6 ± 1.4	$1.5^{+7.1}_{-1.4}$	0.09 ± 0.05	0.06 ± 0.05
LP 349-25 AB	4.5 ± 0.9	-8.0 ± 0.5	0.8	2.2 ± 0.9	0.5 ± 0.3	0.04 ± 0.02	0.08 ± 0.02

Note. — Using our absolute radial velocities in conjunction with the parameters from our relative orbital solutions, we fit for $K_{Primary}$ and γ. We then use those values to find $K_{Secondary}$ and the mass ratio. We combine the mass ratio and the total system mass from the relative orbits to find component masses.

[a]Upper uncertainty set using the uncertainty in $M_{Primary}$ and M_{Tot}

[b]Set to our value

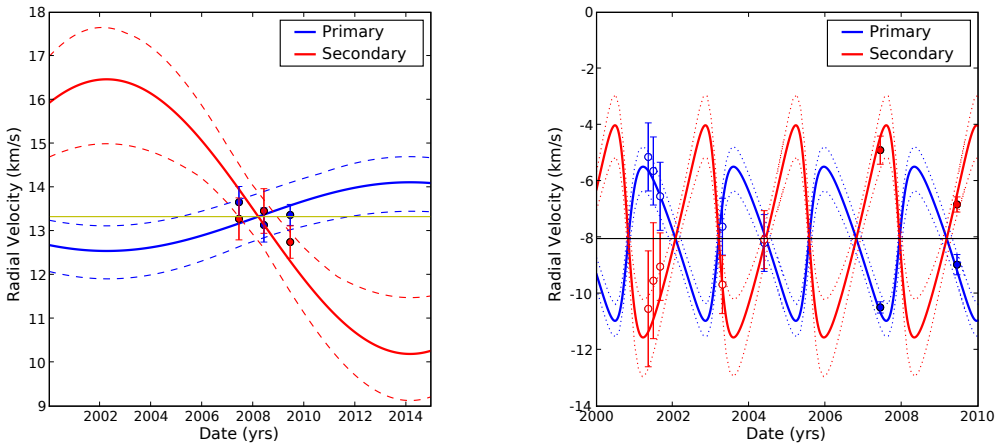

Figure 4.48 **Left:** Best fit absolute orbit for 2MASS 2206-20AB **Right:** Best fit absolute orbit for GJ 569Bab. Radial velocity data from the literature for this system is taken from Zapatero Osorio et al. (2004) and Simon et al. (2005). See section 4.4.3.6 for a discussion of systematic offsets between the radial velocity measurements from each work. Absolute radial velocity data points overplotted with the best fit orbits for both components. The green line represents the best fit systemic velocity. The dotted lines represent the 1σ allowed ranges of radial velocity at a given time.

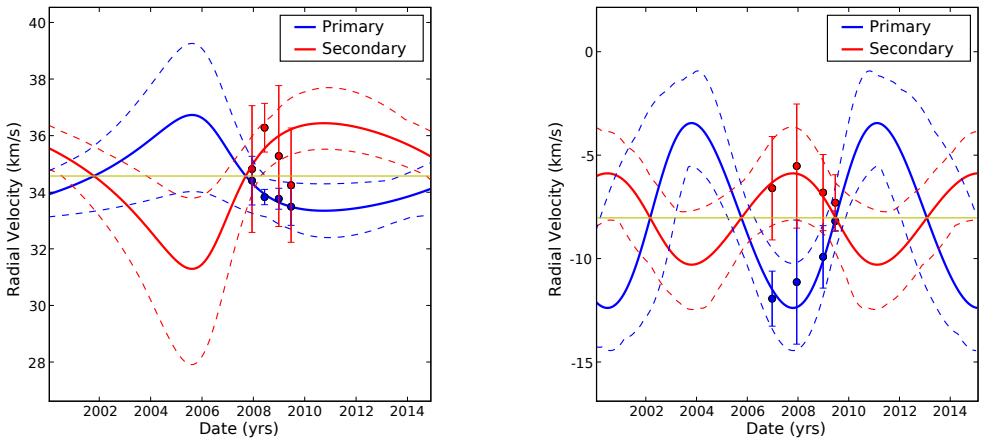

Figure 4.49 **Left:** Best fit absolute orbit for LHS 2397a AB **Right:** Best fit absolute orbit for LP 349-25 AB. Absolute radial velocity data points overplotted with the best fit orbits for both components. The green line represents the best fit systemic velocity. The dotted lines represent the 1σ allowed ranges of radial velocity at a given time.

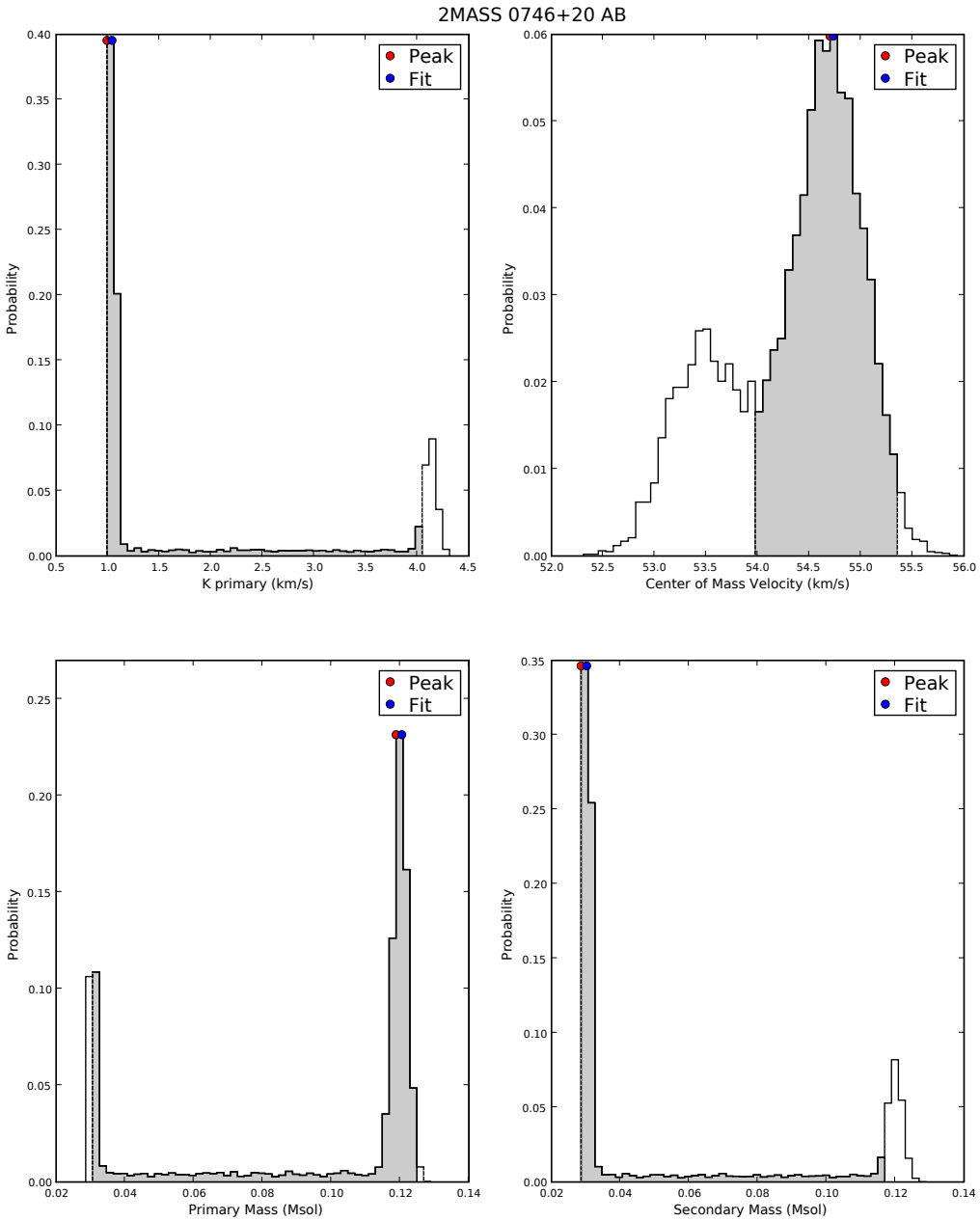

Figure 4.50 One-dimensional PDFs for the absolute orbit of 2MASS 0746+20AB. Fit parameters are $K_{Primary}$ and γ (top panels). The distributions for parameters in common between this orbit and the relative orbit, namely P, e, T_o, and ω, are shown above in Figure 4.31. From $K_{Primary}$ and γ, $K_{Secondary}$ is calculated, giving the mass ratio, which we use in conjunction with the total system mass to derive component masses (bottom panels)

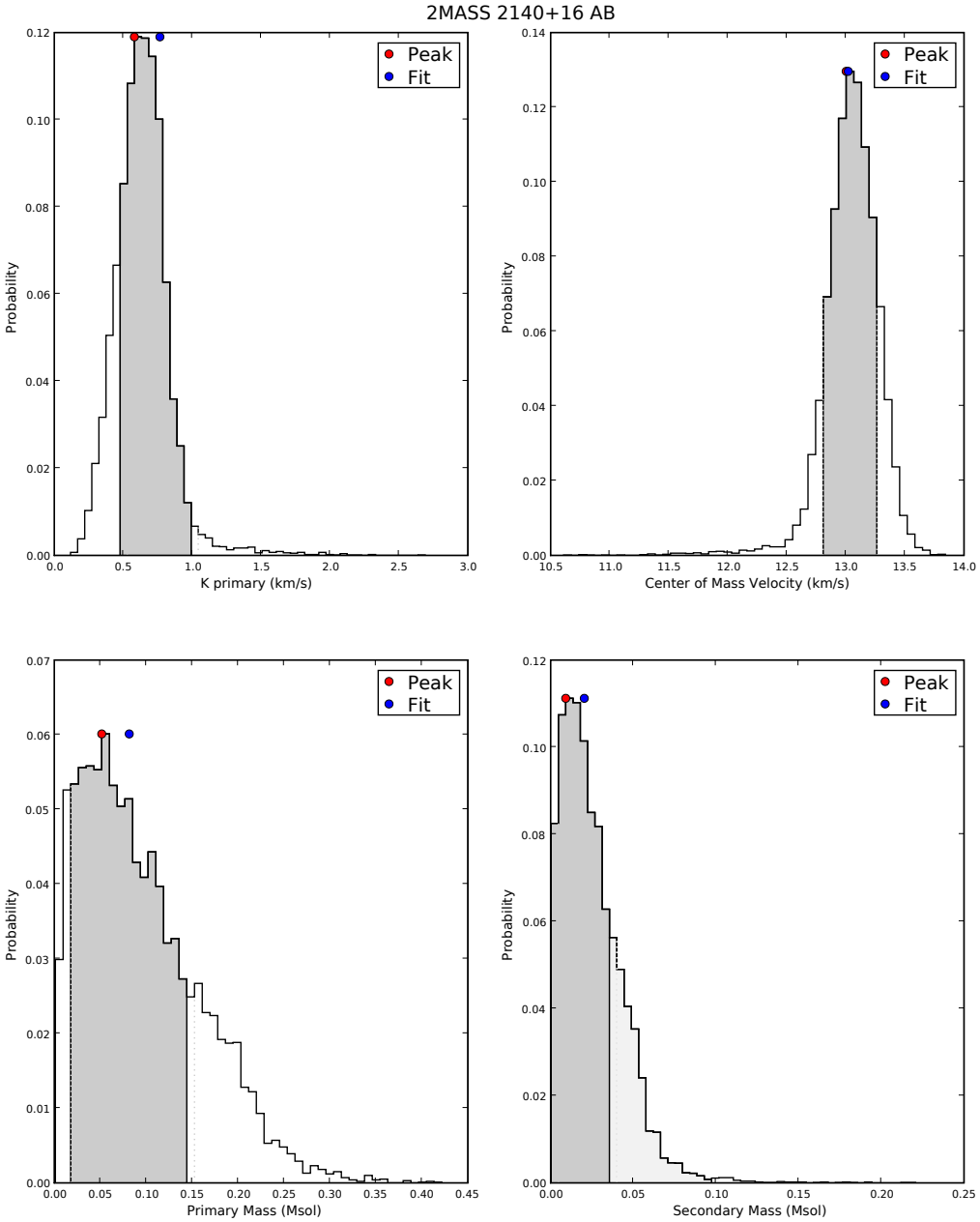

Figure 4.51 One-dimensional PDFs for the absolute orbit of 2MASS 2140+16AB. Fit parameters are $K_{Primary}$ and γ (top panels). The distributions for parameters in common between this orbit and the relative orbit, namely P, e, T_o, and ω, are shown above in Figure 4.39. From $K_{Primary}$ and γ, $K_{Secondary}$ is calculated, giving the mass ratio, which we use in conjunction with the total system mass to derive component masses (bottom panels)

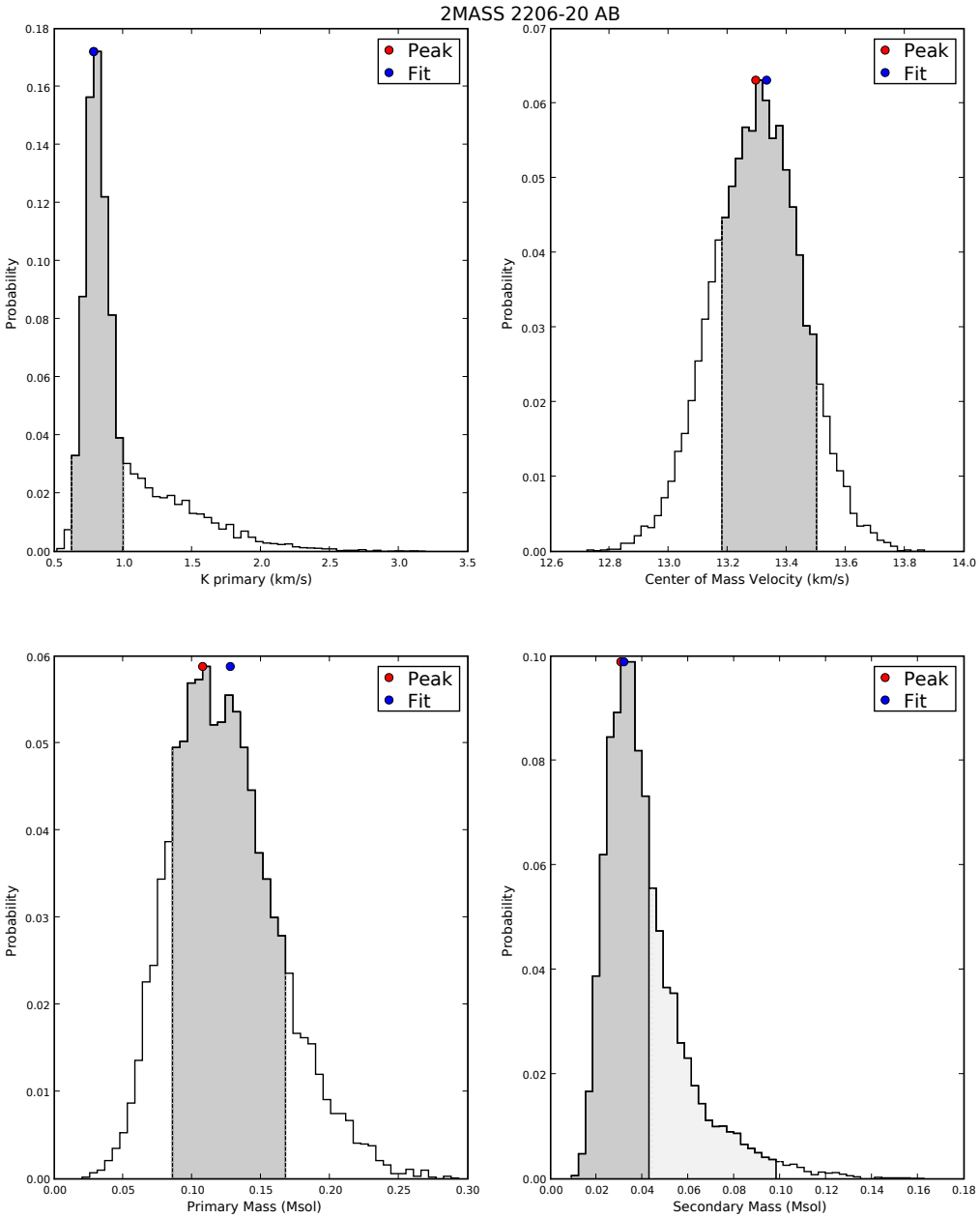

Figure 4.52 One-dimensional PDFs for the absolute orbit of 2MASS 2206-20AB. Fit parameters are $K_{Primary}$ and γ (top panels). The distributions for parameters in common between this orbit and the relative orbit, namely P, e, T_o, and ω, are shown above in Figure 4.40. From $K_{Primary}$ and γ, $K_{Secondary}$ is calculated, giving the mass ratio, which we use in conjunction with the total system mass to derive component masses (bottom panels)

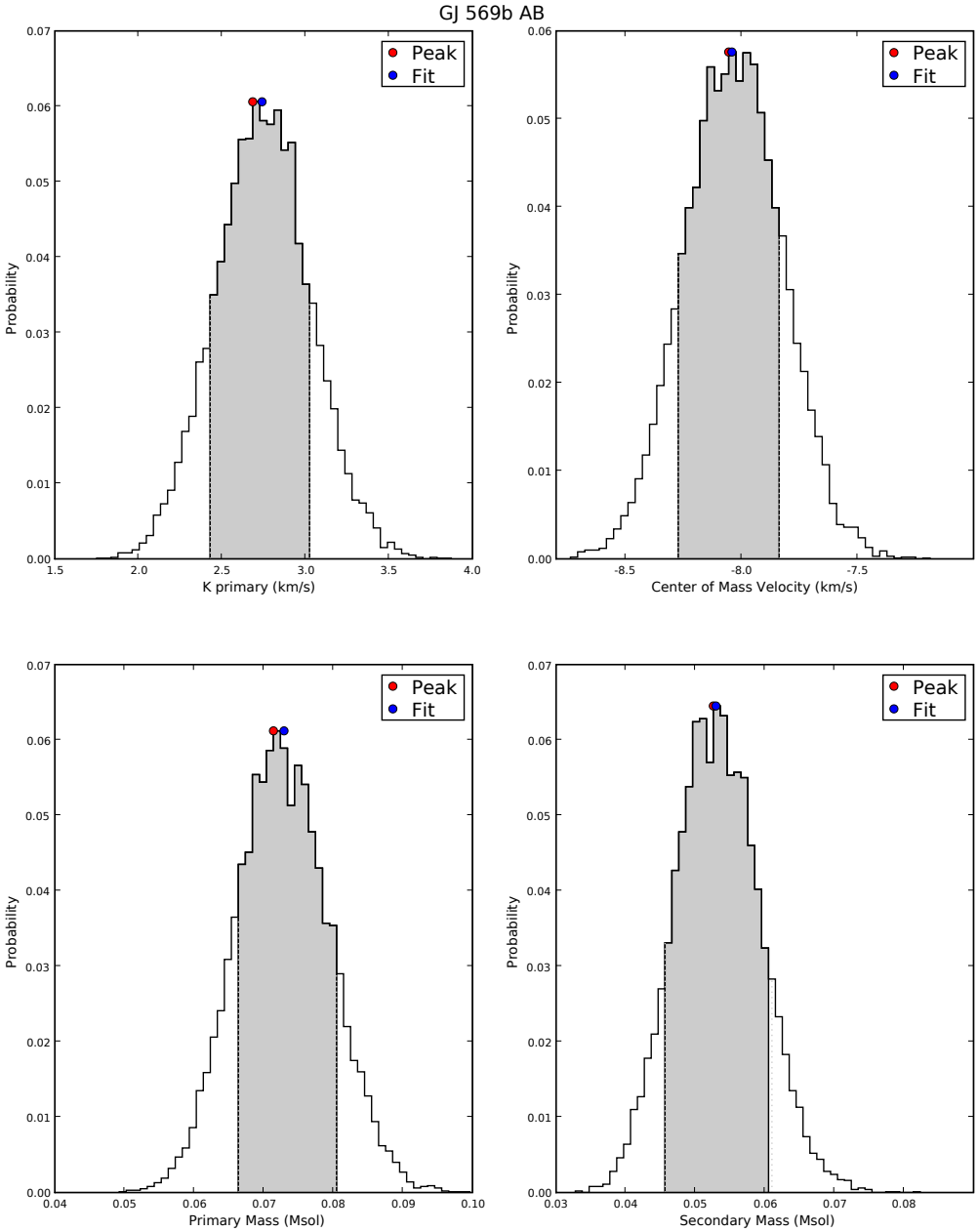

Figure 4.53 One-dimensional PDFs for the absolute orbit of GJ 569Bab. Fit parameters are $K_{Primary}$ and γ (top panels). The distributions for parameters in common between this orbit and the relative orbit, namely P, e, T_o, and ω, are shown above in Figure 4.41. From $K_{Primary}$ and γ, $K_{Secondary}$ is calculated, giving the mass ratio, which we use in conjunction with the total system mass to derive component masses (bottom panels)

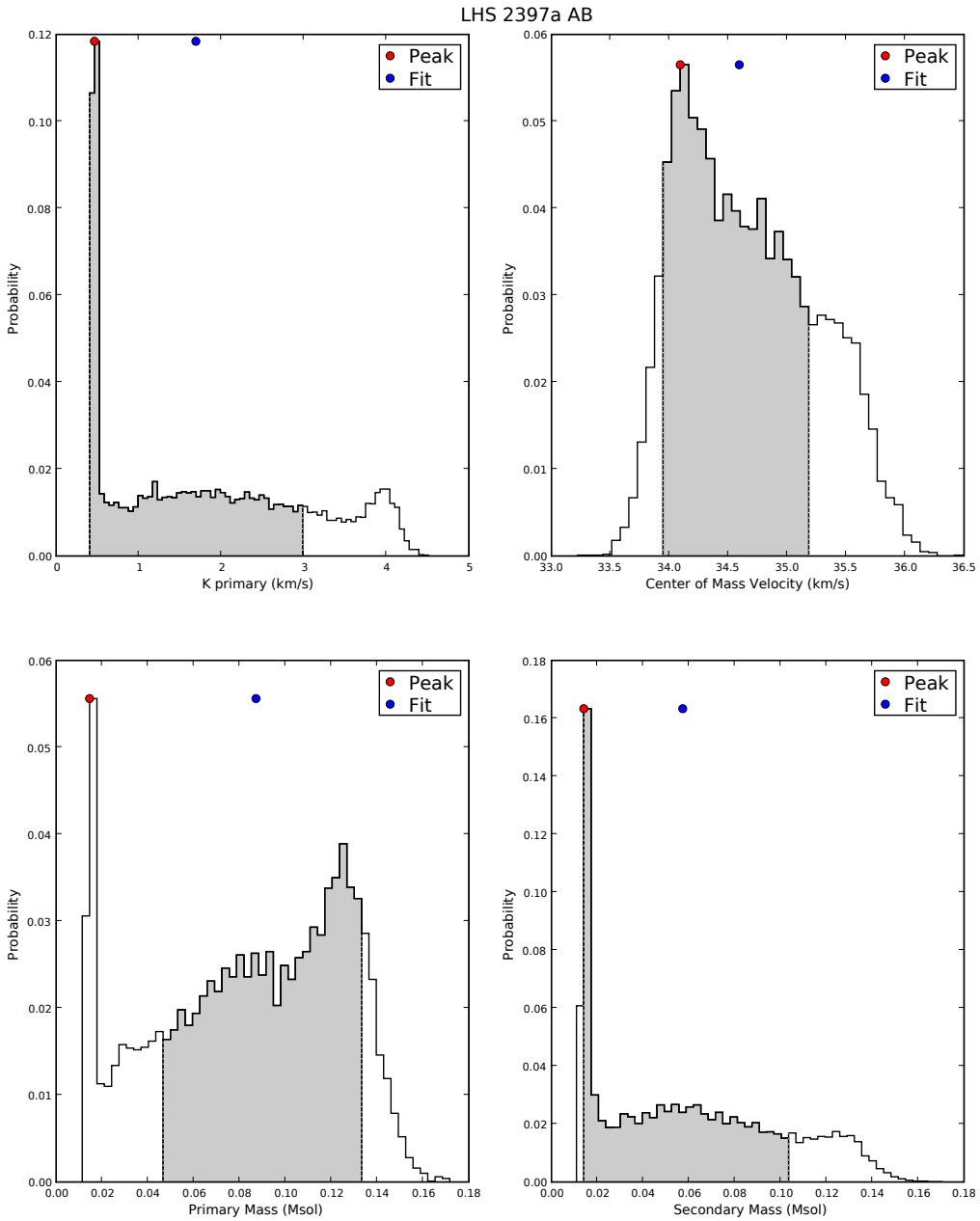

Figure 4.54 One-dimensional PDFs for the absolute orbit of LHS 2397a AB. Fit parameters are $K_{Primary}$ and γ (top panels). The distributions for parameters in common between this orbit and the relative orbit, namely P, e, T_o, and ω, are shown above in Figure 4.43. From $K_{Primary}$ and γ, $K_{Secondary}$ is calculated, giving the mass ratio, which we use in conjunction with the total system mass to derive component masses (bottom panels)

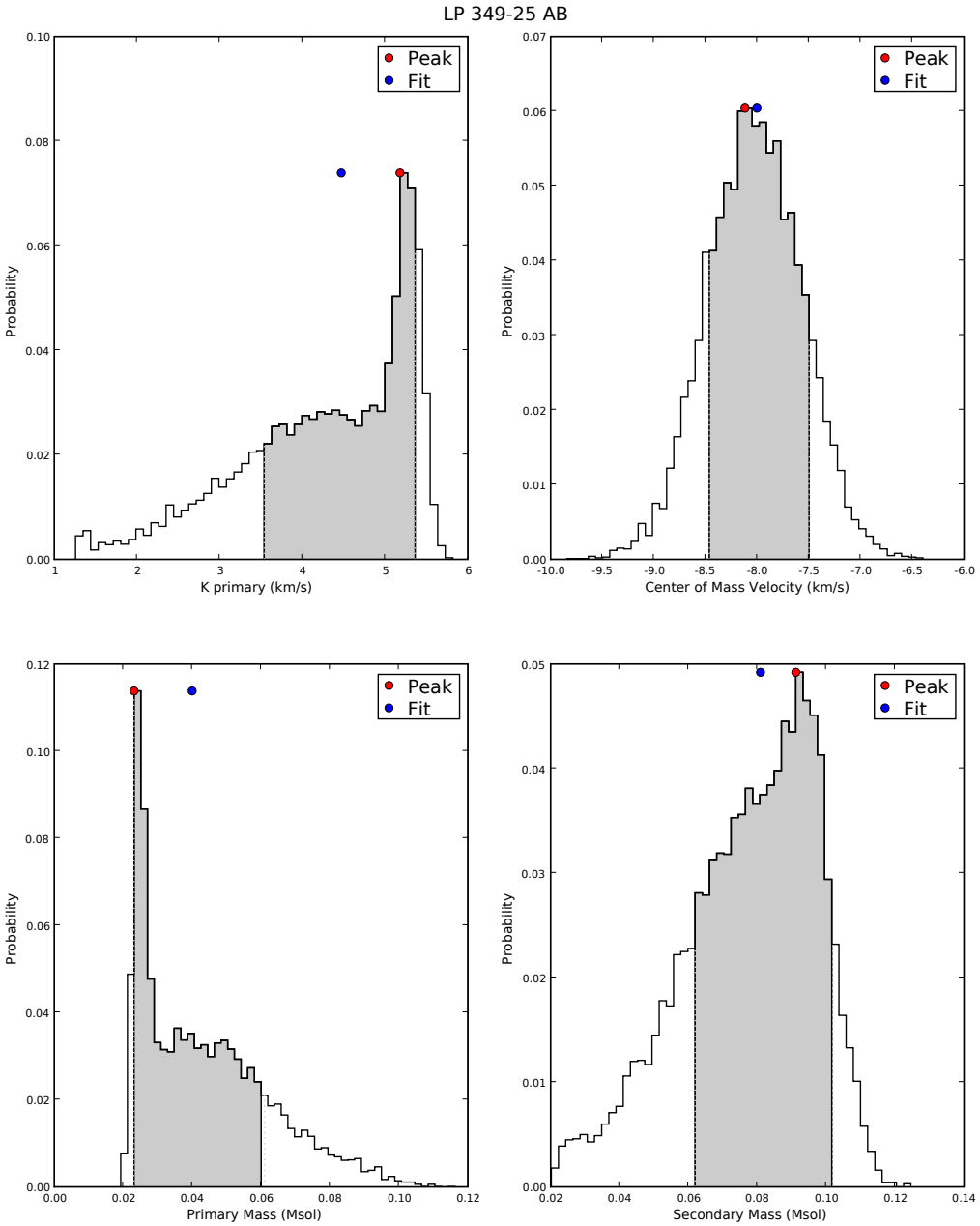

Figure 4.55 One-dimensional PDFs for the absolute orbit of LP 349-25 AB. Fit parameters are $K_{Primary}$ and γ (top panels). The distributions for parameters in common between this orbit and the relative orbit, namely P, e, T_o, and ω, are shown above in Figure 4.44. From $K_{Primary}$ and γ, $K_{Secondary}$ is calculated, giving the mass ratio, which we use in conjunction with the total system mass to derive component masses (bottom panels)

4.4.3 Individual System Remarks

4.4.3.1 2MASS 0746+20AB

2MASS 0746+20 AB originally had its total system mass derived by Bouy et al. (2004). Those authors found a total mass of $0.146^{+0.016}_{-0.006}$ $M_{\odot}$. Our new astrometric and radial velocity data has allowed us to improve this total mass estimate by a factor of 4 to 0.151 $\pm$ 0.003 $M_{\odot}$, or to a precision of 2%. This measurement represents the most precise mass estimate for a VLM binary yet determined. Our individual mass estimates are the first for this system and the first for a binary L dwarf.

4.4.3.2 2MASS 0850+10AB

2MASS 0850+10 AB has two independent measurements of its distance via parallax. The first was from Dahn et al. (2002), 25.6 $\pm$ 2.5 pc and the second was from Vrba et al. (2004), 38.1 $\pm$ 7.3 pc. These values are about 1.5σ discrepant from each other, a fact noted by Vrba et al. (2004), although those authors did not know the cause of this discrepancy. We performed a full Monte Carlo analysis as described in section 4.4.1 using both estimates for distance, which effects the total mass in the relative orbit fit. We choose to present the values of mass as derived from the Vrba et al. (2004) distance estimate here because it has larger uncertainties. Since the current uncertainties in the period and semimajor axis for this system are large, the impact of choosing one distance over the other is negligible.

4.4.3.3 2MASS 0920+35AB

2MASS 0920+35 AB was discovered to be binary by Reid et al. (2001) using HST. A follow-up monitoring campaign of the system was performed by Bouy et al. (2008) using both HST and the VLT in conjunction with their facility AO system. In each of the five observations performed by Bouy et al. (2008), the system was unresolved. These authors postulated that the binary was therefore perhaps on a highly inclined orbit with a period of roughly 7.2 years. When our monitoring of the system began in 2006, the system was again resolved, and remained resolved for all of our measurements until our most recent one in 2009 June. We therefore utilize both the resolved and unresolved measurements to perform our orbit fits. First, we fit the resolved astrometric measurements for relative orbital parameter solutions as described in Section 4.4.1. We then took the output orbital solutions for those trials and calculated predicted separation of the binary at each of the epochs in which it was unresolved - if the predicted separation was above the detection limits given by Bouy et al. (2008) or our 2009 June 10 measurement, it was thrown out. These unresolved measurements therefore provided tighter constraints on the orbital parameters for this system.

The results of the Monte Carlo simulation for this system are shown in Figure 4.33. As shown in this figure, the resulting distribution of periods has a strong bifurcation, whereby ∼45% of the solutions favor an orbital period of ∼3.3 years and a very high eccentricity, and 55% favor the best fit solution of ∼6.7 years and more modest eccentricities. Since these solutions are nearly equally preferred but quite distinct, we display the best fit of both solution families in Figure 4.18, with the shorter period solution plotted in green. The two solution sets cause the current mass uncertainty to be fairly high. However, an additional astrometric measurement before mid-2010 should distinguish between the two sets, as it will

not be resolved for periods of ∼6.7 years but it will be resolved for periods of ∼3.3 years. Further, we have found the inclination of this system to be nearly edge on, meaning it has a non-negligible chance of being an eclipsing system (see section 4.8).

4.4.3.4 2MASS 1534-29AB

The first derivation of the orbit of 2MASS 1534-29AB was performed by Liu et al. (2008), where they calculated a total system mass of 0.056 ± 0.003 $M_{\odot}$. By combining our astrometry with that reported by Liu et al. (2008), we find a slightly higher, but consistent, total system mass of 0.060 ± 0.004 $M_{\odot}$. We note that if we perform our analysis on only the astrometry given in Liu et al. (2008), we obtain a mass of 0.056 ± 0.004 $M_{\odot}$, which is a slightly higher uncertainty than what is reported in that work.

4.4.3.5 2MASS 2140+16AB and 2MASS 2206-20AB

We have acquired sufficient radial velocity data to make the first calculations of the absolute orbits of these systems. However, the uncertainty in the radial velocities is comparable to the distance between the values. Because of this, the best fit is typically the one that minimizes $K_{Primary}$, which in turn maximizes $K_{Secondary}$. This leads to mass relatively high predicted mass ratios. Though there is some spread in the value of mass ratio, as shown in Figures 4.51 and 4.52, the mass ratio is quite peaked at this high value. This leads not only to mass values for the secondary that are likely too low given their approximate spectral types, but also uncertainties that are too small for the secondary given the uncertainty in the mass of the primary. For these two systems, we therefore extend the uncertainty in the secondary mass by combining in quadrature the

uncertainty in the total system mass and the uncertainty in the mass of the primary component. We have noted that we have taken this approach in Table 4.8, and have shaded the histograms in Figures 4.51 and 4.52 to reflect our chosen uncertainties. Though these first estimates of individual mass are fairly uncertain, they will improve with continued monitoring of these systems.

4.4.3.6 GJ 569Bab

The first derivation of the relative orbit of GJ 569Bab was performed by Lane et al. (2001), and was followed with improvements by Zapatero Osorio et al. (2004) and Simon et al. (2006). The work of Zapatero Osorio et al. (2004) and Simon et al. (2006) also contained spatially resolved, high resolution spectroscopy measurements for this systems, which is one of two targets in our sample that is an NGS AO target. Zapatero Osorio et al. (2004) derived the first estimate of the individual component masses of this system using their J band spectroscopic measurements. Simon et al. (2006) made their radial velocity measurements in the H band and noted that their derived center of mass velocity (-8.50 $\pm$ 0.30 km/s) is discrepant from that of Zapatero Osorio et al. (2004, -11.52 $\pm$ 0.45 km/s) by $\sim$3 km/s. Simon et al. (2006) postulate that this stems from the choice of lines used to make their measurements. Zapatero Osorio et al. (2004) use the K I doublet location referenced to laboratory wavelengths while Simon et al. (2006) perform cross-correlation of their full order 48 (λ = 1.58 - 1.60 μm) and 49 (λ = 1.55 - 1.57 μm) spectra with spectral templates. Simon et al. (2006) also note that the relative radial velocities are consistent with what is predicted based on astrometry.

We now note that our spectra, measured in the K band and fit for radial velocity as described in Section 4.3.2, appear to be systematically offset from

both the measurements of Zapatero Osorio et al. (2004) and Simon et al. (2006). We find a center of mass velocity using just our data points of -8.05 ± 0.20 km/s, which is the most consistent of the three sets of measurements with that of the M2V primary of this tertiary system (-7.2 ± 0.2 km/s). We find, as shown in Figure 4.26, that the relative velocities are consistent with what is expected for the relative orbit. Thus the velocity differences truly seem to be driven by an offset in their absolute value. It is possible that these velocity offsets may be related to the orbit of this binary around GJ 569A. To examine whether this is the case, we plot the measured systemic velocity by each of the three studies versus the median date of observation. This is shown in Figure 4.56. While the difference between our measurement and that of Simon et al. (2006) could be consistent with orbital motion around GJ 569A, the large acceleration in radial velocity implied between the Zapatero-Osorio et al. (2004) measurement and the other two points is likely too large to be caused by orbital motion. For GJ 569Bab, which is separated by ∼50 AU from GJ 569A, to have a radial velocity change of ∼2 km/s between 2004 and 2001 would require an orbital eccentricity of >0.99 and a date of periapse passage between 2001 and 2005, an unlikely configuration. Thus, the difference here is likely due to the absolute radial velocity calibration issues described in Simon et al. (2006).

In order to use all the radial velocity measurements to calculate individual masses, we opt to shift all data points from Zapatero-Osorio et al. (2004) and Simon et al. (2006) such that their center of mass velocity is consistent with ours. We also increase the uncertainties in these values such that they incorporate the uncertainties in our value of systemic velocity and in the systemic velocity derived in each work, which we combine in quadrature. We then use these shifted velocities in conjunction with our measurements to derive the absolute orbit, which is shown in Figure 4.48. The application of this offset results in a very nice

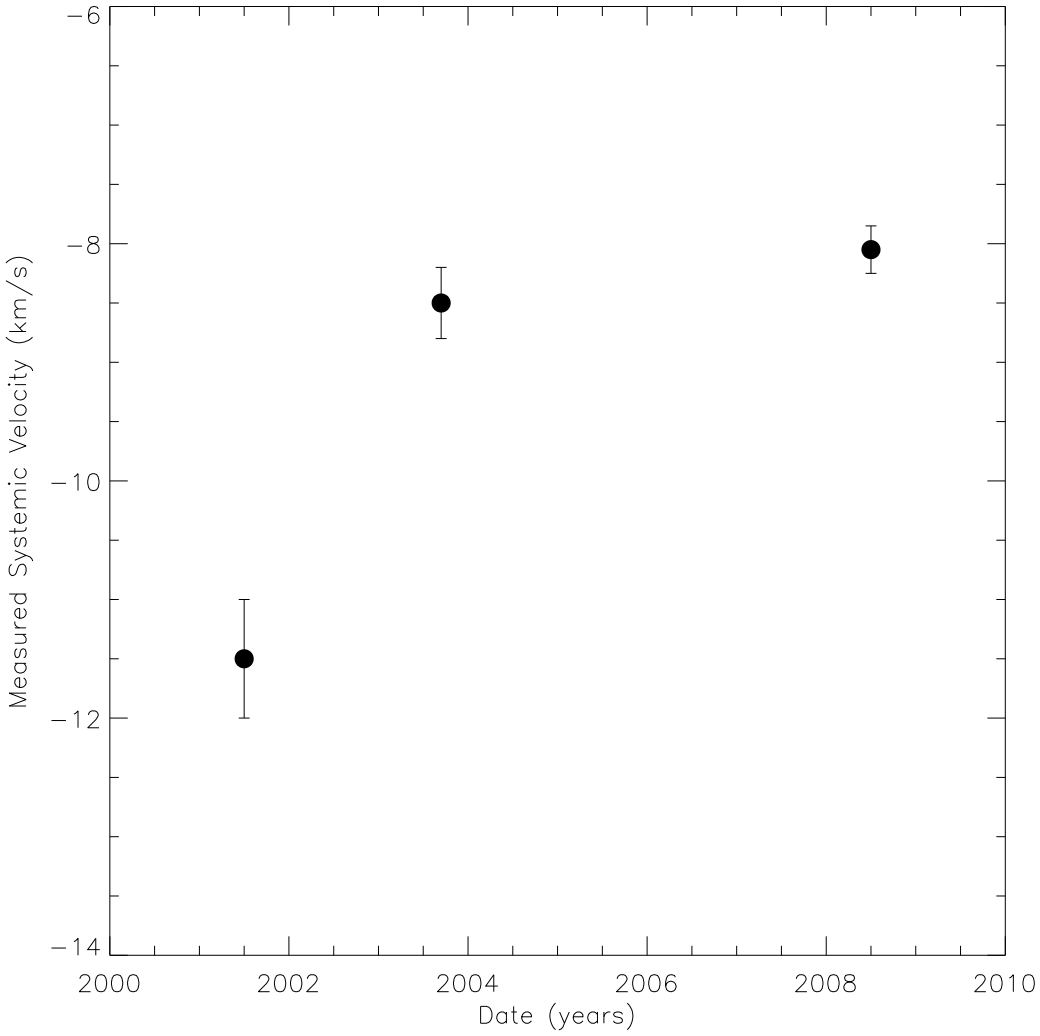

Figure 4.56 The measured systemic velocities from Zapatero-Osorio et al. (2004), Simon et al. (2006), and this study, as a function of the median time of observation. Because this source is a wide companion to GJ 569A, an M star, it is expected to undergo some change in velocity due to its orbit around GJ 569A. While the difference in our systemic velocity with respect to that of Simon et al. (2006) could be consistent with this, the Zapatero-Osorio et al. (2004) is likely too discrepant to be caused by this orbital motion.

fit with a reduced χ^2 of 0.56. We find a mass ratio of 1.4 $\pm$ 0.3, which is lower than the value of 5.25 found by Simon et al. (2006). Those authors postulated that since the mass of the primary appeared to be so much higher than that of the secondary, that the primary may be a binary itself (something potentially suggested by the wider lines seen in GJ 569Ba). Our values of primary and secondary mass suggest that the sources actually have fairly similar masses of 0.073 $\pm$ 0.008 $M_\odot$ and 0.053 $\pm$ 0.006 $M_\odot$. We cannot, however, definitively rule out that GJ 569Ba is comprised of two components, as suggested Simon et al. (2006), although this possibility is more unlikely given that we find the mass of GJ 569Ba to be lower than those authors found.

4.4.3.7 HD 130948BC

The first derivation of the relative orbit of HD 130948BC was performed by Dupuy et al. (2009a), where they calculated a total system mass of 0.109 $\pm$ 0.003 $M_\odot$. By combining our astrometry with that reported by Dupuy et al. (2009a), we find an identical, but slightly more precise, total system mass of 0.109 $\pm$ 0.002 $M_\odot$. Although we only have one radial velocity measurement for this system, which is insufficient to calculate individual masses for the components, our radial velocity measurement allows us to resolve the degeneracy in the values of ω and Ω.

4.4.3.8 LHS 2397a AB

The first derivation of the relative orbit of LHS 2397a AB was performed by Dupuy et al. (2009b), where they calculated a total system mass of $0.146^{+0.015}_{-0.013}$ $M_\odot$. Combining our astrometry with that reported by Dupuy et al. (2009b), we also find a consistent total mass of $0.144^{+0.013}_{-0.012}$ $M_\odot$. Performing our analysis on

just the astrometry given in Dupuy et al. (2009b), we find a slightly different, but consistent, mass of $0.150^{+0.014}_{-0.013}$. Dupuy et al. (2009b) also use their results in conjunction with a bolometric luminosity and the evolutionary models (both Burrows et al. (1997) and Chabrier et al. (2000)) to derive the individual component masses. Here we derive the first individual mass estimates free of assumptions, which allows for a direct comparison to the models. We find component masses of 0.09 ± 0.06 $M_{\odot}$ for the primary and 0.06 ± 0.05 $M_{\odot}$ for the secondary. The well-mapped velocity curve of the primary allows for this absolute orbit to be relatively well-defined with a comparable number of radial velocity measurements to other sources that do not yet have well-defined absolute orbits.

4.5 Bolometric Luminosity and Effective Temperature Derivation

In order to compare the predictions of theoretical evolutionary models to our dynamical mass measurements, estimates of both the effective temperature and bolometric luminosity are required. With input of these parameters, the evolutionary models can be used to derive a mass and an age for a source. Thus, we must derive these parameters for all binary components.

Our method for deriving both of these quantities relies on the spatially resolved photometry we have obtained with our imaging data. In our NIRC2 data, we have measured the flux ratio of the binary components in the J, H, and K' bands, given in Table 4.5. We convert these flux ratios into individual apparent magnitudes using the unresolved photometry for these sources from 2MASS (Cutri et al. 2003). The apparent magnitudes can then be converted into absolute magnitudes using the distances from Table 4.7. We also find the absolute

magnitudes for each system in all other photometric bands for which spatially resolved measurements exist. The majority of these measurements were made in the optical with HST. The absolute photometry for all sources is given in Table 4.9. References are given for photometry taken from the literature.

The determination of effective temperature for these sources is complex. Generally speaking, spectral type is not as accurate a proxy for the temperature of brown dwarfs as it is amongst hydrogen burning stars, with derived temperatures spanning several hundred Kelvin for different sources of the same spectral type (Leggett et al. 2002, Golimowski et al. 2004, Cushing et al. 2008). We therefore opt to perform spectral synthesis modeling using atmospheric models on each source individually, which allows for lower temperature uncertainties for most objects than would be achieved by using a temperature vs. spectral type relationship. Though this introduces a model assumption into our comparison of these sources to evolutionary models, we can use our mass estimates to determine the consistency of the atmospheric and evolutionary models with each other. For our sources of late M to L spectral types, we derive effective temperature using the DUSTY form of the PHOENIX atmosphere models (Hauschildt et al. 1999). These models, in which all refractory elements present in the atmospheres of these objects are assumed to form dust grains, enveloping the synthetic atmosphere in thick dust clouds, have been shown to reproduce the colors and spectra of these types of objects quite well. Updated opacities and grain size distributions have improved the correspondence of these models to observations (Barman et al. in prep, Rice et al. 2009). Among the 30 sources in our dynamical mass sample, 21 have late M to early L spectral types for which the DUSTY models are appropriate. For the two sources in our sample of mid-T spectral type, we use the COND version of the PHOENIX atmosphere models, which have been shown to reproduce the colors and spectra of T dwarfs well. In these models, all refractory

elements have been removed from the atmosphere through an unspecified "rain out process", resulting in dust free atmospheres and blue near infrared colors.

Since temperature can be the most effectively constrained by comparing synthetic atmosphere data over a broad range in wavelengths, we elect to use our spatially resolved photometry to perform the spectral synthesis modeling. Very high resolution versions of the DUSTY models and the wavelength and bandpass information for each of our photometric measurements in Table 4.9 were used to generate a grid of synthetic photometry for objects with T_{Eff} = 1400 - 4500 K for DUSTY and T_{Eff} = 300 - 3000 K for COND, with log g = 4.0 - 5.5. This range of surface gravity should be appropriate for all sources in our sample (McGovern et al. 2004, Rice et al. 2009). We then use this grid to fit the measured photometry for each source, allowing for interpolation between finite grid points. Because the flux values in the grid are defined at the surface of the source, they must be scaled by the radius of the source - thus, we also fit for the radius as a scaling factor. Uncertainties in the derived temperature and radius are then calculated via Monte Carlo simulation, in which 10000 new photometric data points are generated by sampling from a Gaussian distribution centered on each apparent magnitude with a width given by the uncertainty in each magnitude. The apparent magnitudes are then converted to absolute magnitudes using a distance sampled from a Gaussian distribution centered on the values given in Table 4.7 These datapoints are then fit in the same manner, and confidence limits on effective temperature and radius are then calculated by integrating our resulting one-dimensional distribution from the best fit out to a probability of 68%. The best fit SEDs from the atmosphere models are shown overplotted on the photometry for each source in Figures 4.60 through 4.71. The one dimensional PDFs for temperature and radius are show in Figures 4.72 through 4.83. Although surface gravity is also allowed to vary, we do not have sufficient photometric precision

to distinguish between values of surface gravity for these field binaries, and the distributions of surface gravity are essentially flat. In Figure 4.57, we plot our derived effective temperatures as a function of spectral type. The scatter seen amongst the data points stresses the intrinsic scatter in effective temperature with spectral type for these objects. We combine the results of Golimowski et al. (2004), Cushing et al. (2008), and Luhman et al. (2003) to demonstrate previous measures of temperature versus spectral type. This relationship is plotted in red on Figure 4.57, along with error bars representing the range of allowed values by these works. This comparison demonstrates that in the cases where our photometry is well-constrained, the temperatures we derive using atmospheric modeling have much lower uncertainties than we would be able to obtain using spectral type.

Because we have a derived temperature and radius, we can also calculate the PHOENIX model predicted bolometric luminosity. However, this would also generate a model-dependence in our value of luminosity. Instead, we elect to determine bolometric luminosity using the K band bolometric corrections provided by Golimowski et al. (2004). These corrections are a function of spectral type and were derived using sources with photometric measurements over a broad range of wavelengths, integrating under their calculated light curves. The only assumption required to use these corrections is that spectral type is a good proxy for K-band bolometric corrections. In contrast to predicted effective temperature, the change in the K band bolometric correction with spectral type is quite gradual with lower scatter. In addition, Liu et al. (2008) and Dupuy et al. (2009b) showed that by deriving bolometric luminosities through light curve integration of four sources, they obtain values fully consistent with those they would have obtained using the bolometric corrections of Golimowski et al. (2004). To be conservative, we assume an uncertainty in the spectral type of each source of ± 2

spectral subclasses to determine our uncertainty in bolometric correction. Even with this assumption, the bolometric correction uncertainty is never the limiting factor in our bolometric luminosity uncertainty (generally the uncertainty is dominated by the distance uncertainty). Our estimates of bolometric luminosity from using these bolometric corrections are given in Table 4.9. To demonstrate the correspondence between the luminosities calculated in this way and the luminosities predicted by the atmosphere models, we plot the values against each other in Figure 4.58. All points fall along the line of 1:1 correspondence (plotted in red). We therefore feel confident that our model-independent estimates of bolometric luminosity are appropriate for these sources.

In principle, our high resolution spectroscopy can also be used to calculate effective temperature. However, the narrow wavelength coverage in the near infrared provides relatively loose constraints on temperature, with many temperatures being allowed for by our K band spectra. We have, however, performed a few comparisons of our K band spectra to the same models we use for the photometric fitting and find that the results are consistent, with the photometry providing lower uncertainties than the spectroscopy. Ultimately, the best temperatures would be derived by fitting a combination of the photometry and the spectroscopy. However, such fitting has known challenges associate with how data is weighted (Cushing et al. 2008). In the future, we hope to perform fitting of this kind, combining all spectral data.

For the seven sources in our sample in the L/T transitions region, we must take a different approach to obtaining effective temperatures. The DUSTY and the COND models can be thought of as boundary conditions to the processes occurring in brown dwarf atmospheres, meaning each atmosphere is either fully dusty or completely dust free. There is no transitional dust phases represented

in the current versions of these models. Though we attempted to fit sources in this region via the method described above with both models, we obtained very high temperatures and unphysically small radii. Therefore averaging the predictions of the two models does not work. For these sources, we elect to use the bolometric luminosity of the source and assume a radius with a large uncertainty, chosen to conservatively span the values derived in our atmospheric model fitting (1.0 ± 0.3 R_{Jup}). A radius in this range is also what is expected for these objects theoretically. In Figure 4.59, we plot the radii from our fits as a function of spectral type. Although there is a lot of scatter in this relationship due to the mixed ages in our sample, the large uncertainty we have assumed for radii at the L/T transition region should account for this variation. The result of assuming a radius is higher temperature uncertainties for these objects. All derived temperatures and radii are given in Table 4.9.

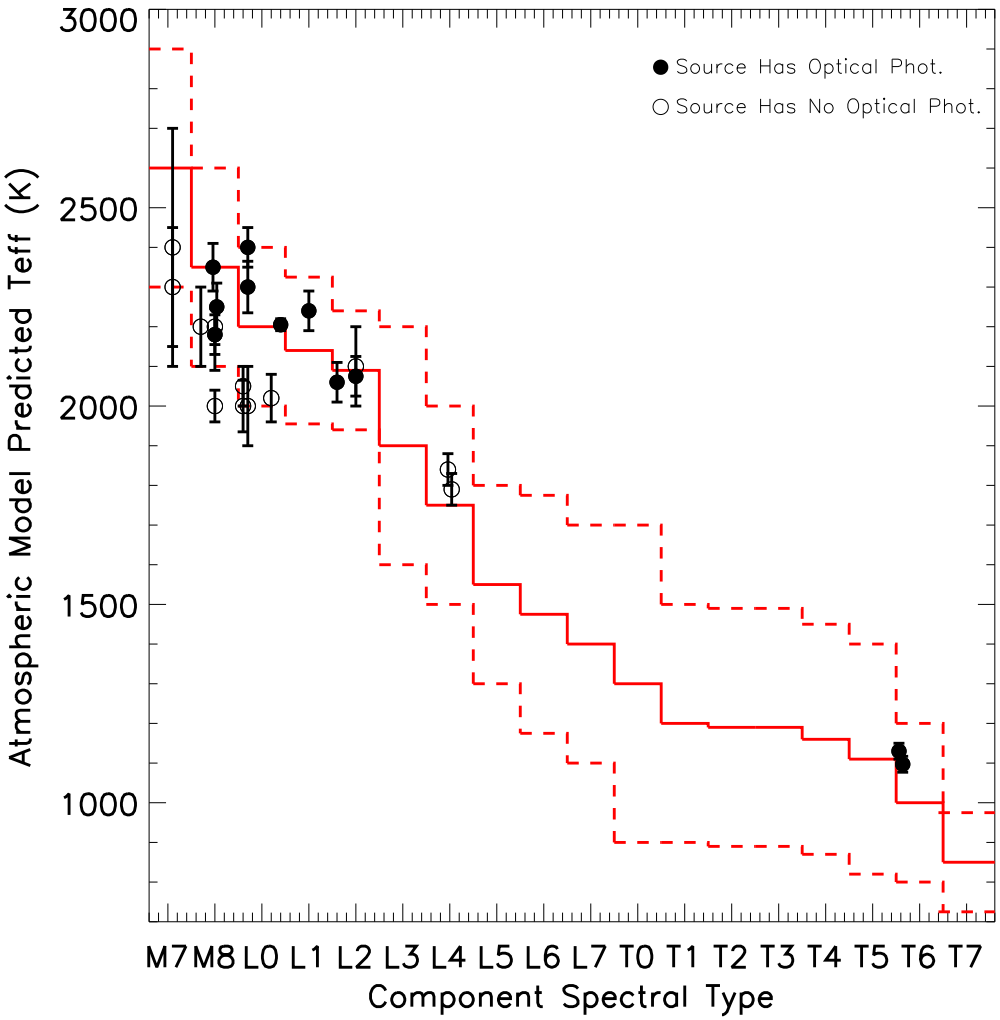

Figure 4.57 The fitted effective temperatures from the atmospheric models are plotted as a function of spectral type. The scatter in the data points further stresses the intrinsic scatter in predicted effective temperature with spectral type. Overplotted in red is an effective temperature/spectral type relationship derived from the results of Golimowski et al. (2004), Cushing et al. (2008), and Luhman et al. (2003). In most cases, the uncertainties in our derived temperatures and smaller temperature than those predicted by the temperature/spectral type relationship.

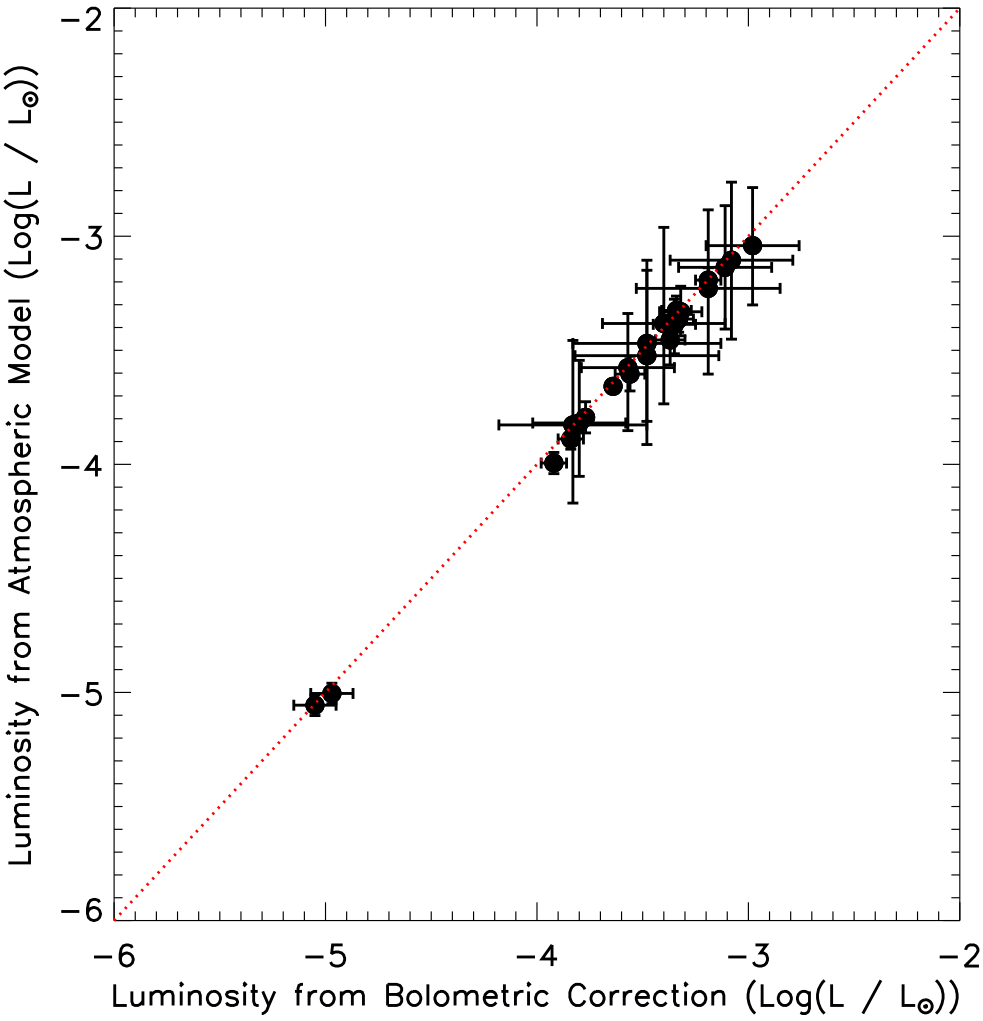

Figure 4.58 The luminosities implied from our atmospheric model fits for T_{Eff} and radius versus the luminosities derived from the bolometric corrections in Golimowski et al. (2004). The red line represents 1:1 correspondence. All values are consistent with each other. We use the luminosities from bolometric corrections for further analysis because they are completely independent of models.

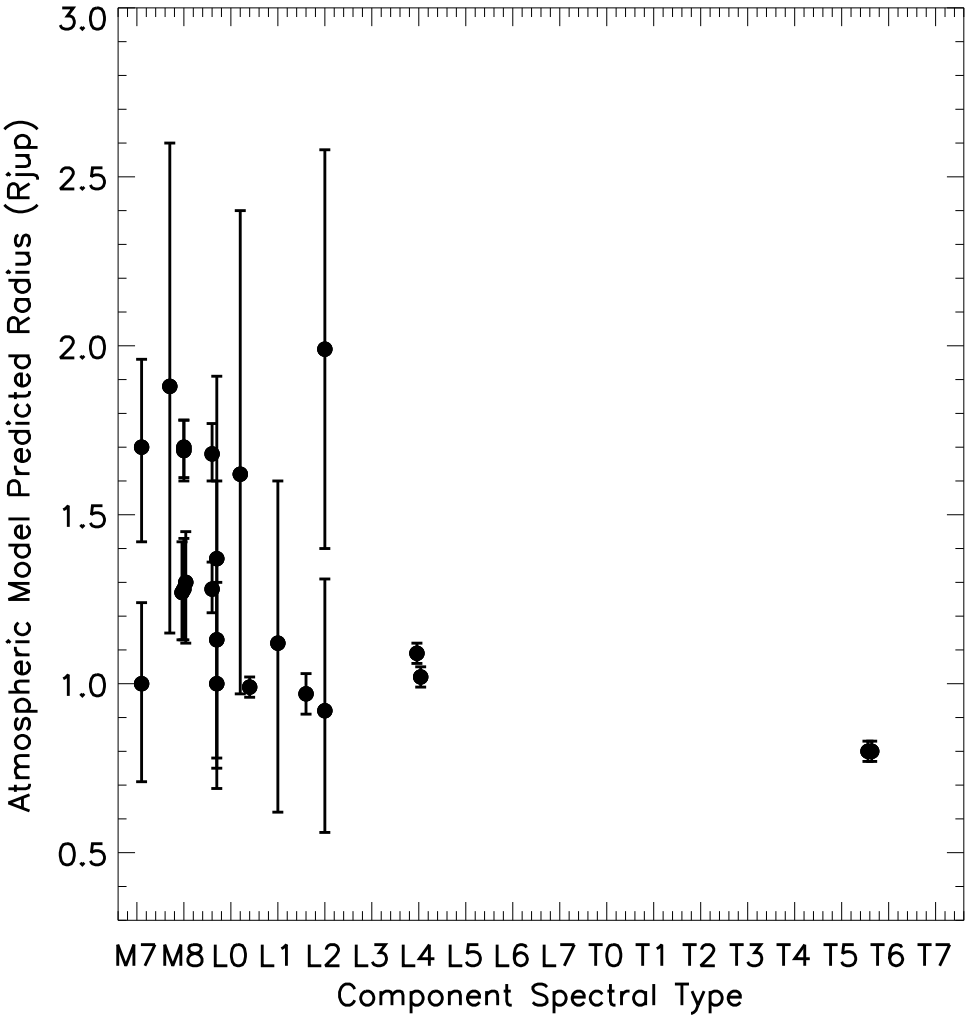

Figure 4.59 The fitted radii from the atmospheric models are plotted as a function of spectral type. A fairly large scatter in the values is seen, but this is expected given the mixed age population of our sample. The values, however, are consistently in the range expected for VLM objects of between 0.5 and 2 R_{Jup}. This result also justifies our choice of assuming a radius of 1.0 $\pm$ 0.3 R_{Jup} for the L/T transition objects that cannot be fit by the atmospheric models.

Table 4.9. Photometric Measurements

Target Name	M_{F625W}	M_{F775W}	M_{814W}	M_{850LP}	M_{F1042}	M_J	M_H	M_{Kp}	L_{Bol} (Log $L/L_\odot$)	T_{Eff} (K)	Rad. (R_{Jup})	Phot. Ref
2MASS 0746+20A	18.36 ± 0.05	15.55 ± 0.05	14.98 ± 0.15	13.81 ± 0.05	—	11.85 ± 0.04	11.13 ± 0.02	10.62 ± 0.02	-3.64 ± 0.02	2205 ± 15	0.99 ± 0.03	1
2MASS 0746+20B	18.86 ± 0.06	16.23 ± 0.07	15.98 ± 0.18	14.57 ± 0.06	—	12.36 ± 0.10	11.57 ± 0.03	10.98 ± 0.02	-3.77 ± 0.02	2060 ± 50	0.97 ± 0.06	1
2MASS 0850+10A	20.93 ± 0.50	18.41 ± 0.48	17.39 ± 0.44	16.17 ± 0.48	—	—	—	11.99 ± 0.42	-4.22 ± 0.18	1590 ± 290	1.0 ± 0.3	2
2MASS 0850+10B	22.24 ± 0.57	19.57 ± 0.50	18.86 ± 0.45	17.03 ± 0.49	—	—	—	12.80 ±0.43	-4.47 ± 0.18	1380 ± 250	1.0 ± 0.3	2
2MASS 0920+35A	—	—	17.90 ± 0.48	—	—	14.43 ± 0.47	13.40 ± 0.45	12.65 ± 0.45	-4.47 ± 0.19	1375 ± 250	1.0 ± 0.3	3
2MASS 0920+35B	—	—	18.78 ± 0.49	—	—	14.47 ± 0.56	13.60 ± 0.46	12.97 ± 0.46	-4.54 ± 0.20	1320 ± 250	1.0 ± 0.3	3
2MASS 1426+15A	16.98 ± 0.87	13.92 ± 0.86	13.49 ± 0.85	12.23 ± 0.86	11.33 ± 0.85	10.69 ± 0.83	10.00 ± 0.83	9.55 ± 0.83	-3.19 ± 0.34	2400 ± 50	$1.37^{+0.54}_{-0.59}$	4
2MASS 1426+15B	17.98 ± 0.87	15.16 ± 0.87	14.89 ± 0.85	13.29 ± 0.86	12.63 ± 0.85	11.46 ± 0.83	10.70 ± 0.83	10.20 ± 0.83	-3.48 ± 0.34	2240 ± 50	$1.12^{+0.48}_{-0.50}$	4
2MASS 1534-29A	—	—	19.57 ± 0.04	—	15.74 ± 0.12	14.61 ± 0.10	14.79 ± 0.11	14.84 ± 0.12	-4.97 ± 0.10	1130 ± 20	0.80 ± 0.03	5
2MASS 1534-29B	—	—	19.87 ± 0.05	—	15.94 ± 0.24	14.77 ± 0.10	15.14 ± 0.13	15.03 ± 0.13	-5.05 ± 0.10	1097 ± 20	0.80 ± 0.03	5
2MASS 1728+39A	—	—	18.35 ± 0.25	—	15.89 ± 0.21	14.68 ± 0.20	13.40 ± 0.20	12.47 ± 0.20	-4.38 ± 0.10	1450 ± 230	1.0 ± 0.3	3
2MASS 1728+39B	—	—	19.00 ± 0.28	—	15.64 ± 0.22	15.00 ± 0.20	13.85 ± 0.20	13.13 ± 0.20	-4.60 ± 0.10	1280 ± 200	1.0 ± 0.3	3
2MASS 1750+44A	—	—	—	—	—	10.30 ± 0.71	9.72 ± 0.71	9.36 ± 0.71	-3.08 ± 0.29	2200 ± 100	$1.88^{+0.72}_{-0.73}$	6
2MASS 1750+44B	—	—	—	—	—	11.26 ± 0.71	10.49 ± 0.72	10.03 ± 0.71	-3.40 ± 0.29	2020 ± 60	$1.62^{+0.78}_{-0.65}$	6
2MASS 1847+55A	—	—	—	—	—	10.19 ± 0.52	9.52 ± 0.52	9.16 ± 0.52	-2.98 ± 0.22	2400 ± 300	$1.70^{+0.26}_{-0.28}$	6
2MASS 1847+55B	—	—	—	—	—	10.43 ± 0.53	9.81 ± 0.55	9.43 ± 0.52	-3.11 ± 0.22	2100 ± 100	1.99 ± 0.59	6
2MASS 2140+16A	—	—	14.05 ± 0.89	—	11.79 ± 0.89	11.33 ± 0.87	10.66 ± 0.87	10.28 ± 0.87	-3.48 ± 0.35	2300 ± 65	$1.13^{+0.47}_{-0.44}$	3
2MASS 2140+16B	—	—	15.56 ± 0.89	—	13.17 ± 0.89	12.28 ± 0.88	11.59 ± 0.89	11.02 ± 0.87	-3.83 ± 0.35	2075 ± 50	$0.92^{+0.39}_{-0.36}$	3
2MASS 2206-20A	—	—	13.59 ± 0.21	—	11.81 ± 0.21	10.92 ± 0.21	10.28 ± 0.22	9.91 ± 0.21	-3.32 ± 0.10	2350 ± 60	$1.27^{+0.15}_{-0.14}$	3
2MASS 2206-20B	—	—	13.67 ± 0.21	—	11.83 ± 0.21	11.07 ± 0.22	10.33 ± 0.24	9.98 ± 0.21	-3.35 ± 0.10	2250 ± 60	$1.30^{+0.15}_{-0.18}$	3
GJ 569Ba	—	—	—	—	—	11.18 ± 0.08	10.47 ± 0.05	9.90 ± 0.06	-3.33 ± 0.07	2000 ± 40	1.69 ± 0.09	7
GJ 569Bb	—	—	—	—	—	11.69 ± 0.08	11.08 ± 0.06	10.43 ± 0.07	-3.56 ± 0.07	2000 ± 65	1.28 ± 0.07	7
HD 130948B	—	—	—	—	—	12.51 ± 0.06	11.74 ± 0.10	10.96 ± 0.03	-3.84 ± 0.06	1840 ± 40	1.09 ± 0.03	8
HD 130948C	—	—	—	—	—	12.82 ± 0.07	12.03 ± 0.11	11.16 ± 0.03	-3.92 ± 0.06	1790 ± 40	1.02 ± 0.03	8
LHS 2397aA	—	—	14.29 ± 0.07	—	—	11.33 ± 0.06	10.52 ± 0.07	10.04 ± 0.07	-3.37 ± 0.07	2180^{+50}_{-90}	1.28 ± 0.15	9
LHS 2397aB	—	—	18.71 ± 0.18	—	—	14.45 ± 0.10	13.62 ± 0.10	12.82 ± 0.07	-4.50 ± 0.07	1350 ± 210	1.0 ± 0.3	9
LP 349-25A	—	—	—	—	—	10.53 ± 0.05	9.93 ± 0.06	9.58 ± 0.06	-3.19 ± 0.06	2200 ± 45	$1.70^{+0.08}_{-0.09}$	6
LP 349-25B	—	—	—	—	—	11.07 ± 0.07	10.35 ± 0.09	9.88 ± 0.09	-3.34 ± 0.07	2050 ± 50	$1.68^{+0.09}_{-0.08}$	6
LP 415-20A	—	—	—	—	—	11.48 ± 0.52	10.98 ± 0.52	10.64 ± 0.52	-3.57 ± 0.22	2300 ± 150	$1.00^{+0.24}_{-0.29}$	6
LP 415-20B	—	—	—	—	—	12.32 ± 0.54	11.49 ± 0.54	11.02 ± 0.53	-3.80 ± 0.22	2000 ± 100	$1.00^{+0.30}_{-0.25}$	6

Note. — References for photometric measurements: (1) Optical from Bouy et al. (2004), NIR from this work; (2) F814W from Bouy et al. (2003), all others from this work; (3) Optical from Bouy et al. (2003), NIR from this work; (4) F814W and F1042M from Bouy et al. (2003), all others from this work; (5) F814W and J from Liu et al. (2008), F1042M from Burgasser et al. (2003), all others from this work; (6) All photometry from this work; (7) Photometry from Lane et al. (2001) and Simon et al. (2006); (8) Photometry from Dupuy et al. (2009a); (9) Optical from Freed et al. (2004), J from Dupuy et al. (2009b), all others from this work

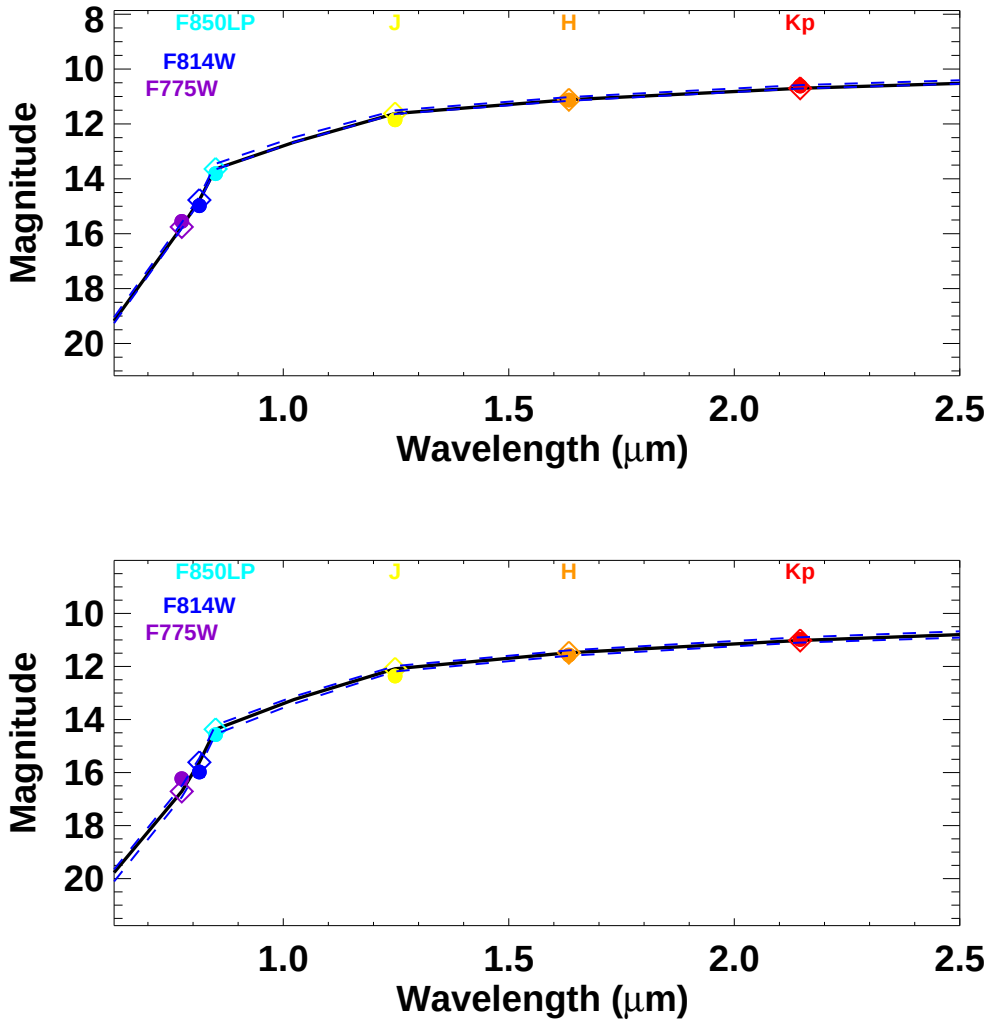

Figure 4.60 Photometry and best fit SEDs for 2MASS 0746+20A (top, 2205 K) and 2MASS 0746+20B (bottom, 2060 K). Photometric measurements are shown as filled circles, and best fit photometry from the DUSTY atmosphere models are show as open diamonds. The full best fit SED (generated by interpolating between the best fit photometry from the models) is overplotted in black, and the 1σ allowed ranges of magnitudes are shown as dashed blue lines.

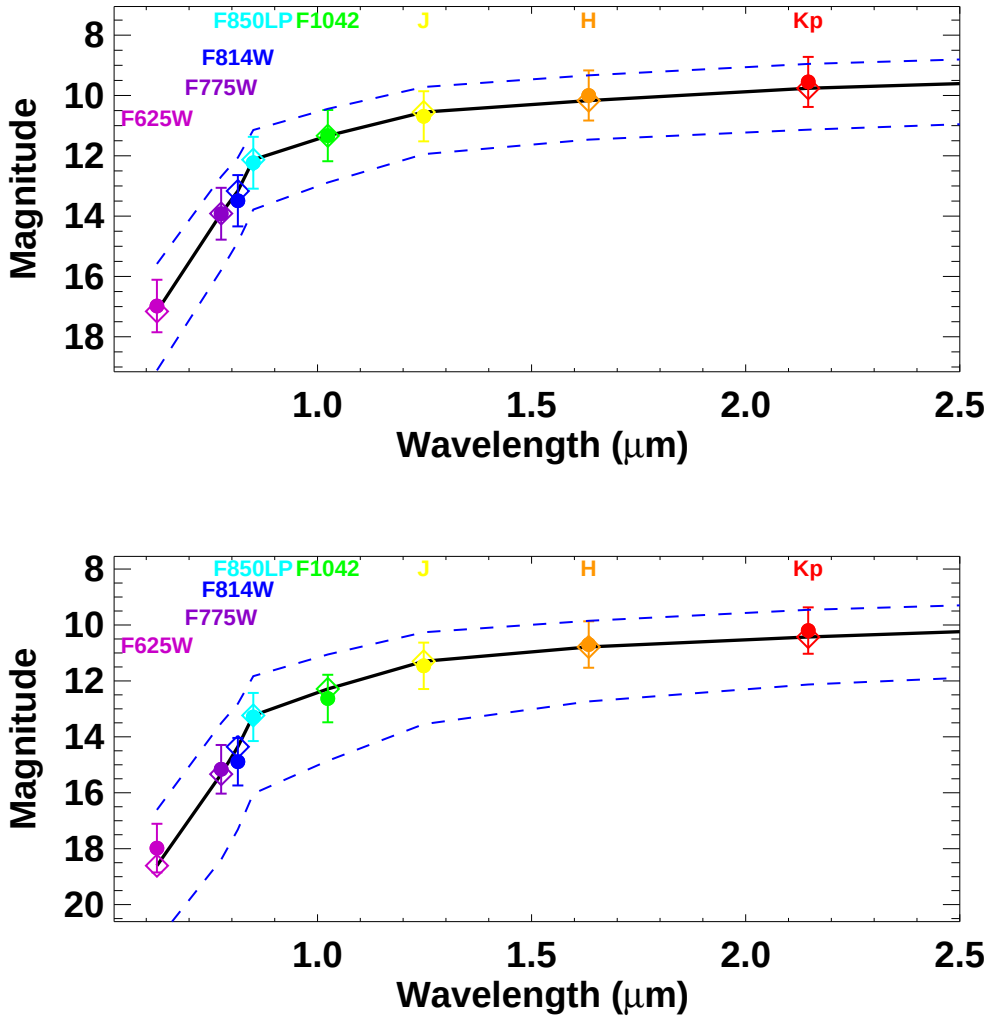

Figure 4.61 Photometry and best fit SEDs for 2MASS 1426+15A (top, 2400 K) and 2MASS 1426+15B (bottom, 2240 K). Photometric measurements are shown as filled circles, and best fit photometry from the DUSTY atmosphere models are show as open diamonds. The full best fit SED (generated by interpolating between the best fit photometry from the models) is overplotted in black, and the 1σ allowed ranges of magnitudes are shown as dashed blue lines.

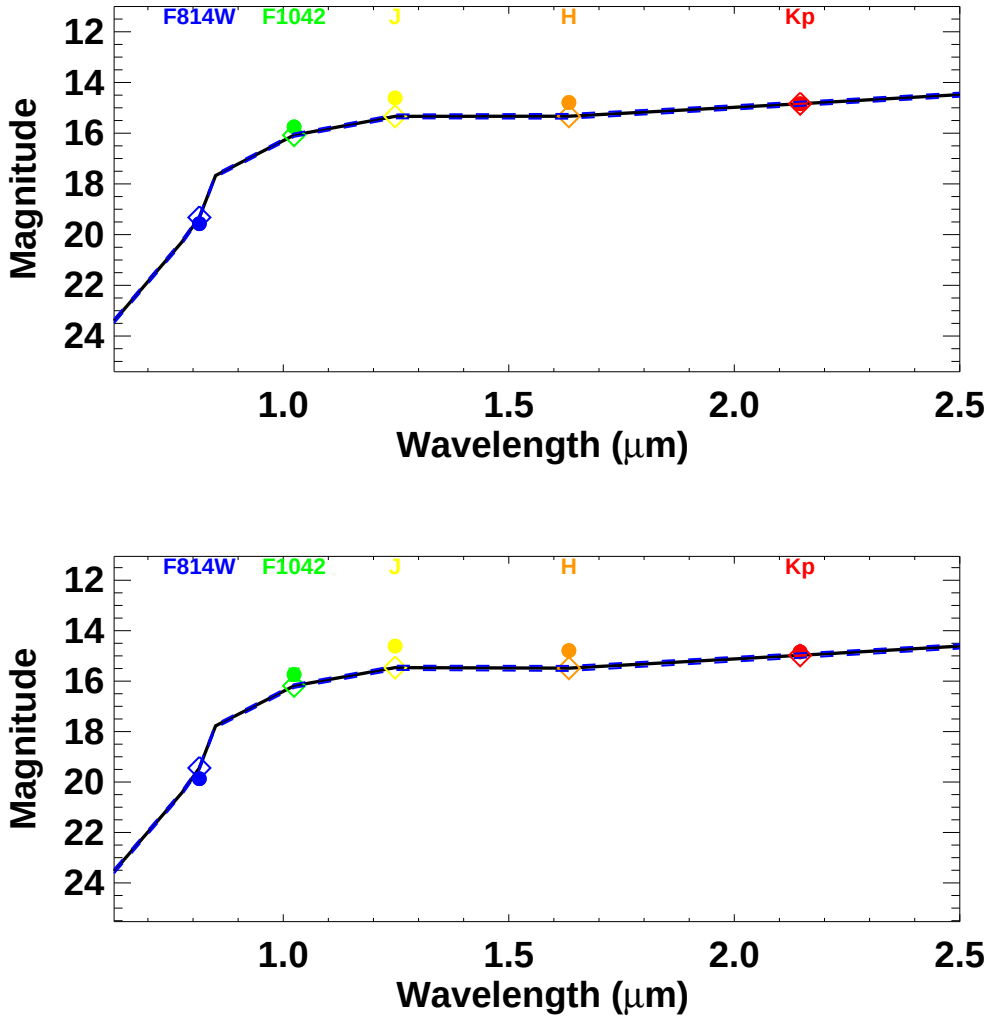

Figure 4.62 Photometry and best fit SEDs for 2MASS 1534-29A (top, 1130 K) and 2MASS 1534-29B (bottom, 1097 K). Photometric measurements are shown as filled circles, and best fit photometry from the COND atmosphere models are show as open diamonds. The full best fit SED (generated by interpolating between the best fit photometry from the models) is overplotted in black, and the 1σ allowed ranges of magnitudes are shown as dashed blue lines.

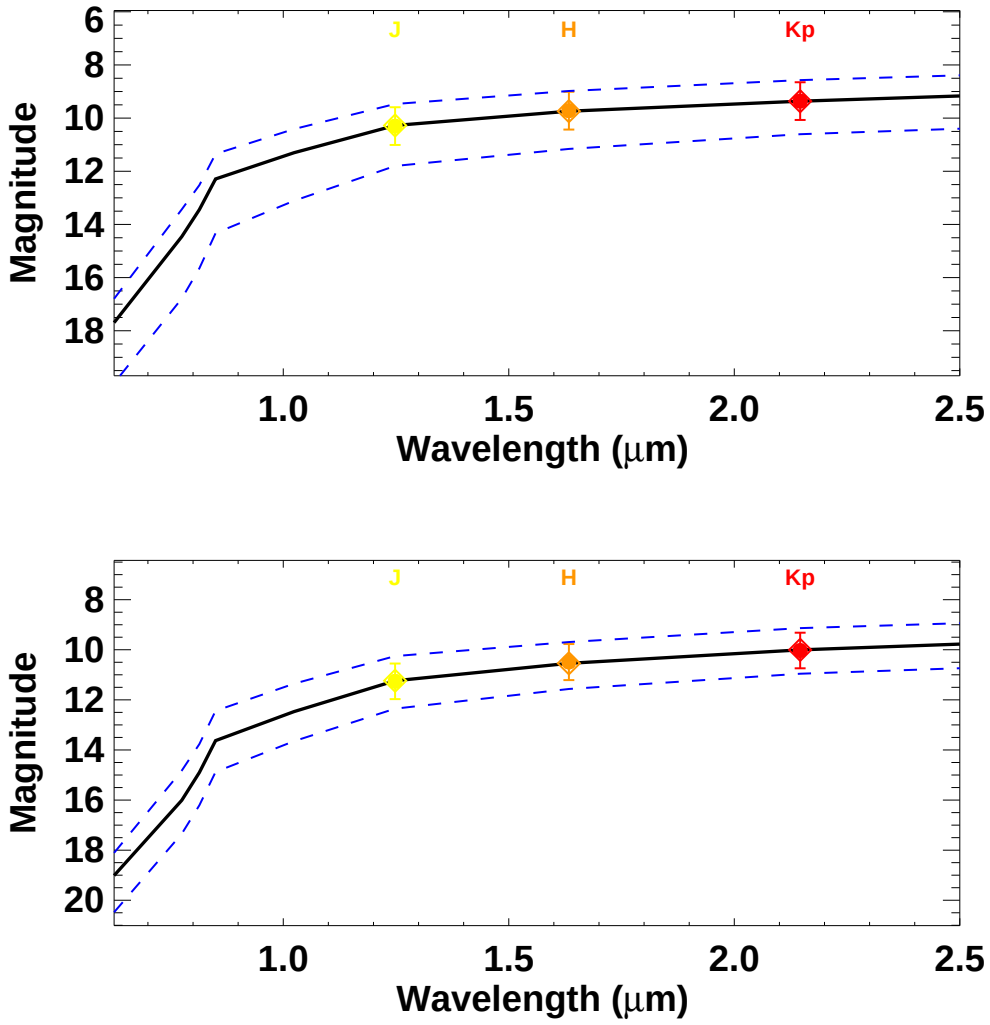

Figure 4.63 Photometry and best fit SEDs for 2MASS 1750+44A (top, 2200 K) and 2MASS 1750+44B (bottom, 2020 K). Photometric measurements are shown as filled circles, and best fit photometry from the DUSTY atmosphere models are show as open diamonds. The full best fit SED (generated by interpolating between the best fit photometry from the models) is overplotted in black, and the 1σ allowed ranges of magnitudes are shown as dashed blue lines.

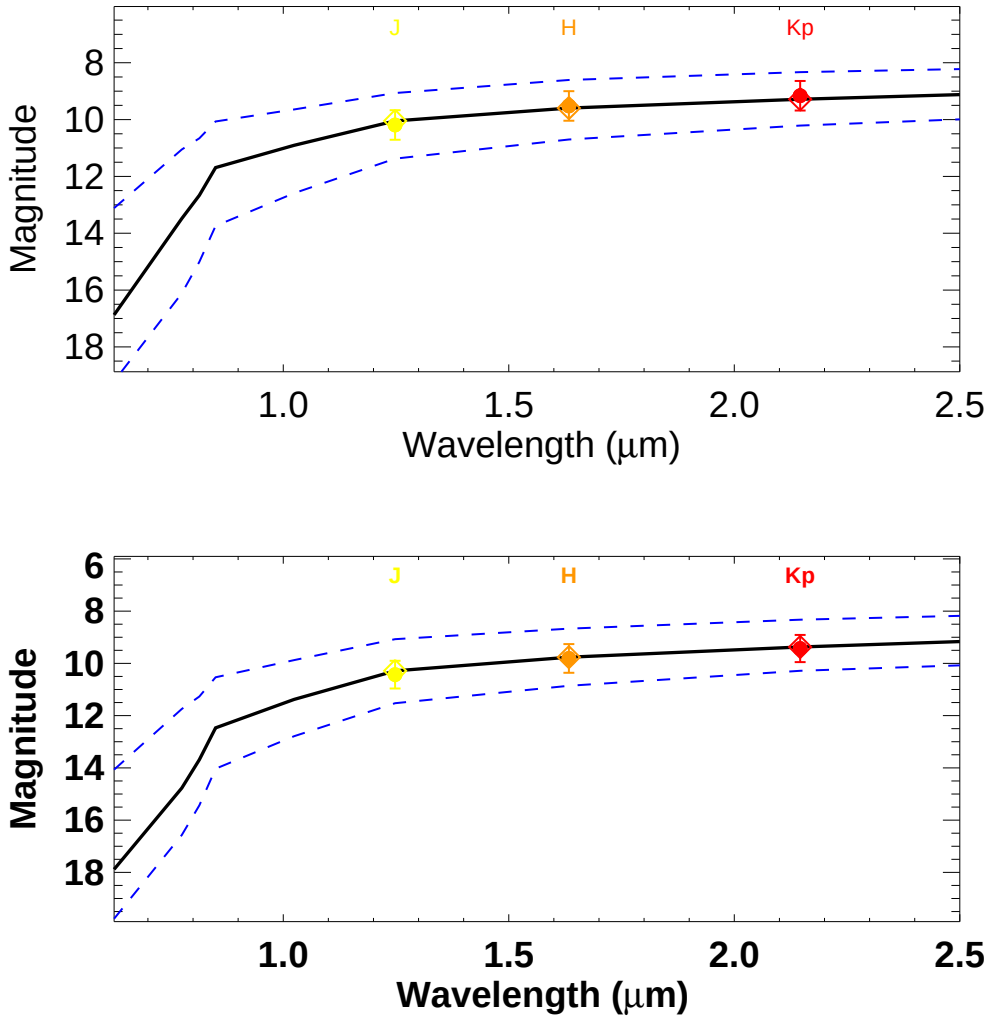

Figure 4.64 Photometry and best fit SEDs for 2MASS 1847+55A (top, 2400 K) and 2MASS 1847+55B (bottom, 2100 K). Photometric measurements are shown as filled circles, and best fit photometry from the DUSTY atmosphere models are show as open diamonds. The full best fit SED (generated by interpolating between the best fit photometry from the models) is overplotted in black, and the 1σ allowed ranges of magnitudes are shown as dashed blue lines.

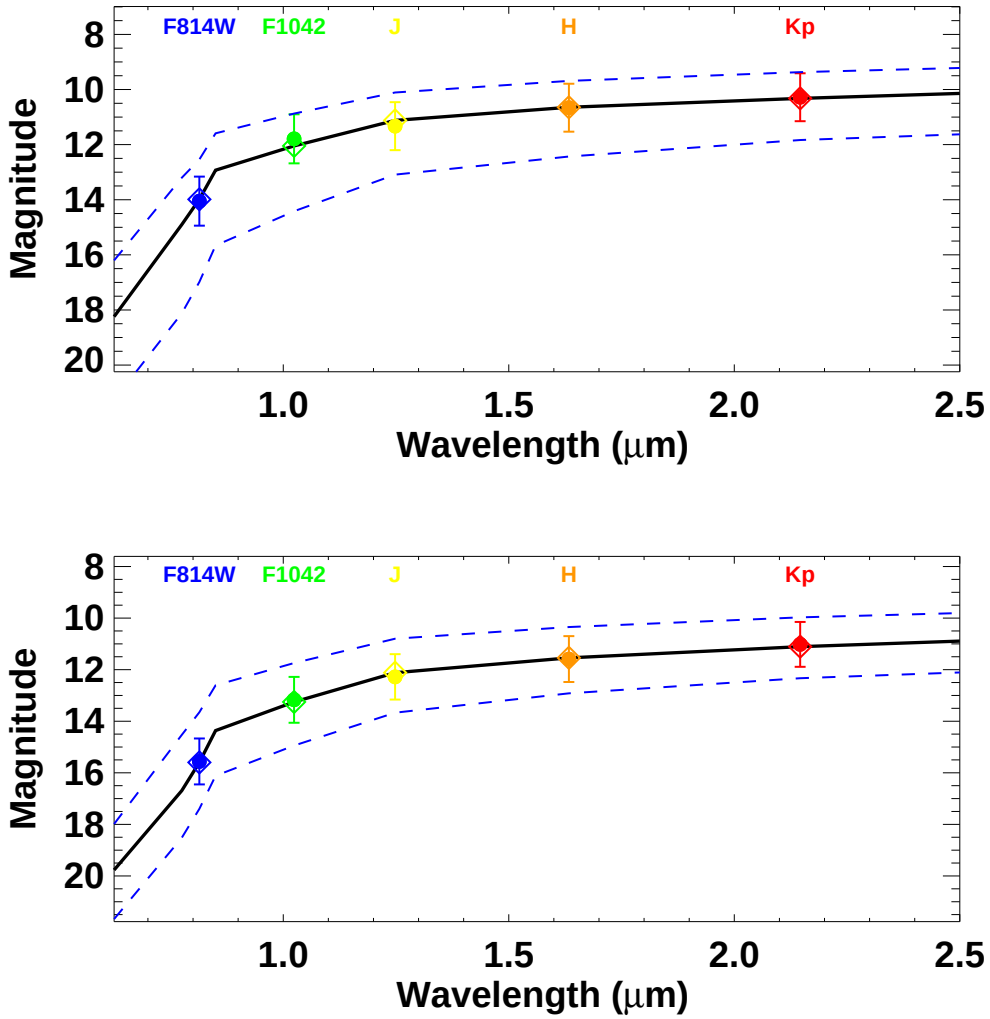

Figure 4.65 Photometry and best fit SEDs for 2MASS 2140+16A (top, 2300 K) and 2MASS 2140+16B (bottom, 2075 K). Photometric measurements are shown as filled circles, and best fit photometry from the DUSTY atmosphere models are show as open diamonds. The full best fit SED (generated by interpolating between the best fit photometry from the models) is overplotted in black, and the 1σ allowed ranges of magnitudes are shown as dashed blue lines.

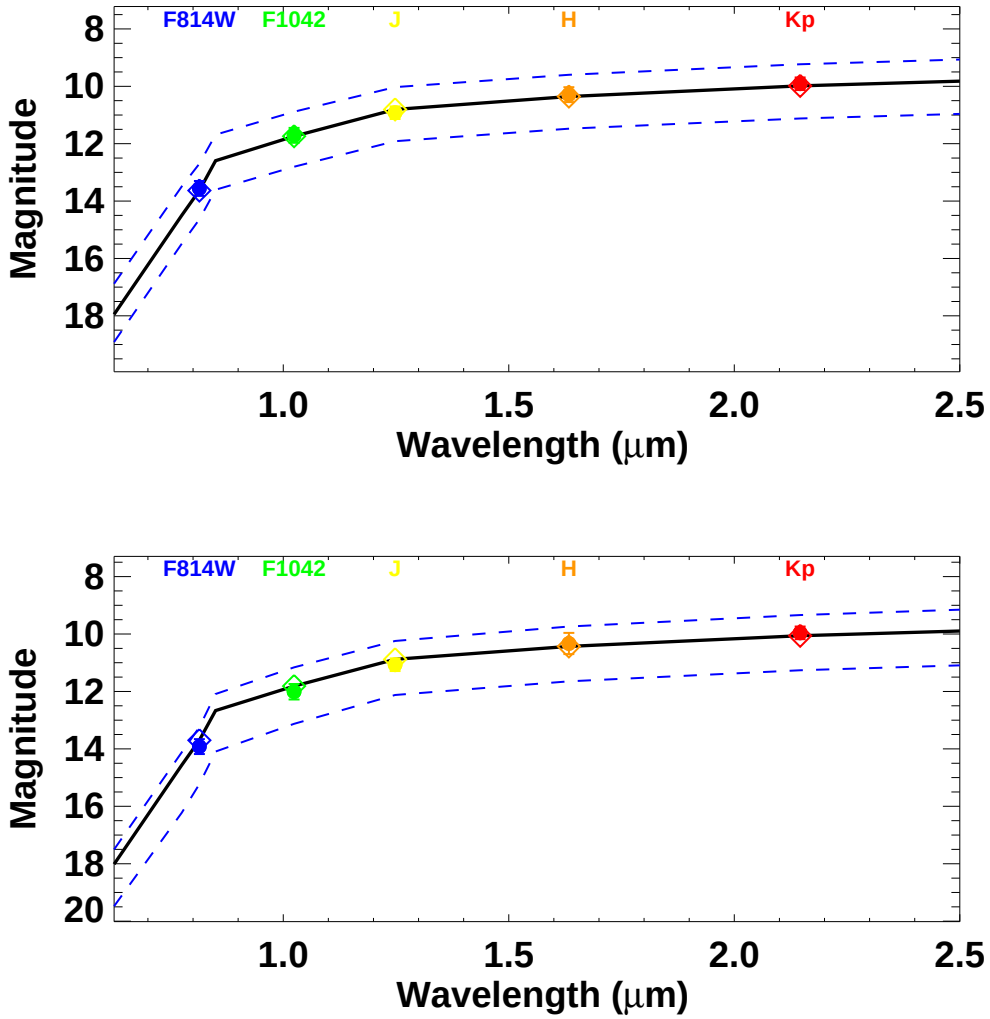

Figure 4.66 Photometry and best fit SEDs for 2MASS 2206-20A (top, 2350 K) and 2MASS 2206-20B (bottom, 2250 K). Photometric measurements are shown as filled circles, and best fit photometry from the DUSTY atmosphere models are show as open diamonds. The full best fit SED (generated by interpolating between the best fit photometry from the models) is overplotted in black, and the 1σ allowed ranges of magnitudes are shown as dashed blue lines.

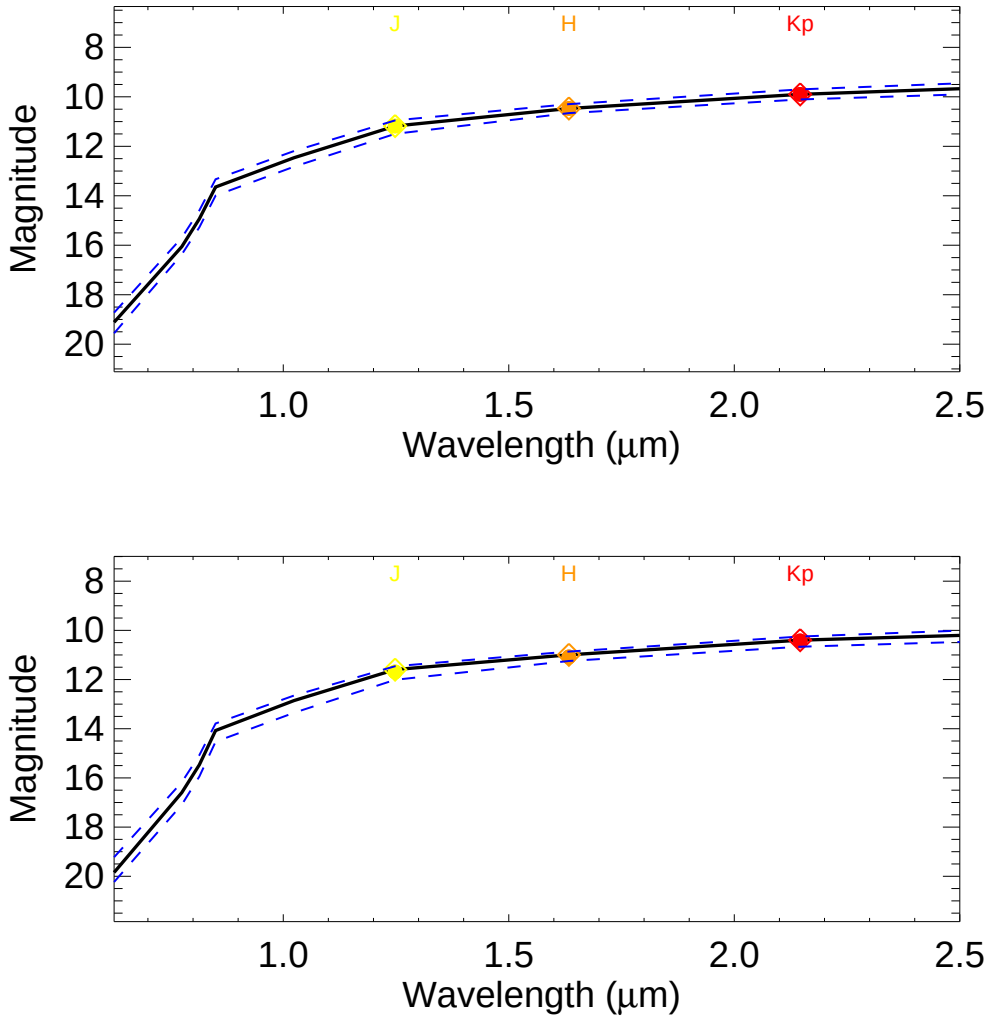

Figure 4.67 Photometry and best fit SEDs for GJ 569Ba (top, 2000 K) and GJ 569Bb (bottom, 2000 K). Photometric measurements are shown as filled circles, and best fit photometry from the DUSTY atmosphere models are show as open diamonds. The full best fit SED (generated by interpolating between the best fit photometry from the models) is overplotted in black, and the 1σ allowed ranges of magnitudes are shown as dashed blue lines.

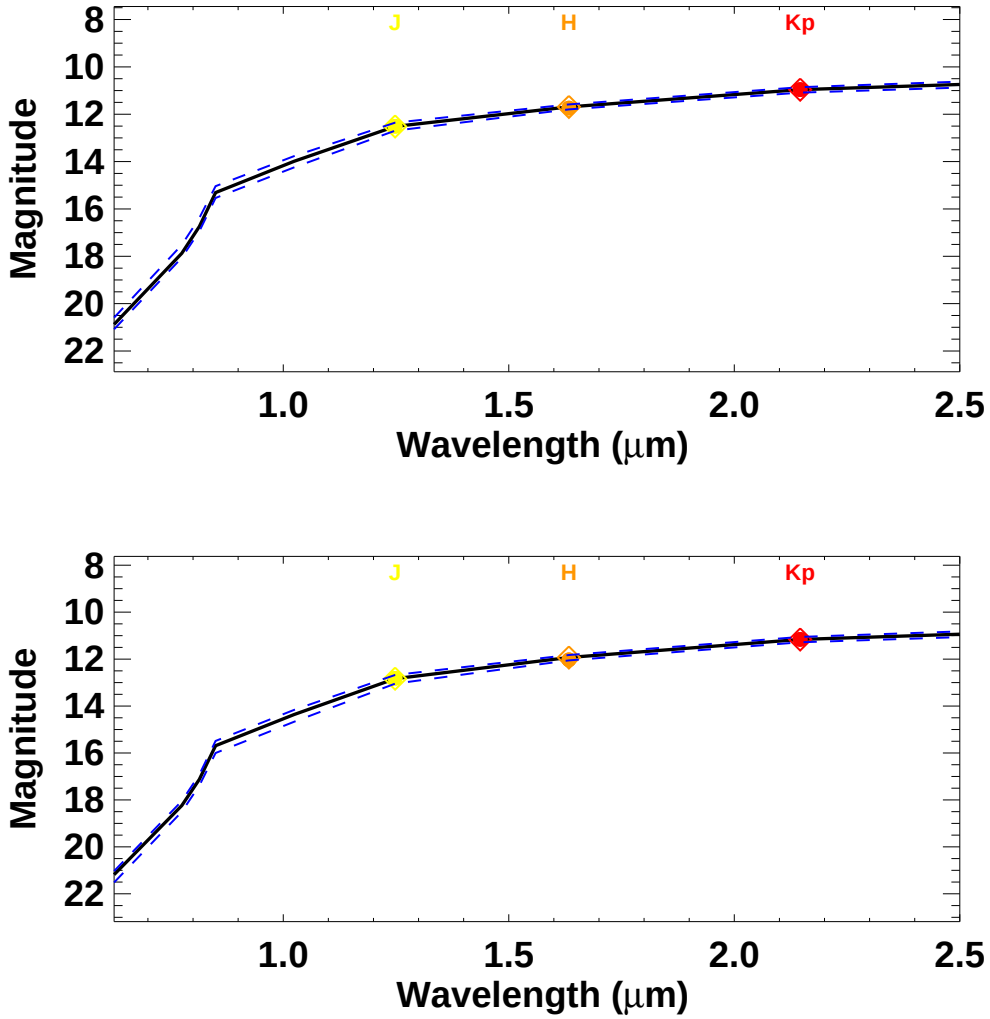

Figure 4.68 Photometry and best fit SEDs for HD 130948B (top, 1840 K) and HD 130948C (bottom, 1790 K). Photometric measurements are shown as filled circles, and best fit photometry from the DUSTY atmosphere models are show as open diamonds. The full best fit SED (generated by interpolating between the best fit photometry from the models) is overplotted in black, and the 1σ allowed ranges of magnitudes are shown as dashed blue lines.

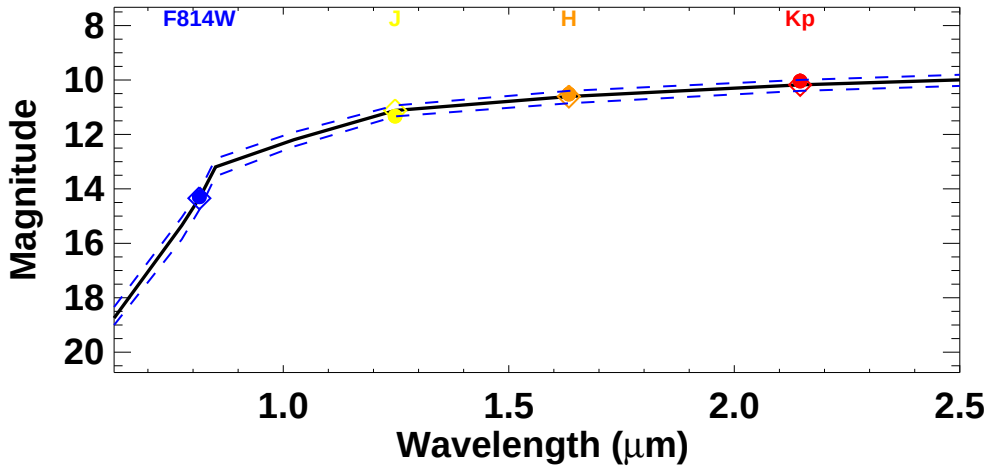

Figure 4.69 Photometry and best fit SEDs for LHS 2397a A (2180 K). Because LHS 2397a B is an L/T transition object, it has not be fit with atmospheric models. Photometric measurements are shown as filled circles, and best fit photometry from the DUSTY atmosphere models are show as open diamonds. The full best fit SED (generated by interpolating between the best fit photometry from the models) is overplotted in black, and the 1σ allowed ranges of magnitudes are shown as dashed blue lines.

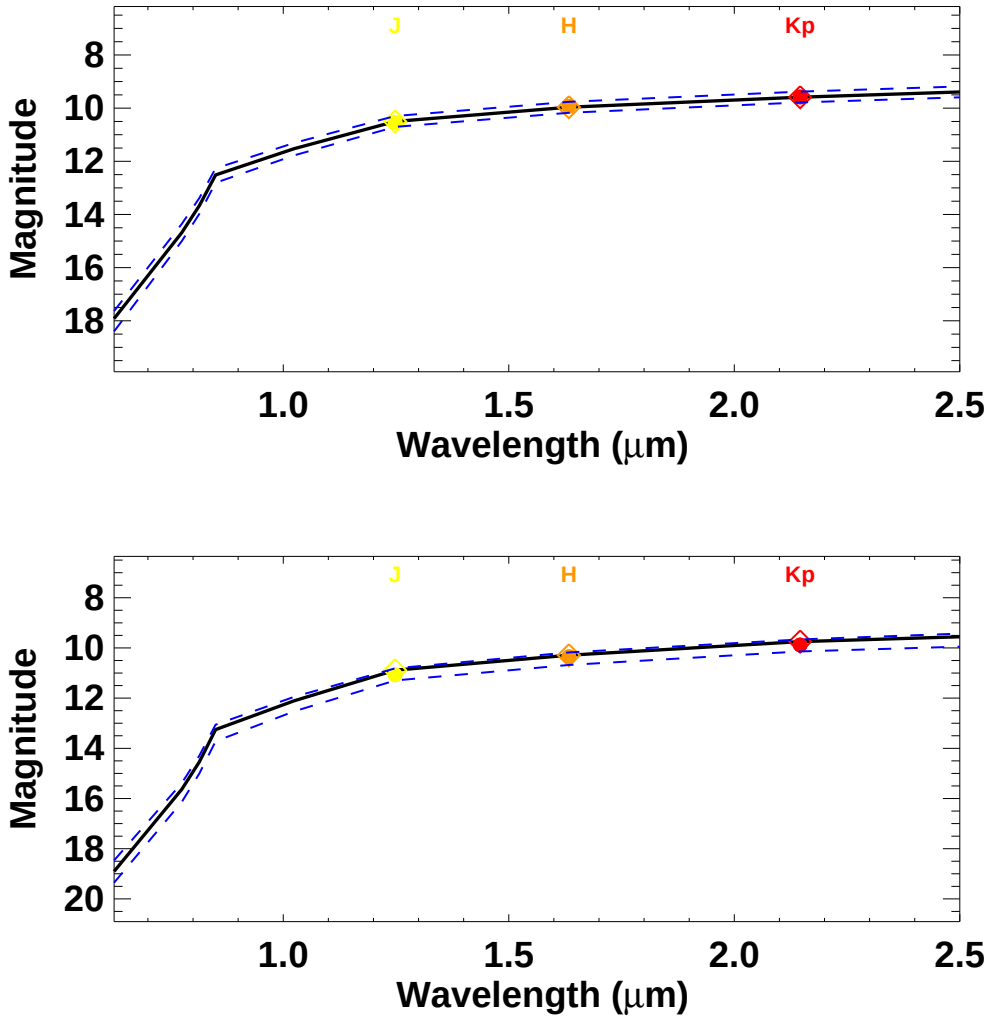

Figure 4.70 Photometry and best fit SEDs for LP 349-25A (top, 2200 K) and LP 349-25B (bottom, 2050 K). Photometric measurements are shown as filled circles, and best fit photometry from the DUSTY atmosphere models are show as open diamonds. The full best fit SED (generated by interpolating between the best fit photometry from the models) is overplotted in black, and the 1σ allowed ranges of magnitudes are shown as dashed blue lines.

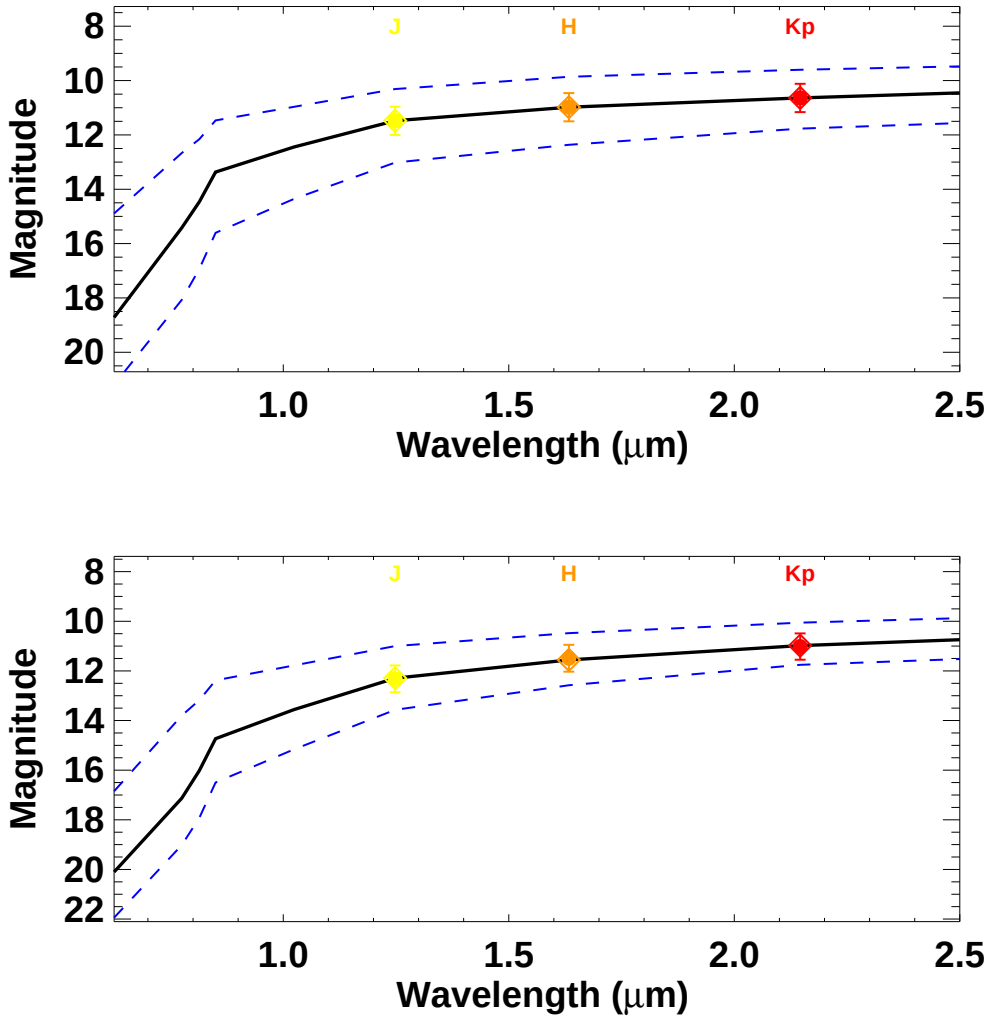

Figure 4.71 Photometry and best fit SEDs for LP 415-20A (top, 2300 K) and LP 415-20B (bottom, 2000 K). Photometric measurements are shown as filled circles, and best fit photometry from the DUSTY atmosphere models are show as open diamonds. The full best fit SED (generated by interpolating between the best fit photometry from the models) is overplotted in black, and the 1σ allowed ranges of magnitudes are shown as dashed blue lines.

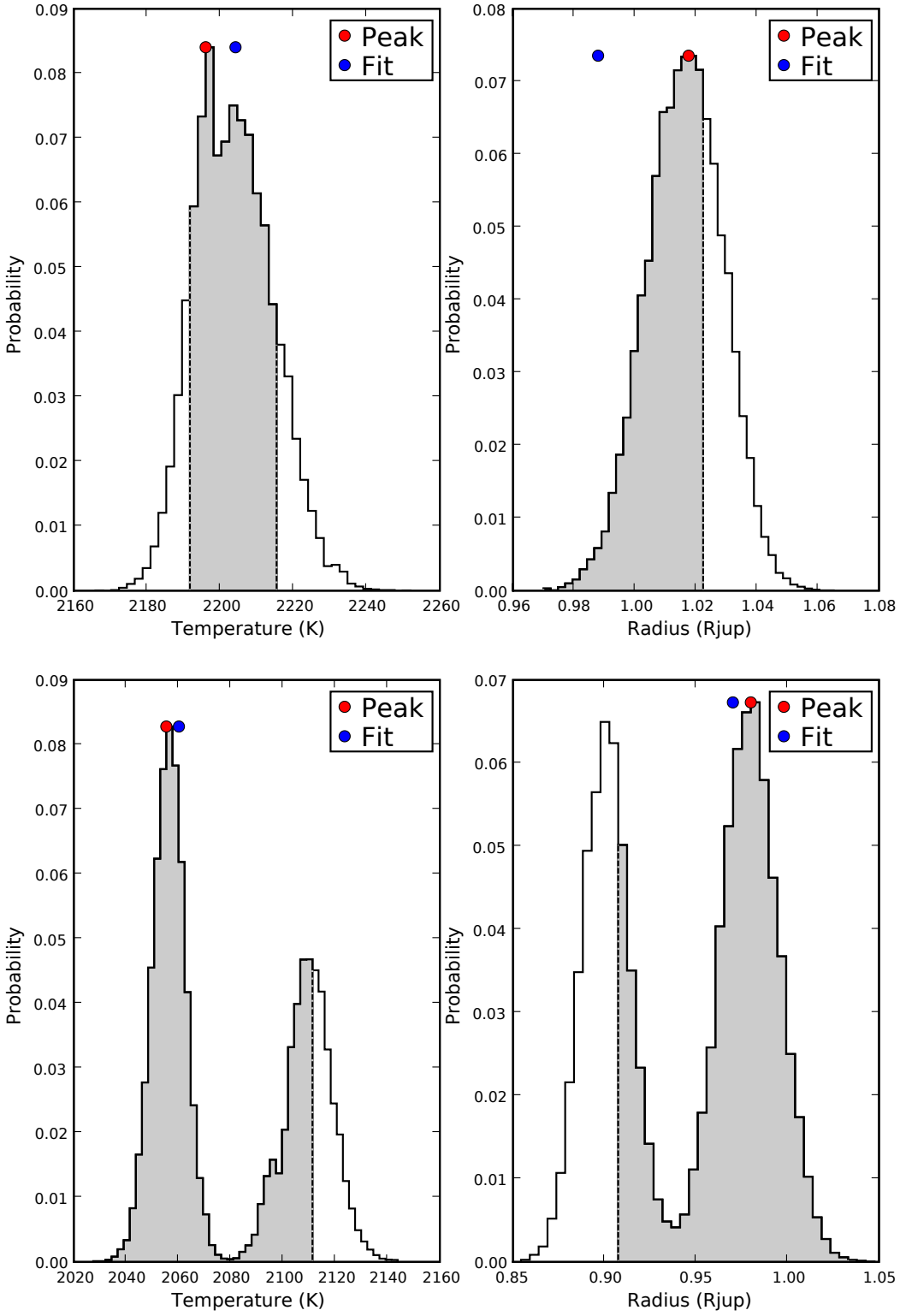

Figure 4.72 One dimensional PDFs of temperature and radius from the spectral synthesis modeling for 2MASS 0746+20A (top) and 2MASS 0746+20B (bottom).

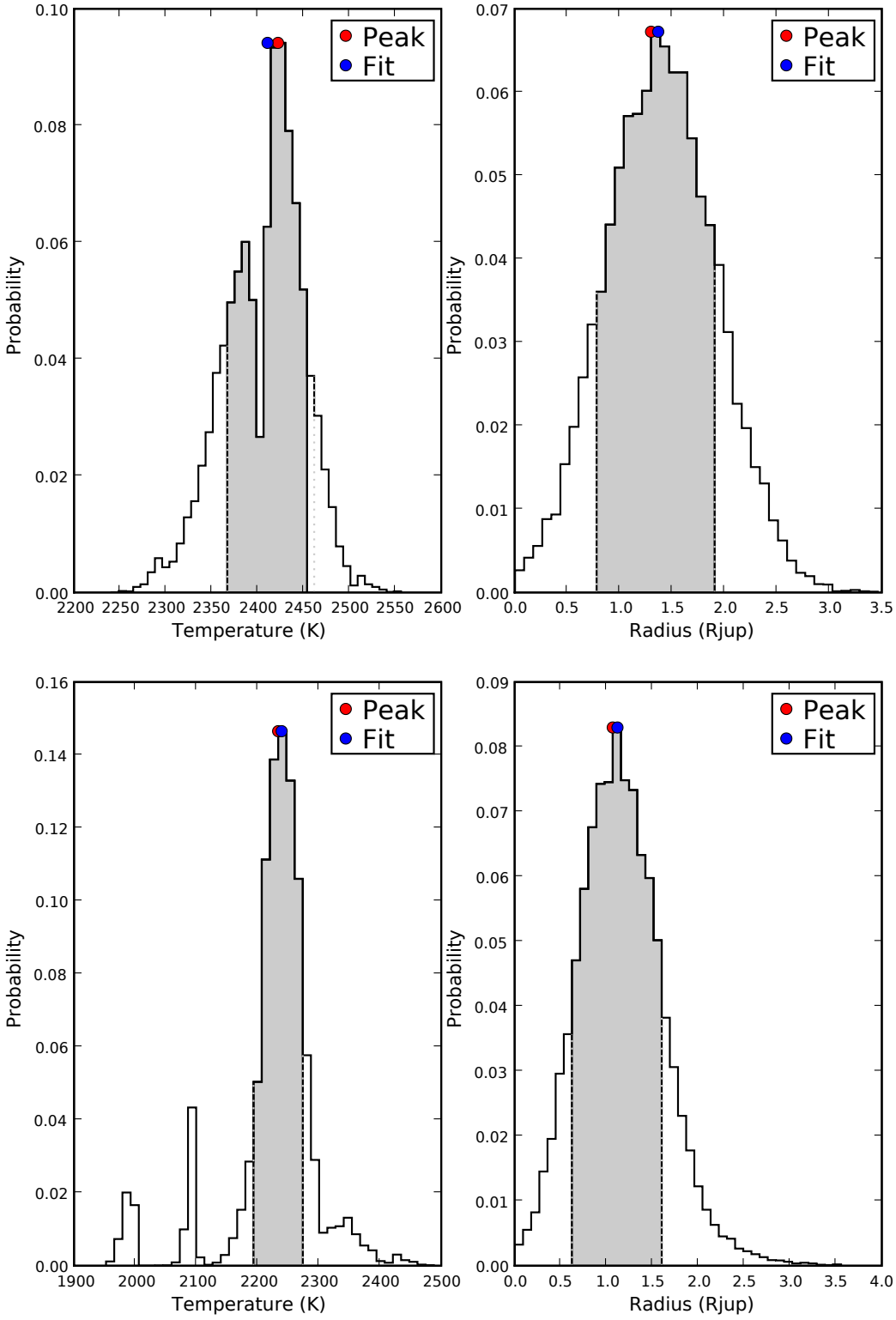

Figure 4.73 One dimensional PDFs of temperature and radius from the spectral synthesis modeling for 2MASS 1426+15A (top) and 2MASS 1426+15B (bottom).

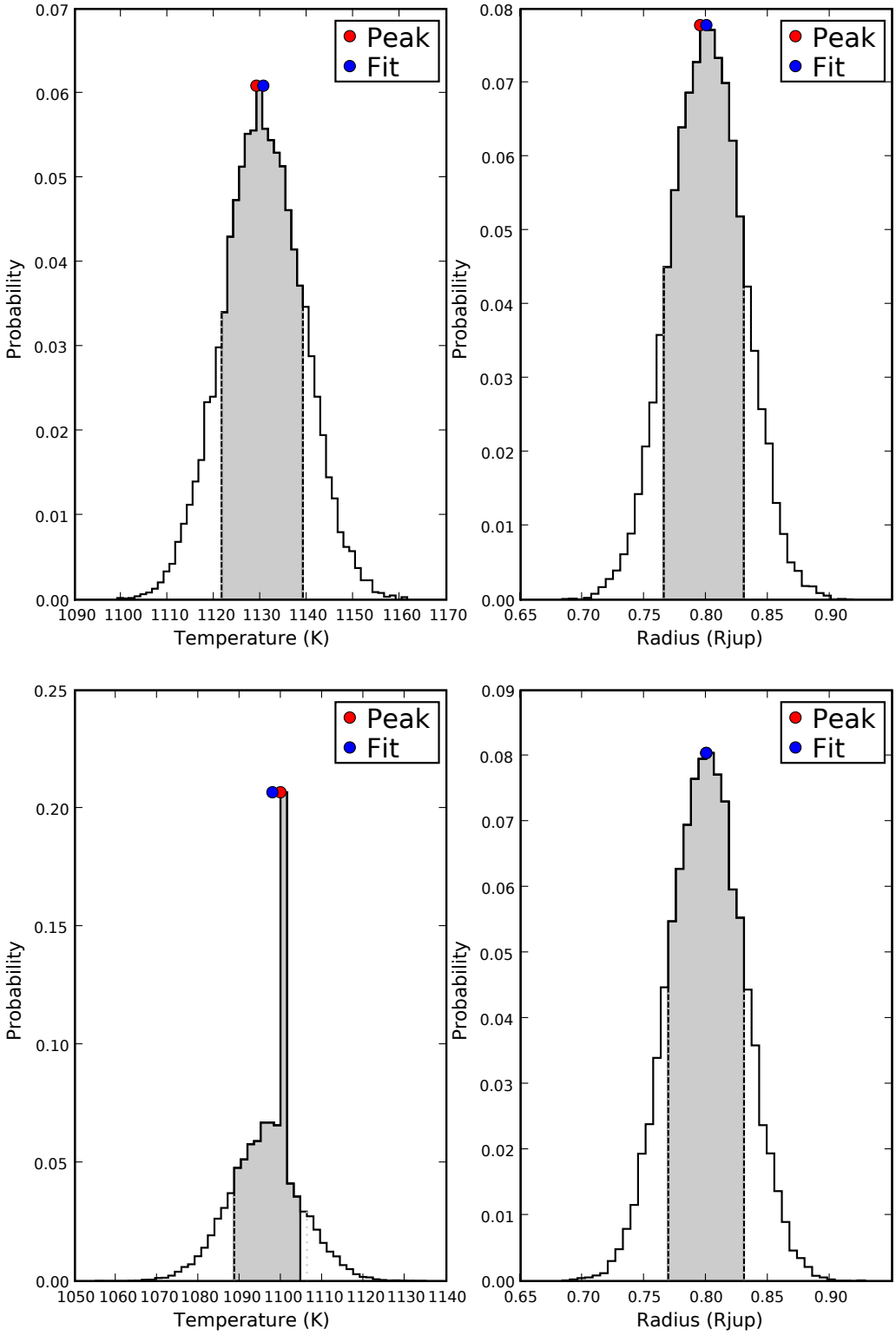

Figure 4.74 One dimensional PDFs of temperature and radius from the spectral synthesis modeling for 2MASS 1534-29A (top) and 2MASS 1534-29B (bottom).

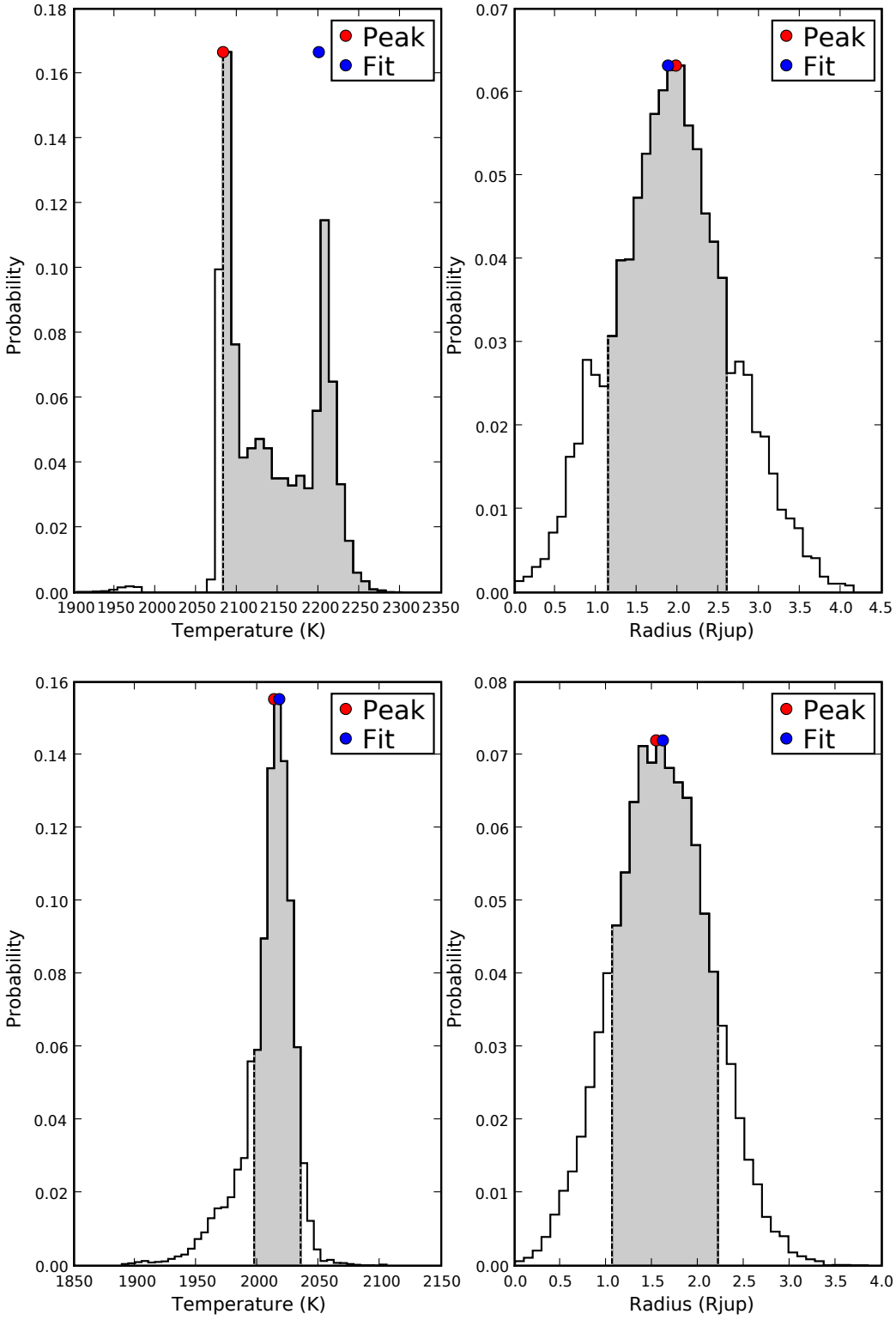

Figure 4.75 One dimensional PDFs of temperature and radius from the spectral synthesis modeling for 2MASS 1705+44A (top) and 2MASS 1750+44B (bottom).

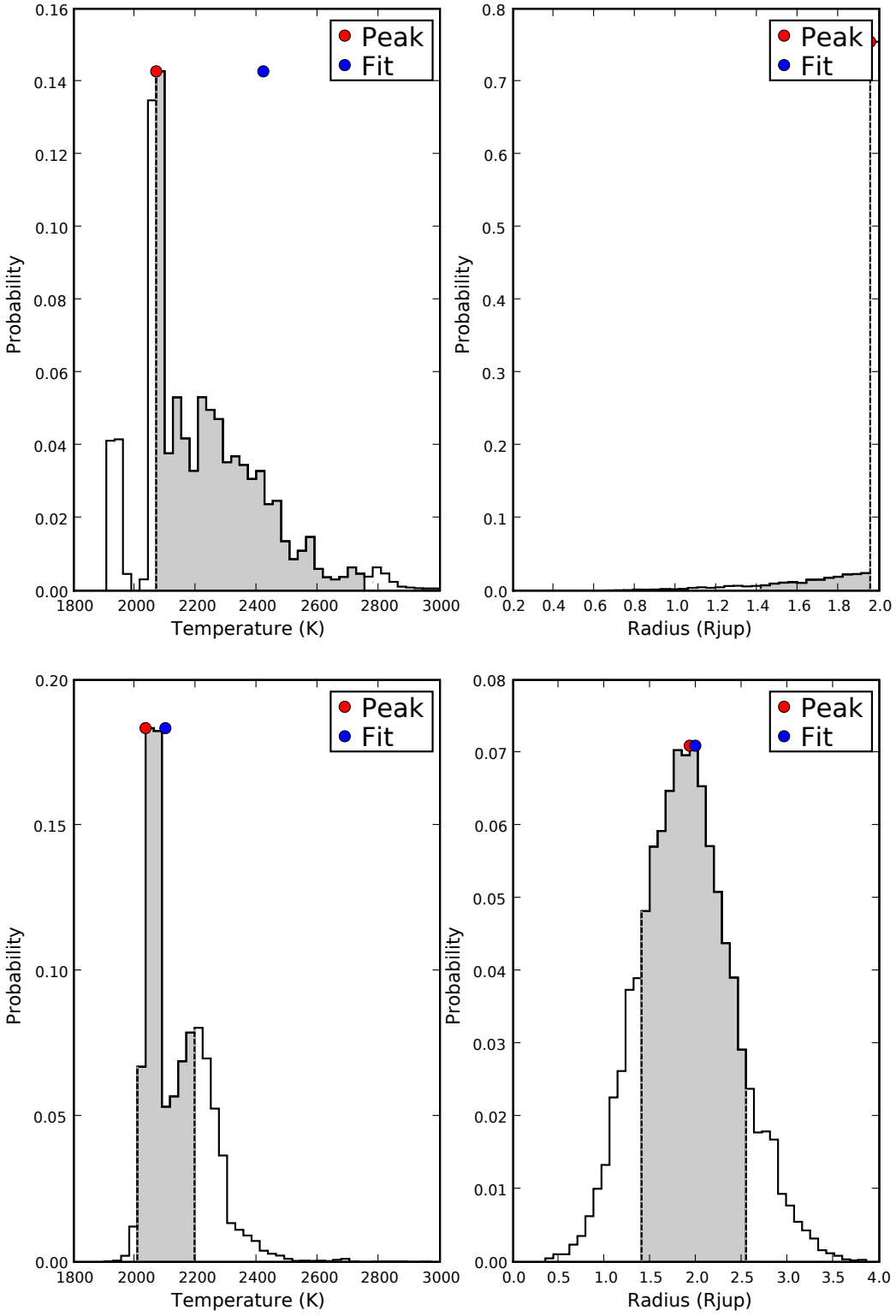

Figure 4.76 One dimensional PDFs of temperature and radius from the spectral synthesis modeling for 2MASS 1847+55A (top) and 2MASS 1847+55B (bottom).

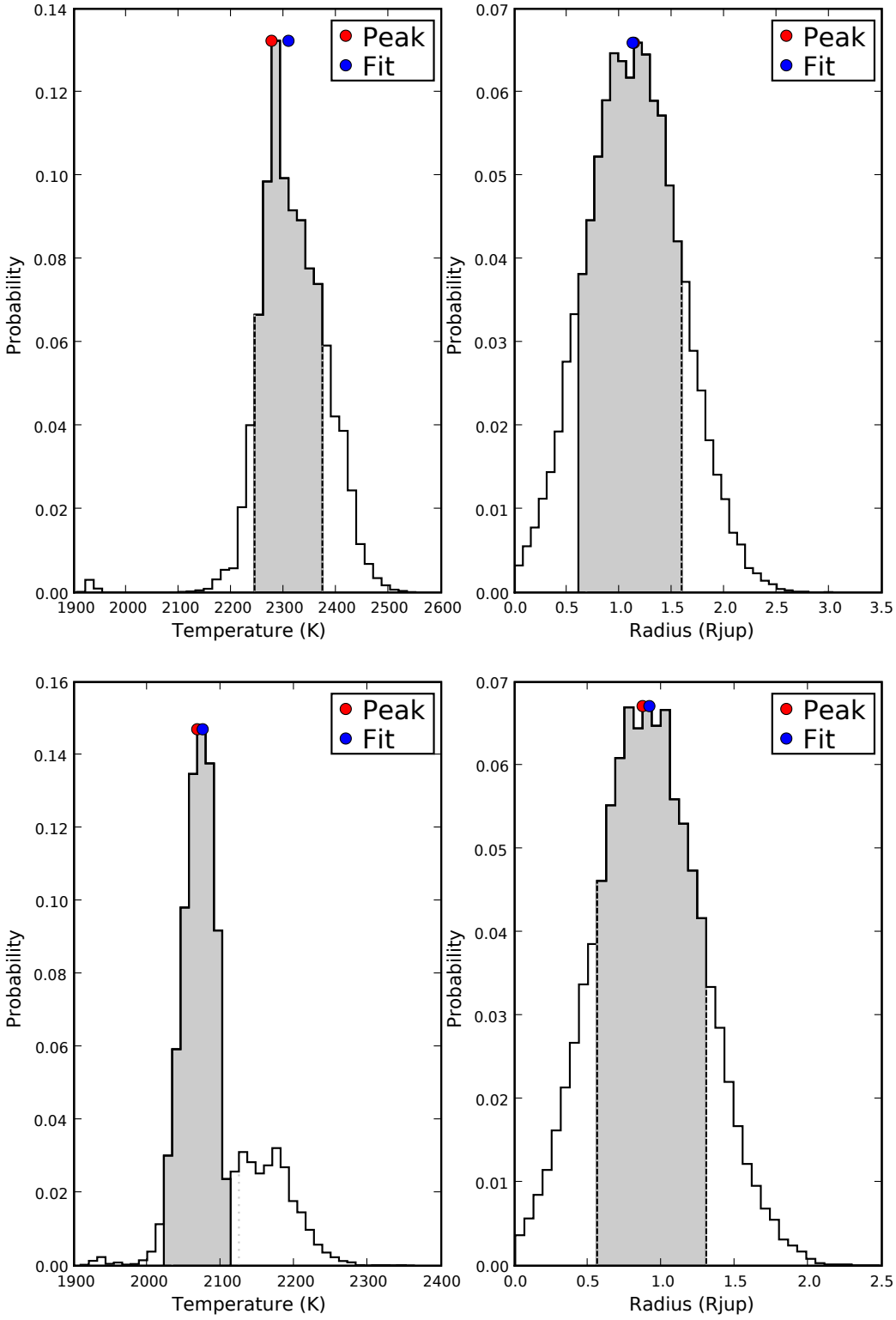

Figure 4.77 One dimensional PDFs of temperature and radius from the spectral synthesis modeling for 2MASS 2140+16A (top) and 2MASS 2104+16B (bottom).

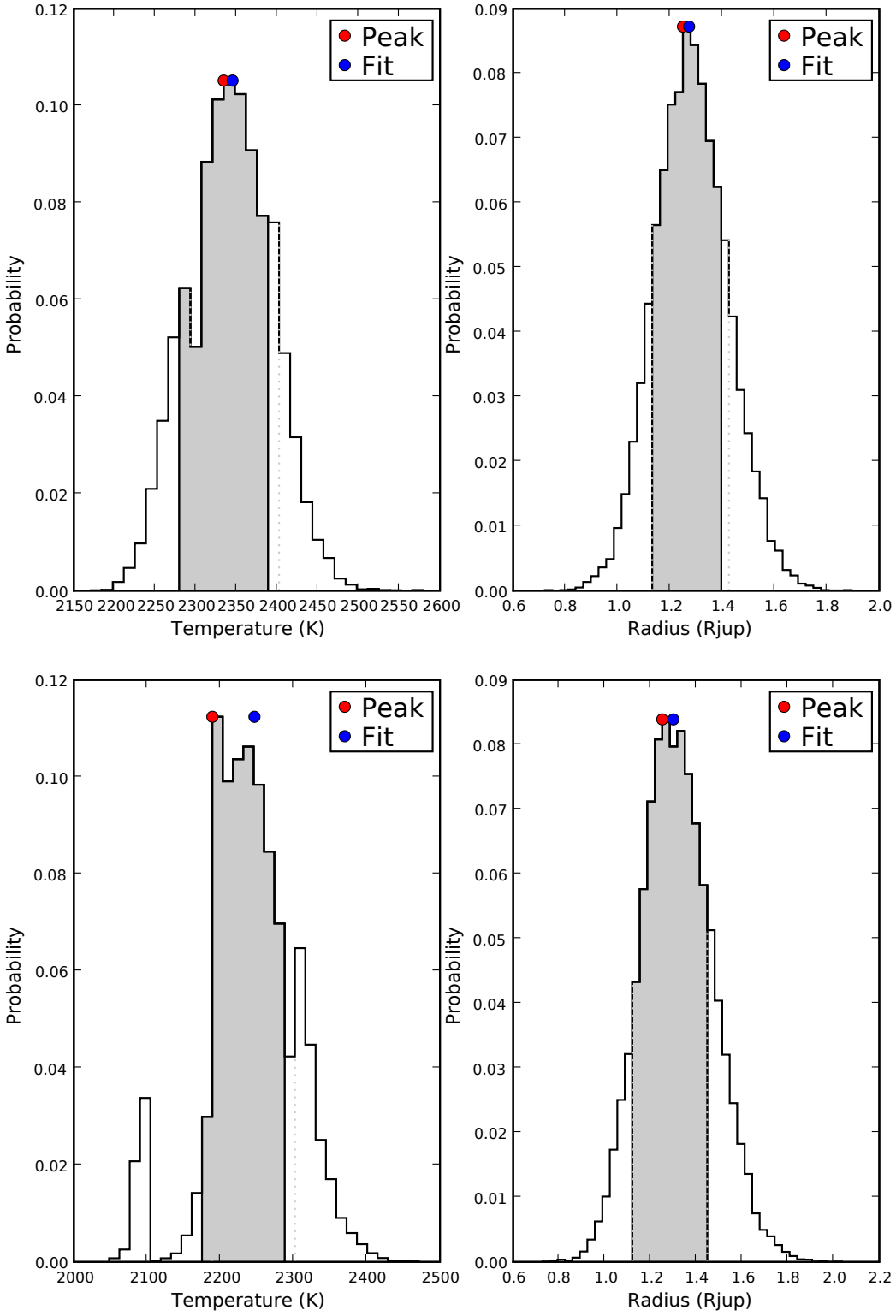

Figure 4.78 One dimensional PDFs of temperature and radius from the spectral synthesis modeling for 2MASS 2206-20A (top) and 2MASS 2206-20B (bottom).

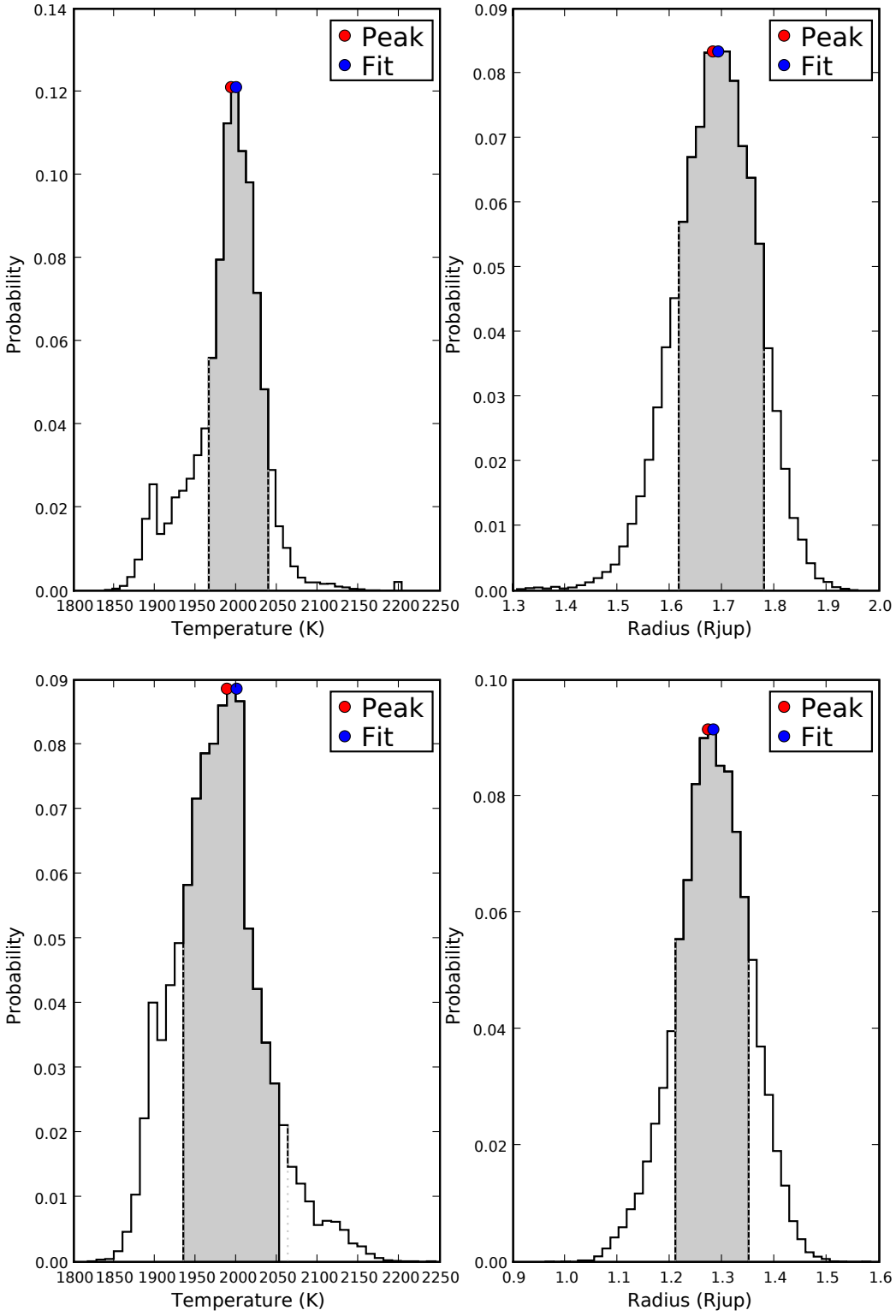

Figure 4.79 One dimensional PDFs of temperature and radius from the spectral synthesis modeling for GJ 569Ba (top) and GJ 569Bb (bottom).

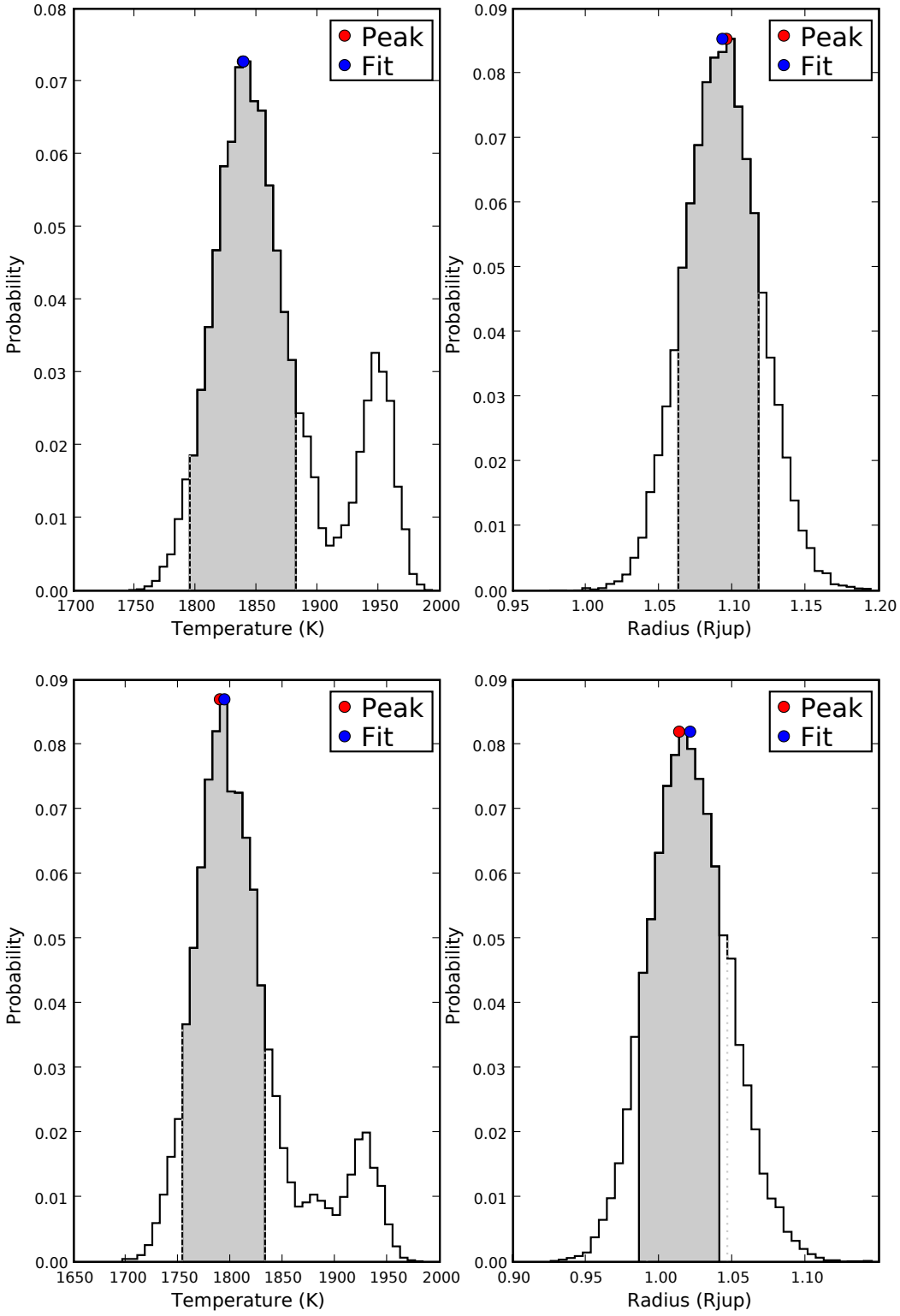

Figure 4.80 One dimensional PDFs of temperature and radius from the spectral synthesis modeling for HD 130948B (top) and HD 130948C (bottom).

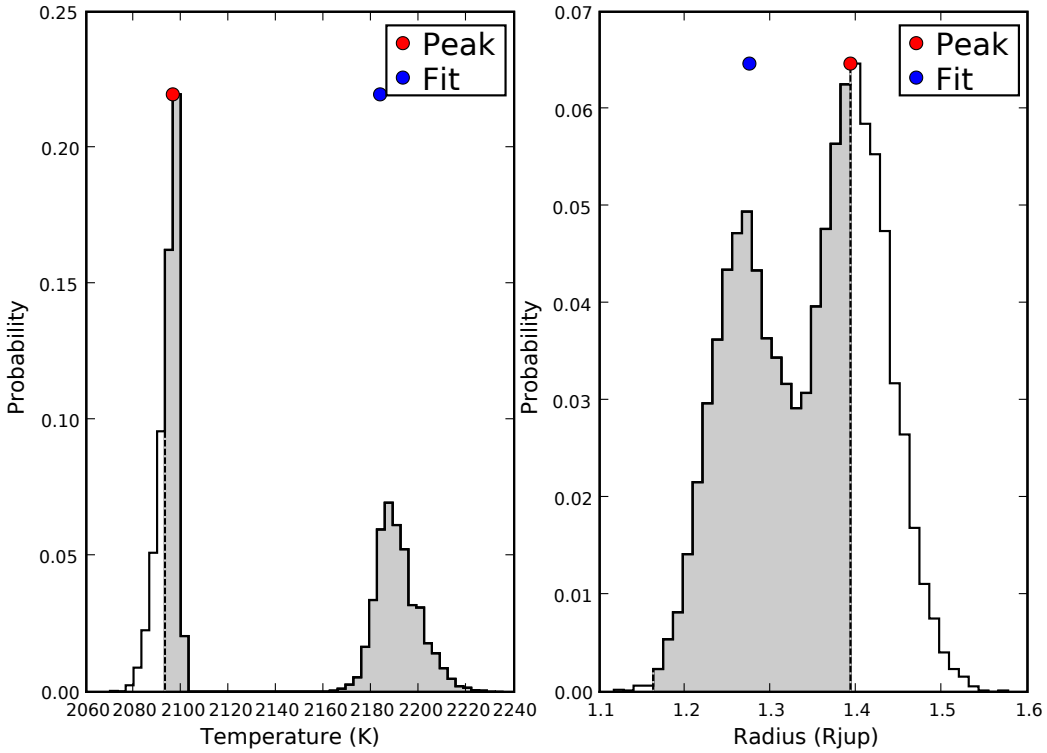

Figure 4.81 One dimensional PDFs of temperature and radius from the spectral synthesis modeling for LHS 2397a A. Since LHS 2397a B is an L/T transition object, it has not been fit with atmospheric models

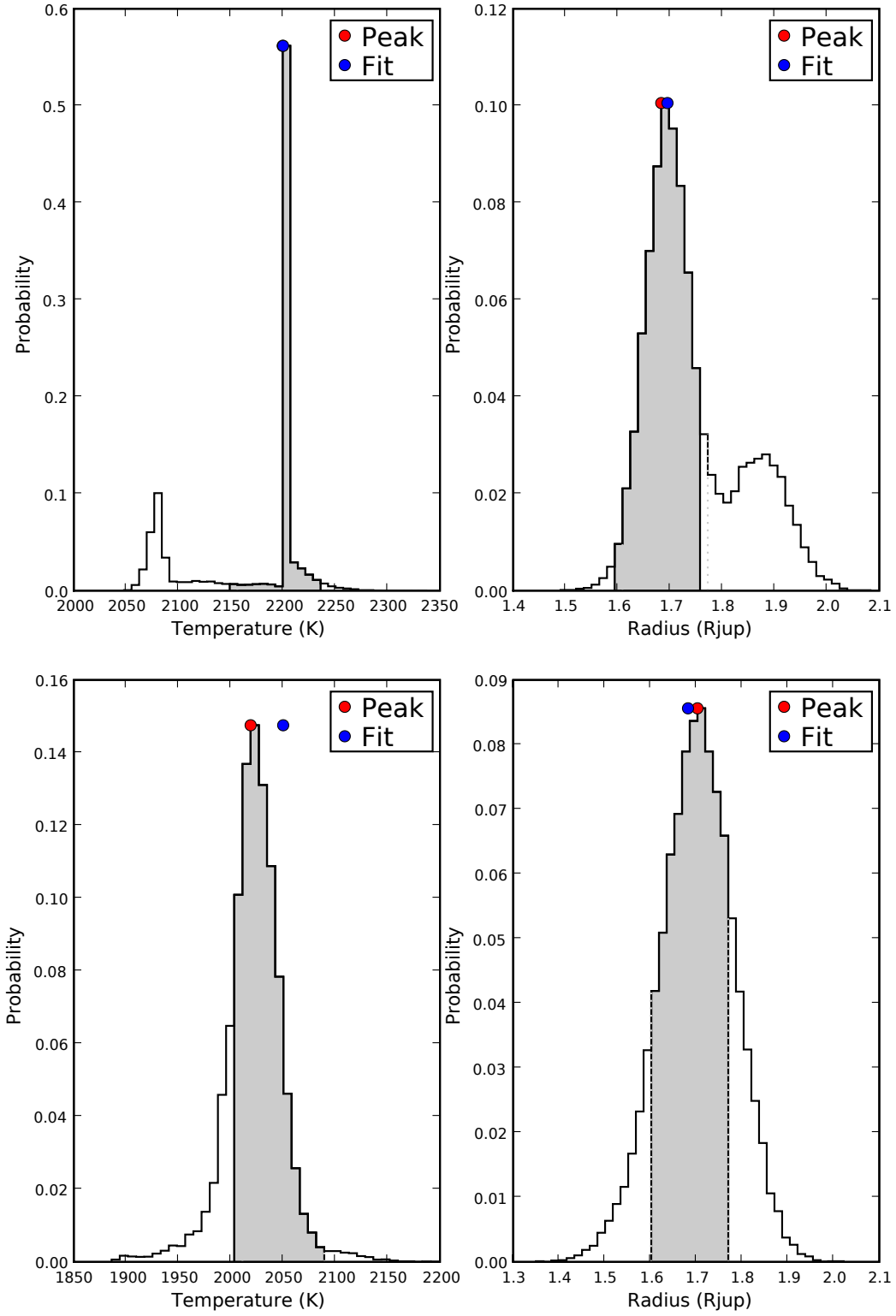

Figure 4.82 One dimensional PDFs of temperature and radius from the spectral synthesis modeling for LP 349-25A (top) and LP 349-25B (bottom).

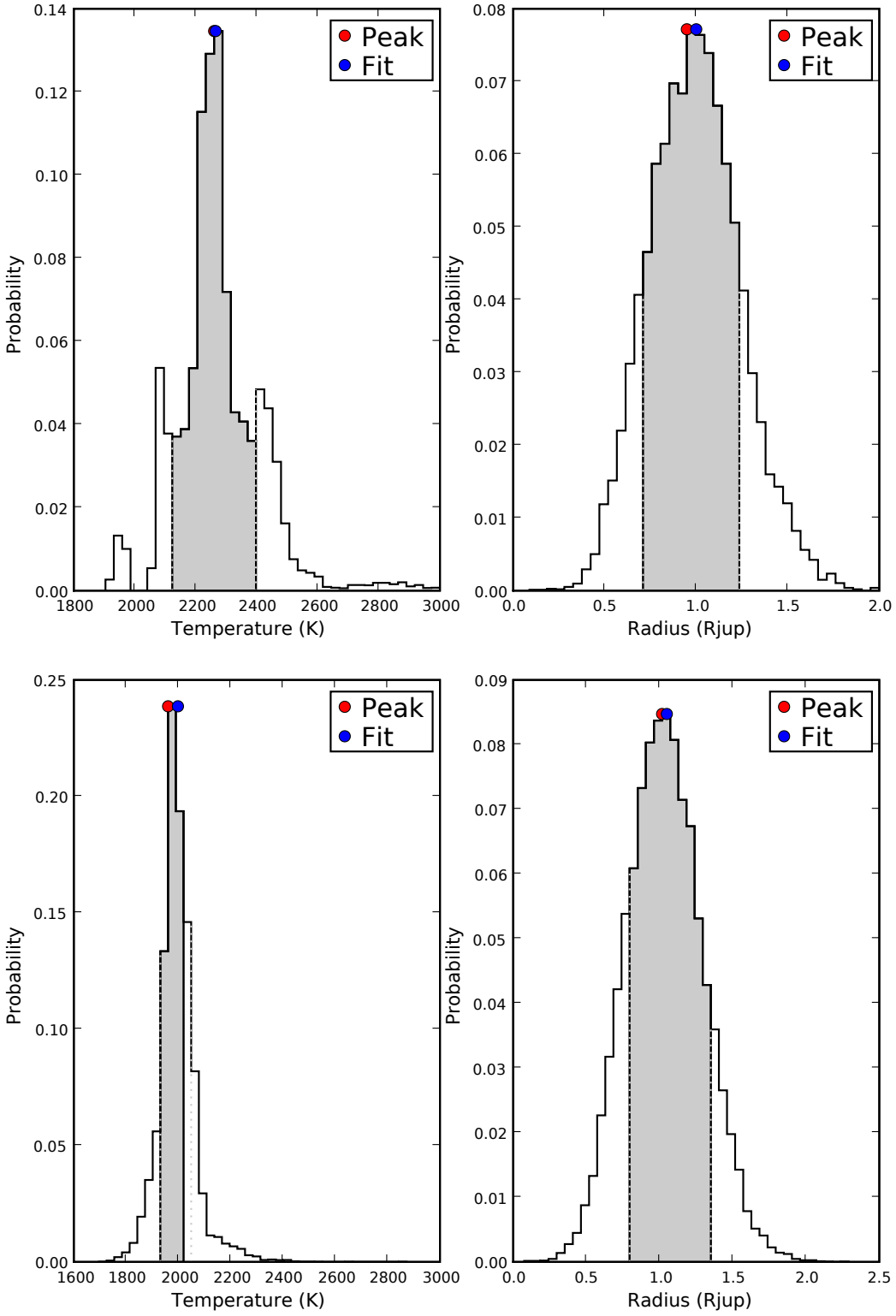

Figure 4.83 One dimensional PDFs of temperature and radius from the spectral synthesis modeling for LP 415-20A (top) and LP 415-20B (bottom).

4.6 Eccentricity Distribution

Using the distributions from our Monte Carlo simulations in section 4.4.1, we can begin to examine the bulk orbital properties of our sample of VLM objects. In particular, we can determine the distribution of eccentricities for our sample (9 of which are constrained to better than 30%), which may shed light on the formation of VLM binaries.

To determine our eccentricity distribution, we performed a Monte Carlo in which we randomly sampled one value of eccentricity per source from the distributions in Section 4.4.1. In each trial, the total number of sources per bin was calculated in bins of width 0.1 over the range of values from 0 to 1. We performed 10,000 of these trials, which gave a distribution for each bin of the number of expected sources. This distribution provided a predicted number of sources in each bin along with an uncertainty. We then combined distributions such that the final bin width was 0.2. The resulting distribution for our 15 sources is shown in the right panel of Figure 4.84.

We find that our sources tend to have moderate to low eccentricities, with the number falling off towards high eccentricities. We have overplotted on Figure 4.84 the result found by Duquennoy & Mayor (1991) for solar-like field stars with periods > 1000 days (all sources in our sample meet this criteria except GJ 569B, which has a period of 865 days). These authors found that longer period systems showed an eccentricity distribution that went as f(e) = 2e, consistent with what is expected if the distribution is a function of energy only (Ambartsumian 1937). Our distribution does not appear to follow this trend. Duquennoy & Mayor (1991) also found that eccentricity appeared to be a function of period, with longer period systems tending towards higher eccentricities (albeit with fairly large scatter past the tidal circularization period of $\sim$10 days). We also examined

the period as function of eccentricity. The relationship for our sample is shown in the right panel of Figure 4.84. We have overplotted the sources from Duquennoy & Mayor (1991) with periods greater than 865 days. Although we have fewer systems than those authors, our sample appears to be following the same trend, with eccentricity tending to increase as a function of period. A 2-dimensional K-S test between our distribution and the distribution from Duquennoy & Mayor (1991) shows that the two samples have an 11% chance of being drawn from the same distribution (therefore being consistent to within 1.6σ), suggesting the distributions are statistically consistent.

In our sample selection, we strove to minimize period in order to obtain mass estimates in a short timescale. We have therefore possibly preferentially selected systems with moderate to low eccentricities due to their relatively short periods. However, the right panel of Figure 4.84 shows that there are many systems in Duquennoy & Mayor (1991) of comparable periods to the majority of our sample that have higher eccentricities. An additional source of selection bias in our sample may stem from our assumptions during sample selection. Highly eccentric systems spend a long fraction of their orbit at wide separations. Binaries that had fairly wide separations at the time of their discovery tended to be cut through our sample selection process as described in Section 4.1. This could lead to highly eccentric systems being preferentially removed from our sample. With more time coverage, additional VLM systems will have their orbital solutions derived and help determine if this "overabundance" of low eccentricity systems is indeed a selection effect. If the overabundance is not a selection effect, it could have interesting implications for the formation and/or dynamical history of VLM binaries, and be another line of evidence in favor of the dynamical evolution of VLM objects being slightly different from that of stars (Konopacky et al. 2007b).

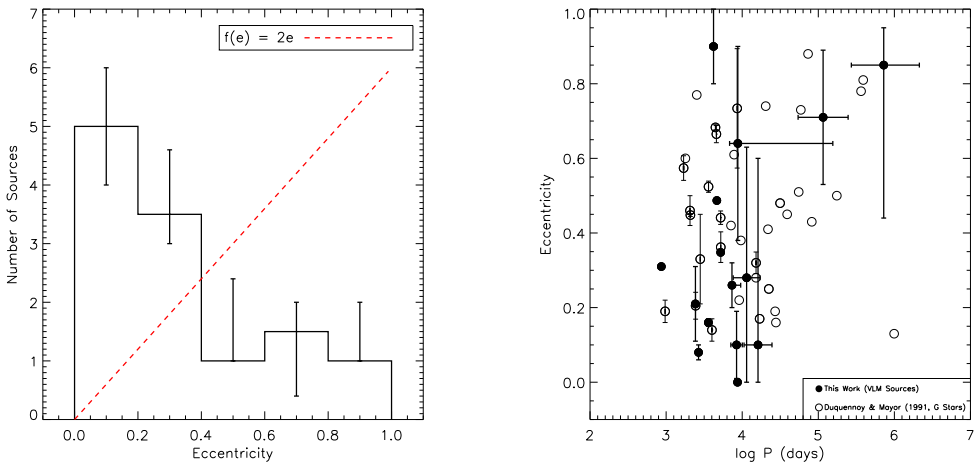

Figure 4.84 **Left:** The eccentricity distribution of our sample based on the eccentricity distributions for each source from the relative orbit Monte Carlos. Overplotted is the relation for field solar-like stars from Duquennoy & Mayor (1991), where f(e) = 2e (normalized to 15 systems). **Right:** Eccentricity as a function of period for the sources in our sample (filled circles). Overplotted are the systems from Duquennoy & Mayor (1991) with periods greater than 865 days (open circles). As in Duquennoy & Mayor (1991), eccentricity tends to increase with period.

4.7 Comparisons to the Predictions of Evolutionary Models

We use our derived temperatures and bolometric luminosities to determine the model-predicted mass for each source in our sample. We consider both the Chabrier et al. (2000) evolutionary models, called DUSTY and COND, and the Burrows et al. (1997) evolutionary models (TUCSON). The DUSTY and COND evolutionary models are named as such because they use the boundary condition between the interior and the atmosphere provided by the DUSTY and COND atmosphere models, respectively. Thus the evolutionary and atmosphere models are not strictly independent. In comparing to the Chabrier et al. (2000) evolutionary models, we are consistently testing model predictions because we have used the same atmospheric models in our analysis. Our comparisons to the Burrows et al. (1997) models thus must be caveated in this regard, as we do not have access to the atmospheric models they employ. However, we still perform the comparison to test the correspondence of these models to our measurements, as the effect of the atmospheric model boundary condition should only have a minor impact on the evolutionary predictions (Chabrier & Baraffe 2004).

To do this comparison, we first interpolate over the surface defined by the grids of temperature, luminosity, mass, and age provided by the evolutionary models using the INTERPOLATE function in the SciPy package for Python. We then determine which temperature and luminosity point on the interpolated surface is the closest to our input value of temperature and luminosity. For the sources from late-M to mid-L, we calculate the predictions of the DUSTY version of the Chabrier et al. (2000) models, while for the T dwarfs we use the COND version on these models. For the L/T transition objects, we calculate the predictions of both sets of Chabrier et al. (2000) models. The Burrows et al. (1997, TUCSON)

models do not assume a different atmospheric treatment for different spectral types and assume that dust species have condensed out of the atmosphere across the entire substellar regime. We therefore compare the predictions of these models to all objects in our sample. These comparisons provide the predicted mass and age for each source.

To determine the uncertainties in each model prediction of mass, we sample from temperatures and luminosities defined by the uncertainties in each for each sources, accounting for the correlations between bolometric luminosity and temperature (Konopacky et al. 2007a)[4]. The range of masses and ages predicted from this sampling, marginalized against the other parameters, provides our uncertainties. The values of mass predicted by each model is provided in Table 4.10. In the left panels of Figures 4.86 through 4.100, we show the location of the components of each binary on an H-R Diagram, with the lines of constant mass for each model overplotted in different colors. For clarity, the isochrones are omitted.

The majority of the sources in our sample have little to no age information - hence, we test for coevality as opposed to correct age prediction by the models. For the two sources with age information, HD 130948 BC ($\sim$500 Myr) and GJ 569Bab ($\sim$100 Myr), the uncertainties on these ages are such that both models predict ages for these systems that are consistent with these values. For all sources in our sample, all binary components are coeval within the uncertainties for all models. Figure 4.85 shows the predicted ages of the binary components in the DUSTY and the TUCSON models plotted versus each other. A line of 1:1 correspondence is overplotted. The predicted coevality is apparent from the

[4]In contrast to Konopacky et al. (2007a), we are not obtaining temperatures based upon the color of our systems. Our atmospheric model fits are only linked to bolometric luminosity through the K band magnitude, and thus the correlations between the two parameters are very weak in this study

Table 4.10. Evolutionary Model Predictions

Target Name	$M_{Primary}$ Tucson ($M_\odot$)	$M_{Secondary}$ (Tucscon ($M_\odot$)	M_{Total} Tucscon ($M_\odot$)	$M_{Primary}$ DUSTY ($M_\odot$)	$M_{Secondary}$ DUSTY ($M_\odot$)	M_{Total} DUSTY ($M_\odot$)	$M_{Primary}$ COND ($M_\odot$)	$M_{Secondary}$ COND ($M_\odot$)	M_{Total} COND ($M_\odot$)
2MASS 0746+20AB	0.050 ± 0.005	0.050 ± 0.010	0.10 ± 0.01	0.066 ± 0.005	0.060±0.010	0.13 ± 0.01	—	—	—
2MASS 0850+10AB	0.04 ± 0.04	0.04 ± 0.04	0.08 ± 0.06	$0.04^{+0.04}_{-0.03}$	$0.04^{+0.04}_{-0.03}$	$0.08^{+0.06}_{-0.04}$	$0.03^{+0.05}_{-0.03}$	$0.03^{+0.05}_{-0.03}$	$0.06^{+0.07}_{-0.04}$
2MASS 0920+35AB	0.04 ± 0.04	$0.03^{+0.05}_{-0.03}$	$0.07^{+0.06}_{-0.05}$	$0.04^{+0.04}_{-0.03}$	$0.03^{+0.05}_{-0.03}$	$0.07^{+0.06}_{-0.04}$	$0.03^{+0.05}_{-0.03}$	$0.03^{+0.05}_{-0.03}$	$0.06^{+0.07}_{-0.04}$
2MASS 1426+15AB	$0.03^{+0.04}_{-0.02}$	$0.04^{+0.04}_{-0.03}$	$0.07^{+0.06}_{-0.04}$	$0.04^{+0.04}_{-0.02}$	0.05 ± 0.03	$0.09^{+0.05}_{-0.04}$	—	—	—
2MASS 1534-29AB	0.06 ± 0.02	0.06 ± 0.02	0.12 ± 0.03	—	—	—	$0.04^{+0.03}_{-0.01}$	$0.04^{+0.04}_{-0.01}$	$0.08^{+0.05}_{-0.01}$
2MASS 1728+39AB	0.04 ± 0.04	$0.03^{+0.05}_{-0.03}$	$0.07^{+0.06}_{-0.05}$	0.04 ± 0.04	0.04 ± 0.04	0.08 ± 0.06	$0.03^{+0.05}_{-0.03}$	$0.03^{+0.04}_{-0.03}$	$0.06^{+0.06}_{-0.04}$
2MASS 1750+44AB	0.01 ± 0.01	$0.01^{+0.03}_{-0.01}$	$0.02^{+0.03}_{-0.01}$	0.02 ± 0.02	0.02 ± 0.02	0.04± 0.03	—	—	—
2MASS 1847+55AB	$0.02^{+0.03}_{-0.02}$	0.01 ± 0.01	$0.03^{+0.03}_{-0.02}$	$0.03^{+0.05}_{-0.02}$	$0.01^{+0.02}_{-0.01}$	$0.04^{+0.05}_{-0.02}$	—	—	—
2MASS 2140+16AB	$0.04^{+0.05}_{-0.03}$	$0.07^{+0.03}_{-0.05}$	0.11 ± 0.06	0.06 ± 0.04	$0.07^{+0.03}_{-0.04}$	$0.13^{+0.05}_{-0.06}$	—	—	—
2MASS 2206-20AB	0.032 ± 0.010	$0.026^{+0.007}_{-0.010}$	$0.058^{+0.012}_{-0.014}$	$0.047^{+0.016}_{-0.012}$	$0.037^{+0.011}_{-0.009}$	$0.084^{+0.019}_{-0.015}$	—	—	—
GJ569B ab	0.01 ± 0.01	0.02 ± 0.01	0.03± 0.01	0.015 ± 0.005	$0.027^{+0.013}_{-0.007}$	$0.042^{+0.014}_{-0.009}$	—	—	—
HD 130948BC	0.030 ± 0.010	0.032 ± 0.010	0.062 ± 0.014	0.035 ± 0.010	$0.037^{+0.013}_{-0.010}$	$0.072^{+0.016}_{-0.014}$	—	—	—
LHS2397a AB	0.02 ± 0.01	0.04 ± 0.04	0.06 ± 0.04	0.03 ± 0.01	0.04 ± 0.04	0.07 ± 0.04	—	$0.03^{+0.04}_{-0.03}$	$0.06^{+0.04}_{-0.03}$[a]
LP 349-25AB	0.014 ± 0.005	0.010 ± 0.005	0.024 ± 0.007	0.024 ± 0.005	0.020 ± 0.005	0.044 ± 0.007	—	—	—
LP 415-20AB	$0.06^{+0.04}_{-0.03}$	0.05 ± 0.03	$0.11^{+0.05}_{-0.04}$	$0.08^{+0.02}_{-0.05}$	$0.06^{+0.02}_{-0.04}$	$0.14^{+0.03}_{-0.06}$	—	—	—

[a]Total mass found by adding DUSTY prediction for primary to COND prediction for secondary

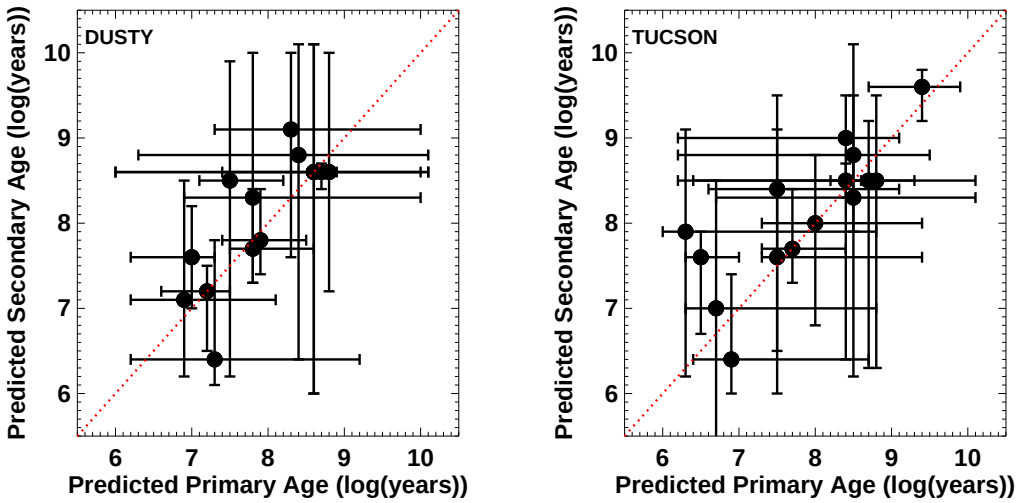

Figure 4.85 The predicted ages for secondary components versus primary components by the DUSTY (**left**) and TUCSON (**right**) models. The line of 1:1 correspondence is plotted in red. Within the uncertainties, all binary components are predicted to be coeval for all models.

figure. The relatively large uncertainty in age estimates stems from the fact that the model isochrones become more closely packed at with increasing age. Because of this fact, empirical age estimates for field objects provide relatively weak constraints on the models.

Since our highest precision measurements are currently in total system mass, we can most effectively compare model predictions to these measurements. To do this, we add the model masses derived for each component together and add their uncertainties in quadrature. The combined mass predictions are also given in Table 4.10. In the right panels of Figures 4.86 through 4.100, we show the combined mass prediction for each model in relation to the allowed total system mass from the relative orbital solutions. We find that for 7 systems, all models underpredict the total system mass by greater than 1σ. These 7 systems have the smallest uncertainties in dynamical mass and primary component spectral types

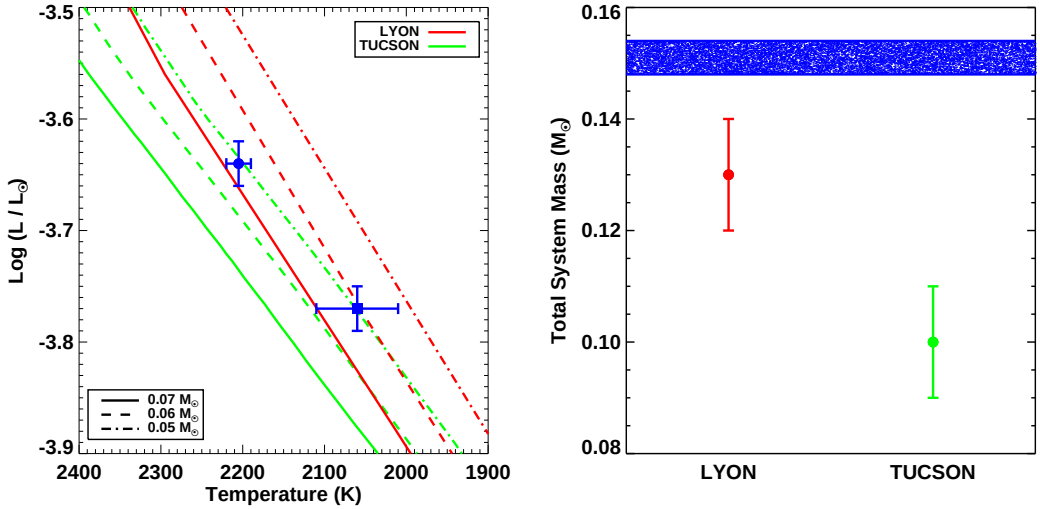

Figure 4.86 **Left:** H-R Diagram showing the location of the components of 2MASS 0746+20AB (circle is the primary, square is the secondary) in relation to the lines of constant mass for the TUCSON and DUSTY evolutionary models. **Right:** The total mass given by the relative orbital solution is plotted as a blue shaded region (the height representing 1σ). The total mass prediction of each model is also plotted. Both models underpredict the total system mass for 2MASS 0746+20 AB.

earlier than L4. For 7 systems, we find that all models considered predict masses that are consistent with the dynamical mass within 1σ. These systems all have mass uncertainties over 60%, and also generally higher temperature uncertainties. Finally, we find that the mass of one system is overpredicted by both models by greater than 1σ and is the only system with a mid-T spectral type.

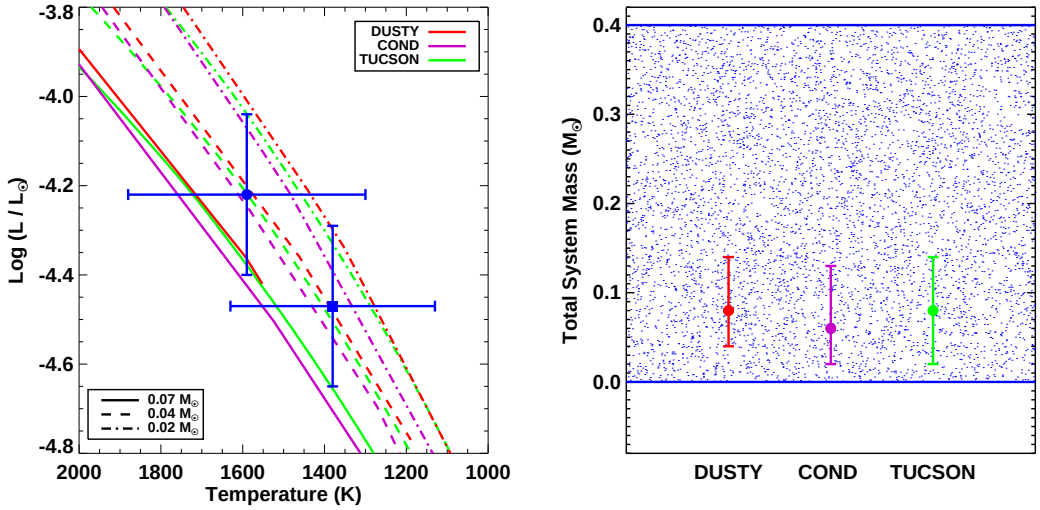

Figure 4.87 **Left:** H-R Diagram showing the location of the components of 2MASS 0850+10AB (circle is the primary, square is the secondary) in relation to the lines of constant mass for the TUCSON, DUSTY, and COND evolutionary models. **Right:** The total mass given by the relative orbital solution is plotted as a blue shaded region (the height representing 1σ). The total mass prediction of each model is also plotted. Within current dynamical mass and temperature uncertainties, all models are consistent with our measurement.

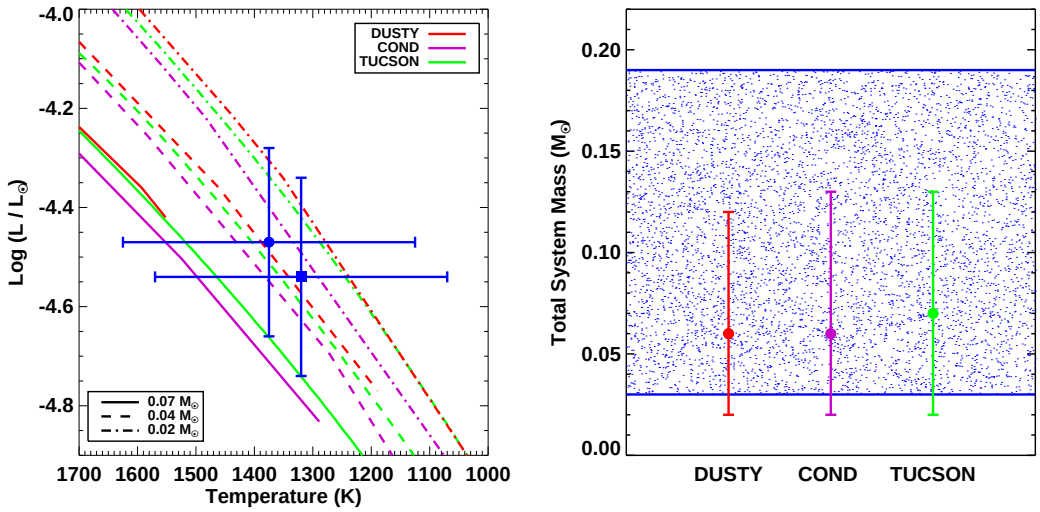

Figure 4.88 **Left:** H-R Diagram showing the location of the components of 2MASS 0920+35AB (circle is the primary, square is the secondary) in relation to the lines of constant mass for the TUCSON, DUSTY, and COND evolutionary models. **Right:** The total mass given by the relative orbital solution is plotted as a blue shaded region (the height representing 1σ). The total mass prediction of each model is also plotted. Within current dynamical mass and temperature uncertainties, all models are consistent with our measurement.

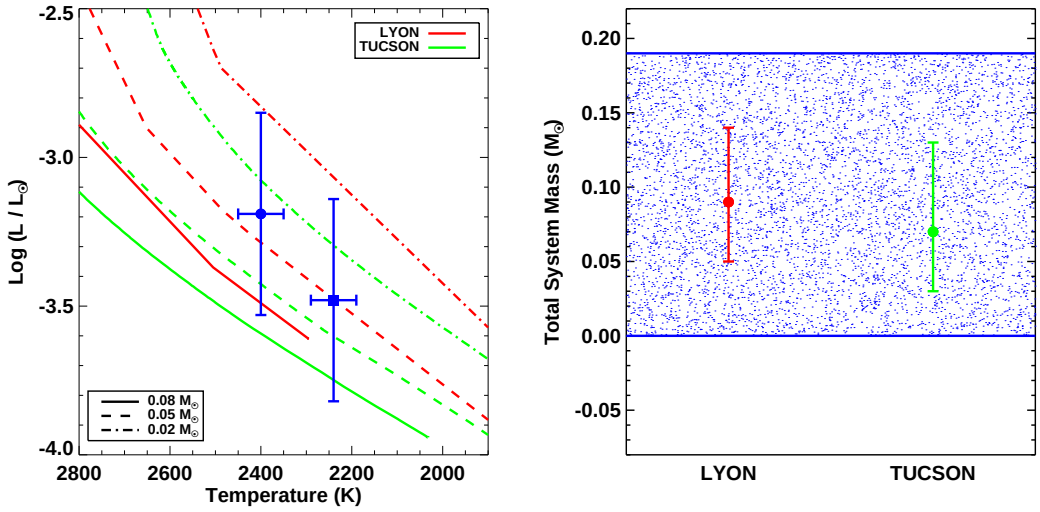

Figure 4.89 **Left:** H-R Diagram showing the location of the components of 2MASS 1426+15AB (circle is the primary, square is the secondary) in relation to the lines of constant mass for the TUCSON and DUSTY evolutionary models. Although the primary appears to have a lower mass than the secondary, implying the models do not predict coevality for the components, within the uncertainties the components are coeval. **Right:** The total mass given by the relative orbital solution is plotted as a blue shaded region (the height representing 1σ). The total mass prediction of each model is also plotted. Within current dynamical mass and temperature uncertainties, all models are consistent with our measurement.

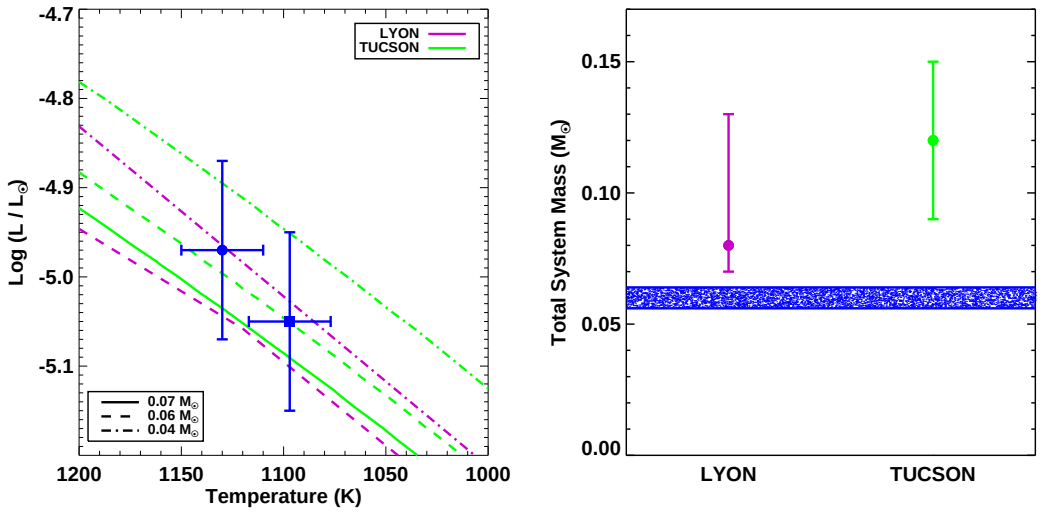

Figure 4.90 **Left:** H-R Diagram showing the location of the components of 2MASS 1534-29AB (circle is the primary, square is the secondary) in relation to the lines of constant mass for the TUCSON and COND evolutionary models. **Right:** The total mass given by the relative orbital solution is plotted as a blue shaded region (the height representing 1σ). The total mass prediction of each model is also plotted. Both models overpredict the dynamical mass of this system.

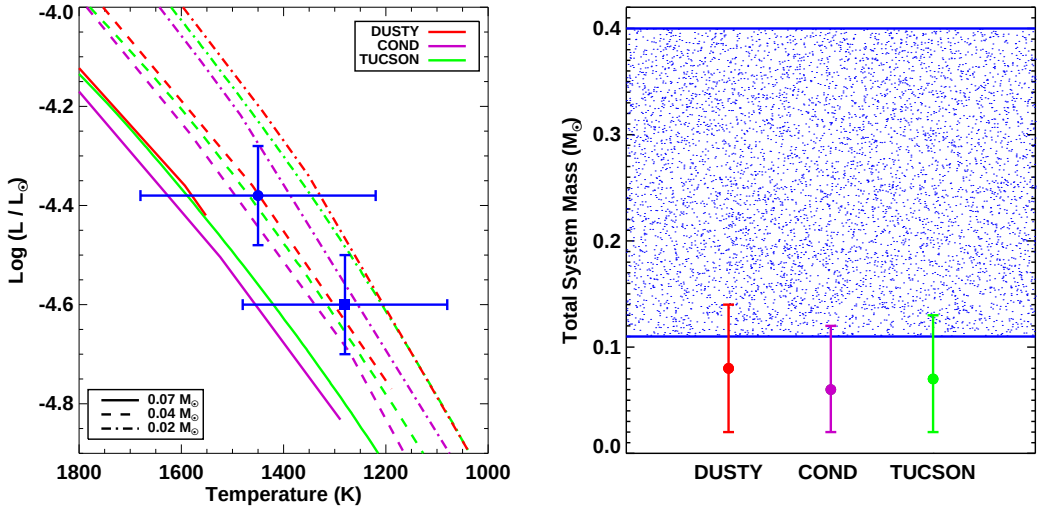

Figure 4.91 **Left:** H-R Diagram showing the location of the components of 2MASS 1728+39AB (circle is the primary, square is the secondary) in relation to the lines of constant mass for the TUCSON, DUSTY, and COND evolutionary models. **Right:** The total mass given by the relative orbital solution is plotted as a blue shaded region (the height representing 1σ). The total mass prediction of each model is also plotted. Within current dynamical mass and temperature uncertainties, all models are consistent with our measurement.

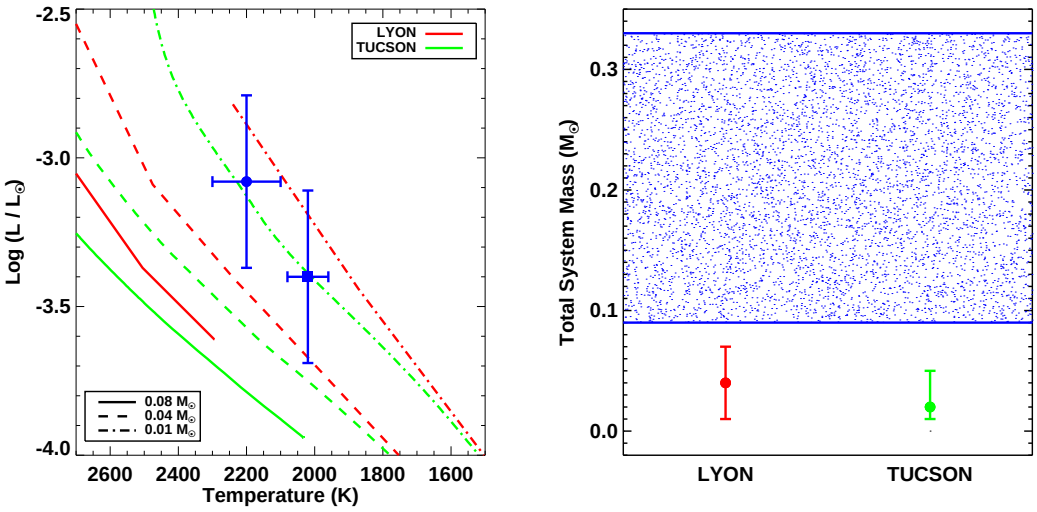

Figure 4.92 **Left:** H-R Diagram showing the location of the components of 2MASS 1750+44AB (circle is the primary, square is the secondary) in relation to the lines of constant mass for the TUCSON and DUSTY evolutionary models. **Right:** The total mass given by the relative orbital solution is plotted as a blue shaded region (the height representing 1σ). The total mass prediction of each model is also plotted. Both models underpredict the total system mass of 2MASS 1750+44AB

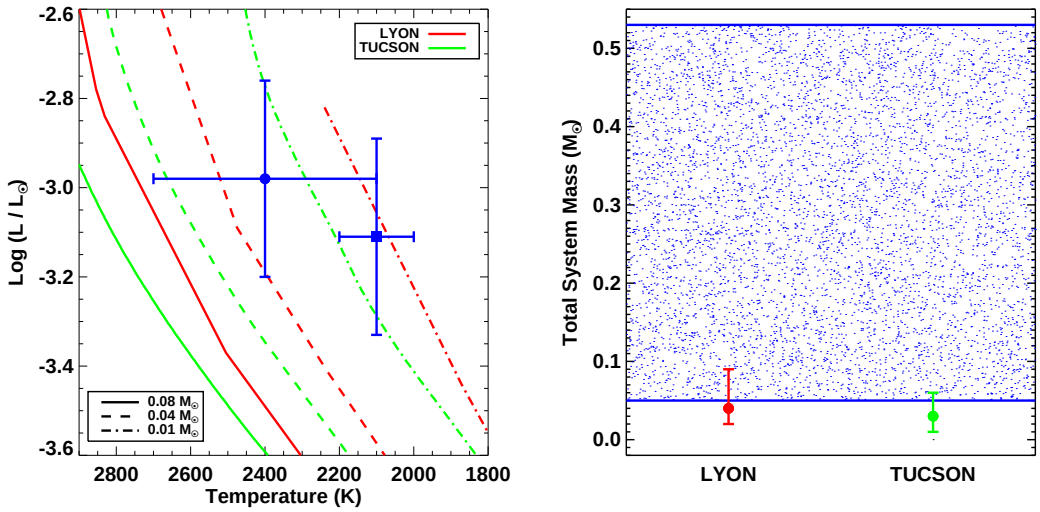

Figure 4.93 **Left:** H-R Diagram showing the location of the components of 2MASS 1847+55AB (circle is the primary, square is the secondary) in relation to the lines of constant mass for the TUCSON and DUSTY evolutionary models. **Right:** The total mass given by the relative orbital solution is plotted as a blue shaded region (the height representing 1σ). The total mass prediction of each model is also plotted. Within current dynamical mass and temperature uncertainties, all models are consistent with our measurement.

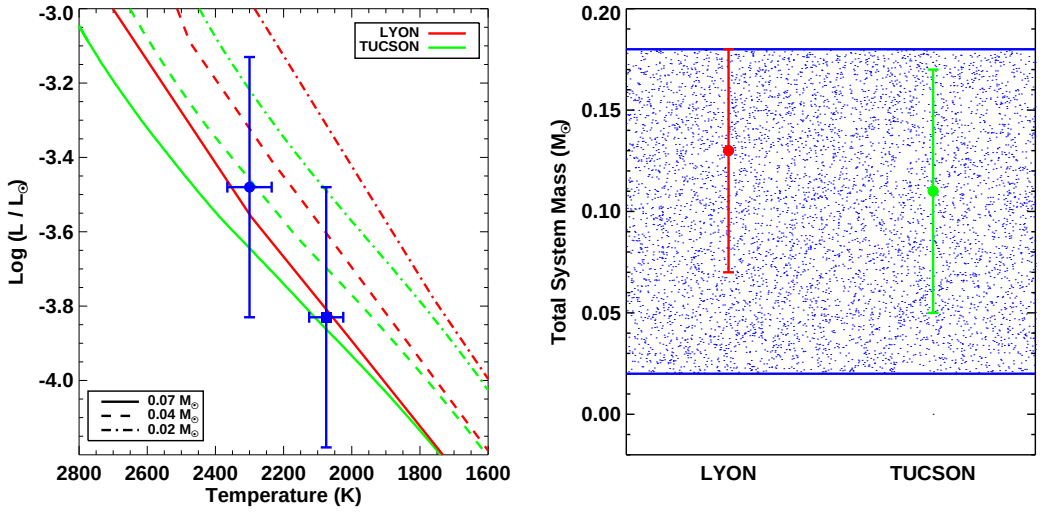

Figure 4.94 **Left:** H-R Diagram showing the location of the components of 2MASS 2140+16AB (circle is the primary, square is the secondary) in relation to the lines of constant mass for the TUCSON and DUSTY evolutionary models. Though secondary is predicted to be more massive than the primary in both models, implying that the components are not coeval, the components are coeval to within their uncertainties. **Right:** The total mass given by the relative orbital solution is plotted as a blue shaded region (the height representing 1σ). The total mass prediction of each model is also plotted. Within current dynamical mass and temperature uncertainties, all models are consistent with our measurement.

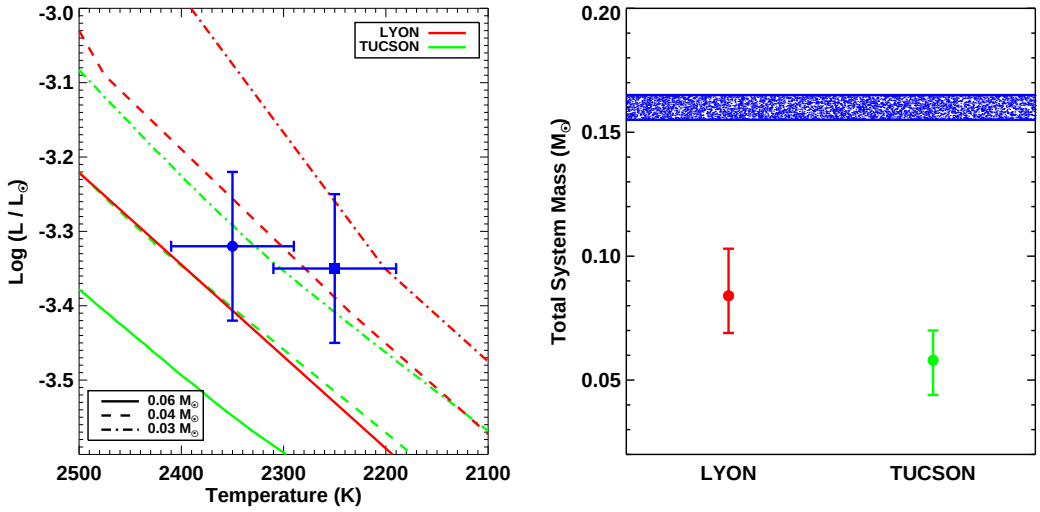

Figure 4.95 **Left:** H-R Diagram showing the location of the components of 2MASS 2206-20AB (circle is the primary, square is the secondary) in relation to the lines of constant mass for the TUCSON and DUSTY evolutionary models. **Right:** The total mass given by the relative orbital solution is plotted as a blue shaded region (the height representing 1σ). The total mass prediction of each model is also plotted. Both models underpredict the total system mass for 2MASS 2206-20 AB.

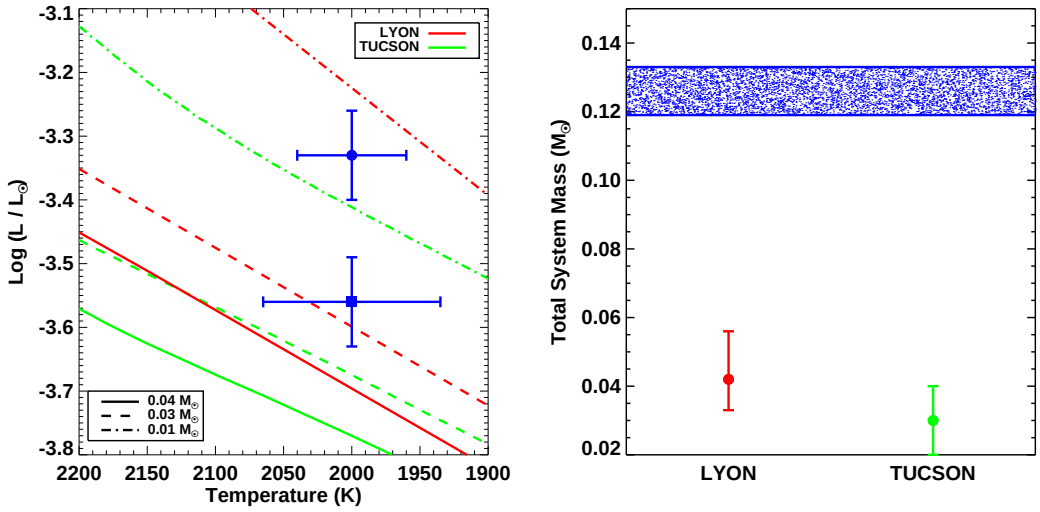

Figure 4.96 **Left:** H-R Diagram showing the location of the components of GJ 569Bab (circle is the primary, square is the secondary) in relation to the lines of constant mass for the TUCSON and DUSTY evolutionary models. Though secondary is predicted to be more massive than the primary in both models, implying that the components are not coeval, the components are coeval to within their uncertainties. **Right:** The total mass given by the relative orbital solution is plotted as a blue shaded region (the height representing 1σ). The total mass prediction of each model is also plotted. Both models underpredict the total system mass for GJ 569Bab.

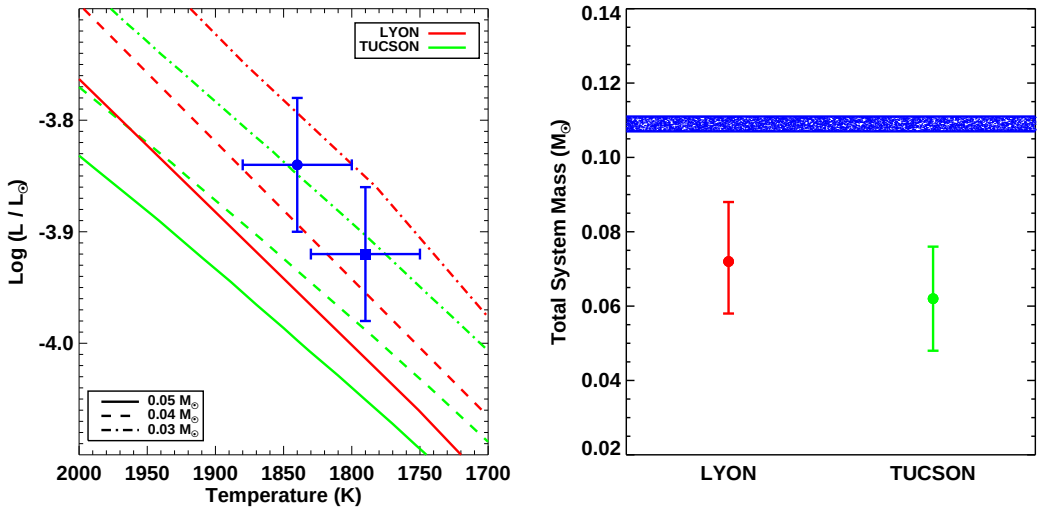

Figure 4.97 **Left:** H-R Diagram showing the location of the components of HD 130948 BC (circle is the primary, square is the secondary) in relation to the lines of constant mass for the TUCSON and DUSTY evolutionary models. Though secondary is predicted to be more massive than the primary in both models, implying that the components are not coeval, the components are coeval to within their uncertainties. **Right:** The total mass given by the relative orbital solution is plotted as a blue shaded region (the height representing 1σ). The total mass prediction of each model is also plotted. Both models underpredict the total system mass for HD 130948 BC.

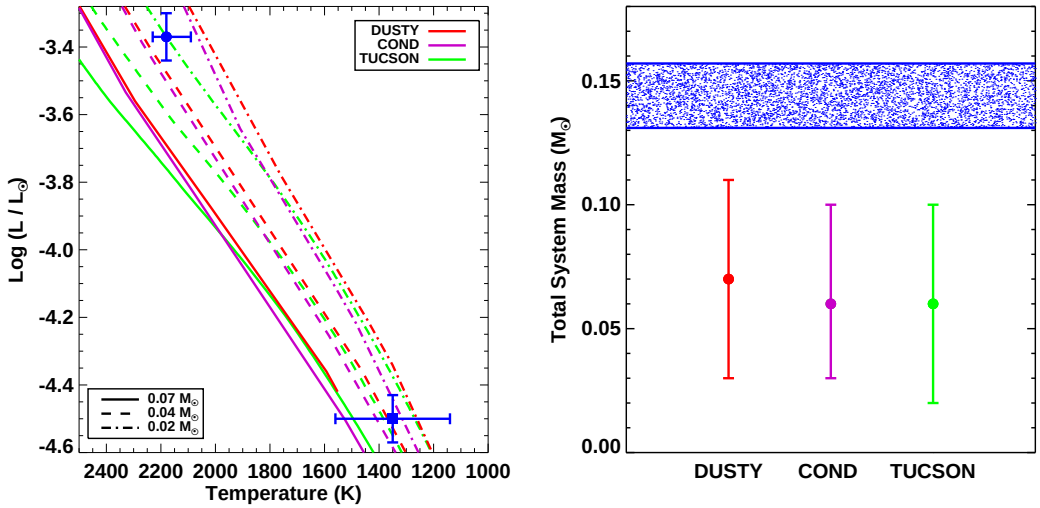

Figure 4.98 **Left:** H-R Diagram showing the location of the components of LHS 2397a AB (circle is the primary, square is the secondary) in relation to the lines of constant mass for the TUCSON, COND (secondary only), and DUSTY evolutionary models. Though secondary is predicted to be more massive than the primary in both models, implying that the components are not coeval, the components are coeval to within their uncertainties, which are dominated by the uncertainty in the temperature of the secondary. **Right:** The total mass given by the relative orbital solution is plotted as a blue shaded region (the height representing 1σ). The total mass prediction of each model is also plotted. Both models underpredict the total system mass for LHS 2387a AB.

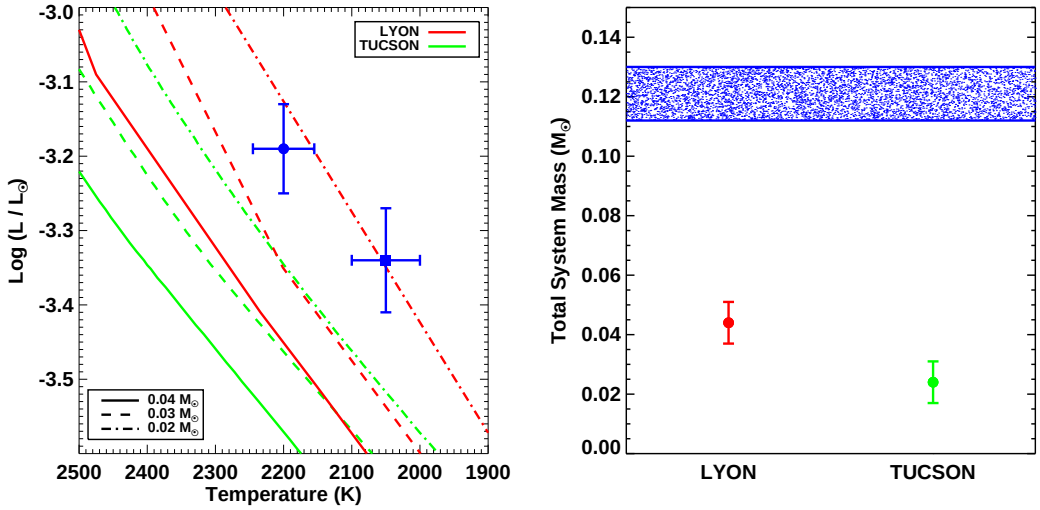

Figure 4.99 **Left:** H-R Diagram showing the location of the components of LP 349-25 AB (circle is the primary, square is the secondary) in relation to the lines of constant mass for the TUCSON and DUSTY evolutionary models. **Right:** The total mass given by the relative orbital solution is plotted as a blue shaded region (the height representing 1σ). The total mass prediction of each model is also plotted. Both models underpredict the total system mass for LP 349-25 AB.

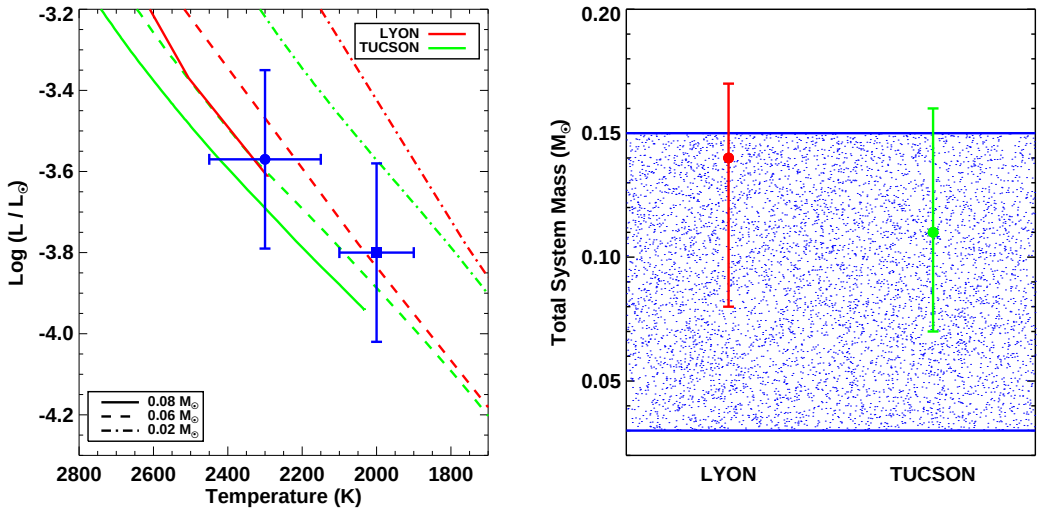

Figure 4.100 **Left:** H-R Diagram showing the location of the components of LP 415-20 AB (circle is the primary, square is the secondary) in relation to the lines of constant mass for the TUCSON and DUSTY evolutionary models. Model comparison problematic here because large portion of the secondary error ellipse falls below the model coverage, implying unphysically old ages. Ranges of model predictions should, however, be reasonable given the large uncertainties in the luminosity and temperature of these components **Right:** The total mass given by the relative orbital solution is plotted as a blue shaded region (the height representing 1σ). The total mass prediction of each model is also plotted. Within the current uncertainties, both models correctly predict the total system mass for LP 415-20 AB.

To illustrate the apparent trend in mass discrepancy with spectral type, we have plotted the percent difference between the model prediction and the total dynamical mass for each model. These plots are shown in Figures 4.101 and 4.102. It is clear that the discrepancies in total system mass peak for those sources with the earliest spectral types in our sample, reach a minimum at the L/T transition (though all sources in this region have fairly large uncertainties in dynamical mass), and then appear again for one T dwarf source.

We can test the predictions of the models a bit further by considering our handful of individual mass measurements. The model predictions versus each individual mass measurement are shown in Figures 4.103 though 4.108. Although our individual mass measurements do not yet have the high precision we have achieved in total mass, we can already see for the most precise cases that the discrepancy holds. That is, for the primary components of 2MASS 2206-20AB, GJ 569Bab, and LHS 2397a AB (which have the highest precision in component mass), the models underpredict the mass. These three systems all have approximate spectral types of M8. We also see that the secondary components of GJ 569Bab and LP 349-25 AB have their masses underpredicted by the models. These systems are both of approximate spectral type M9.

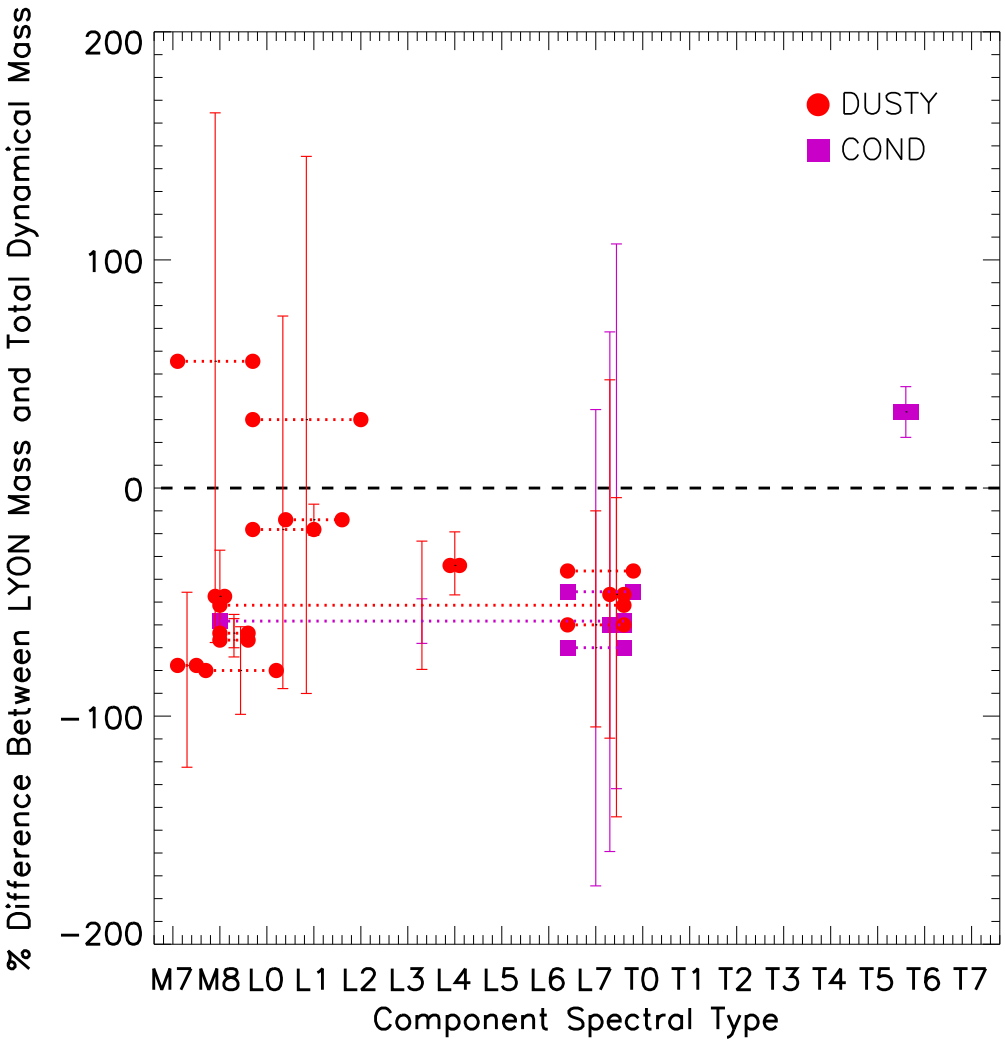

Figure 4.101 The percent difference between the predictions of the Lyon (both DUSTY and COND, Chabrier et al. 2000) models and our total dynamical masses as a function of spectral type. Each system is denoted by the spectral type of its components, which are connected with a horizontal bar. We find that 7 of the 14 systems we have compared to the DUSTY models have their masses underpredicted by these models. These systems all have primary component spectral types earlier than L4. We find that one T dwarf system we compared to the COND models has its mass overpredicted by the models. All sources with primary component spectral types in the L/T transition region have mass predictions that are consistent with the total dynamical mass.

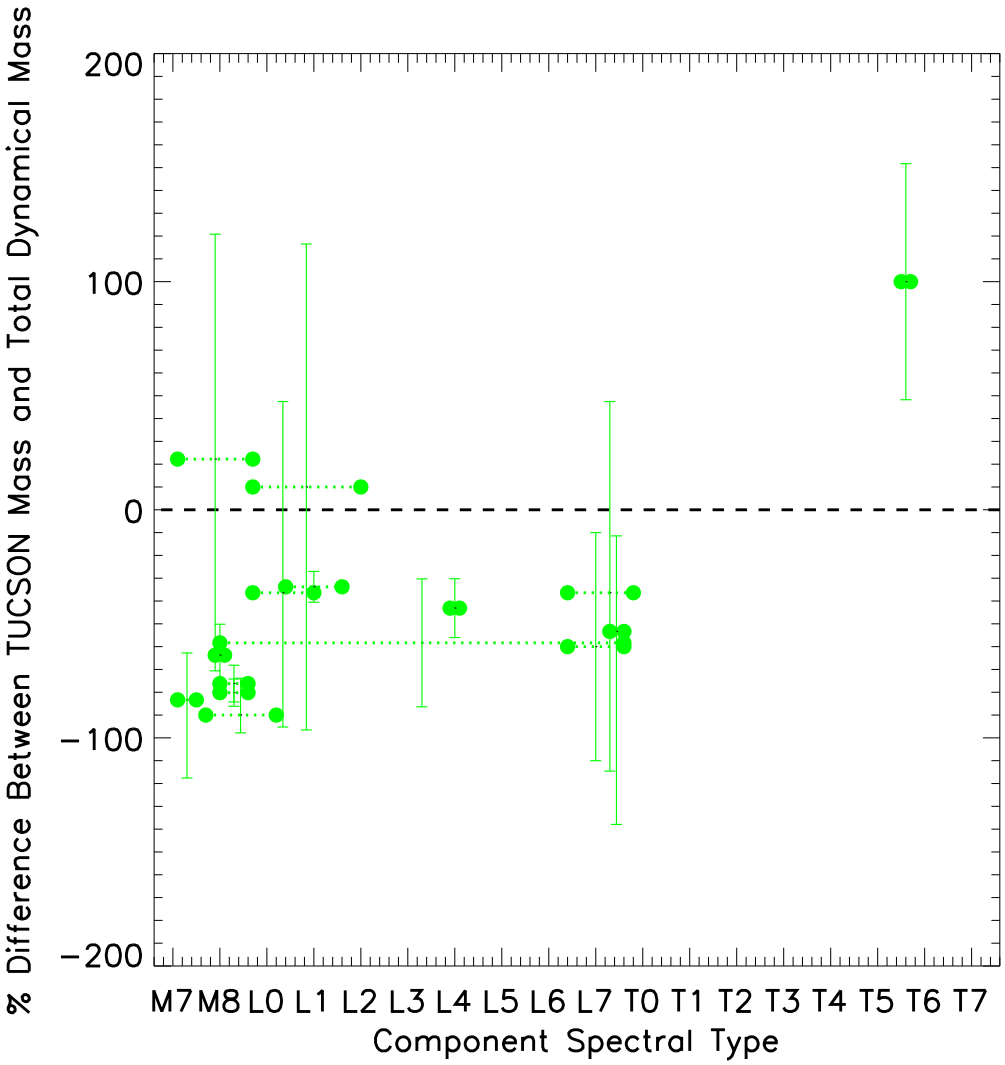

Figure 4.102 The percent difference between the predictions of the TUCSON (Burrows et al. 1997) models and our total dynamical masses as a function of spectral type. We caveat that while we have used different atmospheric models to derive effective temperature than is employed in the Burrows et al. (1997) models, the effect of the atmospheric model is thought to be minor. We have compared all 15 systems to these models. We find that 7 systems have their masses underpredicted by these models, all of which have primary component spectral types earlier than L4. We find that one mid-T system has its mass overpredicted by the models. All sources with primary component spectral types in the L/T transition region have mass predictions that are consistent with the total dynamical mass.

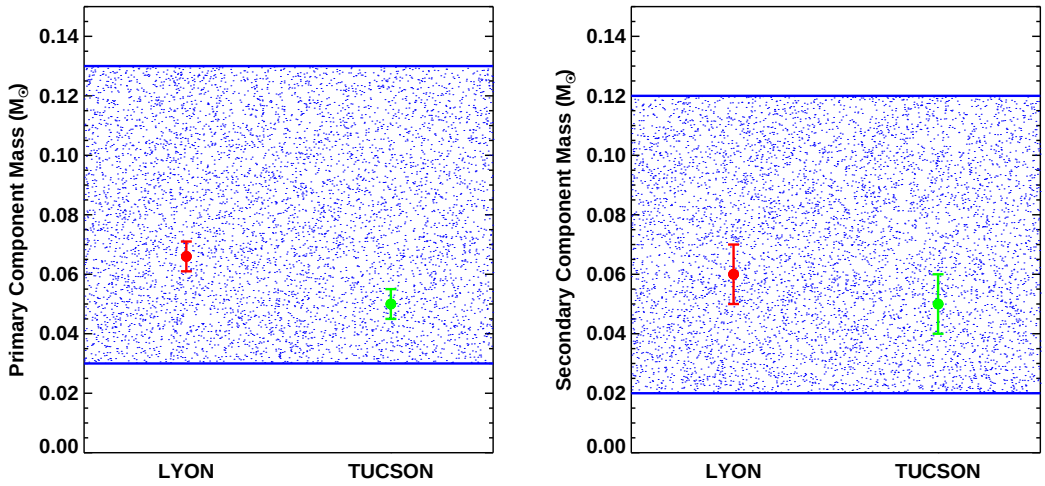

Figure 4.103 **Left**: The component mass of the primary, 2MASS 0746+20 A, given by the absolute orbital solution is plotted as a blue shaded region (the height representing 1σ). The mass prediction of each model is also plotted. Within the current uncertainties, both models correctly predict the mass of 2MASS 0746+20 A. **Right**: The component mass of the secondary, 2MASS 0746+20 B, given by the absolute orbital solution is plotted as a blue shaded region (the height representing 1σ). The mass prediction of each model is also plotted. Within the current uncertainties, both models predict the correct mass for this 2MASS 0746+20 B

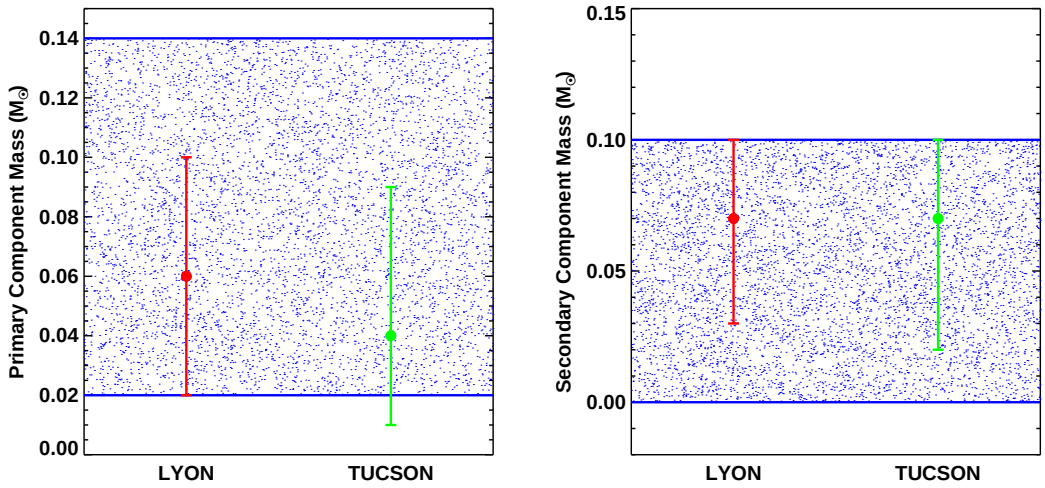

Figure 4.104 **Left**: The component mass of the primary, 2MASS 2140+16 A, given by the absolute orbital solution is plotted as a blue shaded region (the height representing 1σ). The mass prediction of each model is also plotted. With the current uncertainties, both models correctly predict the mass of 2MASS 2140+16 A. **Right**: The component mass of the secondary, 2MASS 2140+16 B, given by the absolute orbital solution is plotted as a blue shaded region (the height representing 1σ). The mass prediction of each model is also plotted. Within the current uncertainties, both models predict the correct mass for this 2MASS 2140+16 B

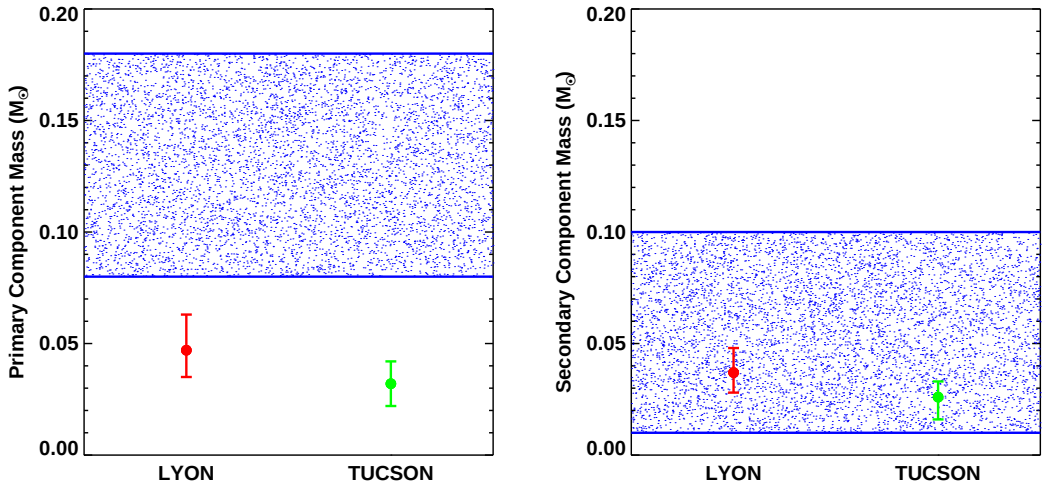

Figure 4.105 **Left**: The component mass of the primary, 2MASS 2206-20 A, given by the absolute orbital solution is plotted as a blue shaded region (the height representing 1σ). The mass prediction of each model is also plotted. Both models underpredict the mass of 2MASS 2206-20 A. **Right**: The component mass of the secondary, 2MASS 2206-20 B, given by the absolute orbital solution is plotted as a blue shaded region (the height representing 1σ). The mass prediction of each model is also plotted. Within the current uncertainties, both models predict the correct mass for this system

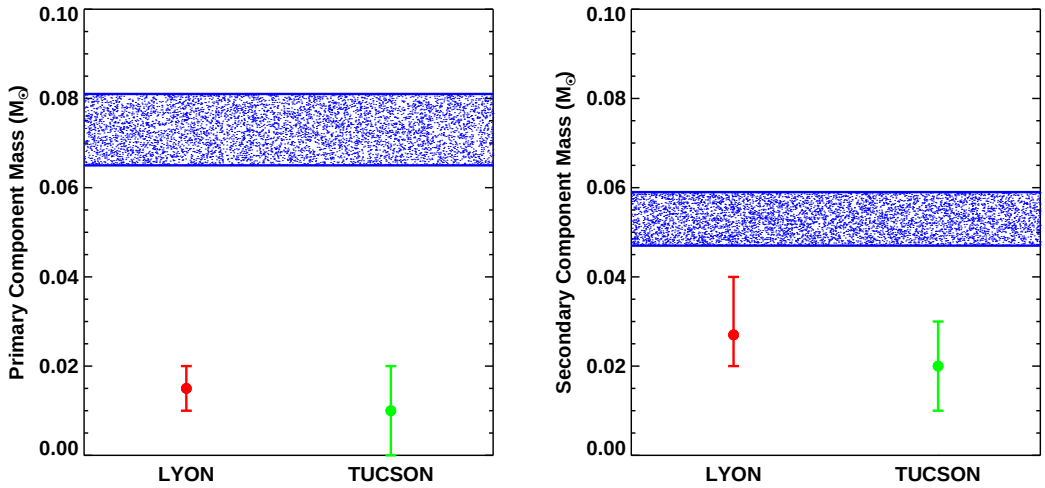

Figure 4.106 **Left**: The component mass of the primary, GJ 569Ba, given by the absolute orbital solution is plotted as a blue shaded region (the height representing 1σ). The mass prediction of each model is also plotted. Both models underpredict the mass of GJ 569Ba. **Right**: The component mass of the secondary, GJ 569Bb, given by the absolute orbital solution is plotted as a blue shaded region (the height representing 1σ). The mass prediction of each model is also plotted. Both models underpredict the mass of GJ 569Bb.

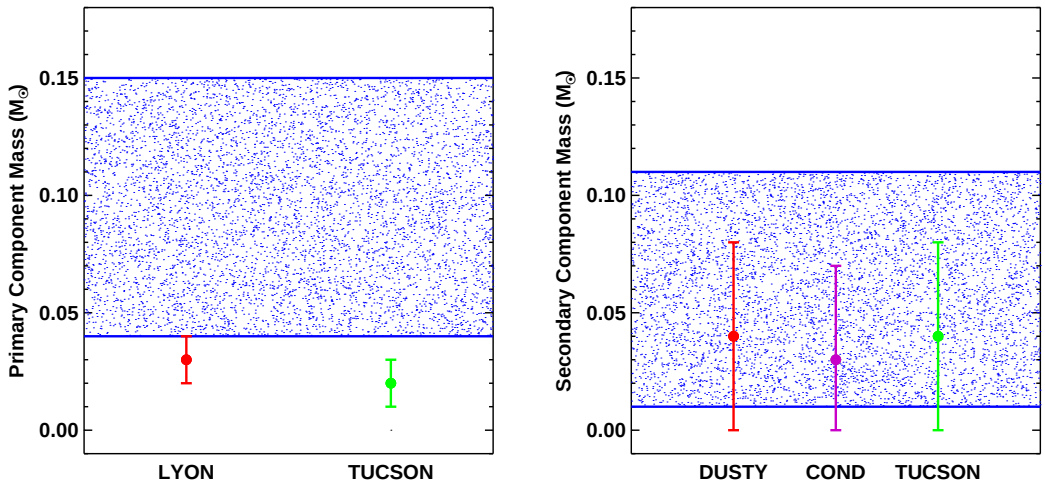

Figure 4.107 **Left**: The component mass of the primary, LHS 2397a A, given by the absolute orbital solution is plotted as a blue shaded region (the height representing 1σ). The mass prediction of each model is also plotted. Within the current uncertainties, the DUSTY models predict a mass marginally consistent with the mass of LHS 2397a A, which the TUCSON models underpredict the mass of this source. **Right**: The component mass of the secondary, LHS 2397a B, given by the absolute orbital solution is plotted as a blue shaded region (the height representing 1σ). The mass prediction of each model is also plotted. Within the current uncertainties, both models predict masses consistent with the dynamical mass of this source.

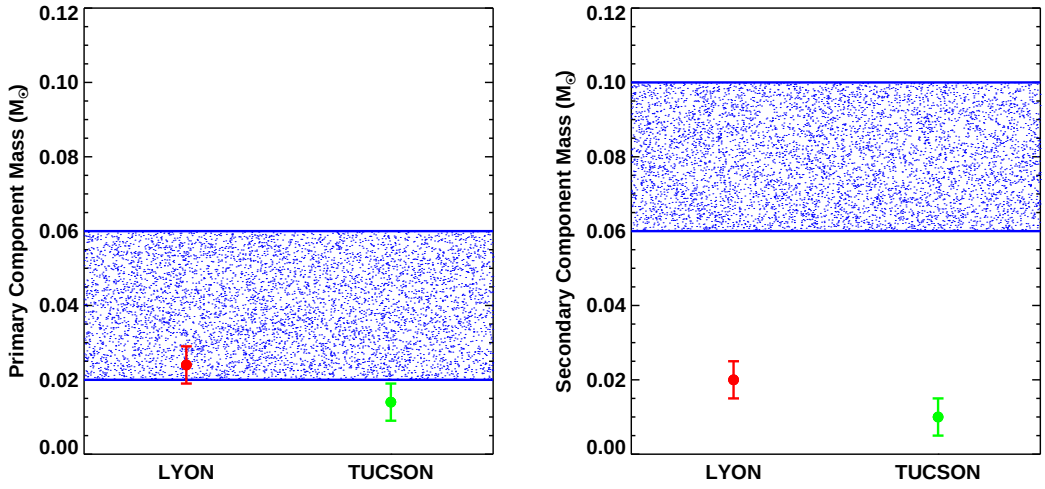

Figure 4.108 **Left**: The component mass of the primary, LP 349-25 A, given by the absolute orbital solution is plotted as a blue shaded region (the height representing 1σ). The mass prediction of each model is also plotted. Within the current uncertainties, both models predict the correct mass for LP 349-25 A. **Right**: The component mass of the secondary, LP 349-25 B, given by the absolute orbital solution is plotted as a blue shaded region (the height representing 1σ). The mass prediction of each model is also plotted. Both models underpredict the mass of LP 349-25 B

For further illustration of these points, we again plot the percent difference between the masses predicted by the models and the dynamical masses, this time plotting the individual component mass. These plots are shown in Figures 4.109 and 4.110[5]. Although the uncertainties are larger, the trend we saw amongst total system mass holds. The earliest spectral types have the strongest discrepancy with the evolutionary models. These figures also demonstrate the power of using individual component masses to perform model comparisons, allowing for the investigation of where discrepancies lie without assumptions (this is particularly apparent in the case of LHS 2397a AB, which has an M8 primary and an L7.5 secondary). In addition, individual component masses effectively double the sample of sources that can be used for comparison (here, we have compared 12 sources, already approaching the 15 we can do with total system masses). Emphasis in the future will be placed on obtaining more precise individual mass estimates for these systems to see if these trends persist.

4.8 Discussion

We have found systematic discrepancies between our measured dynamical masses and the predicted masses from theoretical evolutionary models, where overall the M and L dwarfs have higher dynamical masses than predicted and one T dwarf has a lower dynamical mass than predicted by evolutionary models. We determined the mass predicted by each evolutionary model using our measured parameters of luminosity and temperature, which are related to each other through the canonical equation $L = 4\pi R^2 \sigma T^4$. Our observed bolometric luminosity is the most constrained of these parameters and is free of any model assumptions; therefore, it is

[5]Since only one system has a spectral type later than L5, we do not perform this exercise for the COND models

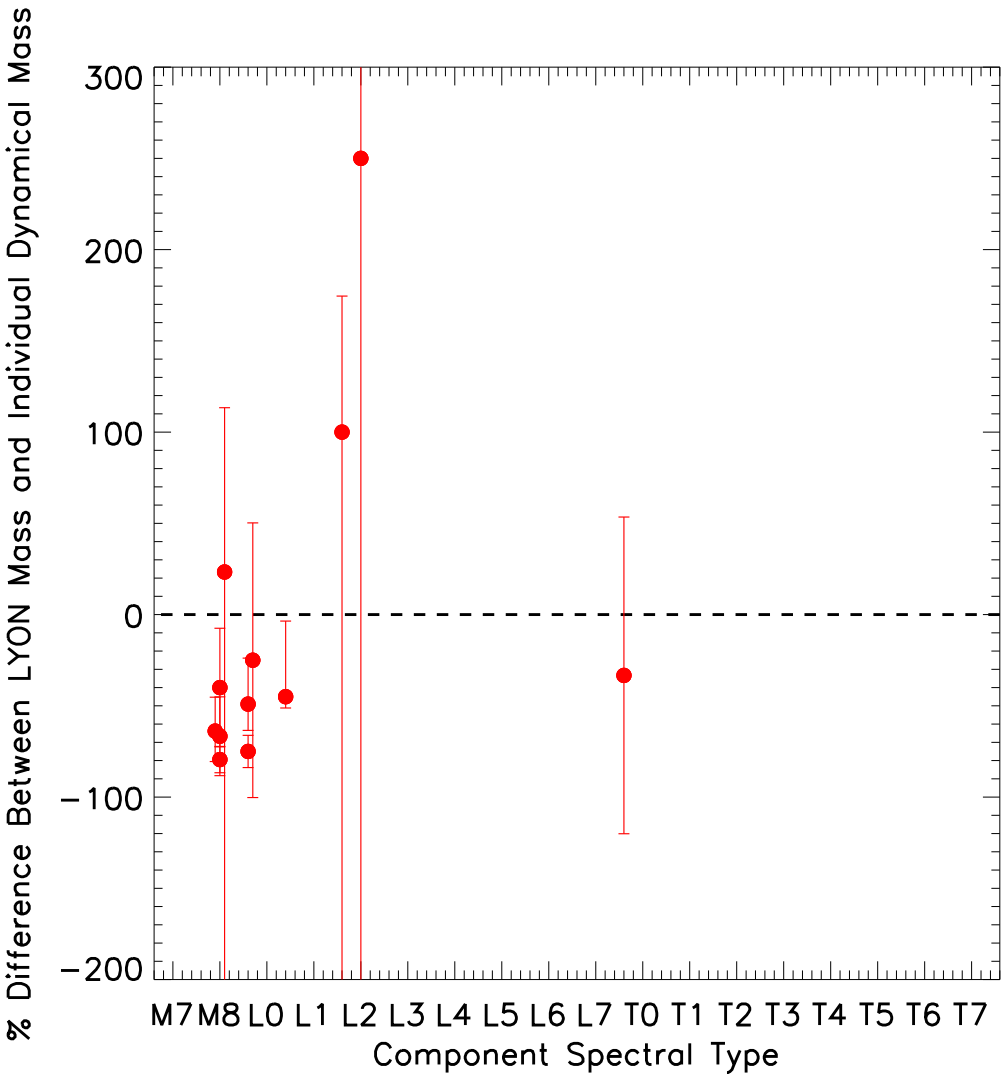

Figure 4.109 The percent difference between the predictions of the DUSTY (Chabrier et al. 2000) models and our individual dynamical masses as a function of spectral type. We compare our 12 individual mass measurements to these models, and find that five sources have their masses underpredicted by these models. All five sources have spectral types of M8 - M9.

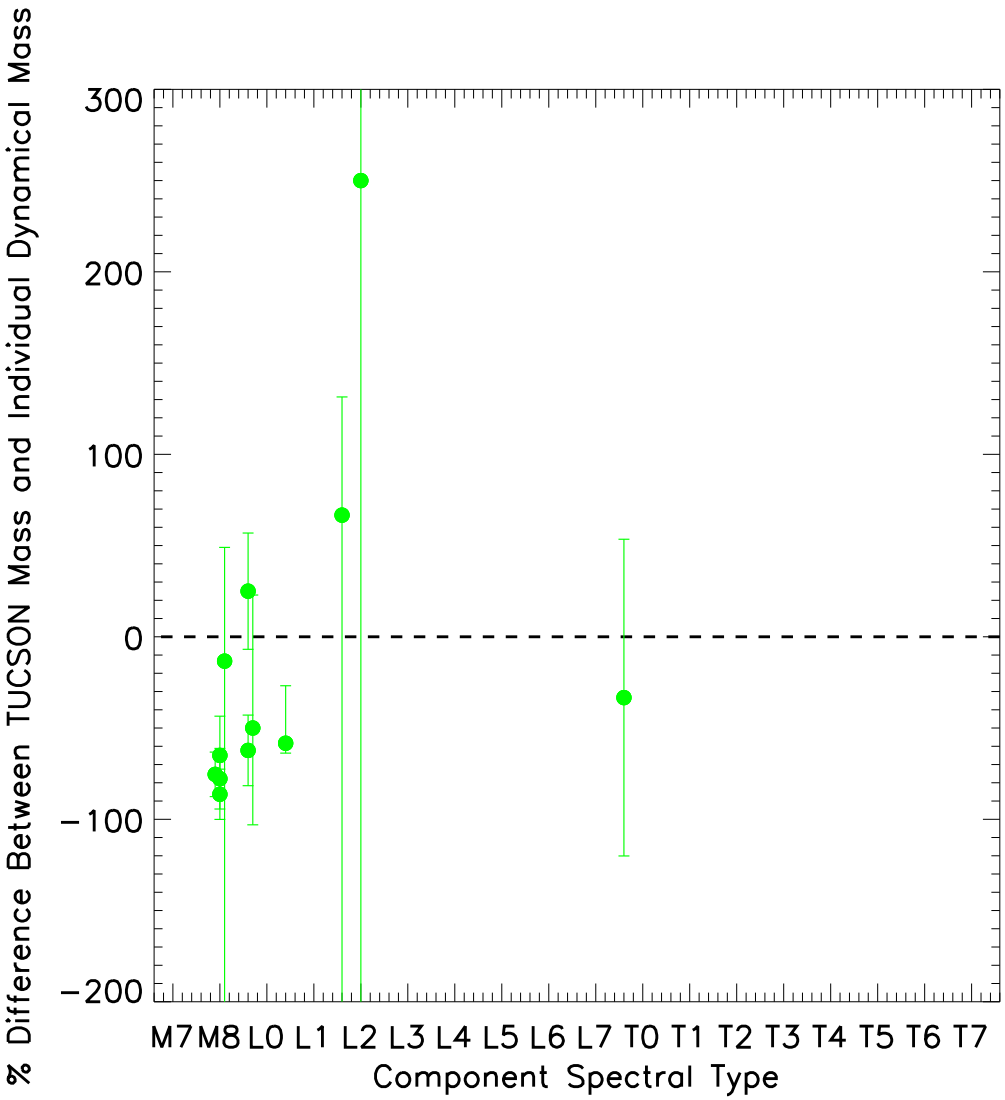

Figure 4.110 The percent difference between the predictions of the TUCSON (Burrows et al. 1997) models and our individual dynamical masses as a function of spectral type. We caveat that while we have used different atmospheric models to derive effective temperature than is employed in the Burrows et al. (1997) models, the effect of the atmospheric model is thought to be minor. We compare our 12 individual mass measurements to these models, and find that five sources have their masses underpredicted by these models. All five sources have spectral types of M8 - M9.

the least likely parameter to contribute to disagreement. Instead, the radius and temperature are the most likely cause of the discrepancy between the predicted evolutionary model masses and our dynamical masses, either those predicted by the evolutionary model or those from our atmospheric model fits. In this section, we explore temperature and radius and discuss other assumptions used with both atmospheric and evolutionary models which may give rise to differences between our measured masses and predicted modeled mass. For reference, we show in Figure 4.111 the location of GJ 569Bb of the H-R Diagram, whose individual mass measurement was underpredicted by the evolutionary models. We show the location of the line of constant mass for a 0.05 $M_{\odot}$ source as given in both the LYON and TUCSON models, which should align with the position GJ 569Bb if there was no discrepancy. The direction of the offset between these lines and the position of GJ 56Bb is representative of the direction of the offset for all discrepant systems of M and L spectral types. Though we cannot make a corresponding plot for the case of our overpredicted T dwarf system, for which we do not have individual component masses, the direction of the offset is opposite that of GJ 569Bb.

We first consider the case in which the driver for the discrepancy is primarily the evolutionary models, which begin with mass and age as input parameters and then predict quantities of radius, temperature, and, in turn, the luminosity. For the sources in the late M through mid L spectral types that are discrepant, the mass lines that agree with our dynamical masses lie at higher temperatures and/or lower luminosities than our input values. To bring these sources into agreement would require either a decrease in the evolutionary model-predicted temperature for these sources of $\sim$100-300 Kelvin or an increase in the radii by a factor of $\sim$1.3-2.0. Meanwhile, for the discrepant T dwarfs, the correct mass lines lie at lower temperatures and/or higher luminosities than our input values. To

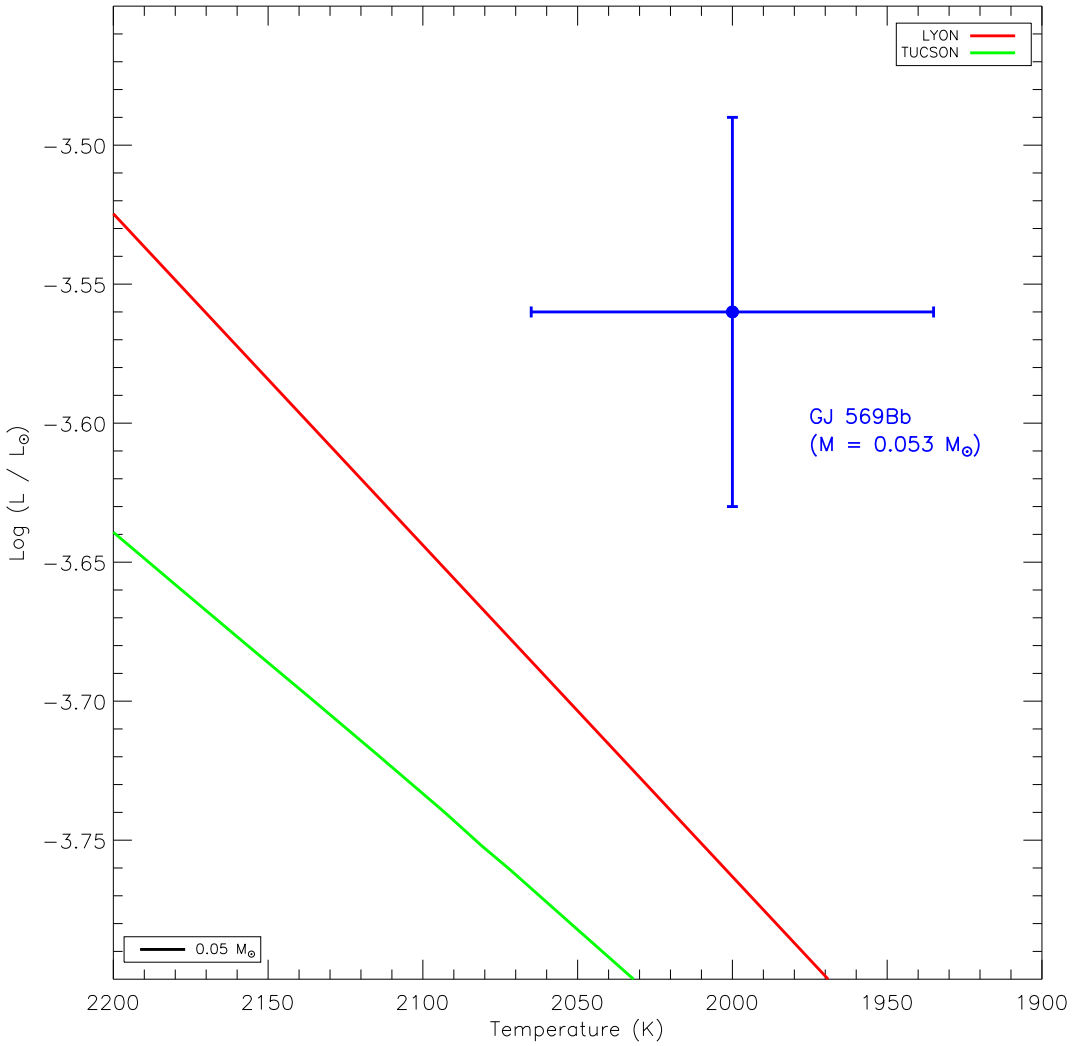

Figure 4.111 Location of GJ 569Bb on the H-R diagram given our derived temperature and luminosity. Since this system had a mass of 0.053 ± 0.006 $M_{\odot}$, it should lie close to the line of constant mass for a 0.05 $M_{\odot}$ object in the evolutionary models. The location of this line for both LYON and TUCSON are also plotted. As with all discrepant sources in our sample of spectral type M or L, the source lies above and to the right of these lines, implying either the temperature is too high in the evolutionary models, the radius is too small in the evolutionary models, or the temperature is too low in the atmosphere models for these sources.

bring them into agreement would require an increase in the evolutionary model predicted temperatures by ∼100 Kelvin, or an increase in the radii by a factor of ∼1.5.

There are a number of implications for the physics of the evolutionary models in this case. If the radii are off, this implies a that mass-radius relationship in these models might be slightly off. The predicted radius for a source is driven almost entirely by the assumed equation of state, with a very minor dependence on the assumed atmosphere (Chabrier et al. 1997). The interiors of very low mass objects are thought to be partially degenerate, and the mass radius relationship is generally modeled to follow a hybrid between the fully degenerate and classical relationships. Objects below the hydrogen burning limit will continually contract throughout their lifetimes, with a general slowing of that contraction after 1 Gyr. A need for a change in the radii for an object of a given mass could imply the need for a slight shift in the rate of contraction, or a slight shift in the radius at which the contraction effectively halts (see Figure 7 of Chabrier et al. 1997). An update of the equation of state from that given by Saumon et al. (1995), which is the equation of state used by both Burrows et al. (1997) and Chabrier et al. (2000), could potentially modify the mass-radius relationship. Indeed, more recent experiments on the behavior of dense plasmas (e.g., Collins et al. 1998) have shown that while the the Saumon et al. (1995) results agree reasonably well, there is room for improvement (Chabrier & Baraffe 2000). Incorporating the results of these new experiments may help resolve the observed discrepancies.

Meanwhile, the effective temperature is driven by the interior energy transport mechanisms for these objects, which is both convective and conductive, as well as the interior/atmospheric boundary conditions. If the required change is in the predicted effective temperature, this implies that adjustments need to be

made to the efficiency of interior energy transport, or an offset is needed interior/atmospheric boundary condition. Energy transport efficiency also relates to the rate at which these objects cool over their lifetimes. An adjustment in this rate could also bring the predicted masses into agreement with our dynamical masses. Finally, magnetic activity could possibly inhibit the efficiency of convection, lowering the effective temperatures of these objects (Chabrier & Baraffe 2000). This may be important for the discrepant sources of spectral type M or L, which have lower temperatures than predicted by the evolutionary models. It has been shown that late M to mid L type objects exhibit magnetic activity (Berger 2006), and thus incorporating the effects of this activity into the models could also lead to partial resolution of the discrepancy.

The other case we consider is that in which the discrepancy is caused by the temperatures and radii predicted by the PHOENIX atmosphere models. In our spectral synthesis modeling, these two parameters are linked through the bolometric luminosity. Because our luminosity is a fixed, model-independent quantity, the parameter that matters in this case in temperature, because the radius is effectively set by the measurement of L_{Bol} and enters only as a scaling factor for the SEDs which are shaped by temperature. Therefore, if the discrepancy is caused by the atmosphere models, it is through the temperature prediction. In this case, the temperatures predicted would be too low in the case of the M and L dwarfs by $\sim$100-300 K, and too high in the case of the T dwarf by about $\sim$100. A change in temperature would cause the atmosphere model predicted radius to change as well, but do so in a way that again maintains correct L_{Bol}.

The PHOENIX atmosphere models we have used are thought to represent the limiting cases in terms of atmospheric dust treatment. That is, the DUSTY models assume an atmosphere fully enveloped in dust clouds, while the COND

assume no dust clouds and the complete removal of refractory elements. If the temperatures predicted for the discrepant M and L dwarfs are too low, it implies that the dust clouds are too opaque, trapping too much radiation. For the T dwarfs, removal of all refractory elements from the atmosphere may have resulted in a drop in opacity that allows too much radiation to escape, causing a higher than predicted temperature. Along these lines, recent work by Helling et al. (2008) has shown that the treatment of dust clouds in atmospheric models has a dramatic effect on the output photometry. They show that the near-infrared colors predicted by different models with different dust treatments can be discrepant by as much as a magnitude. Since we have used photometry to derive our temperatures, this could imply that the dust treatment has lead to incorrect temperature predictions. Though Helling et al. (2008) only compared two test cases, one at 1800 K and one at 1000 K, a rough comparison between the colors of our discrepant sources and those test cases show that models with thinner dust clouds and uniform grain sizes may bring the temperatures into alignment with what is predicted by the evolutionary models.

We note that although we have not accounted for metallicity variation amongst our sources, using atmospheric models with fixed solar composition, our observations are not generally sensitive to metallicity. It has been shown that a factor of 10 difference in metallicity creates about a magnitude of variation in predicted photometry (Burrows et al. 2006). Since we do not expect any of our sources to have metallicities vastly different from solar, we do not have ability to distinguish metallicity with photometry, and hence not accounting for this is unlikely to have dramatically impacted our atmospheric fitting. However, our fits could potentially be slightly improved in the future by accounting for metallicity, which a number of authors have described as the potential "second parameter" that causes variations in the spectral morphology of these objects (Burrows et al.

2006).

Therefore, there are a number of scenarios in which a slight change in the input physics to either the evolutionary models or the atmosphere models (possibly both) could generate agreement between our dynamical masses and the model predicted masses. We note that discrepancies between the evolutionary and atmosphere models have been noted before for three of our systems. The systems HD 130948BC, LHS 2397a AB, and 2MASS 1534-29 AB had their relative orbits derived by Dupuy et al. (2009a), Dupuy et al. (2009b), and Liu et al. (2008). Though their approach to model comparison is different, whereby they use spectral synthesis by Cushing et al. (2008) as a proxy for performing atmospheric fitting on the sources, they find similar results to what we see here. Namely, they see that there is an offset between the evolutionary and atmosphere models, though they make the comparison only in terms of temperature (using their luminosities and total system masses with a mass ratio assumption to derive an evolutionary model predicted temperature). The temperature offsets they see in three comparisons are similar to what we derive here, though they only look at sources individually as opposed to the systematic tests across the entire substellar regime we have performed here. For the sources they compare, they find that their M and L dwarfs appear to have higher temperatures predicted by the evolutionary models than the atmosphere models and their T dwarf source has a lower temperature in the evolutionary models than the atmospheric models. Thus, though their approach is different and they only examine a few sources, they arrive at similar conclusions.

We also note that if the discrepancies between the models and the dynamical masses continue to follow the same trend, the implication for pushing into the planetary mass regime is that, like the T dwarfs, the masses of planets would

be overestimated by the evolutionary models. For instance, in the case of the directly-imaged extrasolar system, HR 8799, relatively high masses of 7, 10, and 10 M_{Jup} have been derived using evolutionary models (Marois et al. 2008). These higher masses have generated some difficulty in terms of allowing for systemic stability over long timescales (Goździewski & Migaszewski 2009, Fabrycky & Murray-Clay 2008). The decrease of these masses by only a few percent would imply the system was much more stable over long timescales. Thus, this work may have important implications for the masses derived for directly imaged extrasolar planets using evolutionary models.

Future work will thus focus on improving dynamical mass estimates, with an emphasis on obtaining more individual mass measurements. With additional radial velocity measurements, individual mass measurements can approach the level of precision we have achieved for our total system masses. This will effectively double the sample of sources for which we can perform comparisons to theoretical models.

Perhaps a more powerful measurement than mass alone is the derivation of radii for these sources. Radii allow for the independent calculation of effective temperature free of an model assumption. This would allow us to test *both* the evolutionary and the atmospheric models independently of each other. Thus far, only one eclipsing binary brown dwarf has been reported (Stassun et al. 2006), providing the only empirical measurement of a brown dwarf radius (for a very young system in Orion). For our sample, we hope to measure radii through the derivation of accurate surface gravities, which provide radius estimates if the masses are known. We currently can plot the mass-radius relationship we have derived using those sources with individual mass measurements and our atmospheric-model calculated radii. We have done this in Figure 4.112. This

figure shows that the measurement of surface gravities will allow for the measurement of radii independently from the models, allowing us to calibrate the mass-radius relationship in addition to directly calculating temperature. To measure gravities, we require high resolution spectra with gravity sensitive features. Our K band spectra, which were obtained to achieve the highest precision in radial velocity, are not suitable for this purpose as they are dominated primarily by water features, which are not gravity sensitive (Allard et al. 1997). However, alkali lines such as potassium in the J band have been shown to be quite gravity sensitive (McGovern et al. 2004, Rice et al. 2009), and can be used for this purpose. Thus, obtaining spatially resolved, high resolution J band spectra for our sources is a high priority for this project.

Additionally, one source in our sample, 2MASS 0920+35 AB (which has components in the L/T transition region), is on a highly inclined orbit with an inclination of 88.6 $\pm$ 1.2^o. Assuming that the components have a radius of 1 R_{Jup}, the system will be an eclipsing system if it has an inclination between 89.89^o and 90.15^o. Based on our full relative orbital solution distribution, we find the system has an 6.8% of eclipsing. If we consider only those solutions with a $\sim$6.5 year period, we find the system has a only a 3.1% chance of eclipsing. If we instead only consider those solutions with a $\sim$3.5 year period, the system has an 11.3% chance of eclipsing. In Figure 4.113, we plot the probability distribution of eclipse dates. The highest probability of eclipse occurred in April of 2009. The next most likely date of eclipse is in mid-2012. The duration of the eclipse would most likely be between 2 and 4 hours. If this system does eclipse, it will provide allow for a direct measurement of its radius, allowing for a very powerful test of models at the L/T transition region.

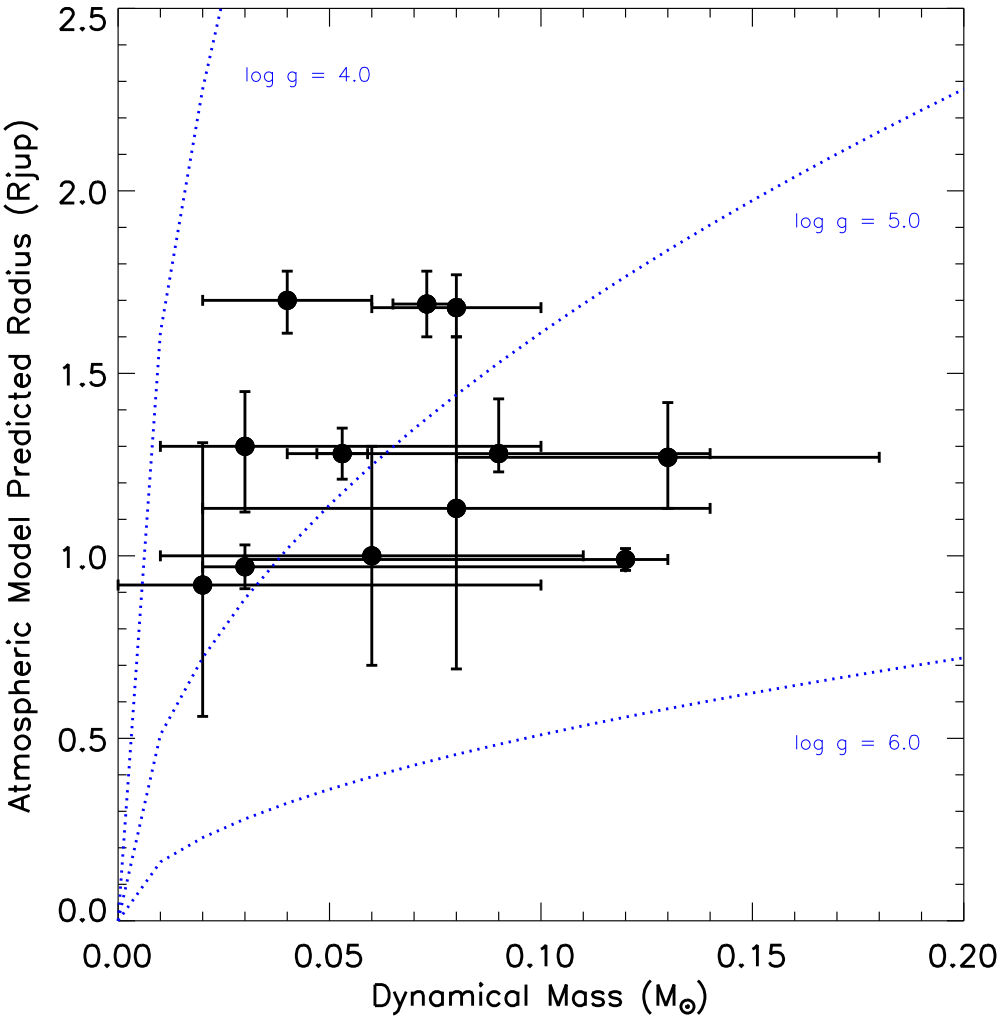

Figure 4.112 The atmospheric model-predicted radii versus the masses for sources with individual mass estimates. Overplotted are lines of constant surface gravity. With the direct measurement of surface gravity for these objects, we can find model-independent radii and reduce the scatter in this relationship.

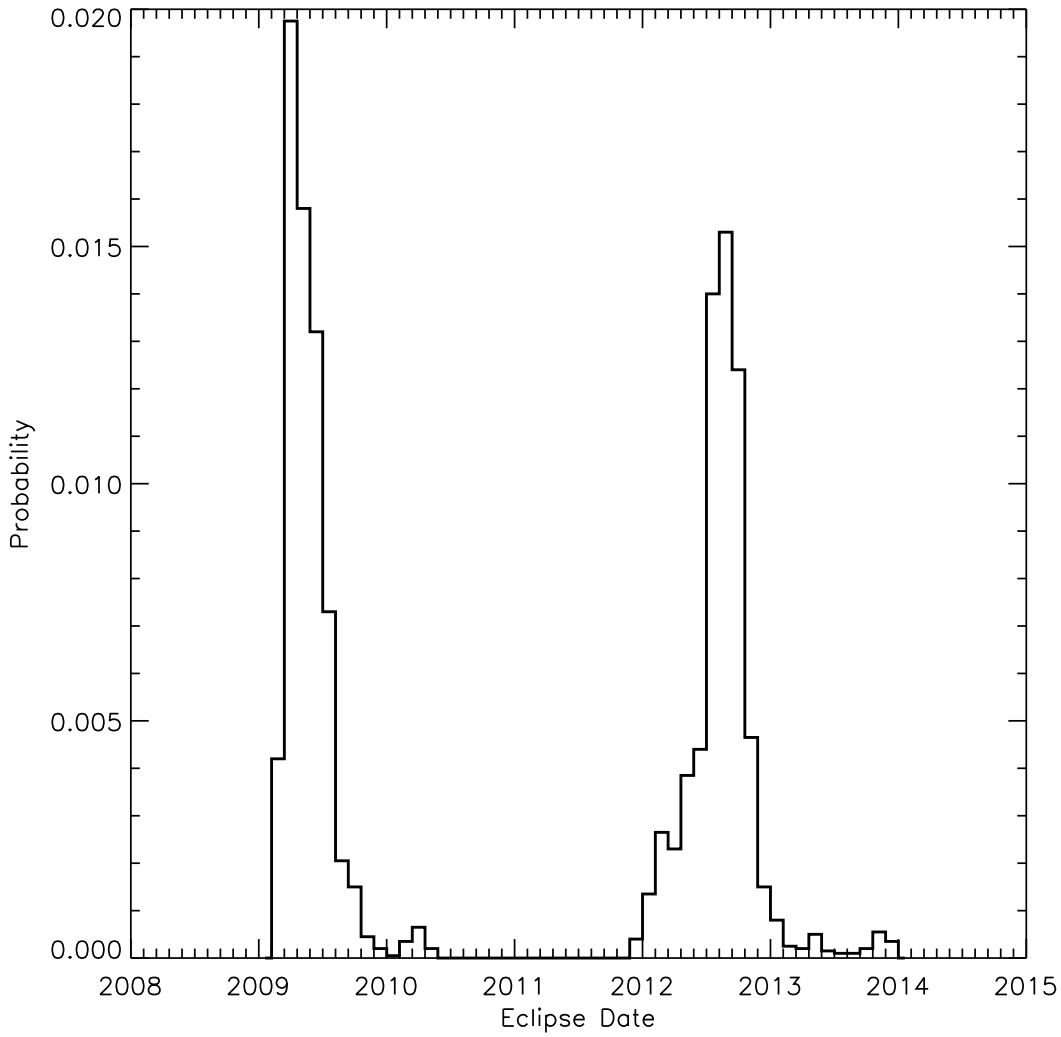

Figure 4.113 The probability of eclipse as a function of date of occurence for 2MASS 0920+35 AB. Overall, the system has a 6.8% chance of being an eclipsing system, with the most likely date of eclipse having occured in April of 2009. The next most likely date of an eclipse is in mid-2012.

4.9 Conclusions

We have calculated relative orbital solutions for 15 very low mass binary systems, using a combination of astrometric and radial velocity data obtained with the Keck Observatory LGS AO system. For 10 of these systems, this is the first derivation of the relative orbits. We have also calculated the absolute orbital solutions for 6 systems, 5 of which are the first for those systems. Further, we have performed spectral synthesis modeling 12 of these systems using their spatially resolved photometry and the PHOENIX atmosphere models. This provides as estimate of the temperatures of each source.

The masses we have calculated based on these orbital solutions and our derived temperatures have allowed us to perform the first comprehensive comparison of a sample of VLM objects to theoretical evolutionary models. We find that for 6 systems, their total system masses are underpredicted by both evolutionary models considered. In these systems, 11 of the 12 components have spectral types earlier than L4. We find that one binary T dwarf has its total system mass overpredicted by the evolutionary models. The additional 8 systems, which include all 3 L/T transition systems in our sample, have evolutionary model predictions consistent with the dynamical masses. We postulate that for those systems in which we see a discrepancy, the possible cause is either an incorrect radius prediction by the evolutionary models, an incorrect temperature prediction by the evolutionary models, or an incorrect temperature prediction by the atmospheric models.

Future work will focus on improving the precision of our dynamical masses, with a particular emphasis on obtaining more individual masses across a broader range of spectral types. We will also obtain radius measurements for our sources, primarily through the calculation of surface gravity, which will allow us to test the evolutionary and atmospheric models independently. These measurements

will provide powerful new tests of the evolutionary models.

CHAPTER 5

Conclusions

This thesis attempts to constrain the formation and evolution of brown dwarfs using observations of brown dwarf multiple systems. At the time this thesis began, there were two classes of outstanding questions regarding the formation of substellar objects. First, with traditional star formation mechanisms unable to generate sources with masses this low, new formation theories presented viable methods of forming these objects. These theories had been tested using multiplicity studies of field very low mass (VLM) objects, but only a few surveys of young VLM objects in star forming regions, where the impact of dynamical evolution is minimized, had been performed at the outset of this work. Second, the internal evolution of VLM objects as predicted by interior and atmospheric models was a matter of some debate. For instance, there remain many challenges and discrepancies between different evolutionary models that attempt to properly account for the unique properties of these objects, including partially degenerate interiors, molecular opacities, and atmospheric dust formation. Both of these outstanding issues have been addressed in this thesis. My main conclusions are:

- We used the W.M. Keck laser guide star adaptive optics system (LGS AO) to monitor the orbital motion of VLM visual binaries. We monitored them using both imaging and high resolution spectroscopy at the high spatial resolution achieved with the LGS AO system. This is the first work that

utilizes the high resolution spectrograph, NIRSPEC, in conjunction with the LGS AO system to achieve the combination of high spatial and spectral resolution on optically faint sources. NIRSPEC+LGS AO is one of the only systems in the world, ground or space, capable of these observations, and this portion of our program is unique to all other monitoring programs of VLM objects.

- Through our monitoring of VLM binaries, we derived the relative orbital solutions for 15 systems, which allowed us to obtain total system masses for these objects. This is the first mass derivation for 10 systems, tripling the number of mass measurements for VLM objects. Using our spectroscopy, we also derived absolute orbits for 6 of these systems. With these orbits, we have calculated individual component masses. This is the first assumption-free and model-free derivation of component masses for 5 of these 6 systems. Together, these masses represent the most comprehensive sample of substellar masses yet assembled across the entire substellar regime, from late M to mid T.

- Using our mass measurements, we tested the predictions of theoretical evolutionary models of VLM objects. We took the unique approach of considering each object on an individual basis and performing spectral synthesis modeling on each binary component (not in the L/T transition region) using the PHOENIX atmosphere models. This allowed us to derive effective temperatures for each object as predicted by these atmospheric models.

- Our comparison to the predictions of evolutionary models revealed systematic offsets that are correlated with spectral type. Specifically, we found that six systems of late M through mid L spectral type have their masses *underpredicted* by both evolutionary models considered (Burrows et al. 1997,

Chabrier et al. 2000), and one T dwarf has its mass *overpredicted* by both models. These seven systems have the highest precision mass measurements in our sample. This discrepancy can be driven either by the evolutionary models or the atmosphere models, or possibly a combination of both. We speculated that the cause is either the uncalibrated mass-radius relationship assumed by the evolutionary models (driven by the assumed interior physics), the cooling curves assumed by the evolutionary models (driven by a combination of the assumed interior and atmosphere physics), or the dust treatment in the atmosphere models.

- We found one L/T transition system, 2MASS 0920+35AB, that has a 6.8% chance of being an eclipsing binary. If this system is eclipsing, it will allow for a direct measurement of the radii of the components. Radius measurements are an important step in the calibration of evolutionary models, as direct radius measurements provide direct measurements of effective temperature. Radius measurements also allow for the calibration of the mass-radius relationship, which is an uncalibrated quantity that contributes to the evolutionary models. A future direction for this work will be on obtaining surface gravity measurements for our sample, from which we can derive radii.

- We performed the first analysis of the eccentricity distribution amongst VLM binaries. We found that there is an overabundance of low eccentricity systems with respect to higher mass stars. Though selection effects may have created this overabundance, we find that on average our systems have lower eccentricities than G stars with comparable periods.

- We have also performed a survey of young, VLM binaries in the Taurus star-forming region using speckle interferometry at Keck. Of 13 objects

surveyed, 5 were found to be binary for the first time in this survey. At the time this survey was completed, it increased the number of known, young VLM binaries by ∼50%.

- We placed constraints on formation theories for VLM binaries with our sample of Taurus objects, four of which have separations over 30 AU and mass ratios <0.6. These properties argued against the ejection scenario of brown dwarf formation, which predicts a very low binary frequency and no systems with separations >20 AU.

- The results from our Taurus sample, when combined with the results of other surveys of young, VLM objects, are distinct from those seen amongst field brown dwarfs, which have a statistically significant preference for separations <10 AU and mass ratios near 1. These results implied that field VLM objects are more tightly bound than young VLM objects. We also found a higher multiplicity fraction of 18 ± 4% for young systems than the 8 ± 2% seen amongst field objects. We argue that these differences imply that these objects undergo dynamical evolution ∼5-10 Myr after formation.

- We successfully completed a pilot study for our dynamical mass survey of VLM objects by deriving the orbital solution for the young M dwarf TWA 5Aab. We used the mass as determined from the orbit of this system to perform tests of theoretical evolutionary models for very young systems. Our pilot study showed that it is important to account for correlated uncertainties when performing comparisons to evolutionary models.

This thesis has significantly helped constrain theories of the formation and evolution of substellar objects through observational studies relating to their multiplicity and dynamics. Several avenues of study can expand on the results found

here. Additional individual dynamical masses can be used to place further constraints on the predictions of theoretical models. In particular, individual masses of objects across the entire substellar regime would provide powerful systematic tests of the models. This can be achieved either using the methods used in this thesis, or by finding more eclipsing binary systems. The Kepler Mission (Borucki et al. 2003) may identify new VLM eclipsing binaries. However, the mission is performed at optical wavelengths, and likely will be more sensitive to late M to mid L dwarf systems. The Monitor Project, using multiple telescopes at optical wavelengths, (Aigrain et al. 2007) can identify new eclipsing VLM in nearby star forming regions. Near-infrared photometric monitoring campaigns would be the most effective at identifying eclipsing VLM binaries.

Once masses are obtained, a high priority will be determining their radii so that the mass-radius relationship for VLM objects can be calibrated. As this thesis showed, the essentially uncalibrated mass-radius relationship may lead to discrepancies in the mass predictions of evolutionary models. If the mass-radius relationship can be calibrated, it may have important implications for distinguishing between low mass brown dwarfs and planets. It has been shown that objects that form via gravitational collapse may have a slightly different mass-radius relationship than objects that form in a disk due to the presence of a rocky core (Chabrier et al. 2009). If the mass-radius relationship for brown dwarfs is derived, it could potentially be used to determine how a substellar object formed, and thus whether or not an object is a planet or a low mass brown dwarf.

Additional multiplicity studies of field brown dwarfs would also serve to increase our understanding of VLM objects. There is currently a lack of high resolution imaging studies of T dwarfs, particularly those that have been recently discovered with new all sky-surveys such as UKIRT Infrared Deep Sky

Survey (UKIDSS, Warren et al. 2007) and Canada-France Brown Dwarf Survey (CFBDS, Delorme et al. 2008). These surveys have identified a large number of previously unknown T dwarfs. The Wide Field Infrared Survey Explorer (WISE, Mainzer et al. 2005) will also identify a large number of ultra-cool dwarfs, for which the multiplicity properties will be important to determine. In addition, the number of surveys for spectroscopic VLM binaries is far behind that of visual binary surveys. Spectroscopic surveys can probe the multiplicity properties of VLM objects at the closest separations. NIRSPEC is an ideal instrument for this purpose, as it can target brown dwarfs in the infrared, where they are intrinsically brighter.

Amongst young VLM objects, several multiplicity studies of have been performed since the publication of Konopacky et al. (2007b, Chapter 2). The regions of Chamaeleon I (Ahmic et al. 2007, Joergens 2008) and Orion (Maxted et al. 2008) have been surveyed, but many star forming regions still have not had the multiplicity of their lowest mass members probed. The above surveys have continued to show that the multiplicity fraction of young VLM objects is below that of solar-type stars, but generally higher than that of field VLM objects. New discoveries of young, wide brown dwarfs have continued to challenge formation theories like the ejection scenario (Kraus et al. 2007, Luhman et al. 2009, Allers et al. 2009).

The further development of adaptive optics technology will have important implications for studies of VLM objects. The technology of Next Generation Adaptive Optics (NGAO) is currently under development at Keck, and will achieve very high strehl ratios in the near-infrared, with good performance at optical wavelengths. The ability to achieve near-diffraction limited performance in the optical will allow for multiplicity studies of VLM objects at even closer

separations than can be currently resolved. This will allow for unprobed regions of separation parameter space to be surveyed, and also uncover ideal objects for dynamical mass studies. Spatially resolved optical measurements are also important for measuring the full SED of these objects, and are currently only possible with the Hubble Space Telescope (HST). Once HST is no longer operational, NGAO represents one of the only possibilities for obtaining these measurements.

In the next 10 years, several extremely large telescopes will be built, with important implications for the study of substellar objects. The unprecedented spatial resolution possible with telescopes such as the Thirty Meter Telescope (TMT, Crampton & Simard 2006) will allow not only for studies of very tight VLM binaries in the field, but also allow for multiplicity studies of more distant star forming regions at comparable physical separations to what can currently be achieved for nearby regions. This will enable comparisons of the multiplicity properties of VLM objects in all regions across the same range of separation parameter space. TMT will also have unprecedented sensitivity, which will allow for high resolution spectroscopy to be obtained for the coolest, faintest objects (K magnitude >15) with relative ease.

These future studies will benefit from the groundwork laid by this thesis. By constraining the formation and evolution of these objects with essential empirical measurements, new observations of brown dwarfs and even planets can be compared with more confidence to models. With continued progress in this arena, the mysteries surrounding substellar objects will be unveiled.

APPENDIX A

Radio Observations of Very Low Mass Binaries

When compiling our sample of very low mass (VLM) binaries for the dynamical mass work presented in Chapter 4, it was noted that the limiting factor in the precision we could obtain for our masses was often the distance to the source. Several of the sources in our sample had parallax measurements through the United States Naval Observatory (USNO) infrared parallax program (Dahn et al. 2002, Vrba et al. 2004), but that program is no longer in operation. We therefore explored other methods for other methods of obtaining precise parallaxes for those sources without previous measurements.

The Very Large Baseline Array (VLBA) is capable of extremely precise parallax measurements. Previous VLBA parallaxes of various radio-bright stellar sources (e.g., Loinard et al. 2007, Hirota et al. 2007) have shown that the typical parallax achievable with is about 0.05 mas, or six times better than what was achieved with USNO (which had uncertainties of $\gtrsim$0.3 mas). Distances with precisions of this level would allow for the derivation of very precise masses.

To be detectable with the VLBA, sources must have a brightness at 8.4 GHz (X Band) of $\gtrsim$0.5 mJy. Though early M dwarfs had been found to have significant radio emission driven by substantial magnetic fields, it was thought that fully convective stars (M $\leq 0.3 M_{\odot}$) could not generate magnetic fields of similar strength, and thus should not be radio sources. However, numerous authors have detected non-thermal radio emission coincident with VLM objects at frequencies

ranging from 1.7 to 8.4 GHz (e.g, Berger et al. 2006, Osten et al. 2006), with fluxes sufficient for detection with the VLBA. Therefore, we put together a small radio observing program to determine if sources in our sample had radio emission of sufficient brightness to obtain a VLBA parallax measurement.

For the goal of a simple detection, the best facility to use is the Very Large Array (VLA), which can achieve the lowest sensitivity limits in the shortest time at 8.4 GHz. We used the VLA in C north B configuration on 2008 February 16-19 to obtain measurements of 10 of our dynamical mass sample sources (project ID AK0687). The resolution of the VLA in this configuration is $\sim$1", providing us with only a 0.01% chance of finding a background object within 2" of our sources. These 10 sources had no previous radio measurements, and 9 had no previous parallax measurements. A log of the observations is given in Table A.1. We observed each target for 1 hour, with an additional 0.3 hours per target spent on nearby phase and flux calibrators. This integration time gave us a 5σ detection limit of 0.1 mJy. The data were reduced using standard techniques in AIPS[1]. Our reduced data revealed no sources brighter than 0.1 mJy. Thus none of these 10 sources had sufficient brightness at 8.4 GHz for detection with the VLBA.

We also found an observation from the NRAO VLA Archive Survey pilot of the source 2MASS 0746+20 AB at 8.4 GHz in B configuration (taken on 2007 July 17). The source had a brightness of 0.8 mJy in this observation. The source appeared coincident with the location of 2MASS 0746+20 AB. We were awarded 8 hours of observing time with the VLBA to attempt to detect this source. These observations were taken on 2007 August 2, and a source was detected. However, the source's position was offset from the position of 2MASS 0746+20AB and inconsistent with what was expected based upon its proper motion (-0.4 mas/yr,

[1]www.aips.nrao.edu

Table A.1. Log of VLA 8.4 GHz Observations

Target Name	Date of Observation (UT)	Flux Calibrator	Phase Calibrator
2MASS 1047+40AB	2008 Feb 19	3C286	1033+395
2MASS 1426+15AB	2008 Feb 17	3C286	1415+133
2MASS 1430+29AB	2008 Feb 18	3C286	1407+284
2MASS 1600+17AB	2008 Feb 19	3C286	1608+104
2MASS 1750+44AB	2008 Feb 17	3C286	1753+441
2MASS 1847+55AB	2008 Feb 17	3C286	1927+612
2MASS 2140+16AB	2008 Feb 17	3C48	2139+143
2MASS 2206-20AB	2008 Feb 17	3C48	2213-254
GJ 568Bab	2008 Feb 17	3C286	1446+173
LP 415-20AB	2008 Feb 16	3C147	0431+206

Dahn et al. 2002). We therefore determined that this source was not 2MASS 0746+20 AB. Though we were not successful at detecting any sources, the VLBA remains a promising facility for the measurement of extremely precise parallaxes.

Bibliography

Adams, F. C., Proszkow, E. M., Fatuzzo, M., & Myers, P. C. 2006, ApJ, 641,504

Adelman-McCarthy, J. K., et al. 2007, ApJS, 172, 634

Ahmic, M., Jayawardhana, R., Brandeker, A., Scholz, A., van Kerkwijk, M. H., Delgado-Donate, E., & Froebrich, D. 2007, ApJ, 671, 2074

Aigrain, S., Hodgkin, S., Irwin, J., Hebb, L., Irwin, M., Favata, F., Moraux, E., & Pont, F. 2007, MNRAS, 375, 29

Allard, F., Hauschildt, P. H., Alexander, D. R., & Starrfield, S. 1997, ARAA, 35, 137

Allard, F., Hauschildt, P. H., Alexander, D. R., Tamanai, A., & Schweitzer, A. 2001, ApJ, 556, 357

Allers, K. N., et al. 2009, ApJ, 697, 824

Ambartsumian, V. A. 1937, Astron. Zh., 14, 207

Ardila, D., Martín, E., & Basri, G. 2000, AJ, 120, 479

Baraffe, I., Chabrier, G., Allard, F., & Hauschildt, P. H. 1995, ApJL, 446, L35

Baraffe, I., Chabrier, G., Allard, F., & Hauschildt, P. H. 1998, A&A, 337, 403

Baraffe, I., Chabrier, G., & Barman, T. 2008, AAP, 482, 315

Basri, G., & Martín, E. L. 1999, AJ, 118, 2460

Basri, G., & Reiners, A. 2006, AJ, 132, 663

Bate, M. R., Bonnell, I. A., & Bromm, V. 2002, MNRAS, 332, L65

Becklin, E. E., & Zuckerman, B. 1988, Nature, 336, 656

Berger, E. 2006, ApJ, 648, 629

Bertout, C., Robichon, N., & Arenou, F. 1999, A&A, 352, 574

Bevington, P. R. & Robinson, K. D. 1992, Data Reduction and Error Analysis for the Physical Sciences (New York: McGraw-Hill)

Billères, M., Delfosse, X., Beuzit, J.-L., Forveille, T., Marchal, L., & Martín, E. L. 2005, A&A, 440, L55

Blake, C. H., Charbonneau, D., White, R. J., Marley, M. S., & Saumon, D. 2007, ApJ, 666, 1198

Bonnell, I. A., Clark, P., & Bate, M. R. 2008, MNRAS, 389, 1556

Borucki, W. J., et al. 2003, Proc. SPIE, 4854, 129

Boss, A. P. 2002, ApJ, 568, 743

Bouy, H., Brandner, W., Martín, E. L., Delfosse, X., Allard, F., & Basri, G. 2003, AJ, 126, 1526

Bouy, H., et al. 2004, A&A, 423, 341

Bouy, H., Martín, E. L., Brandner, W., & Bouvier, J. 2005, AJ, 129, 511

Bouy, H., et al. 2008, A&A, 481, 757

Bouy, H., Martín, E. L., Brandner, W., Zapatero-Osorio, M. R., Béjar, V. J. S., Schirmer, M., Huélamo, N., & Ghez, A. M. 2006, A&A, 451, 177

Brandeker, A., Jayawardhana, R., & Najita, J. 2003, AJ, 126, 2009

Brandner, W., et al. 2000, AJ, 120, 950

Burgasser, A. J., Kirkpatrick, J. D., Reid, I. N., Brown, M. E., Miskey, C. L., & Gizis, J. E. 2003, ApJ, 586, 512

Burgasser, A. J., Kirkpatrick, J. D., Cruz, K. L., Reid, I. N., Leggett, S. K., Liebert, J., Burrows, A., & Brown, M. E. 2006, ApJS, 166, 585

Burgasser, A. J., Reid, I. N., Leggett, S. K., Kirkpatrick, J. D., Liebert, J., & Burrows, A. 2005, ApJL, 634, L177

Burgasser, A. J., Reid, I. N., Siegler, N., Close, L., Allen, P., Lowrance, P., & Gizis, J. 2007, Protostars and Planets V, 427

Burrows, A., Hubbard, W. B., Saumon, D., & Lunine, J. I. 1993, ApJ, 406, 158

Burrows, A., et al. 1997, ApJ, 491, 856

Burrows, A., Sudarsky, D., & Hubeny, I. 2006, ApJ, 640, 1063

Chabrier, G., & Baraffe, I. 1997, A&A, 327, 1039

Chabrier, G., & Baraffe, I. 2000, ARAA, 38, 337

Chabrier, G., Baraffe, I., Allard, F., & Hauschildt, P. 2000, ApJ, 542, 464

Chabrier, G., Baraffe, I., Leconte, J., Gallardo, J., & Barman, T. 2009, American Institute of Physics Conference Series, 1094, 102

Chiu, K., Fan, X., Leggett, S. K., Golimowski, D. A., Zheng, W., Geballe, T. R., Schneider, D. P., & Brinkmann, J. 2006, AJ, 131, 2722

Christou, J. C. 1991, PASP, 103, 1040

Close, L. M., et al. 2005, Nature, 433, 286

Close, L. M., Richer, H. B., & Crabtree, D. R. 1990, AJ, 100, 1968

Close, L. M., Siegler, N., Freed, M., & Biller, B. 2003, ApJ, 587, 407

Close, L. M., Siegler, N., Potter, D., Brandner, W., & Liebert, J. 2002, ApJL, 567, L53

Collins, G. W., et al. 1998, Science, 281, 1178

Crampton, D., & Simard, L. 2006, Proc. SPIE, 6269,

Cruz, K. L., Burgasser, A. J., Reid, I. N., & Liebert, J. 2004, ApJL, 604, L61

Cruz, K. L., Reid, I. N., Liebert, J., Kirkpatrick, J. D., & Lowrance, P. J. 2003, AJ, 126, 2421

Cutri, R. M., et al. 2003, The IRSA 2MASS All-Sky Point Source Catalog, NASA/IPAC Infrared Science Archive. http://irsa.ipac.caltech.edu/applications/Gator/

Cushing, M. C., et al. 2008, ApJ, 678, 1372

Dahn, C. C., et al. 2002, AJ, 124, 1170

D'Antona, F., & Mazzitelli, I. 1985, ApJ, 296, 502

D'Antona, F., & Mazzitelli, I. 1997, Memorie della Societa Astronomica Italiana, 68, 807

Delfosse, X., et al. 2004, Spectroscopically and Spatially Resolving the Components of the Close Binary Stars, 318, 166

Delorme, P., et al. 2008, AAP, 484, 469

The Denis Consortium 2005, VizieR Online Data Catalog, 1, 2002

Diolaiti, E., Bendinelli, O., Bonaccini, D., Close, L. M., Currie, D. G., & Parmeggiani, G. 2000, Proc. SPIE, 4007, 879

Duchêne, G., Beust, H., Adjali, F., Konopacky, Q. M., & Ghez, A. M. 2006, A&A, 457, L9

Duchêne, G., Ghez, A. M., McCabe, C., & Weinberger, A. J. 2003, ApJ, 592, 288

Dupuy, T. J., Liu, M. C., & Ireland, M. J. 2009, ApJ, 692, 729

Dupuy, T. J., Liu, M. C., & Ireland, M. J. 2009, ApJ, 699, 168

Duquennoy, A., & Mayor, M. 1991, A&A, 248, 485

Fabrycky, D. C. & Murray-Clay, R. A. 2008, arXiv:0812.0011v1 [astro-ph]

Figer, D. F., et al. 2003, ApJ, 599, 1139

Figer, D. F., Najarro, F., Morris, M., McLean, I. S., Geballe, T. R., Ghez, A. M., & Langer, N. 1998, ApJ, 506, 384

Fischer, D. A., & Marcy, G. W. 1992, ApJ, 396, 178

Fisher, R. T. 2004, ApJ, 600, 769

Forveille, T., et al. 2005, A&A, 435, L5

Freed, M., Close, L. M., & Siegler, N. 2003, ApJ, 584, 453

Ghez, A. M., et al. 2003, ApJL, 586, L127

Ghez, A. M., Neugebauer, G., & Matthews, K. 1993, AJ, 106, 2005

Ghez, A. M., Salim, S., Hornstein, S. D., Tanner, A., Lu, J. R., Morris, M., Becklin, E. E., & Duchêne, G. 2005, ApJ, 620, 744

Ghez, A. M., et al. 2008, ApJ, 689, 1044

Ghez, A. M., Weinberger, A. J., Neugebauer, G., Matthews, K., & McCarthy, D. W., Jr. 1995, AJ, 110, 753

Gizis, J. E., Reid, I. N., Knapp, G. R., Liebert, J., Kirkpatrick, J. D., Koerner, D. W., & Burgasser, A. J. 2003, AJ, 125, 3302

Golimowski, D. A., et al. 2004, AJ, 127, 3516

Goodwin, S. P., & Whitworth, A. 2007, A&A, 466, 943

Goździewski, K., & Migaszewski, C. 2009, MNRAS, 397, L16

Grossman, A. S., Hays, D., & Graboske, H. C., Jr. 1974, A&A, 30, 95

Guenther, E. W., & Wuchterl, G. 2003, A&A, 401, 677

Guieu, S., Dougados, C., Monin, J.-L., Magnier, E., & Martín, E. L. 2006, A&A, 446, 485

Hauschildt, P. H., Allard, F., & Baron, E. 1999, ApJ, 512, 377

Helling, C., et al. 2008, MNRAS, 391, 1854

Hilditch, R. W. 2001, An Introduction to Close Binary Stars (Cambridge: Cambridge University Press)

Hillenbrand, L. A., & White, R. J. 2004, ApJ, 604, 741

Hirota, T., et al. 2007, PASJ, 59, 897

Joergens, V. 2006, A&A, 446, 1165

Joergens, V. 2008, AAP, 492, 545

Joergens, V., & Guenther, E. 2001, A&A, 379, L9

Kastner, J. H., Zuckerman, B., Weintraub, D. A., & Forveille, T. 1997, Science, 277, 67

Kenyon, M. J., Jeffries, R. D., Naylor, T., Oliveira, J. M., & Maxted, P. F. L. 2005, MNRAS, 356, 89

Kenyon, S. J., & Hartmann, L. 1995, ApJS, 101, 117

Kirkpatrick, J. D. 2005, ARAA, 43, 195

Koerner, D. W., Kirkpatrick, J. D., McElwain, M. W., & Bonaventura, N. R. 1999, ApJL, 526, L25

Konopacky, Q. M., Ghez, A. M., Duchêne, G., McCabe, C., & Macintosh, B. A. 2007a, AJ, 133, 2008

Konopacky, Q. M., Ghez, A. M., Rice, E. L., & Duchêne, G. 2007b, ApJ, 663, 394

Kraus, A. L., & Hillenbrand, L. A. 2007, ApJ, 664, 1167

Kraus, A. L., White, R. J., & Hillenbrand, L. A. 2005, ApJ, 633, 452

Kraus, A. L., White, R. J., & Hillenbrand, L. A. 2006, ApJ, 649, 306

Kroupa, P., Bouvier, J., Duchêne, G., & Moraux, E. 2003, MNRAS, 346, 354

Kumar, S. S. 1963, ApJ, 137, 1121

Labeyrie, A. 1970, A&A, 6, 85

Lane, B. F., Zapatero Osorio, M. R., Britton, M. C., Martín, E. L., & Kulkarni, S. R. 2001, ApJ, 560, 390

Leggett, S. K. 1992, ApJS, 82, 351

Leggett, S. K., et al. 2002, ApJ, 564, 452

Liu, M. C., Dupuy, T. J., & Ireland, M. J. 2008, ApJ, 689, 436

Loinard, L., Torres, R. M., Mioduszewski, A. J., Rodríguez, L. F., González-Lópezlira, R. A., Lachaume, R., Vázquez, V., & González, E. 2007, ApJ, 671, 546

Lowrance, P. J., et al. 1999, ApJL, 512, L69

Lu, J. R., Ghez, A. M., Hornstein, S. D., Morris, M. R., Becklin, E. E., & Matthews, K. 2009, ApJ, 690, 1463

Luhman, K. L. 2004, ApJ, 617, 1216

Luhman, K. L. 2004, ApJ, 614, 398

Luhman, K. L., Mamajek, E. E., Allen, P. R., Muench, A. A., & Finkbeiner, D. P. 2009, ApJ, 691, 1265

Luhman, K. L., Stauffer, J. R., Muench, A. A., Rieke, G. H., Lada, E. A., Bouvier, J., & Lada, C. J. 2003, ApJ, 593, 1093

Macintosh, B., et al. 2001, Young Stars Near Earth: Progress and Prospects, 244, 309

Mainzer, A. K., Eisenhardt, P., Wright, E. L., Liu, F.-C., Irace, W., Heinrichsen, I., Cutri, R., & Duval, V. 2005, Proc. SPIE, 5899, 262

Makarov, V. V., & Fabricius, C. 2001, A&A, 368, 866

Mamajek, E. E. 2005, ApJ, 634, 1385

Marois, C., Macintosh, B., Barman, T., Zuckerman, B., Song, I., Patience, J., Lafrenière, D., & Doyon, R. 2008, Science, 322, 1348

Martín, E. L., Barrado y Navascués, D., Baraffe, I., Bouy, H., & Dahm, S. 2003, ApJ, 594, 525

Martín, E. L., Brandner, W., Bouy, H., Basri, G., Davis, J., Deshpande, R., & Montgomery, M. M. 2006, A&A, 456, 253

Martín, E. L., Koresko, C. D., Kulkarni, S. R., Lane, B. F., & Wizinowich, P. L. 2000, ApJL, 529, L37

Matthews, K., Ghez, A. M., Weinberger, A. J., & Neugebauer, G. 1996, PASP, 108, 615

Matthews, K., & Soifer, B. T. 1994, Infrared Astronomy with Arrays, The Next Generation, ed. I. McLean (Dordrecht: Kluwer), 239

Maxted, P. F. L., Jeffries, R. D., Oliveira, J. M., Naylor, T., & Jackson, R. J. 2008, MNRAS, 385, 2210

McGovern, M. R., Kirkpatrick, J. D., McLean, I. S., Burgasser, A. J., Prato, L., & Lowrance, P. J. 2004, ApJ, 600, 1020

McLean, I. S., Graham, J. R., Becklin, E. E., Figer, D. F., Larkin, J. E., Levenson, N. A., & Teplitz, H. I. 2000, Proc. SPIE, 4008, 1048

Mohanty, S., Jayawardhana, R., & Barrado y Navascués, D. 2003, ApJL, 593, L109

Nakajima, T., Oppenheimer, B. R., Kulkarni, S. R., Golimowski, D. A., Matthews, K., & Durrance, S. T. 1995, Nature, 378, 463

Neuhäuser, R., Brandner, W., Alves, J., Joergens, V., & Comerón, F. 2002, A&A, 384, 999

Neuhäuser, R., Guenther, E. W., Petr, M. G., Brandner, W., Huélamo, N., & Alves, J. 2000, A&A, 360, L39

Osten, R. A., Hawley, S. L., Bastian, T. S., & Reid, I. N. 2006, ApJ, 637, 518

Padoan, P., Cambrésy, L., & Langer, W. 2002, ApJL, 580, L57

Padoan, P., & Nordlund, Å. 2004, ApJ, 617, 559

Palla, F., & Stahler, S. W. 1999, ApJ, 525, 772

Potter, D., Martín, E. L., Cushing, M. C., Baudoz, P., Brandner, W., Guyon, O., & Neuhäuser, R. 2002, ApJL, 567, L133

Reid, I. N., & Gizis, J. E. 1997, AJ, 113, 2246

Reid, I. N., Gizis, J. E., Kirkpatrick, J. D., & Koerner, D. W. 2001, AJ, 121, 489

Reid, I. N., Kirkpatrick, J. D., Liebert, J., Gizis, J. E., Dahn, C. C., & Monet, D. G. 2002, AJ, 124, 519

Reid, I. N., Lewitus, E., Allen, P. R., Cruz, K. L., & Burgasser, A. J. 2006, AJ, 132, 891

Rice, W. K. M., Armitage, P. J., Bate, M. R., & Bonnell, I. A. 2003, MNRAS, 339, 1025

Rice, E. L., Barman, T. S., McLean, I. S., Prato, L., & Kirkpatrick, J.D. 2009, ApJ, submitted

Saumon, D., Chabrier, G., & van Horn, H. M. 1995, ApJS, 99, 713

Siegler, N., Close, L. M., Cruz, K. L., Martín, E. L., & Reid, I. N. 2005, ApJ, 621, 1023

Siegler, N., Close, L. M., Mamajek, E. E., & Freed, M. 2003, ApJ, 598, 1265

Simon, M., Dutrey, A., & Guilloteau, S. 2000, ApJ, 545, 1034

Simon, M., Bender, C., & Prato, L. 2006, ApJ, 644, 1183

Song, I., Zuckerman, B., & Bessell, M. S. 2003, ApJ, 599, 342

Stamatellos, D., & Whitworth, A. P. 2009, MNRAS, 392, 413

Stassun, K. G., Mathieu, R. D., & Valenti, J. A. 2006, Nature, 440, 311

Steffen, A. T., et al. 2001, AJ, 122, 997

Swenson, F. J., Faulkner, J., Rogers, F. J., & Iglesias, C. A. 1994, ApJ, 425, 286

Tamazian, V. S., Docobo, J. A., White, R. J., & Woitas, J. 2002, ApJ, 578, 925

Torres, G., Guenther, E. W., Marschall, L. A., Neuhäuser, R., Latham, D. W., & Stefanik, R. P. 2003, AJ, 125, 825

Umbreit, S., Burkert, A., Henning, T., Mikkola, S., & Spurzem, R. 2005, ApJ, 623, 940

van Dam, M. A., et al. 2006, PASP, 118, 310

Vrba, F. J., et al. 2004, AJ, 127, 2948

Warren, S. J., et al. 2007, MNRAS, 381, 1400

Watkins, S. J., Bhattal, A. S., Boffin, H. M. J., Francis, N., & Whitworth, A. P. 1998, MNRAS, 300, 1205

Webb, R. A., Zuckerman, B., Platais, I., Patience, J., White, R. J., Schwartz, M. J., & McCarthy, C. 1999, ApJL, 512, L63

Weinberg, M. D., Shapiro, S. L., & Wasserman, I. 1987, ApJ, 312, 367

Weintraub, D. A., Saumon, D., Kastner, J. H., & Forveille, T. 2000, ApJ, 530, 867

White, R. J., Ghez, A. M., Reid, I. N., & Schultz, G. 1999, ApJ, 520, 811

White, R. J., et al. 2009, in prep

Whitworth, A. P., & Stamatellos, D. 2006, A&A, 458, 817

Whitworth, A. P., & Zinnecker, H. 2004, A&A, 427, 299

Wizinowich, P., et al. 2000, PASP, 112, 315

Wizinowich, P. L., et al. 2006, PASP, 118, 297

Woitas, J., Köhler, R., & Leinert, C. 2001, A&A, 369, 249

Yelda, S., Lu, J. R., Ghez, A. M., Clarkson, W., & Anderson, J. 2009, in prep

Zapatero Osorio, M. R., et al. 2008, A&A, 477, 895

Zapatero Osorio, M. R., Béjar, V. J. S., Martín, E. L., Rebolo, R., Barrado y Navascués, D., Bailer-Jones, C. A. L., & Mundt, R. 2000, Science, 290, 103

Zapatero Osorio, M. R., Lane, B. F., Pavlenko, Y., Martín, E. L., Britton, M., & Kulkarni, S. R. 2004, ApJ, 615, 958

Zuckerman, B., & Song, I. 2004, ARAA, 42, 685